

Spectroscopic Signatures of Doorway-Mediated Intersystem Crossing

by

Kyle Lee Bittinger

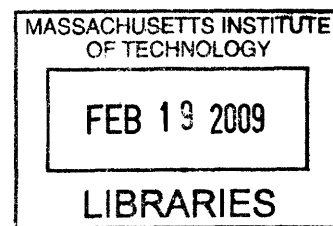
Submitted to the Department of Chemistry
in partial fulfillment of the requirements for the degree of
Doctor of Philosophy

at the

MASSACHUSETTS INSTITUTE OF TECHNOLOGY

February 2009

© Massachusetts Institute of Technology 2009. All rights reserved.



Author
Department of Chemistry
October 13, 2008

Certified by
Robert W. Field
Haslam and Dewey Professor of Chemistry
Thesis Supervisor

Accepted by
Robert W. Field
Chairman, Department Committee on Graduate Theses

This doctoral thesis has been examined by a Committee of the Department of Chemistry that included

Professor Sylvia T. Ceyer |
(Chairperson)

Professor Andrei Tokmakoff A . . .
..... U

Professor Robert W. Field ^
(Thesis Supervisor)

Spectroscopic Signatures of Doorway-Mediated Intersystem Crossing

by

Kyle Lee Bittinger

Submitted to the Department of Chemistry
on October 13, 2008, in partial fulfillment of the
requirements for the degree of
Doctor of Philosophy

Abstract

Intersystem crossing in acetylene, C_2H_2 , is described by a doorway-mediated model, where singlet-triplet mixing between the first excited singlet state, S_1 , and the manifold of low-lying $T_{1,2}$ states is controlled by special vibrational levels of the third excited triplet state, T_3 . However, the influence of T_3 doorway states on the $\tilde{A}^1A_u \leftarrow \tilde{X}^1\Sigma_g^+$ spectrum of acetylene is not well characterized for most S_1 vibrational levels. The doorway model is formulated to account for the LIF/SEELEM spectra of S_1 vibrational sublevels that are weakly perturbed by T_3 doorway states. The structure and properties of a doorway-mediated effective Hamiltonian are discussed, and a method for spectral deconvolution is presented for the doorway model. The dependence of fluorescence center-of-gravity on the time delay of a gated integration region is developed as an analysis tool for LIF spectroscopy. Triplet perturbations in the spectra of four S_1 vibrational sublevels are discussed in terms of the doorway model, using this new tool. IR-UV double resonance LIF/SEELEM spectroscopy is used to investigate the role of the torsional and “cis”-bending vibrational modes of S_1 in the promotion of vibrational overlap between levels of S_1 and T_3 . A collisional method for the population of metastable molecules in a pulsed supersonic expansion is presented and discussed.

Thesis Supervisor: Robert W. Field

Title: Haslam and Dewey Professor of Chemistry

Acknowledgments

The ideas and experiments that shaped this thesis were proposed and refined during seven years of weekly meetings and discussion with my thesis advisor, Professor Robert W. Field. His influence permeates each chapter of this document, from the complex-energy effective Hamiltonian formulation to the mercury-photosensitized acetylene experiments. Perhaps the quality of Bob Field that is most contagious is his constantly renewed curiosity, which is driven by a sense that a new, all-revealing spectroscopic experiment is just around the corner. His patient encouragement, thoughtful collaboration, and lightning-fast correspondence were crucial to this work. He has also contributed to the refinement of my taste in blues and American folk music, directing me in particular to the music of Charlie Poole and Hound Dog Taylor. Not only is Bob Field a top-tier spectroscopist, but he knows a good autoharp anthology when he hears one.

My labmates are also to be credited in the realization of this thesis. Wilton Virgo, who entered the group as a postdoc in 2006, worked with me in the trenches (literally, between laser tables) to capture every wavenumber of spectrum presented herein. His ideas, advice, and consistent optimism brought progress in the triplet project from a slow crawl to a steady gallop. I am delighted and confident to hand the triplet project over to a team of capable leaders, Sam Lipoff and Erika Robertson. I know they will find success in any of several avenues that are currently open for triplet project research. Former project members Ryan Thom, Selen Altunata, and Adya Mishra provided a solid foundation to me, and I hope I have done the same for the next generation. I also acknowledge the triplet project UROPs, Shervin Fatehi, Jessica Hagelstein, Yuki Jung, and Jessica Lam, as well as our collaborators, Severine Boyé, Mattijs de Groot, Soji Tsuchiya, and H. Kanamori, for their part in this work.

The last three years of research on the triplet project brought a new dimension of collaboration with the singlet project. As a singlet project postdoc, Hans Bechtel expanded the realm of possibility for experiments in the Field Group. He was a source of experimental inspiration and advice, and it was only with his assistance

that the research presented in Chapter 6 of this thesis was possible. Adam Steeves has helped me so much over the course of my time in the Field group that he deserves the title of honorary postdoc (and I encourage Bob Field to consider a pay raise for him commensurate with that position). Professor Anthony Merer, during the course of his work with the singlet project, gave me important advice and guidance on triplet perturbations, and I thank him as well. Josh Baraban's assistance is cited in Chapter 6, but I would also like to credit his important contributions in both scientific and IT matters. It was on his suggestion that I investigated the relationship between the doorway state energy and the third moment of spectral intensity, detailed in Chapter 3.

Steve Coy has contributed to my growth as a spectroscopist in many group meetings, and also took the time to give me a special education on random matrix theory. Rydberg project members Jason Clevenger, Dan Byun, Jeff Kay, Serhan Altunata, and of course Kirill Kuyanov deserve credit for not only taking the time to consider problems in the land of $S = 1$, but also for expanding my background in Rydberg states, spin $1/2$ systems, and quantum defect theory. Vladimir Petrović deserves a special mention; he has played the role of friend as well as scientist and collaborator. Huzeifa Ismail, honorary Field Group member, was another comrade in the laboratory. Barratt Park and Tony Colombo have not only brought new directions of research to the group, but have also brought a new spirit of friendship to the group as a whole.

Throughout my stay at MIT, my friends have provided me with encouragement, fulfillment, and an escape from the unforgiving world of molecular spectroscopy. Stefan Zajic, Jessica Brooks, Lisa Smith, Ben Scott, Nick McCarthy, Jeff Hipp, and many others have shared in the joys and worries of my life during this work. My fellow audio engineers at WMBR, Bryan Cord, Mike Reed, Andy Hong, and most especially Ramsey Tantawi, acted almost like a second research group for several years. My bandmates, Jeff Breeze, Ben Macri, Joe Mahoney, Kris Thompson, Ben Lucal, and most especially Andy Tefft, also acted as my collaborators and support network during my years at MIT.

My final thanks goes to my wife, Tara Bledsoe, and my wonderful and supportive family. Tara and I were married during my fifth year as a graduate student, and it was only with her love and patience that I was able to accomplish this work. She is truly the love of my life. Tara's family has welcomed me as one of their own from day one, and I acknowledge their love and support. My mom and dad, my brother and my sister-in-law Jessica, my grandmother, and my grandfather, loved me and taught me lessons that I use every day, in and out of the laboratory. Their love and encouragement played a huge role in this work. This thesis is dedicated to my wife Tara, my family, and especially to the memory of my father.

Contents

1	Introduction	35
1.1	Objectives	35
1.2	Spectroscopic investigations of acetylene triplet states	36
1.3	Survey of the low-lying triplet electronic states of acetylene: <i>ab initio</i> calculations	39
1.4	A hierarchy of electronic coupling in acetylene: evidence from Zeeman anticrossing experiments	42
1.5	T_3 -mediated intersystem crossing in acetylene: evidence from laser-induced fluorescence and quantum beats	45
1.6	Detection of laser-excited metastables by surface electron ejection . .	46
1.7	Summary	47
2	Models of doorway-mediated intersystem crossing and their consequences in LIF and SEELEM spectra	51
2.1	Introduction	51
2.2	Don't think of a doorway: three alternate arrangements of the effective Hamiltonian	52
2.2.1	The mixed basis	53
2.2.2	The embedded bright state arrangement	56
2.2.3	Formulation as a complex-energy effective Hamiltonian	60
2.3	Doorway-mediated coupling and SEELEM intensity distribution . . .	68
2.3.1	The bright state term	70
2.3.2	The doorway term	73

2.3.3	The cross term	74
2.4	The local doorway model	75
2.5	The distant doorway model	76
2.6	The local doorway plus direct coupling model	78
2.7	The double doorway model	81
3	Deconvolution of spectral data to produce a doorway-coupling model	
	Hamiltonian	85
3.1	Introduction	85
3.2	Lawrance-Knight-Lehmann deconvolution: Construction of a direct-coupling model Hamiltonian	89
3.3	Extended deconvolution: Construction of a doorway-coupling model Hamiltonian	92
3.4	Application to high-resolution spectra of acetylene	103
3.5	Conclusion	106
4	SEELEM/LIF spectroscopy of acetylene: Spectral signatures of energetically distant doorway levels	109
4.1	Introduction	109
4.2	Theory: $S_1 \sim T_3$ rotational energy level spacing and spin-orbit matrix elements	112
4.3	Theory: Signatures of doorway-mediated intersystem crossing in delayed, incoherent fluorescence measurements	119
4.3.1	Characteristics of an incoherent, high-resolution fluorescence spectrum after a time delay	121
4.3.2	Dependence of the intensity-weighted center of gravity on time delay	125
4.4	Experiment	130

4.5	SEELEM/LIF spectroscopy of four S_1 vibrational levels located at higher energy than the minimum of the $S_1 \sim T_3$ seam of intersection .	132
4.5.1	The 3^24^2 $K'=1$ sublevel: evidence for an energetically distant T_3 doorway level plus a localized T_3 level crossing	133
4.5.2	The 2^13^2 $K'=1$ sublevel: assignment of K_a for an energetically distant T_3 doorway level	138
4.5.3	The 2^23^1 $K'=1$ sublevel: a local T_3 perturbation in the presence of small $S_1 \sim T_3$ matrix elements	143
4.5.4	The 3^3 $K'=2$ sublevel: spectral patterns in the presence of large $S_1 \sim T_3$ matrix elements	147
4.6	Conclusion	151
5	IR-UV double resonance LIF/SEELEM spectroscopy of the 3^34^1 $K'=0$ and 3^36^1 $K'=0$ vibrational sublevels of S_1 acetylene	155
5.1	Introduction	155
5.2	Experiment	157
5.3	Results	159
5.4	Analysis	172
5.4.1	LIF Spectrum: Characterization of mediating T_3 levels	172
5.4.2	SEELEM Spectrum: Characterization of the local manifold of $T_{1,2}$ levels	189
5.5	Discussion	196
5.6	Conclusion	199
6	A pulsed supersonic jet source of molecules in long-lived, electronically excited states	201
6.1	Introduction	201
6.2	Theory: Optical pumping of atomic metastables via two-photon transitions	202
6.3	Experiments: $Xe^* + N_2$	208

6.4	Experiments: $\text{Hg}^* + \text{C}_2\text{H}_2$	215
6.5	Future Work	222
6.6	Conclusions	225
7	Conclusions	227

List of Figures

- 1-1 The tier model is illustrated for two molecules, (a) $(\text{CH}_3)\text{CCCH}$ and (b) $(\text{CH}_3)_3\text{SiCCH}$. The tiers of energy levels are arranged horizontally on the diagram. Nonzero matrix elements between levels in the effective Hamiltonian are indicated by connecting lines. The figure is reproduced from Reference [117]. 37
- 1-2 Principal molecular orbital configurations for the four lowest energy *trans*-bent excited states of acetylene [137]. The vertical position of an orbital in the diagram does not accurately reflect its total energy: stabilization of the $\pi^*(a_g)$ antibonding orbital in *trans*-bent geometries is much larger than the de-stabilization of the $\pi(a_u)$ bonding orbital [133]. The four electronic states, T_1 , T_2 , T_3 , and S_1 , are listed in order of increasing energy (T_e). For simplicity, the fully filled orbitals, $(1\sigma_g)^2(1\sigma_u)^2(2\sigma_g)^2(2\sigma_u)^2(3\sigma_g)^2$, are not shown. The S_1 and T_3 electronic states differ by one antibonding spin-orbital. 40
- 1-3 Summary of normal modes for planar, *trans*-bent S_1 (\tilde{A}^1A_u) acetylene. The bending modes, ν_3 , ν_4 , and ν_6 , are of particular interest for their role in $S_1 \sim T_3$ mixing and cis-trans isomerization in S_1 41

1-4	Diagram of the LIF/SEELEM apparatus. Laser radiation in the UV is provided by the frequency doubled output of a Nd:YAG-pumped dye laser. The laser radiation enters the vacuum chamber (not shown), and crosses the path of the molecular beam, indicated by a dashed line, approximately 2.5 cm downstream from a pulsed nozzle. Fluorescence is gathered by $f/4$ optics at the point of laser excitation, passes through a UG-11 filter, and is collected by a photomultiplier tube (PMT). Laser-excited metastable molecules travel through a 3 mm diameter skimmer and into a second, differentially pumped vacuum chamber. Approximately 34 cm from the point of laser excitation, the metastables collide with the metal surface of the SEELEM detector, and ejected electrons are collected by an electron multiplier, located immediately below the metal surface.	48
2-1	Schematic of a doorway-mediated Hamiltonian. A single bright basis state, $ s\rangle$, is connected to a single doorway basis state, $ \ell\rangle$, which is, in turn, connected to a block of prediagonalized dark states, $\{ m\rangle\}$	53
2-2	Schematic of a doorway-mediated ISC Hamiltonian after transformation to a mixed basis. The mixed basis states $ \tilde{s}\rangle$ and $ \tilde{\ell}\rangle$ have mixed bright~doorway character, and both have matrix elements with the ensemble of dark states.	54
2-3	Shown in the plot are contributions to the fractional bright state character in a nominal dark eigenstate $ M\rangle$ arising from three terms: borrowing through the mixed basis state $ \tilde{s}\rangle$, borrowing through the other mixed basis state $ \tilde{\ell}\rangle$, and a cross term. Also shown is the ratio of the cross term to the square terms, which exhibits a maximum at the energy midpoint between $E_{\tilde{s}}$ and $E_{\tilde{\ell}}$	57
2-4	Schematic of a doorway-mediated Hamiltonian arranged according to the embedded bright state picture. The form of the matrix is equivalent to a direct coupling model.	58

2-5 Widths of the nominal bright and doorway eigenstates in a complex-energy doorway Hamiltonian. To demonstrate the weak coupling regime (left), the coupling matrix element $V_{s\ell}$ is set to 0.25 times the magnitude of the doorway width Γ_ℓ . For the intermediate coupling regime (center), $V_{s\ell} = \Gamma_\ell$; for the strong coupling regime (right), $V_{s\ell} = 4\Gamma_\ell$ 62

2-6 Dark state intensity distributions for a doorway coupled system where $\delta\epsilon_{s\ell} = 0.5$ and $\delta\Gamma_{s\ell} = 1$. Three coupling regimes result from the relative magnitude of $V_{s\ell}$: weak coupling ($V_{s\ell} = \delta\Gamma_{s\ell}/10$), intermediate coupling ($V_{s\ell} = \delta\Gamma_{s\ell}$), and strong coupling ($V_{s\ell} = 10\delta\Gamma_{s\ell}$). Note the different scales of both the x and y axes for each plot. The widths Γ_S of the $|S\rangle$ intensity term are $0.005\Gamma_\ell$, $0.26\Gamma_\ell$, and $0.48\Gamma_\ell$ for the weak, intermediate, and strong coupling regimes, respectively. 65

2-7 A comparison of the intensity distribution results from direct diagonalization (solid line) and perturbation theory (dashed line) in the weak coupling regime. 66

2-8 A doorway-mediated Hamiltonian in the strong coupling limit, where the mixing is complete in both the real and imaginary parts of the eigenfunctions. 67

2-9 Schematic of a double doorway Hamiltonian. A single bright basis state $|s\rangle$ is connected to a local doorway basis state $|\ell\rangle$ and a distant doorway basis state $|\ell'\rangle$, which are, in turn, connected to a block of prediagonalized dark states $\{|m\rangle\}$ 81

- 3-1 Top: Diagram of a direct-coupling model Hamiltonian. One vector of matrix elements connects a single bright state, $|s\rangle$, to a prediagonalized set of dark basis states, $\{|m\rangle\}$. Middle: Diagram of a doorway-coupling Hamiltonian. A single bright basis state, $|s\rangle$, is connected to a single doorway basis state $|\ell\rangle$, which is connected in turn to a pre-diagonalized block of dark states, $\{|m\rangle\}$. Bottom: Diagram of a doorway-coupling Hamiltonian in the embedded bright state arrangement. The form of the matrix is equivalent to the direct-coupling model, without the need for a matrix rotation. All model Hamiltonians in the figure are symmetric and real; only nonzero elements in the upper diagonal are shown. 88
- 3-2 Thick vertical lines: Dark basis state energies and matrix elements obtained by discrete LKL deconvolution of a portion of the NO_2 spectrum reported by Smalley *et. al.* [107]. The single bright state energy obtained from deconvolution is displayed as a vertical line in the negative direction. The original absorption spectrum is shown as a set of gaussian lineshapes superimposed on the deconvolution results. 97
- 3-3 Thick vertical lines: Dark basis state energies and matrix elements obtained by an extended LKL deconvolution of a portion of the NO_2 spectrum reported by Smalley *et. al.* [107]. The bright state energy obtained from the first stage of deconvolution is displayed as a dashed vertical line in the positive direction, scaled to the bright~doorway matrix element. The energy of the single doorway state is displayed as a vertical line in the negative direction. The original absorption spectrum is shown as a set of Gaussian lineshapes superimposed on the deconvolution results. Note that the energies for the combined set of bright and dark states in the doorway-coupled basis satisfy the usual level trapping rules for dark states in a direct-coupled basis. 98

3-4	Interaction density spectrum for coupling to the doorway state, computed from a portion of the NO ₂ spectrum reported by Smalley <i>et. al.</i> [107]. These results are in agreement with those of Cable and Rhodes (compare to their Figure 11) [20].	100
3-5	Comparison of discrete and continuous extended deconvolution results for the same spectrum. The dark state energies and squared matrix elements in the discrete formulation correspond to the peaks of the interaction density spectrum in the continuous formulation. The rising wings of the interaction density spectrum arise from the nonzero tails of the Lorentzian peaks, which cause the inverse of the Green's function to accumulate at the edges of the computed spectrum.	101
3-6	Continuous deconvolution carried out for Lorentzian broadened line-shapes of 6 cm ⁻¹ fwhm, corresponding to 1/2 the average level spacing of the spectrum. The continuous deconvolution result is consistent with the discrete result to a resolution of 6 cm ⁻¹ . The rising wings of the interaction density spectrum arise from the nonzero tails of the Lorentzian peaks, which cause the inverse of the Green's function to accumulate at the edges of the computed spectrum.	102
3-7	Comparison between Altunata and Field's S parameter and the bright state - doorway state energy difference ($E_s - E_\ell$) obtained from extended LKL deconvolution [5]. To coincide with the formula for doorway state energy, the S parameter results are scaled by the squared bright~doorway matrix element, which is equal to the variance of spectral intensity.	105

3-8	The S_1 and T_3 basis state energies obtained from extended LKL deconvolution are shown together with the reduced term values of Mishra <i>et al.</i> [85]. Top: e -symmetry basis state energies obtained from R-branch transitions. Bottom: f -symmetry basis state energies obtained from Q-branch transitions. The deperturbed energies from deconvolution lie between the nominal S_1 and T_3 eigenstate energies inferred from the spectrum, as they must.	107
4-1	Approximate energy separation between singlet and triplet vibrational sublevels, plotted as a function of J . The relative energy of the F_2 spin component is approximately constant. The relative energies of the F_1 and F_3 spin components change at a rate of approximately 2 cm^{-1} per J' . Dotted lines indicate the approximate average vibrational level spacing for the S_1 and T_3 electronic states in the $45,000 \text{ cm}^{-1}$ energy region.	115
4-2	Rotational factors of spin-orbit matrix elements between rovibrational levels of the S_1 and T_3 electronic states, $K_S=1$ ($J \geq K_S$). The plot includes matrix elements for the F_3 ($\Delta N = +1$) and F_1 ($\Delta N = -1$) components of a T_3 sublevel with $K_T = 0, 1, 2$. In all cases, the rotational factors vary by less than a factor of 2 as a function of J	117
4-3	Rotational factors of spin-orbit matrix elements between rovibrational levels of the S_1 and T_3 electronic states, $K_S=2$. The plot includes matrix elements for the F_3 ($\Delta N = +1$) and F_1 ($\Delta N = -1$) components of a T_3 sublevel with $K_T = 1, 2, 3$. The rotational factors are essentially the same as those for $K_S = 1$	118
4-4	The intensity of fluorescence from a mixed eigenstate at time $R = t/\tau_s$, plotted as a function of bright state character.	124
4-5	Dependence of the intensity ratio I_1/I_2 on time delay for a model two-state system.	127

4-6	Time development of the center of gravity for a model system containing two basis states.	128
4-7	The location of a rapid shift in center of gravity (within several units of $\tau_s = 270$ ns) may be used to infer the $S_1 \sim T_3$ mixing fraction. The characteristic time of the shift is defined by the value of delay time where the relative intensities of the nominal S_1 eigenstate and the nominal $T_{1,2}$ eigenstates are equal. The mixing fraction is plotted here as a function of the location of a rapid shift in center of gravity, defined as the delay time where $I_1 = I_2$	129
4-8	Simultaneously recorded SEELEM (upper trace) and LIF (lower trace) spectra of the 3^24^2 $K' = 1$ sublevel of the \tilde{A}^1A_u state of C_2H_2 . The LIF spectrum is integrated in two time regions: an early time window ($0.5\tau_s - 2\tau_s$, solid trace) and a delayed time window ($10\tau_s - 18\tau_s$, dashed trace). The peak positions are blueshifted in the delayed fluorescence spectrum for all transitions, with the exception of Q(2). Interactions with a remote perturber level of slightly lower energy than the nominal S_1 level are apparent in the delayed fluorescence spectrum of the Q(2) and R(1) transitions.	134
4-9	Dependence of the intensity-weighted center of gravity on delay for a series of individually resolved transitions, Q(1-3) (top), and R(0-3) (bottom), in the LIF spectrum of 3^24^2 $K' = 1$. Local perturbations in the Q(2) and R(1) transitions cause the behavior of the center of gravity to be different from those of the other transitions as the delay time is increased.	135

- 4-10 Simultaneously recorded SEELEM (upper trace) and LIF (lower trace) spectra of the 2^13^2 $K'=1$ sublevel of the \tilde{A}^1A_u state of C_2H_2 . The LIF spectrum is integrated in two time regions: an early time window ($0.5\tau_s - 2\tau_s$, solid trace) and a delayed time window ($10\tau_s - 18\tau_s$, dashed trace). The Q(1) and Q(2) transitions are redshifted in the delayed fluorescence spectrum, in contrast to the Q(3,4,5,6) transitions. The upper states of the P(2) and Q(1) transitions, with the same J' but opposite parity, show similar redshifts in the delayed fluorescence spectrum. 139
- 4-11 Dependence of the intensity-weighted center of gravity on delay for a series of individually resolved rotational transitions, Q(1-6), in the LIF spectrum of 2^13^2 $K'=1$. The center of gravity of the Q(1) and Q(2) transitions is identical to the peak positions in the SEELEM spectrum at delay $> 15\tau_s$ 140
- 4-12 Energy level diagram of the $K_T = 1, 2$ sublevels of a possible T_3 doorway state. In this possible scenario, which is ruled out for the S_1 2^13^2 $K'=1$ sublevel, a $K_S = 1$ sublevel is perturbed by both the $K_T = 1$ and $K_T = 2$ sublevels of the same T_3 vibrational level. The T_3 sublevels are separated by an energy of $30-90\text{ cm}^{-1}$. For two sublevels of the same vibrational level, the relative sign of the spin-orbit matrix element is determined only by a rotational factor. In this case, one rotational factor is positive, and the other is negative. 142
- 4-13 Simultaneously recorded SEELEM (upper trace) and LIF (lower trace) spectra of the 2^23^1 $K'=1$ sublevel of the \tilde{A}^1A_u state of C_2H_2 . The LIF spectrum is integrated in two time regions: an early time window ($0.5\tau_s - 2\tau_s$, solid trace) and a delayed time window ($8\tau_s - 12\tau_s$, dashed trace). The upper states of the Q(1) and R(0) transitions, which have the same quantum number $J' = 1$ but opposite parities, are shifted in opposite directions in the delayed fluorescence spectrum. 144

4-14 Dependence of the intensity-weighted center of gravity on delay for a series of rovibronic transitions, Q(1–4) (top), and R(0–3) (bottom), in the LIF spectrum of 2^23^1 $K'=1$. As delay increases, the center of gravity for the Q(1) transition rapidly increases to its final value, where it matches the peak of the SEELEM distribution at $46007.87+0.03$ cm^{-1} . For the R(0) transition, the center of gravity decreases to $46010.35-0.3$ cm^{-1} at a delay of $18\tau_s$ 145

4-15 Simultaneously recorded SEELEM (upper trace) and LIF (lower trace) spectra of the 3^3 $K'=2$ sublevel of the \tilde{A}^1A_u state of C_2H_2 . The LIF spectrum is integrated in two time regions: an early time window ($0.5\tau_s-2\tau_s$, solid trace) and a delayed time window ($10\tau_s-18\tau_s$, dashed trace). The individual transitions each split into at least two strongly mixed components. Although the energy splitting between the components is on the order of the experimental resolution, the splitting is discernible because the nominal singlet and triplet components have different relative intensities in the early and delayed-LIF spectra. One splitting in the R(4) transition is barely resolved in this spectrum. . . 148

4-16 Dependence of the intensity-weighted center of gravity on delay for a series of individually resolved transitions, R(1–7), in the LIF spectrum of the 3^3 $K'=2$ sublevel. The individual transitions have an overall bias toward lower energies at long delay times, indicating an interaction with a T_3 doorway level at lower energy than the S_1 level. 149

- 5-1 Schematic diagram of the IR-UV double resonance methods used in this study. In the survey method, the Q(1)-Q(5) transitions terminating in the $v_3'' + v_4''$ level of the ground state are pumped at a single IR laser frequency. From the populated f -symmetry rotational levels, Q-branch transitions in the UV are permitted to the $3^34^1 K'=0$ sublevel, and P or R-branch transitions are permitted to the $3^36^1 K'=0$ sublevel. In the individual line method, a single P or R-branch transition is excited in the ground state. In this case, e -symmetry levels of $v_3'' + v_4''$ are excited by the IR laser, and the selection rules for P, R vs. Q branches in the UV are reversed. 161
- 5-2 Simultaneously recorded SEELEM (upper trace) and LIF (lower trace) spectra of the $3^36^1 K'=0$ sublevel of the \tilde{A}^1A_u state of C_2H_2 . The P(2) line of the $\tilde{X}^1\Sigma_g^+ v_3'' + v_4''$ level is used as an intermediate state in the experiment, so only the Q(1) line is observed, according to Figure 5-1. The LIF spectrum is integrated in two time regions: an early time window ($0.5\tau_s - 2\tau_s$, solid trace) and a delayed time window ($10\tau_s - 18\tau_s$, dashed trace). Two additional lines, labeled with dashed markers, are observed in the delayed LIF spectrum on either side of the nominally singlet eigenstate. The intensity envelope of the delayed LIF spectrum closely resembles that of the SEELEM spectrum – this effect is echoed in Figures 5-3 to 5-6. 163
- 5-3 Simultaneously recorded SEELEM (upper trace) and LIF (lower trace) spectra of the $3^36^1 K'=0$ sublevel of the \tilde{A}^1A_u state of C_2H_2 . The P(3) line of the $\tilde{X}^1\Sigma_g^+ v_3'' + v_4''$ level is used as an intermediate state in the experiment, so only the Q(2) line is observed, according to Figure 5-1. The LIF spectrum is integrated in two time regions: an early time window ($0.5\tau_s - 2\tau_s$, solid trace) and a delayed time window ($10\tau_s - 18\tau_s$, dashed trace). A line splitting of $\sim 2 \text{ cm}^{-1}$ is observed in the LIF spectrum, with the longer-lifetime (nominally triplet) component located at higher energy. 164

5-4 Simultaneously recorded SEELEM (upper trace) and LIF (lower trace) spectra of the 3^36^1 $K'=0$ sublevel of the \tilde{A}^1A_u state of C_2H_2 . The P(4) line of the $\tilde{X}^1\Sigma_g^+ v_3'' + v_4''$ level is used as an intermediate state in the experiment, so only the Q(3) line is observed, according to Figure 5-1. The LIF spectrum is integrated in two time regions: an early time window ($0.5\tau_s - 2\tau_s$, solid trace) and a delayed time window ($10\tau_s - 18\tau_s$, dashed trace). The transition at 42038.3 cm^{-1} has a short lifetime, and belongs to an unassigned singlet sublevel. A small line splitting of less than 0.05 cm^{-1} is apparent from the shifted peak position in the delayed LIF spectrum relative to the early LIF spectrum. The longer-lifetime (nominally triplet) component is located to higher energy. 165

5-5 Simultaneously recorded SEELEM (upper trace) and LIF (lower trace) spectra of the 3^36^1 $K'=0$ sublevel of the \tilde{A}^1A_u state of C_2H_2 . The R(3) line of the $\tilde{X}^1\Sigma_g^+ v_3'' + v_4''$ level is used as an intermediate state in the experiment, so only the Q(4) line is observed, according to Figure 5-1. The LIF spectrum is integrated in two time regions: an early time window ($0.5\tau_s - 2\tau_s$, solid trace) and a delayed time window ($10\tau_s - 18\tau_s$, dashed trace). A line splitting of $\sim 0.2 \text{ cm}^{-1}$ is observed in the LIF spectrum, with the longer-lifetime (nominally triplet) component located at higher energy. 166

5-6 Simultaneously recorded SEELEM (upper trace) and LIF (lower trace) spectra of the 3^36^1 $K'=0$ sublevel of the \tilde{A}^1A_u state of C_2H_2 . The R(4) line of the $\tilde{X}^1\Sigma_g^+ v_3'' + v_4''$ level is used as an intermediate state in the experiment, so only the Q(5) line is observed, according to Figure 5-1. The LIF spectrum is integrated in two time regions: an early time window ($0.5\tau_s - 2\tau_s$, solid trace) and a delayed time window ($10\tau_s - 18\tau_s$, dashed trace). No line splittings are observed in the LIF spectrum. . . 167

- 5-7 Diagram of transitions among M_J sublevels terminating in the $J' = 0$ rotational level of $3^36^1 K'=0$. When the IR and UV lasers are polarized in a perpendicular geometry, transitions terminating in the $J' = 0$ rotational level of the excited state are permitted according to the selection rules $\Delta M_J = 0$ (first step), $\Delta M_J = \pm 1$ (second step). When the IR and UV lasers are polarized in a parallel geometry, transitions terminating in the $J' = 0$ rotational level of the excited state are forbidden according to the selection rule $M_J = 0 \leftrightarrow M_J = 0$ when $\Delta J = 0$ 169
- 5-8 Simultaneously recorded SEELEM (upper trace) and LIF (lower trace) spectra of the $3^36^1 K'=0$ sublevel of the \tilde{A}^1A_u state of C_2H_2 . The Q-branch of the $\tilde{X}^1\Sigma_g^+ v_3'' + v_4''$ level is used as an intermediate transition in the experiment. As a result, P- and R-branch lines are observed into the upper state, according to Figure 5-1. The P(1) transition to the upper state is forbidden in a parallel IR-UV laser polarization geometry. A spectrum recorded with this laser geometry is shown as a dashed line. Lines appearing unambiguously in the SEELEM spectrum are indicated by solid arrows. Lines indicated by dashed arrows are more uncertain. 170
- 5-9 Simultaneously recorded SEELEM (upper trace) and LIF (lower trace) spectra of the $3^36^1 K'=0$ sublevel of the \tilde{A}^1A_u state of C_2H_2 . The Q-branch of the $\tilde{X}^1\Sigma_g^+ v_3'' + v_4''$ level is used as an intermediate transition in the experiment. As a result, P- and R-branch lines are observed into the upper state, according to Figure 5-1. The LIF spectrum is integrated in two time regions: an early time window ($0.5\tau_s - 2\tau_s$, solid trace) and a delayed time window ($10\tau_s - 18\tau_s$, dashed trace). A line splitting of $\sim 2 \text{ cm}^{-1}$ is observed in the LIF spectrum, with the longer-lifetime (nominally triplet) component located at higher energy. 171

- 5-10 Simultaneously recorded SEELEM (upper trace) and LIF (lower trace) spectra of the 3^34^1 $K'=0$ sublevel of the \tilde{A}^1A_u state of C_2H_2 . The Q-branch of the $\tilde{X}^1\Sigma_g^+ v_3'' + v_4''$ level is used as an intermediate transition in the experiment. As a result, Q-branch lines are observed into the upper state, according to Figure 5-1. The LIF spectrum is integrated in two time regions: an early time window ($0.5\tau_s - 2\tau_s$, solid trace) and a delayed time window ($10\tau_s - 18\tau_s$, dashed trace). Line splittings ranging from 0.06 to 0.3 cm^{-1} are observed in the delayed LIF spectrum of all rotational lines. With one exception, the longer-lifetime (nominally triplet) components are located at lower energy than the shortest-lifetime (nominally singlet) component. 173
- 5-11 Simultaneously recorded SEELEM (upper trace) and LIF (lower trace) spectra of the 3^34^1 $K'=0$ sublevel of the \tilde{A}^1A_u state of C_2H_2 . The P(3) line of the $\tilde{X}^1\Sigma_g^+ v_3'' + v_4''$ level is used as an intermediate state in the experiment, so only the P(2) line is observed into the upper state, according to Figure 5-1. The LIF spectrum is integrated in two time regions: an early time window ($0.5\tau_s - 2\tau_s$, solid trace) and a delayed time window ($10\tau_s - 18\tau_s$, dashed trace). A line splitting of -0.2 cm^{-1} is observed in the delayed fluorescence, confirming the assignment of the low-energy component as $J' = 1$ 174
- 5-12 Rotational factors of spin-orbit matrix elements between rovibrational levels of the S_1 and T_3 electronic states, where $K_S=0$. A $K_S=0$ level may mix with T_3 levels with $K_T = 0, 1$. Spin orbit perturbations are forbidden according to parity when $\Delta K = \Delta N = 0$ 182
- 5-13 Diagram of spin-orbit rotational selection rules between the S_1 3^34^1 , 3^36^1 $K'=0$ sublevels and T_3 sublevels with $K_T = 0$. When $K_T = K_S = 0$, each singlet sublevel may only mix with zero-order triplet sublevels of the same vibrational symmetry. 184

- 5-14 Diagram of spin-orbit rotational selection rules between the S_1 3^34^1 , 3^36^1 $K'=0$ sublevels and T_3 sublevels with $K_T = 1$. In this case, the singlet sublevels are permitted to mix with a zero-order triplet sublevel of any vibrational symmetry. 185
- 5-15 Lorentzian fitting results for the $J' = 1 - 5$ SEELEM spectra of the 3^36^1 $K' = 0$ sublevel. The parameter Γ , equal to the half-width at half-maximum of the distribution, is proportional to the product of the $S_1 \sim T_3$ mixing angle and the average $T_3 \sim T_{1,2}$ matrix element. The value of Γ is given in units of cm^{-1} 193
- 5-16 Modified reduced term value plot for the 3^36^1 $K' = 0$ level of S_1 acetylene. An approximate term energy $1.04 J'(J' + 1)$ is subtracted from the total S_1 rotational energies (large markers) and the energies of nominal triplet eigenstates observed in the SEELEM spectrum (small markers). For each SEELEM-detectable state, a horizontal bar denotes the relative magnitude of the spin-orbit matrix element $H_{\ell m}$. The width of the horizontal bars is normalized separately for each value of J' . The energy spacing and matrix elements show a remarkable uniformity, which is expected from an extensively mixed manifold of $T_{1,2}$ levels. 195
- 6-1 Diagram of possible two-photon excitation schemes for population of the 6^3P_0 and 6^3P_2 metastable excited states of Hg. Excitation to the 7^3S_1 level is followed by spontaneous decay to both metastable levels, while excitation to the 6^3D_2 is followed spontaneous decay to only one of the metastable levels, 6^3P_2 . The various schemes, labeled (a)-(e), are described in the text. A dashed arrow is used to indicate two-photon excitation schemes that utilize photons of two different frequencies. 205

- 6-2 Diagram of the interfering excitation pathways in $J' = 1 \leftarrow J'' = 0$ two-photon transitions with equal frequency photons. Any choice of polarization results in equal but opposite amplitudes and for the two possible photon orderings. Since amplitudes for both orderings of the photons are summed and then squared in Equation 6.2, two-photon transition probability is rigorously cancelled by interference between alternate excitation pathways. The figure on the left illustrates the pathways for left and right circularly polarized photons, while the figure to the right illustrates the pathways for z -polarized and right circularly polarized photons. The phase of each transition amplitude is indicated by either a solid or dashed arrow. 207
- 6-3 Potential energy curves and vibrational levels of the three lowest energy triplet electronic states of nitrogen, N_2 . The $A^3\Sigma_u^+$ state is metastable, with a fluorescence lifetime in the hundreds of microseconds. Molecules in the $W^3\Delta_u$ state decay slowly to the near-degenerate $B^3\Pi_g$ electronic state via IR fluorescence. The fluorescence lifetime for $B^3\Pi_g \rightarrow A^3\Sigma_u^+$ emission is several μs . It is this 400–500 nm fluorescence that we measure to observe the preparation of metastable N_2 . Also shown in the figure is the energy of the xenon 3P_2 state, which is known to populate the $v'=5$ level of the nitrogen $B^3\Pi_g$ state in gas-phase collisions [62]. Less is known about electronic energy transfer from Xe into the $W^3\Delta_u$ state of nitrogen. The figure is adapted from Reference [61]. 209
- 6-4 Laser-Induced Fluorescence (LIF) spectrum of the one-color, two-photon transition $Xe^3D_2 \leftarrow \leftarrow^1 S_0$, recorded under static cell conditions. The LIF signal results from spontaneous emission to the metastable 3P_2 state at 823 nm. 211

- 6-5 (Top) Laser-Induced Fluorescence (LIF) spectrum of the one-color, two-photon transition $\text{Xe } ^3D_2 \leftarrow\leftarrow^1 S_0$, recorded in a supersonic expansion. (Bottom) Time dependence of $\text{Xe } ^3D_2 \rightarrow ^3 P_2$ emission (solid trace), compared to a signal that results from scattered laser light (dashed trace, normalized to intensity of Xe fluorescence). The fluorescence signal results from spontaneous emission to the metastable 3P_2 state at 823 nm ($\tau = 28$ ns). 212
- 6-6 Time dependence of $\text{N}_2 B ^3\Pi_g \rightarrow A ^3\Sigma_u^+$ emission, induced by collisions with metastable $\text{Xe}^* (^3P_2)$. The excitation chamber of the SEELEM apparatus was sealed and filled with a 50:50 mixture of Xe and N_2 , to a total pressure of 210 mTorr. Metastable $\text{Xe}^*(^3P_2)$ was populated by spontaneous emission, following the $6 ^3D_2 \leftarrow\leftarrow 6 ^1S_0$ two-photon transition. 213
- 6-7 Time dependence of $\text{Xe } 6 ^3D_2 \rightarrow 6 ^3P_2$ (top plot) and $\text{N}_2 B ^3\Pi_g \rightarrow A ^3\Sigma_u^+$ (bottom plot) emission, following the two-photon excitation of $\text{Xe } (^3D_2)$ in a supersonic expansion. The xenon and nitrogen emission signals occur on vastly different timescales. Xenon fluorescence (823 nm, $\tau = 28$ ns) is emitted when the optically excited state decays spontaneously to the metastable $6 ^3P_2$ state. Nitrogen molecules are electronically excited during the expansion process by collisions with metastable xenon atoms. Near-resonant vibrational levels of the nitrogen $B ^3\Pi_g$ state decay spontaneously to the metastable $A ^3\Sigma_u^+$ state ($\tau \approx 10 \mu\text{s}$), accompanied by 600–800 nm fluorescence. 214
- 6-8 Diagram of the heated pulsed valve developed for experiments with mercury. The “Bern Valve” can be safely heated to 250° C. A small vial of mercury is housed in the heated region, close to the nozzle orifice (far right). 216

6-9	SEELEM-TOF spectra of several vibrational bands of \tilde{A} phenylacetylene. Yttrium was used as a low work function surface in the experiment. The excitation laser was tuned to the frequency of highest intensity in each band. The bands are labeled according to their frequency above the \tilde{A} state origin.	218
6-10	Laser-Induced Fluorescence (LIF) spectrum of the one-color, two-photon transition $\text{Hg } 6^3D_2 \leftarrow\leftarrow 6^1S_0$, recorded under static cell conditions. The LIF signal results from spontaneous emission to the metastable 6^3P_2 state at 365 nm.	219
6-11	SEELEM time of flight (TOF) detection of metastable mercury produced via the direct excitation $\text{Hg}^*(6^3P_2) \leftarrow \text{Hg}(6^1S_0)$ at 44042.98 cm^{-1} . The pulsed valve was heated to 250° C to increase the number density of mercury. The two traces are recorded in repeated experiments.	220
6-12	Comparison of signal to background in the SEELEM time of flight (TOF) detection of metastable mercury produced via the direct excitation $\text{Hg}^*(6^3P_2) \leftarrow \text{Hg}(6^1S_0)$ at 44042.98 cm^{-1} . The lighter trace is recorded with the pulsed valve on, and the black trace is recorded with the valve off.	221
6-13	Simultaneously recorded LIF and SEELEM spectra for the two-color, stepwise excitation of $\text{Hg}(^3S_1)$ via the 3P_1 level. An interference filter was used to record only $\text{Hg}(^3S_1) \rightarrow \text{Hg}(^3P_2)$ emission, which results in the population of metastable Hg atoms. The SEELEM spectrum shows the intensity of metastables that survive a $700 \mu\text{s}$ flight time. The structure in the atomic lineshape is the result of hyperfine splittings in mercury.	223

6-14 SEELEM spectrum of the two-color, stepwise excitation of $\text{Hg}(^3S_1)$ via the 3P_1 level. The lower spectrum shows mercury seeded in Xe gas, while the upper spectrum shows mercury seeded in acetylene. The larger overall signal level in the mercury/acetylene mixture is the result of electronic excitation transfer between $\text{Hg}(^3P_2)$ and $\text{C}_2\text{H}_2(T_3)$. The bern nozzle was used for both measurements, heated to 250°C 224

List of Tables

2.1	Eigenstate energy difference and width of the nominal bright eigenstate $ S\rangle$ for the systems depicted in Figure 2-6. In the weak coupling regime, the energy separation of the eigenstates $ S\rangle$ and $ L\rangle$ is approximately that of the zero-order states $ s\rangle$ and $ \ell\rangle$. The nominal bright eigenstate $ S\rangle$ borrows little coupling width from the doorway state, and remains narrow. In the strong coupling regime, the eigenstates are separated in energy by $2V_{s\ell}$ and have similar widths.	64
3.1	Key parameters of the doorway-coupling model Hamiltonian may be calculated directly from the absorption spectrum without LKL deconvolution. The bright state energy, bright~doorway matrix element, and doorway state energy have simple relationships to the moments of the spectrum. For clarity, moments of the absorption spectrum are defined explicitly in the table.	96
3.2	Extended deconvolution results for the $3_0^3K_0^1$ vibrational subband of S_1 acetylene. The energies of the zero-order bright state, E_s , and doorway state, E_ℓ , are given, as well as the zero-order energy difference, $\Delta E_{s\ell}$, and bright~doorway matrix element, $H_{s\ell}$. All values are in units of cm^{-1}	104

4.1	The four acetylene S_1 vibrational levels considered in this study, listed here, have total vibronic energies in the critical region above the minimum of the $S_1 \sim T_3$ electronic seam of intersection ($\simeq 45300 \text{ cm}^{-1}$) and below the first dissociation barrier ($\simeq 46300 \text{ cm}^{-1}$) [88]. An order-of-magnitude estimate of the observed SEELEM:LIF intensity ratio is included.	133
5.1	Variance of the integrated LIF spectrum for each transition observed in the S_1 3^34^1 $K'=0$ and 3^36^1 $K'=0$ sublevels. The quantity $\sqrt{\sigma_{LIF}^2}$ is a lower bound for the $S_1 \sim T_3$ doorway matrix element, H_{sl} . Also shown is the time-integrated center of gravity for each transition, E_{ave} , as well as the integration region used in the analysis. All values are in units of cm^{-1}	179
5.2	Spin-orbit perturbation selection rules between the S_1 3^34^1 , 3^36^1 vibrational levels and vibrational levels of the T_3 electronic state. Matrix elements for spin-orbit interaction may be nonzero when the vibronic symmetry of the singlet and triplet levels transforms as the appropriate molecule-fixed spin function, Γ_σ . When $\Delta K = 0$, singlet sublevels may only mix with T_3 sublevels of the same vibrational symmetry. The restriction is lifted when $\Delta K = 1$	181
5.3	The vibrational normal modes of the S_1 and T_3 electronic states. The mode number of the torsional mode is changed in T_3 relative to S_1 , because g/u symmetry operations are not present in the C_2 molecular symmetry group of T_3	183

5.4 Calculated vibrational overlap integrals between $S_1\ 3v_3 + v_4$ and levels of diabaticized T_3 within an energy separation of 300 cm^{-1} . The energies and vibrational overlap integrals are calculated in the harmonic approximation, according to the methods outlined by Thom and coworkers [122]. Integrals with an absolute magnitude of less than 1×10^{-6} are not shown, including those that are zero by symmetry. The five vibrational levels of T_3 with the largest absolute vibrational overlap integrals are marked with a (\triangleright). One T_3 level, containing 6 quanta of the *trans*-bending vibration (ν_4), is calculated to have an extremely large vibrational overlap integral (~ 0.1) with $S_1\ 3v_3 + v_4$. Overall, the T_3 *trans*-bending vibration and torsional vibration (ν_2) are observed to promote vibrational overlap. The mean and median of the absolute values of the T_3 vibrational overlap integrals for $S_1\ 3v_3 + v_4$ are shown below the table. 187

5.5 Calculated vibrational overlap integrals between $S_1\ 3v_3 + v_6$ and levels of diabaticized T_3 within an energy separation of 300 cm^{-1} . The energies and vibrational overlap integrals are calculated in the harmonic approximation, according to the methods outlined by Thom and coworkers [122]. Integrals with an absolute magnitude of less than 1×10^{-6} are not shown, including those that are zero by symmetry. The five vibrational levels of T_3 with the largest absolute vibrational overlap integrals are marked with a (\triangleright). One T_3 level, containing 3 quanta of the *trans*-bending vibration (ν_4) and one quantum of the *cis*-bending vibration (ν_6), is calculated to have an extremely large vibrational overlap integral (~ 0.2) with $S_1\ 3v_3 + v_6$. All five T_3 levels with the largest absolute vibrational overlap factors contain a combination of the T_3 *trans* and *cis*-bending vibrations (ν_4 and ν_6). The mean and median of the absolute values of the vibrational overlap integrals for $S_1\ 3v_3 + v_6$ are larger than those for $S_1\ 3v_3 + v_4$ by less than a factor of two. . . 188

5.6	<p>Estimation of the product $\alpha H_{\ell m}$ from the SEELEM spectra of five transitions in $S_1 \ 3^3 6^1 \ K'=0$. The quantity α represents the $S_1 \sim T_3$ mixing angle in a single doorway-mediated effective Hamiltonian, and the $H_{\ell m}$ represents the doorway $\sim T_{1,2}$ matrix element (held constant) in a simple statistical coupling model. The fitted Lorentzian width for the SEELEM spectrum, Γ_{SEELEM}, and the directly-counted density of $T_{1,2}$ states, ρ_m, are used to determine $\alpha H_{\ell m}$.</p>	192
6.1	<p>Calculated two-photon transition probabilities for the five excitation schemes discussed in the text. The calculation indicates that one color TPA to $\text{Hg}^*(7 \ ^3 S_1)$ is exactly zero. Transition probabilities for excitation to the $\text{Hg}^*(6 \ ^3 D_2)$ level are two orders of magnitude larger than the weakly allowed two-color, two-photon transition probabilities for excitation to $\text{Hg}^*(7 \ ^3 S_1)$.</p>	206

Chapter 1

Introduction

1.1 Objectives

Intramolecular decay processes in electronically excited organic molecules are dominated by the properties of triplet states [78, 79]. Molecules in triplet states are long-lived (metastable); optical transitions between triplet states and the ground state violate the selection rule $\Delta S = 0$. Because triplet states are optically inaccessible from the ground state, they are a difficult target for spectroscopists. From a chemical standpoint, molecules in triplet states are energy carriers. The long lifetimes ($\tau > 30 \mu\text{s}$) and chemically significant internal energies ($E_T > 30,000 \text{ cm}^{-1}$) of triplet molecules make them important chemical reaction intermediates [24].

Intersystem Crossing (ISC) is the dynamical manifestation of mixing between singlet and triplet excited states [101, 60, 72, 124]. ISC is understood primarily as a statistical process, where an electronically excited state decays into a bath of undistinguished triplet states. The general behavior of ISC is categorized by the product of the average singlet-triplet matrix element, $\langle H_{sm} \rangle$, and the local vibrational density of triplet states, ρ_m [101, 60, 42]. When $\langle H_{sm} \rangle \rho_m \ll 1$, the system is said to be in the “small-molecule limit.” In the small molecule limit, singlet~triplet mixing may often be treated as a two-level problem, and the properties of the individual singlet and triplet levels may be determined by deperturbation. When $\langle H_{sm} \rangle \rho_m \gg 1$, the system approaches the “large molecule limit.” In that case, the density of triplet

states is so large that the natural width of singlet~triplet mixed eigenstates exceeds the average energy spacing. The problem of singlet~triplet mixing is treated in a statistical manner, based on the average properties of the triplet levels. When $\langle H_{sm} \rangle \rho_m \approx 1$, the system is in the “intermediate case,” characterized by mixing between one singlet level and a small number of discrete triplet levels.

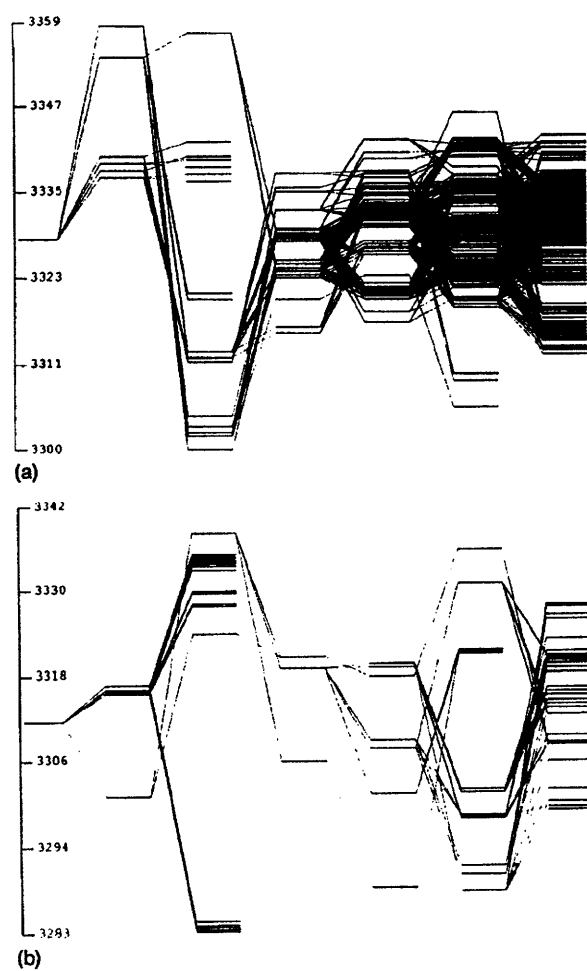
For many molecules, the dynamics of intersystem crossing cannot be classified simply by one of the schemes above. A more general “tier” model is proposed to understand the dynamics of systems where some of the mixing occurs indirectly in the zero-order picture [117, 118]. A diagram of the tier model is shown in Figure 1-1. Such a situation is found in the acetylene molecule, where vibrational levels of the T_3 electronic state mediate mixing between the first excited singlet state, S_1 , and the remaining triplet states, $T_{1,2}$. At energies below the first dissociation limit, the product $\langle H_{S_1 T_3} \rangle \rho_{T_3}$ is much less than 1. Thus, $S_1 \sim T_3$ mixing is categorized in the small molecule limit. Conversely, the product $\langle H_{T_3 T_{1,2}} \rangle \rho_{T_{1,2}}$ is on the order of 1. Mixing between the first and second tiers is categorized in the intermediate case.

In the limit of small T_3 level density, the tier model simplifies to a “doorway-mediated” model. In most cases, one vibrational level of T_3 , called the doorway state, dominates the $S_1 \sim T_3$ mixing. In this thesis, the doorway model for intersystem crossing is examined and characterized for cases where a doorway state is non-degenerate with a perturbed singlet level.

1.2 Spectroscopic investigations of acetylene triplet states

The first spectroscopic detection of acetylene in the triplet state was reported by Burton and Hunziker in 1972 [19]. They produced triplet acetylene molecules by the process of mercury photosensitization. Mercury photosensitization is the electronic excitation of molecules in collisions with excited mercury atoms. The excited atoms are produced by absorption of 254 nm radiation from a mercury resonance lamp. The

Figure 1-1: The tier model is illustrated for two molecules, (a) $(\text{CH}_3)\text{CCCH}$ and (b) $(\text{CH}_3)_3\text{SiCCH}$. The tiers of energy levels are arranged horizontally on the diagram. Nonzero matrix elements between levels in the effective Hamiltonian are indicated by connecting lines. The figure is reproduced from Reference [117].



process has been known to photochemists since the 1920's [24, 22]. Triplet acetylene was detected by collisional excitation of biacetyl, which emits phosphorescence in the visible region of the spectrum [19].

Subsequent experiments investigated the geometry of triplet acetylene. The spectrum of a triplet-triplet transition in the near infrared was observed by Wendt and coworkers [132]. Triplet acetylene was again produced by a method of mercury photosensitization. The spectrum was assigned to the only allowed triplet-triplet transition among the low-lying electronic states of acetylene, $\tilde{d}^3A_2 \leftarrow \tilde{a}^3B_2$. This confirmed the existence of the predicted lowest energy triplet state, *cis*-bent \tilde{a}^3B_2 . Subsequently, Lisy and Klemperer used a low-energy electron gun to produce metastable acetylene molecules in an effusive beam, which they detected via electron ejection from a cesium surface located 80 cm downstream [69, 45]. They measured a negligible electric dipole moment for the lowest energy metastable triplet state, consistent with a *trans*-bent structure at approximately 4.7 eV.

The relative energies of the observed *cis* and *trans* triplet states were the subject of some debate, due to the two apparently conflicting observations. The apparent disparities are explained by the fact that spin-orbit perturbations of high vibrational levels of the ground state are electronically allowed for the *cis*-bent state, but only vibronically allowed for the *trans*-bent state [73]. Since the *cis*-bent triplet is more efficiently mixed with high vibrational levels of the ground state, it is less efficiently detected via electron emission from a metal surface. The observation of Lisy and Klemperer is therefore consistent with the *ab initio* determination that the lowest triplet state of acetylene is *cis*-bent [73].

Electron Energy Loss Spectroscopy (EELS) has provided some more recent low-resolution information on the linear triplet structures [36, 119]. Assignments of the *cis* and *trans*-bent triplet states in condensed phase EELS of acetylene is in general agreement with the theory, which we review in the next section [76].

1.3 Survey of the low-lying triplet electronic states of acetylene: *ab initio* calculations

The valence electronic states of acetylene result from the promotion of one electron from a bonding π orbital to an antibonding π^* orbital. Figure 1-2 shows the principal molecular orbital configurations for the four lowest energy excited electronic states of acetylene [137]. The in-plane antibonding orbital, $\pi^*(a_g)$, is stabilized by a change in CCH bond angle, while the out-of-plane antibonding orbital is not [130, 33, 133]. Balanced against the destabilization of fully filled σ -bonding orbitals, this effect gives rise to potential energy minima in *cis*-bent and *trans*-bent geometries for the low-lying electronic states of acetylene, S_1 , T_1 , T_2 , and T_3 .

The $\tilde{A}^1A_u \leftarrow \tilde{X}^1\Sigma_g$ electronic transition is localized in the *trans*-bent well of acetylene, and the process of intersystem crossing between singlet and triplet excited states proceeds locally in this geometry. For this reason, we no longer explicitly write the geometry when referring to the valence electronic states of acetylene; a *trans*-bent geometry is implied unless otherwise stated. The normal modes of S_1 (\tilde{A}^1A_u) acetylene are summarized in Figure 1-3, for reference.

Potential surfaces for the T_1 and T_2 states of acetylene have been computed in many *ab initio* studies [33, 133, 68, 137, 27, 28, 76, 31, 128]. The T_1 and T_2 states have planar, *trans*-bent equilibrium geometries, similar to S_1 [33, 133, 137]. The minimum of the S_1 electronic surface is above the T_1 and T_2 *cis*-*trans* isomerization barriers [126, 105].

The equilibrium geometry of T_3 is near-linear, *trans*-bent, and twisted approximately 75° out of plane along the torsional coordinate [128, 122]. The electronic energy of T_3 has been determined in several *ab initio* calculations [76, 128, 122]. The most recent calculation of the T_3 electronic surface, carried out by Bryan Wong and coworkers, determined an energy separation $T_e(S_1) - T_e(T_3)$ of only 270 cm^{-1} [122].

Figure 1-2: Principal molecular orbital configurations for the four lowest energy *trans*-bent excited states of acetylene [137]. The vertical position of an orbital in the diagram does not accurately reflect its total energy: stabilization of the $\pi^*(a_g)$ antibonding orbital in *trans*-bent geometries is much larger than the de-stabilization of the $\pi(a_u)$ bonding orbital [133]. The four electronic states, T_1 , T_2 , T_3 , and S_1 , are listed in order of increasing energy (T_e). For simplicity, the fully filled orbitals, $(1\sigma_g)^2(1\sigma_u)^2(2\sigma_g)^2(2\sigma_u)^2(3\sigma_g)^2$, are not shown. The S_1 and T_3 electronic states differ by one antibonding spin-orbital.

	T_1	T_2	T_3	S_1
	B_u	A_u	B_u	A_u
$\pi^*(b_g)$	—	—	—↑	—
$\pi^*(a_g)$	—↑	—↑	—	—↓
$\pi(a_u)$	↑↓	↑	↑	↑
$\pi(b_u)$	↑	↑↓	↑↓	↑↓

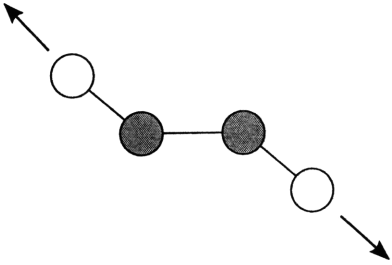
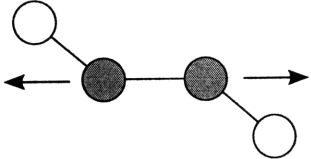
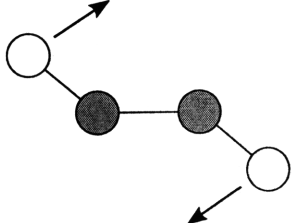
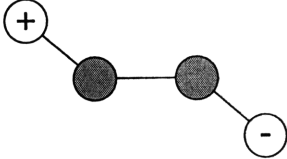
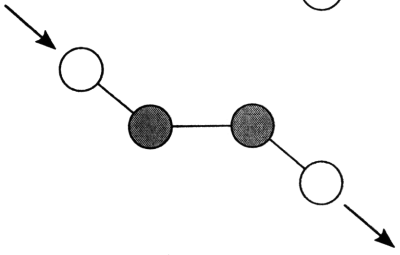
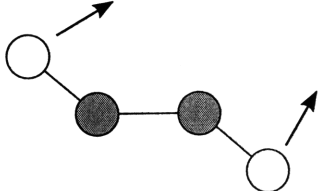
		Symmetry (C _{2h})		
		Mode		Description
	ν_1	a_g		symmetric C-H stretch
	ν_2	a_g		symmetric C-C stretch
	ν_3	a_g		symmetric in-plane bend <i>trans</i> bend
	ν_4	a_u		torsion
	ν_5	b_u		antisymmetric C-H stretch
	ν_6	b_u		antisymmetric in-plane bend <i>cis</i> bend

Figure 1-3: Summary of normal modes for planar, *trans*-bent S_1 (\tilde{A}^1A_u) acetylene. The bending modes, ν_3 , ν_4 , and ν_6 , are of particular interest for their role in $S_1 \sim T_3$ mixing and *cis-trans* isomerization in S_1 .

1.4 A hierarchy of electronic coupling in acetylene: evidence from Zeeman anticrossing experiments

A series of Zeeman Anticrossing (ZAC) experiments, carried out by Dupré and coworkers, established a hierarchy of singlet~triplet mixing in acetylene [41, 38, 39, 37]. The mixing is controlled by the relative magnitudes of matrix elements between electronic states. The conclusions of the Dupré ZAC experiments are of fundamental importance to the work in this thesis. We summarize the experiments in some detail.

In a Zeeman anticrossing experiment, the frequency of an excitation laser is fixed on an optical transition terminating in a nominally singlet rovibronic level of the molecule, and a magnetic field strength is scanned. As the magnetic field is increased, the energies of triplet levels tune through resonance with the singlet. Relative to the singlet level at $E = 0$, the energy of a triplet level is (by the linear Zeeman effect)

$$E - E_0 = g M_s \mu_B (B - B_0), \quad (1.1)$$

where E_0 is zero-field energy of the triplet level, g is the g -factor of the triplet level, M_s is the lab-fixed projection of spin, B_0 is the field required to bring the level to resonance with the singlet, and μ_B is the Bohr magneton [72]. An excited electron that is not coupled to the molecular axis (Hund's case (b) limit) has a g -factor of 2.0023. When the singlet level and one of the weakly interacting background levels are tuned to exactly the same energy by the magnetic field, they become 50:50 mixed. Under these circumstances, the fluorescence intensity decreases by 50%. The *width* of the lineshape in the ZAC spectrum is proportional to the matrix element between the bright state and the interacting level:

$$\Delta B = \frac{4V}{g\mu_B}. \quad (1.2)$$

Dupré and coworkers measured the 0 – 8 T anticrossing spectra of the $J' = 0$, $K' = 0$ rovibronic levels in $S_1 \nu'_3 = 0 - 3$ [41]. The density of mixed-triplet levels was

observed to increase rapidly with excitation in ν_3 . Because the observed density of states is larger than the number of $T_{1,2}$ levels, they concluded that the triplet levels must mix with and contaminate the denser manifold of S_0 levels. However, increased $T_{1,2} \sim S_0$ coupling does not by itself make more mixed-triplet levels accessible to cross with the S_1 level. The S_1 level can only undergo triplet-mediated mixing with S_0 levels over an energy range on the order of the $S_1 \sim T$ matrix element. Therefore, they concluded that coupling between S_1 and a subset of the triplet levels T must increase to make the dense manifold of mixed $T_{1,2} \sim S_0$ levels observable in the experiment.

A rapid increase in anticrossing linewidth with excitation in ν_3 was observed in the same study [41]. Since the linewidth is proportional to the $S_1 \sim T$ matrix element, this supports the conclusion that the $S_1 \sim T$ coupling is increasing with excitation in ν_3 . Accounting for both observations, the authors are able to exclude several possible mechanisms for the increase in anticrossing density. Direct $S_1 \sim S_0$ internal conversion is ruled out because there is no way to account for a sudden increase in $S_1 \sim S_0$ vibrational overlap integrals. The possibility that proximity to the S_0 dissociation limit may increase the total density of states is ruled out because any increase in state density would be accompanied by a decrease in vibrational overlap integrals.

Dupré and Green characterized a wide anticrossing in the $3\nu'_3$ $J' = 0$ $K' = 0$ level, attributed to a triplet level with relative energy $\Delta E = \pm 6.67 \text{ cm}^{-1}$ [38]. Thom and coworkers provide a useful summary of this experiment and its interpretation in their recent article [122]. Many weak anticrossings with nominal S_0 levels can be seen perturbing the strong $S_1 \sim T$ anticrossing. The zero-field matrix element is 0.29 cm^{-1} if $K_T = 0$, or 0.58 cm^{-1} if $K_T = 1$ [122].

In further studies, Dupré and coworkers undertook the individual analysis of approximately 60 anticrossings from the $\nu'_3 = 0 - 2$ spectra [39]. The analysis reveals a large variation in measured g factors, which implies that the $T_{1,2}$ levels are highly mixed. Mixing between triplet states causes the g factors to vary from the expected value of 2. Strong $S_0 \sim T_{1,2}$ mixing is ruled out because it would result in dilution of

$T_{1,2}$ character and cause the g factors to be close to zero. The authors also observed that all quantum beat frequencies vary as a function of field strength, which implies that the perturbing levels have significant triplet character [39]. Direct mixing (“internal conversion”) between S_1 and S_0 is therefore ruled out, since it would cause the frequencies of quantum beats to be approximately constant as a function of magnetic field strength ($M_S = 0$ for all singlet levels).

In the final paper of the series, Dupré derives the product $\rho_{vib} \cdot \langle V \rangle$ from the Fourier transform of anticrossing spectra for $v_3 = 0 - 4$ [37]. He determines that the product $\rho_{vib} \cdot \langle V \rangle$ increases exponentially from $0v_3$ to $4v_3$. The density of vibrational states does not increase appreciably over this energy range, so the effect must arise from an increasing matrix element.

The authors proposed an order of interaction strengths: $T_1 \sim T_2 \gg S_1 \sim T \gg S_1 \sim T_{1,2} \gg S_0 \sim T_{1,2} \gg S_1 \sim S_0^1$ [37]. The first inequality is supported by the large variation in measured g factors, which indicates that the $T_{1,2}$ levels are extensively mixed [39]. The inequality $S_1 \sim T_{1,2} \gg S_0 \sim T_{1,2}$ allows for the large number of S_0 levels detected in the ZAC experiments [41]. The third inequality, $S_0 \sim T_{1,2} \gg S_1 \sim S_0$, implies that the internal conversion process from S_1 to S_0 is triplet-mediated, as supported by the variation in quantum beat frequencies with magnetic field [39].

Two mechanisms are put forward to explain the rapid increase in anticrossing density with excitation in ν'_3 : an $S_1 \sim T_3$ curve crossing and a T_2 linear isomerization barrier [41, 37]. Under the first mechanism, the observed $S_1 \sim T$ coupling is induced by a sparse manifold of T_3 levels, most of which are located outside the tuning range of the magnetic field. Under the second proposed mechanism, the T_2 linear isomerization barrier leads to trapping of $T_{1,2}$ amplitude in the region of the S_1 near-linear turning point. Although the second mechanism is energetically possible, subsequent *ab initio* calculations have determined that the linear T_2 barrier lies too low to account for the ν'_3 dependence of singlet~triplet mixing in S_1 [126, 105, 27, 28, 128].

¹The authors do not explicitly state the inequality $S_1 \sim T \gg S_1 \sim T_{1,2}$, but it is implied by the rapid increase in anticrossing density with excitation in ν'_3 .

1.5 T_3 -mediated intersystem crossing in acetylene: evidence from laser-induced fluorescence and quantum beats

The T_3 -mediated doorway model of acetylene singlet-triplet mixing is further supported by measurements of Laser-Induced Fluorescence (LIF) and Zeeman quantum beats. Ochi and coworkers recorded LIF spectrum of the $3^2 K'=1$, $3^3 K'=1$, and $3^4 K'=1$ sublevels of S_1 acetylene, measuring fluorescence lifetimes and the magnetic field dependence of quantum beats for each observed line [94]. They observe a local triplet perturbation in the $3^3 K'=1$ level, which is predicted to be energetically proximal to a $S_1 \sim T_3$ surface crossing.

The 1994 study of Drabbels and coworkers is perhaps the only experiment, aside from ZAC measurements, to record a fully resolved spectrum of the $3^3 K'=1$ and $3^4 K'=1$ sublevels [34]. They attribute the splittings in the spectrum to direct $S_1 \sim T_{1,2}$ mixing, but this interpretation is inconsistent with the profound changes in singlet-triplet mixing over the 44,000–46,000 cm^{-1} energy range. Subsequent analysis has shown that the Drabbels spectrum contains evidence for a local $S_1 \sim T_3$ perturbation, which mediates the $S_1 \sim T_{1,2}$ mixing [5].

Recent investigations in our laboratory have led to the observation of many more triplet-perturbed levels in S_1 acetylene, as a dividend in the deperturbation of the non-symmetric bending polyads [83, 113]. Levels with excitation in the non-symmetric bending modes are of particular interest because motion along these coordinates may promote or reduce $S_1 \sim T_3$ vibrational overlap integrals. Further information about the non-symmetric bending modes, ν_4 and ν_6 , would shed new light on the nature of $S_1 \sim T_3 \sim T_{1,2}$ dynamics. This problem is addressed in Chapter 5.

1.6 Detection of laser-excited metastables by surface electron ejection

The experimental technique of Surface Electron Ejection by Laser-Excited Metastables (SEELEM) was developed by Ofer Sneh and Ori Cheshnovsky to study intermediate-case ISC in organic molecules such as aniline and isoquiniline [109, 110, 108, 112, 111]. It is based on the well-established technique of metastable detection by electron ejection from surfaces [51]. The use of laser excitation to populate metastable states in SEELEM is somewhat paradoxical because, by definition, direct optical transitions to such states are strongly forbidden. The method of SEELEM detection sidesteps the problem of weak optical transitions by maintaining a low level of background electron signal.

In essence, the SEELEM detector consists of a grounded metal surface and an electron multiplier. To eject an electron from the grounded metal surface of the SEELEM detector, a molecule must possess a vertical excitation energy in excess of the work function, Φ , of the metal. A gold surface was used in most of the experiments described in this thesis, $\Phi = 5.1$ eV. Sneh and coworkers have shown that excess vibrational energy in the molecule does not affect the SEELEM sensitivity [109]. The exception that proves the rule is Wodke's experiments on the NO molecule, where vibrations in the excited state have a drastic impact on the electron affinity [135].

The SEELEM technique was applied to the study of smaller molecules by Wodke and coworkers [100, 35, 89, 55]. The SEELEM apparatus at MIT was designed and built by Kevin Cunningham and Selen Altunata, first as a single-chamber supersonic jet apparatus, and later as a differentially-pumped, two-chamber molecular beam apparatus [29, 2]. The apparatus was refined by subsequent workers, such as Ryan Thom, who re-engineered the mounting and electrical connections for the detector itself [121].

Previous acetylene SEELEM experiments have focused on the $3\nu'_3$ $K'=1$ sublevel of the S_1 electronic state. Humphrey *et. al.* observed an enhancement in SEELEM intensity for rotational lines of $3\nu'_3$ $K'=1$ with $J' < 4$ [55]. They attributed this effect to

a near-degenerate vibrational sublevel of the T_3 electronic state. The SEELEM spectrum of this sublevel was investigated further by Selen Altunata, who demonstrated the relationship between the relative energy of the perturbing T_3 level and moments of the SEELEM intensity distribution [4]. Mishra and Thom provided new SEELEM assignments and carried out a deperturbation of the perturbing triplet sublevel using a reduced term value plot and an effective Hamiltonian fit [85].

A schematic diagram of the current LIF/SEELEM arrangement is shown in Figure 1-4. Laser radiation in the UV is provided by the frequency doubled output of a Nd:YAG-pumped dye laser. The laser radiation enters the vacuum chamber (not shown), and crosses the path of the molecular beam, indicated by a dashed line, approximately 2.5 cm downstream from a pulsed nozzle. Fluorescence is gathered by $f/4$ optics at the point of laser excitation, passes through a UG-11 filter, and is collected by a photomultiplier tube (PMT). Laser-excited metastable molecules travel through a 3 mm diameter skimmer and into a second, differentially pumped vacuum chamber. Approximately 34 cm from the point of laser excitation, the metastables collide with the metal surface of the SEELEM detector. Ejected electrons are collected by an electron multiplier that is located immediately below the metal surface.

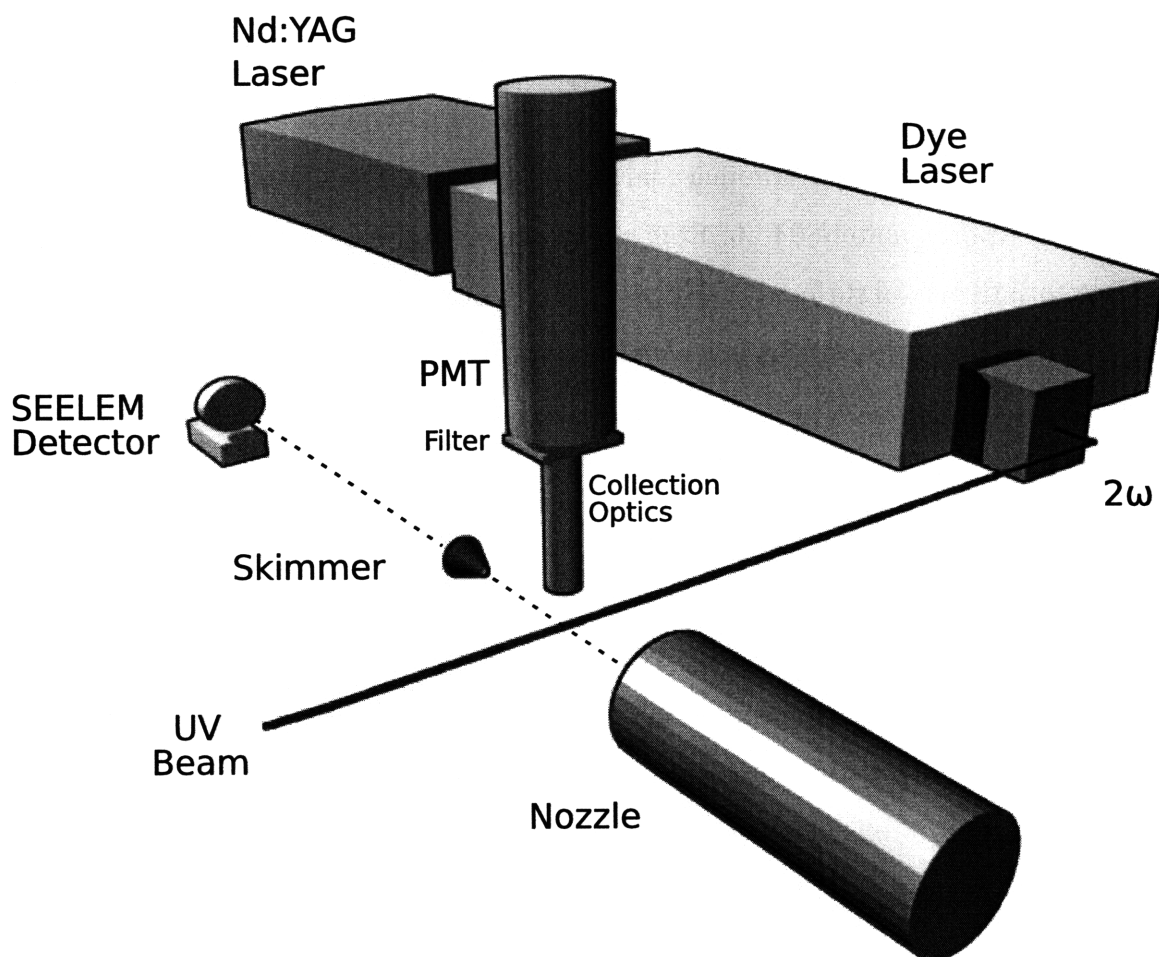
1.7 Summary

A doorway-mediated intersystem crossing model is well accepted for the acetylene molecule. However, its impact on the spectrum of most S_1 levels is poorly understood. Triplet perturbations in the spectrum of S_1 acetylene are “seemingly random,”² but the doorway model insists emphatically that the perturbations are *not* random. In this thesis, we establish and develop the connection between the doorway model and spectroscopic measurements. This task has required new theory, new types of experiments, and new methods of analysis.

In Chapter 2, we evaluate the problem of doorway-mediated intersystem crossing using three different frameworks: a mixed $S_1 \sim T_3$ basis set, an “embedded bright

²A direct quote from a well-known spectroscopist, who shall remain nameless.

Figure 1-4: Diagram of the LIF/SEELEM apparatus. Laser radiation in the UV is provided by the frequency doubled output of a Nd:YAG-pumped dye laser. The laser radiation enters the vacuum chamber (not shown), and crosses the path of the molecular beam, indicated by a dashed line, approximately 2.5 cm downstream from a pulsed nozzle. Fluorescence is gathered by $f/4$ optics at the point of laser excitation, passes through a UG-11 filter, and is collected by a photomultiplier tube (PMT). Laser-excited metastable molecules travel through a 3 mm diameter skimmer and into a second, differentially pumped vacuum chamber. Approximately 34 cm from the point of laser excitation, the metastables collide with the metal surface of the SEELEM detector, and ejected electrons are collected by an electron multiplier, located immediately below the metal surface.



state” picture, and a complex Hamiltonian model. Using these frameworks, the statistical properties of LIF and SEELEM intensity distributions are derived for several doorway-mediated model Hamiltonians. Of particular interest is the nature of interference effects, as well as the spectroscopic signatures of the doorway state, in each model Hamiltonian.

Moving beyond statistical properties, we demonstrate in Chapter 3 that the parameters of a doorway-mediated model Hamiltonian are determined by the frequencies and relative intensities observable in the spectrum. The method of “doorway deconvolution” is presented as an extension to the standard Lawrance-Knight-Lehmann deconvolution technique. The parameters of the model Hamiltonian are also derived in terms of the statistical moments of the spectrum.

In Chapter 4, we report on new SEELEM/LIF spectra for a number of S_1 vibrational levels. We discuss the ubiquitous role of T_3 vibrational levels as mediators of $S_1 \sim T_{1,2}$ mixing, and show how the identity of a doorway level is imprinted on the spectrum. A theory of delayed fluorescence is developed and used as a primary tool to understand the spectral patterns of doorway-mediated mixing.

The non-symmetric bending modes of S_1 acetylene, ν'_4 and ν'_6 , play an important role in the process of intersystem crossing. However, these two vibrations are normally mixed by strong Darling-Dennison and a -type Coriolis resonances. In Chapter 5, we present the results of IR-UV double resonance SEELEM/LIF experiments, where, by a careful choice of quantum numbers, the ν'_4 and ν'_6 vibrational modes are unaffected by the two strong resonance mechanisms.

In Chapter 6, we develop a new method for the production of metastable molecules in a molecular beam. The basis of this method is two-photon optical pumping of metastable atoms, followed by atom-to-molecule electronic excitation transfer in collisions. The selection rules and transition probabilities for two-photon excitation of the atoms are discussed for mercury and xenon. The method is applied to two chemical systems, $\text{Xe}^* + \text{N}_2$ and $\text{Hg}^* + \text{C}_2\text{H}_2$.

In Chapter 7, we conclude and summarize the prospects for future research.

Chapter 2

Models of doorway-mediated intersystem crossing and their consequences in LIF and SEELEM spectra

2.1 Introduction

The traditional basis set for describing intersystem crossing is diagonal in “brightness.” For the first excited state of closed-shell molecules, the basis set typically consists of a singlet bright state coupled directly to many triplet dark states. This type of basis reflects the response of the system to excitation by a photon, and is useful for understanding systems in both the large molecule and small molecule limits. In the small molecule limit, experimental results may often be deperturbed explicitly due to the small number of interacting states. In the large molecule limit, many states are involved in the interaction, and analysis focuses on properties of the *ensemble* of dark states rather than the deperturbation of individual states. As experimental techniques evolve, the dividing line between small and large molecules is pushed back, expanding the domain of complete deperturbation and determinism.

In the case intermediate between the large and small molecule limits, a few special dark states may mediate the coupling between one bright state and the remaining ensemble of dark states. When this happens, the directly observable spectrum and the inferred dynamics of the system depend on both the ensemble properties of the bath of dark states and the individual properties of the mediating states (hereafter, doorway states). Thus, an approach to intersystem crossing in the intermediate case must combine the properties of the large and small molecule limits.

A theory of the spectral signatures of doorway-mediated intersystem crossing (DMISC) for systems containing a single bright state is presented below. In section 2.2, we discuss three ways to re-formulate the problem of doorway-mediated coupling, derive LIF intensity expressions for each, and compare the results. In section 2.3, we turn to evaluating terms in the SEELEM intensity for doorway-mediated systems. Using these intensity expressions, we examine the spectral signatures of DMISC for several model Hamiltonians. The models examined are: a local doorway, a distant doorway, a local doorway plus direct coupling, and a double (local + distant) doorway.

2.2 Don't think of a doorway: three alternate arrangements of the effective Hamiltonian

We begin with a simple doorway-mediated Hamiltonian arranged in the traditional manner. A single bright basis state $|s\rangle$ is connected to a single doorway basis state $|\ell\rangle$ by a spin-orbit matrix element $H_{s\ell}$. The doorway basis state is, in turn, connected to a block of prediagonalized dark states $\{|m\rangle\}$ by a vector of matrix elements $\{H_{\ell m}\}$. Such a Hamiltonian is shown in Figure 3-2b. The labels s , ℓ , and m used here are chosen to be consistent with those used in the book *Energy Dissipation in Molecular Systems*, by Tramer, Jungen, and Lahmani [124].

This form of the Hamiltonian illustrates the dynamics of the system, understood in terms of sequential intersystem crossing into a hierarchy of coupled states. However,

Figure 2-1: Schematic of a doorway-mediated Hamiltonian. A single bright basis state, $|s\rangle$, is connected to a single doorway basis state, $|\ell\rangle$, which is, in turn, connected to a block of prediagonalized dark states, $\{|m\rangle\}$.

$$\begin{bmatrix} E_s & H_{s\ell} & & & & & \\ & E_\ell & H_{\ell 1} & H_{\ell 2} & H_{\ell 3} & \cdots & \\ & & E_1 & & & & \\ & & & E_2 & & & \\ & & & & E_3 & & \\ & & & & & \ddots & \end{bmatrix}$$

other patterns of interaction between the bright state and the dark states are not immediately apparent unless we do some more work.

A crucial quantity from the standpoint of dynamics is the fractional bright state character of each eigenstate of the system. This determines the radiative lifetime and absorption linestrength of each state observed in the spectrum. We examine this property for three formulations of the effective Hamiltonian, and draw parallels between the results.

2.2.1 The mixed basis

Our first strategy for determining the distribution of fractional bright state character among the dark states is to prediagonalize the interaction between the bright state and the doorway state. This creates a new basis of “mixed” bright and doorway basis states, which we refer to as the mixed basis. From the mixed basis, we use perturbation theory to evaluate intensity-lending among the dark states. Due to this use of perturbation theory in the second step, we approach the mixed basis using a working assumption of a system in the strong coupling limit, defined below.

The strong coupling limit of DMISC is characterized by a strong doorway~bright state interaction compared to the average doorway~dark state interaction. As a first step, the problem is recast from a basis that contains one bright state and one doorway state to a basis that diagonalizes the bright~doorway interaction. The mixed bright

Figure 2-2: Schematic of a doorway-mediated ISC Hamiltonian after transformation to a mixed basis. The mixed basis states $|\tilde{s}\rangle$ and $|\tilde{\ell}\rangle$ have mixed bright~doorway character, and both have matrix elements with the ensemble of dark states.

$$\begin{bmatrix} E_{\tilde{s}} & H_{\tilde{s}1} & H_{\tilde{s}2} & H_{\tilde{s}3} & \cdots \\ & E_{\tilde{\ell}} & H_{\tilde{\ell}1} & H_{\tilde{\ell}2} & H_{\tilde{\ell}3} & \cdots \\ & & E_1 & & & \\ & & & E_2 & & \\ & & & & E_3 & \\ & & & & & \ddots \end{bmatrix}$$

and mixed doorway basis states are defined as

$$\begin{aligned} |\tilde{s}\rangle &= (1 - \alpha^2)^{1/2} |s\rangle + \alpha |\ell\rangle \\ |\tilde{\ell}\rangle &= -\alpha |s\rangle + (1 - \alpha^2)^{1/2} |\ell\rangle, \end{aligned} \tag{2.1}$$

where α is the bright~doorway mixing amplitude. Using this basis, the prediagonalized block of mixed basis states is connected to the prediagonalized block of dark states by an off-diagonal block of matrix elements $H_{\tilde{s}m}$ and $H_{\tilde{\ell}m}$. Figure 2-2 shows a schematic of the Hamiltonian using a mixed basis.

Two rows of matrix elements connect the mixed states to the dark states, suggesting two separate direct-coupled systems. However, **correlations between the two rows of matrix elements make the distribution of fractional bright state character for a doorway-mediated system different from that of two independent direct-coupled systems.** The matrix elements $H_{\tilde{s}m}$ and $H_{\tilde{\ell}m}$ can be written in terms of the zero-order matrix element $H_{\ell m}$ and the $|s\rangle$, $|\ell\rangle$ mixing amplitude α :

$$\begin{aligned} H_{\tilde{s}m} &= +\alpha H_{\ell m} \\ H_{\tilde{\ell}m} &= +(1 - \alpha^2)^{1/2} H_{\ell m}. \end{aligned} \tag{2.2}$$

More patterns in bright state coupling through $|\tilde{s}\rangle$ and $|\tilde{\ell}\rangle$ are apparent in the distribution of fractional bright state character among the eigenstates of the system.

The fractional bright state character of any nominal dark state that appears in the spectrum may be evaluated in terms of the mixed basis using perturbation theory. We approximate the overlap of a nominal dark state eigenfunction $|M\rangle$ with the bright state $|s\rangle$ by making a first order correction to the dark state basis function $|m\rangle$. Using the mixed basis defined above,

$$\langle M|s\rangle = \alpha(1 - \alpha^2)^{1/2} H_{\ell m} \left\{ \frac{1}{\Delta E_{m\bar{s}}} - \frac{1}{\Delta E_{m\bar{\ell}}} \right\}, \quad (2.3)$$

The fractional bright state character of $|M\rangle$ may be written as

$$|\langle M|s\rangle|^2 = \alpha^2(1 - \alpha^2) H_{\ell m}^2 \left\{ \frac{1}{\Delta E_{m\bar{s}}^2} + \frac{1}{\Delta E_{m\bar{\ell}}^2} - \frac{2}{\Delta E_{m\bar{s}} \Delta E_{m\bar{\ell}}} \right\}. \quad (2.4)$$

The three terms in the braces of Equation 2.4 correspond to intensity lending through the mixed bright state $|\bar{s}\rangle$, the mixed doorway state $|\bar{\ell}\rangle$, and a cross term. If this cross term is neglected, the fractional bright state character of dark states behaves as *two separate direct-coupled systems of equal coupling strength*, each with an effective matrix element $\alpha(1 - \alpha^2)^{1/2} H_{\ell m}$. One of the square terms dominates the intensity equation when $\Delta E_{m\bar{\ell}}$ becomes very large compared to $\Delta E_{m\bar{s}}$ or *vice versa*.

The cross term is important when the energy difference between the mixed basis states $\Delta E_{\bar{s}\bar{\ell}}$ is comparable in magnitude to the coupling width $2\pi|\alpha^2(1 - \alpha^2)H_{\ell m}^2|\rho_m$. The functional form of the cross term has several interesting properties. First, its sign does not depend on the relative signs of the bright~doorway and doorway~dark matrix elements, only on the relative signs of the energy denominators, $\Delta E_{m\bar{s}}$ and $\Delta E_{m\bar{\ell}}$. The cross term, with its $(-)$ sign included, is *always positive at energies that lie between those of the primary and secondary mixed states*, and negative outside this range.

The cross term has a local minimum at the energy midpoint of the mixed basis states, $\bar{E}_{s\ell} = (E_{\bar{s}} + E_{\bar{\ell}})/2$. The fractional intensity increase for dark states due to the cross term, in other words its ratio with respect to the sum of the square terms,

takes an especially simple form on an energy scale with zero chosen at $\bar{E}_{s\ell}$,

$$\left(-\frac{2}{\Delta E_{m\bar{s}}\Delta E_{m\bar{\ell}}}\right)/\left(\frac{1}{\Delta E_{m\bar{s}}^2} + \frac{1}{\Delta E_{m\bar{\ell}}^2}\right) = \frac{\Delta E_{\bar{s}\bar{\ell}} - \bar{E}_m}{\Delta E_{\bar{s}\bar{\ell}} + \bar{E}_m}, \quad (2.5)$$

where $\bar{E}_m = E_m - \bar{E}_{s\ell}$. This ratio in Equation 2.5 depends only on the energy difference $\Delta E_{\bar{s}\bar{\ell}}$ between the mixed basis states $|\bar{s}\rangle$ and $|\bar{\ell}\rangle$, and is independent of both the bright~doorway mixing coefficient and the doorway~dark matrix element. The cross term ratio from equation 2.5 is plotted in figure 2-3 along with the three terms in the expression for fractional bright state character, equation 2.4.

The equation for fractional bright state character of a dark state in the $|s\rangle$, $|\ell\rangle$ mixed basis contains two classes of terms: square terms and a cross term. The square terms are equivalent in the vicinity of each mixed state, and can be considered as appropriate for two separate, equal-magnitude, direct-coupled systems of dark states. These quasi-direct systems interact via the cross term, which *always* skews the intensities of the dark states toward the energy midpoint of the mixed basis states. This is an important result, because it means that dark state intensity patterns in the vicinity of the bright state can act as a “pointer” to the doorway state. Moreover, the fractional contribution of the cross term to the fractional bright state character is independent of the matrix elements of the system.

2.2.2 The embedded bright state arrangement

In the limit of weak doorway~bright coupling compared to the average doorway~dark coupling, we can take the opposite approach with respect to perturbation theory. Here, the doorway~dark interactions are diagonalized, and perturbation theory is used to evaluate the remaining bright~doorway interaction. The results of this analysis will be compared to the equations from the strong coupling regime, and an instructive correspondence will be made. The relationship between the weak and strong coupling limits will be made even more clear when we formulate the problem as a complex-energy effective Hamiltonian, in Section 2.2.3.

The effective Hamiltonian is re-ordered so the bright state is embedded among

Figure 2-3: Shown in the plot are contributions to the fractional bright state character in a nominal dark eigenstate $|M\rangle$ arising from three terms: borrowing through the mixed basis state $|\tilde{s}\rangle$, borrowing through the other mixed basis state $|\tilde{\ell}\rangle$, and a cross term. Also shown is the ratio of the cross term to the square terms, which exhibits a maximum at the energy midpoint between $E_{\tilde{s}}$ and $E_{\tilde{\ell}}$.

Figure 2-4: Schematic of a doorway-mediated Hamiltonian arranged according to the embedded bright state picture. The form of the matrix is equivalent to a direct coupling model.

$$\begin{bmatrix} E_\ell & H_{\ell 1} & H_{\ell 2} & H_{\ell s} & H_{\ell 3} & \cdots \\ & E_1 & & & & \\ & & E_2 & & & \\ & & & E_s & & \\ & & & & E_3 & \\ & & & & & \ddots \end{bmatrix}$$

the dark states. After re-ordering, the Hamiltonian is equivalent in form to a direct-coupled system, with the doorway state occupying the position normally held by the bright state. A schematic diagram of this arrangement is shown in figure 2-4.

To derive equations for the fractional bright state character of a nominally dark eigenstate, we adopt separate strategies in the vicinity of the bright state $|s\rangle$ and doorway state $|\ell\rangle$. In the vicinity of $|s\rangle$, contamination of dark states by the bright state may be evaluated by making a second-order correction to the dark state wavefunction. This yields a fractional bright state character of

$$|\langle M|s\rangle|^2 = \frac{H_{s\ell}^2 H_{\ell m}^2}{\Delta E_{ms}^2 \Delta E_{m\ell}^2}. \quad (2.6)$$

To compare this expression with the mixed basis results, one adjustment must be made. Since we are evaluating nominal dark state intensities in the vicinity of E_s , $|\Delta E_{ms}| \ll |\Delta E_{s\ell}|$, and $|\Delta E_{m\ell}| \approx |\Delta E_{s\ell}|$. In light of this approximation, the fractional bright state character becomes

$$|\langle M|s\rangle|^2 = \frac{H_{s\ell}^2 H_{\ell m}^2}{\Delta E_{ms}^2 \Delta E_{s\ell}^2} \approx \alpha^2 H_{\ell m}^2 \frac{1}{\Delta E_{ms}^2}, \quad (2.7)$$

since $\alpha \approx H_{s\ell}/\Delta E_{s\ell}$. Using this, we look for an equivalence with the mixed basis intensity formula, equation 2.4:

$$|\langle M|s\rangle|^2 = \alpha^2 (1 - \alpha^2) H_{\ell m}^2 \left\{ \frac{1}{\Delta E_{m\bar{s}}^2} + \frac{1}{\Delta E_{m\bar{\ell}}^2} - \frac{2}{\Delta E_{m\bar{s}} \Delta E_{m\bar{\ell}}} \right\}.$$

Since the bright~doorway coupling is weak, two approximations to the mixed basis results are appropriate:

$$\begin{aligned} (1 - \alpha^2)^{1/2} &\approx 1 \\ (E_{\tilde{s}}, E_{\tilde{\ell}}) &\approx (E_s, E_\ell). \end{aligned} \tag{2.8}$$

With these approximations, the mixed basis expression becomes:

$$|\langle M|s\rangle|^2 \approx \alpha^2 H_{\ell m}^2 \left\{ \frac{1}{\Delta E_{ms}^2} + \frac{1}{\Delta E_{m\ell}^2} - \frac{2}{\Delta E_{ms} \Delta E_{m\ell}} \right\}, \tag{2.9}$$

and it is clear that our result for the embedded bright state arrangement in the vicinity of $|s\rangle$ (Eq. 2.7) is equal to the square term for borrowing from the bright state in the mixed basis.

We now turn to deriving an expression for fractional bright state character in the vicinity of the doorway state $|\ell\rangle$. Since the doorway~dark interactions are strong, the effective Hamiltonian is diagonalized in the vicinity of the doorway state, forming a set of prediagonalized states $\{|\tilde{m}\rangle\}$. Each state in this doorway block $|\tilde{m}\rangle$ is a linear combination of dark and doorway states:

$$|\tilde{m}\rangle = C_{\ell\tilde{m}} |\ell\rangle + \sum_m C_{m\tilde{m}} |m\rangle. \tag{2.10}$$

After diagonalization of the doorway block, mixing between the zero-order bright state and the doorway block states may be evaluated using perturbation theory. The doorway component $|\ell\rangle$ of each diagonalized state $|\tilde{m}\rangle$ is contaminated to first order with bright state amplitude

$$\langle \ell^{(1)}|s\rangle = -\frac{H_{s\ell}}{\Delta E_{s\ell}}, \tag{2.11}$$

and the dark state components $|m\rangle$ are not. From this equation, the fractional bright state character in $|\tilde{m}\rangle$ follows immediately,

$$|\langle \tilde{m}|s\rangle|^2 = C_{\ell\tilde{m}}^2 \frac{H_{s\ell}^2}{\Delta E_{s\ell}^2}. \tag{2.12}$$

To compare the above expression with the mixed basis formulas, we rewrite Eq. 2.12 using the perturbation-theory approximation for $C_{\ell\tilde{m}}, H_{\ell\tilde{m}}/\Delta E_{\ell\tilde{m}}$:

$$C_{\ell\tilde{m}}^2 \frac{H_{s\ell}^2}{\Delta E_{s\ell}^2} \approx \frac{H_{\ell\tilde{m}}^2}{\Delta E_{\ell\tilde{m}}^2} \frac{H_{s\ell}^2}{\Delta E_{s\ell}^2} \approx \alpha^2 H_{\ell\tilde{m}}^2 \frac{1}{\Delta E_{\ell\tilde{m}}^2}. \quad (2.13)$$

Adjusting for notation, this is equal to the second term of the mixed basis equation. Thus, the embedded bright state result for the doorway block plays the role of the square term for the mixed doorway basis state in the earlier formulation.

The effective Hamiltonian for doorway mediated intersystem crossing in the weak bright-doorway coupling limit has been rearranged to account for relatively strong doorway~dark interactions. This is called the embedded bright state arrangement, because the bright state has “switched places” with one of the dark states in the traditional direct-coupling Hamiltonian. After using a combination of diagonalization and perturbation theory to analyze the intensity distribution of dark states, the results from this arrangement were shown to correspond to the square terms in the strong coupling limit. Thus, the intensity expressions from the embedded bright state arrangement emerge as a subset of the mixed basis equations.

The consequences of the embedded bright state arrangement extend beyond the evaluation of systems in the weak coupling limit. The fact that the Hamiltonian can be arranged to have the same form as a direct-coupling Hamiltonian has ramifications for eigenstate energies and spectral deconvolution; we discuss these at length in Chapter 3.

2.2.3 Formulation as a complex-energy effective Hamiltonian

As a third alternative, the dynamics of intensity lending to a bath of dark states can be viewed as a process of irreversible decay from the bright and doorway basis states into a quasi-continuum of dark states. The decay widths are embedded into the energies of the bright and doorway basis states by adding an imaginary component, $E = \epsilon - i\Gamma/2$. Because the effects of dark state coupling are folded into the bright and doorway states, the complex energy formulation reduces the doorway-canonical Hamiltonian to a 2-level system.

The complex-energy Hamiltonian for a single doorway system may be written as

$$\mathbf{H} = \begin{bmatrix} \epsilon_s & V_{sl} \\ V_{sl} & \epsilon_\ell - i\Gamma_\ell/2 \end{bmatrix}. \quad (2.14)$$

The width of the doorway state is related to the average doorway~dark matrix element by the golden rule relation $\Gamma_\ell = 2\pi \langle V_{\ell m}^2 \rangle \rho_m$.

Results for a two-level complex-energy Hamiltonian are derived in detail in chapter 9 of reference [66]. Following the derivation therein, we rewrite the Hamiltonian as two terms:

$$\mathbf{H} = (\bar{\epsilon}_{sl} - i\bar{\Gamma}_{sl}/2)\mathbf{I} + \begin{bmatrix} \delta\epsilon_{sl} - i\delta\Gamma_{sl}/2 & V_{sl} \\ V_{sl} & -(\delta\epsilon_{sl} - i\delta\Gamma_{sl}/2) \end{bmatrix}. \quad (2.15)$$

The re-centered energies have the values

$$\bar{\epsilon}_{sl} = (\epsilon_s + \epsilon_\ell)/2 \quad (2.16a)$$

$$\delta\epsilon_{sl} = (\epsilon_s - \epsilon_\ell)/2. \quad (2.16b)$$

Since the bright state is not connected to the bath of dark states in a doorway-mediated Hamiltonian, $\Gamma_s = 0$, and

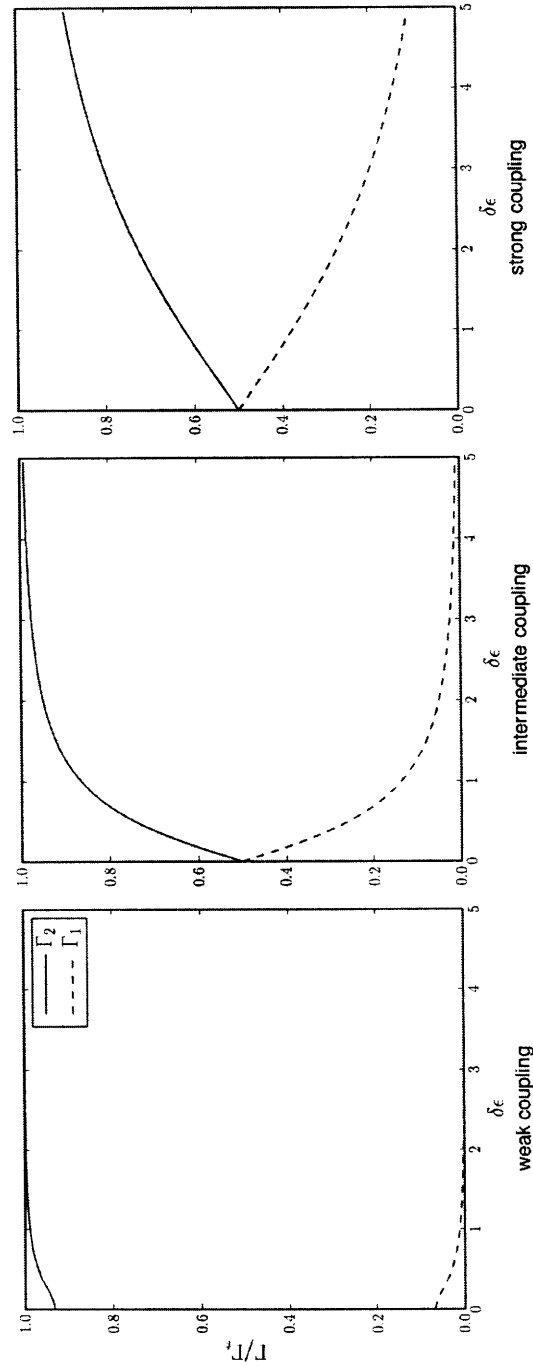
$$\bar{\Gamma}_{sl} = \Gamma_\ell/2 \quad (2.17a)$$

$$\delta\Gamma_{sl} = -\Gamma_\ell/2. \quad (2.17b)$$

Diagonalization of this Hamiltonian leads to level repulsion in the real components of the energy, as for real Hamiltonians. However, the imaginary components of the eigenvalues are closer to the average width $\Gamma_\ell/2$, as the bright state borrows some decay width from the doorway state.

Figure 2-5 shows the width of the nominal singlet and triplet eigenstates of equation 2.14 for several magnitudes of bright~doorway coupling. In the weak coupling regime, $V_{sl} \ll \Gamma_\ell$. The bright state borrows little width from the doorway state, even

Figure 2-5: Widths of the nominal bright and doorway eigenstates in a complex-energy doorway Hamiltonian. To demonstrate the weak coupling regime (left), the coupling matrix element $V_{s\ell}$ is set to 0.25 times the magnitude of the doorway width Γ_ℓ . For the intermediate coupling regime (center), $V_{s\ell} = \Gamma_\ell$; for the strong coupling regime (right), $V_{s\ell} = 4\Gamma_\ell$.



when the difference in real energy, $\delta\epsilon_{s\ell}$, is zero. In the intermediate coupling regime, the eigenstate widths converge to the average width $\Gamma_\ell/2$ when $\delta\epsilon_{s\ell} = 0$. In the strong coupling case, the difference in the widths $|S\rangle$ and $|L\rangle$ approaches $\Gamma_\ell/2$ less rapidly as $\delta\epsilon_{s\ell}$ increases.

We now turn to evaluating the dark state intensity distribution using the complex energy formulation. The energies and widths of the eigenstates $|S\rangle$ and $|L\rangle$ are given by the real and imaginary parts of their eigenvalues:

$$\epsilon_S = \bar{\epsilon}_{s\ell} \pm \text{Re}(\mathcal{E}) \qquad \Gamma_S = \bar{\epsilon}_{s\ell} \pm \text{Im}(\mathcal{E}) \qquad (2.18a)$$

$$\epsilon_L = \bar{\epsilon}_{s\ell} \mp \text{Re}(\mathcal{E}) \qquad \Gamma_L = \bar{\epsilon}_{s\ell} \mp \text{Im}(\mathcal{E}) \qquad (2.18b)$$

where the energy eigenvalue \mathcal{E} is given by

$$\mathcal{E} = \sqrt{(\delta\epsilon_{s\ell} - i\delta\Gamma_{s\ell}/2)^2 + V_{s\ell}^2}, \qquad (2.19)$$

and the choice of sign in equation 2.18 is given by the sign of $\delta\epsilon_{s\ell}$ in equation 2.16. We must also determine the bright state character of the eigenstates $|S\rangle$, $|L\rangle$. The bright state amplitudes are obtained from the eigenvectors of the Hamiltonian,

$$\alpha_S = \langle \tilde{S} | s \rangle = \sqrt{\frac{(\delta\epsilon_{s\ell} - i\delta\Gamma_{s\ell}/2) + \mathcal{E}}{2\mathcal{E}}} \qquad (2.20a)$$

$$\alpha_L = \langle \tilde{L} | s \rangle = \sqrt{\frac{(\delta\epsilon_{s\ell} - i\delta\Gamma_{s\ell}/2) - \mathcal{E}}{2\mathcal{E}}}. \qquad (2.20b)$$

With these tools in hand, we evaluate the intensity distribution by deriving the absorption cross section for the system in terms of the Green's function $G(E) = \lim_{\gamma \rightarrow 0} [\mathbf{H} - (E + i\gamma)\mathbf{I}]^{-1}$:

$$\sigma(E) \propto \text{Im}(\langle g | \mu G(E) \mu | g \rangle). \qquad (2.21)$$

When the Green's function is evaluated over the eigenvectors of \mathbf{H} , only two diagonal

Table 2.1: Eigenstate energy difference and width of the nominal bright eigenstate $|S\rangle$ for the systems depicted in Figure 2-6. In the weak coupling regime, the energy separation of the eigenstates $|S\rangle$ and $|L\rangle$ is approximately that of the zero-order states $|s\rangle$ and $|\ell\rangle$. The nominal bright eigenstate $|S\rangle$ borrows little coupling width from the doorway state, and remains narrow. In the strong coupling regime, the eigenstates are separated in energy by $2V_{s\ell}$ and have similar widths.

$V_{s\ell}/\delta\Gamma_{s\ell}$	Coupling regime	$\delta\epsilon_{SL}/\delta\epsilon_{s\ell}$	Γ_S/Γ_ℓ
1/10	Weak	1.02	0.005
1	Intermediate	2.06	0.257
10	Strong	20.00	0.475

elements remain:

$$Im G(E) = |\alpha_S|^2 \frac{\Gamma_S}{(\epsilon_S - E)^2 + \Gamma_S^2} + |\alpha_L|^2 \frac{\Gamma_L}{(\epsilon_L - E)^2 + \Gamma_L^2}. \quad (2.22)$$

Therefore, the intensity distribution for the complex energy Hamiltonian is the sum of two Lorentzian functions, with energies and widths given by the eigenvalues of the Hamiltonian, and weighted in magnitude by the fractional bright state character.

Figure 2-6 shows the terms of Eq. 2.22 for each of the three coupling regimes. In order to show details of the intensity distribution for each regime, the scale of the axes was adjusted for each subplot. Although the scales were chosen carefully to show the general trends in the distributions, the plots cannot simultaneously and clearly communicate the dramatic changes in $\delta\epsilon_{SL}$ and Γ_S as the magnitude of $V_{s\ell}$ changes. For this reason, these quantities are listed in table 2.1.

In the weak coupling regime, the nominal bright eigenstate $|S\rangle$ is much narrower than that of the nominal doorway eigenstate $|L\rangle$, which remains nearly at its original width. To compare with our earlier results from the embedded bright state picture, we analyze the weakly coupled system presented above in terms of the perturbation theory developed in the previous section. Figure 2-7 shows a comparison between the complex Hamiltonian results and those derived from perturbation theory using equation 2.6. To make this comparison, the effective matrix element $V_{\ell d}$ was calculated from the width Γ_ℓ of the doorway state using the golden rule. The perturbation

Figure 2-6: Dark state intensity distributions for a doorway coupled system where $\delta\epsilon_{sl} = 0.5$ and $\delta\Gamma_{sl} = 1$. Three coupling regimes result from the relative magnitude of V_{sl} : weak coupling ($V_{sl} = \delta\Gamma_{sl}/10$), intermediate coupling ($V_{sl} = \delta\Gamma_{sl}$), and strong coupling ($V_{sl} = 10\delta\Gamma_{sl}$). Note the different scales of both the x and y axes for each plot. The widths Γ_S of the $|S\rangle$ intensity term are $0.005\Gamma_\ell$, $0.26\Gamma_\ell$, and $0.48\Gamma_\ell$ for the weak, intermediate, and strong coupling regimes, respectively.

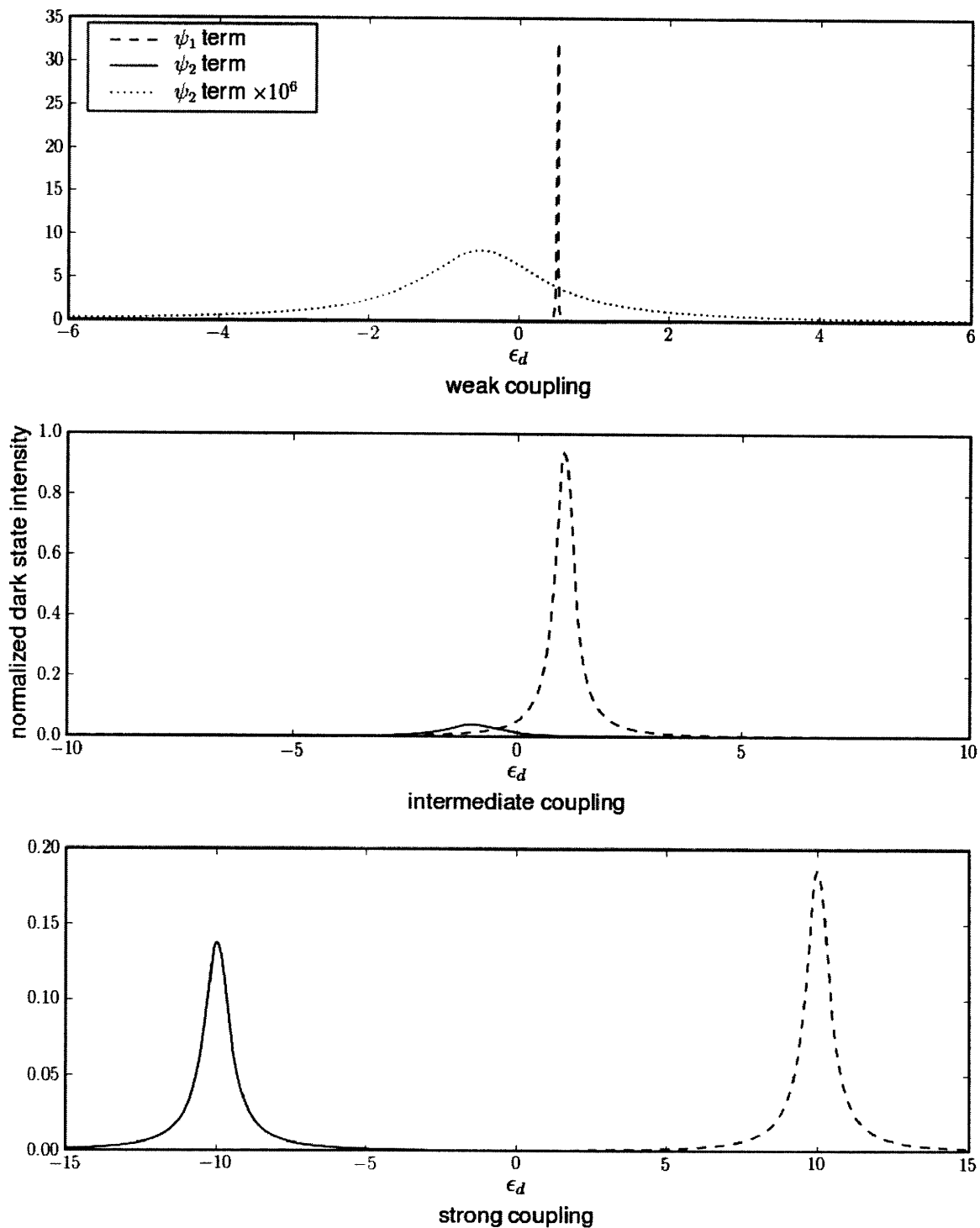


Figure 2-7: A comparison of the intensity distribution results from direct diagonalization (solid line) and perturbation theory (dashed line) in the weak coupling regime.

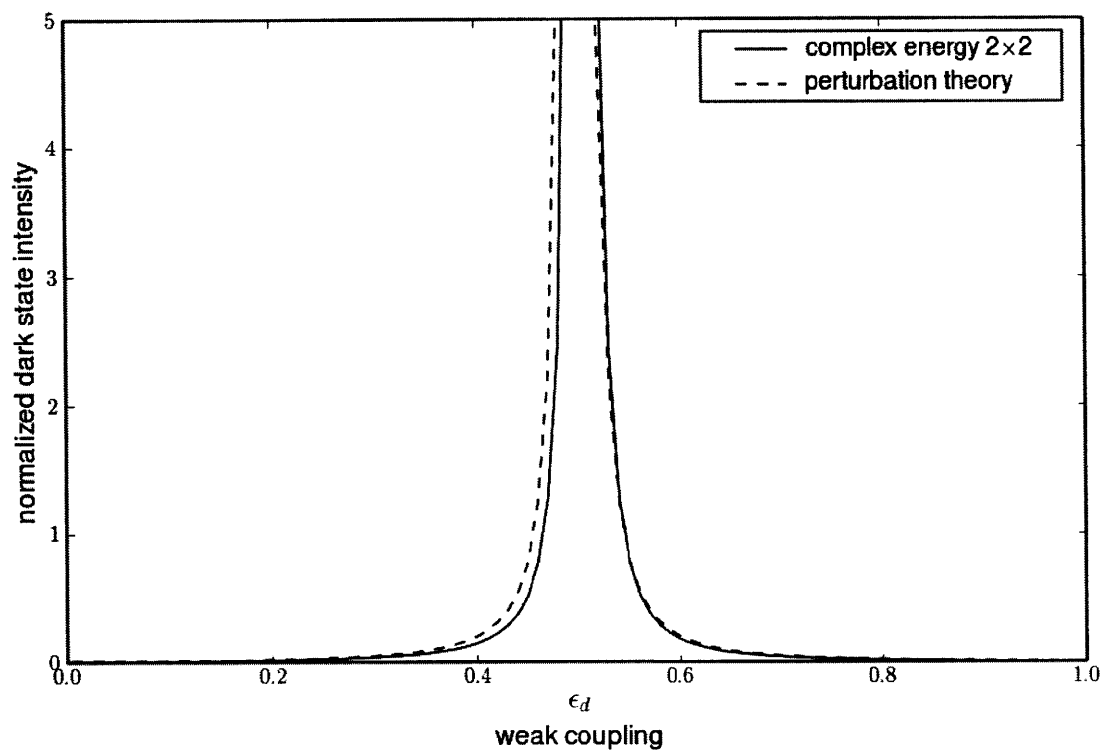
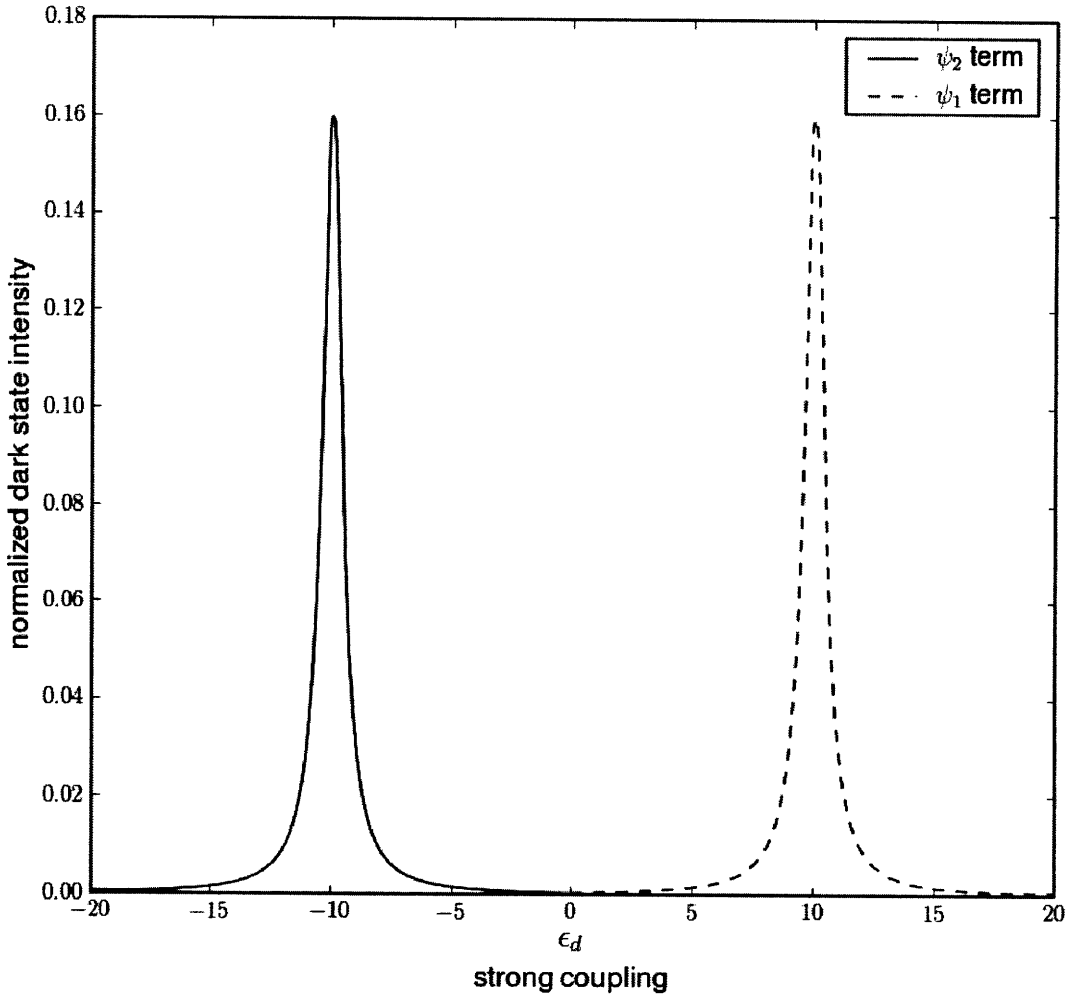


Figure 2-8: A doorway-mediated Hamiltonian in the strong coupling limit, where the mixing is complete in both the real and imaginary parts of the eigenfunctions.



results show only a slight offset in energy, due to the use of the approximation $\epsilon_S \approx \epsilon_s$.

In the strong coupling regime, we make a qualitative comparison to the earlier results derived for the mixed basis. The strong coupling intensity formula, equation 2.4, predicts identical dark state intensity distributions in the vicinity of both the bright and doorway states. In the bottom plot of figure 2-6, it can be seen that the system is approaching this limit. A more extreme example is shown in figure 2-8, where the zero-order (real) energy spacing $\delta\epsilon_{sl}$ has been decreased to $0.01\delta\Gamma_{sl}$. In this case, the mixing between $|S\rangle$ and $|L\rangle$ is complete in both intensity (real part) and width (imaginary part).

A complex energy effective Hamiltonian has been used to reduce the doorway-

mediated coupling problem to a two level system. The dark state intensity distribution was presented graphically for the weak, intermediate, and strong coupling regimes. The distributions derived from diagonalizing the 2×2 complex energy Hamiltonian were shown to have the same trends as those obtained using perturbation theory for the mixed basis and the embedded bright state picture. As for the results from the embedded bright state arrangement, the complex energy Hamiltonian formula does not include a cross term in the distribution of fractional bright state character. We will return to the complex energy formulation later in Section 2.6, when we consider the local doorway plus direct coupling model.

2.3 Doorway-mediated coupling and SEELEM intensity distribution

In a molecular beam experiment, detection by surface electron ejection by laser-excited metastables (SEELEM) produces a spectrum that is sensitive to eigenstates with only a small amount of fractional bright state character. This detection channel is complementary to laser-induced fluorescence, which is sensitive to eigenstates containing a large amount of fractional bright state character. The intensity information in a SEELEM spectrum, in conjunction with LIF, provides a complete description of the distribution of fractional bright state character among an ensemble of predominantly dark eigenstates. However, the relationship between SEELEM intensity and fractional bright state character is somewhat more complicated than it is for LIF. In this section, we derive SEELEM intensity expressions and discuss interference between detection pathways involving the bright and doorway basis state.

An eigenstate $|M\rangle$ of a doorway-coupled system is written as a linear combination of the zero-order bright state, doorway state, and dark states:

$$|M\rangle = C_s |s\rangle + C_\ell |\ell\rangle + \sum_m C_m |m\rangle \quad (2.23)$$

The SEELEM detection probability for a molecule in eigenstate $|M\rangle$ is modeled as

the product of three factors: excitation probability, survival probability, and electron ejection probability. The excitation probability is proportional to the fractional bright state character:

$$P_{ex} = A_{ex} C_s^2 \quad (2.24)$$

where A_{ex} is a constant factor for the bright state in question.

Following Altunata, we write the survival probability in terms of the bright state character [4]:

$$P_{surv} = \exp(-R_m C_s^2). \quad (2.25)$$

The factor R_m is defined as ratio of flight time in the molecular beam to the fluorescence lifetime of a pure bright state:

$$R_m = \frac{t_{\text{flight}}}{\tau_s}. \quad (2.26)$$

The molecular beam flight time t_{flight} is a constant for the experiment, while the pure bright state lifetime τ_s is a property of the bright state in question.

The electron ejection probability is more complicated, since it depends on the probability of de-excitation to the ground state upon impact with the metal surface. If the energy released upon de-excitation is greater than the work function of the metal, an electron may be ejected from the metal surface and detected with an electron multiplier.

Normally, the metal surface used for SEELEM detection is chosen such that the vertical excitation energy of the bright state is greater than the work function of the metal. However, the doorway state may also contain enough vertical excitation energy to eject electrons from the metal surface. In this case, there is an additional possibility that interference between the phases of bright and doorway amplitudes in $|M\rangle$ might lead to changes in the total angle-energy averaged electron cross section. We address these complications by separating the electron ejection probability into

three terms: a bright state term, a possible doorway term, and a possible cross term:

$$\begin{aligned} P_{ej} &= P_{ej}^{(s)} + P_{ej}^{(\ell)} + P_{ej}^{(\times)} \\ &= A_{ej}^{(s)} C_s^2 + A_{ej}^{(\ell)} C_\ell^2 + A_{ej}^{(\times)} C_s C_\ell \end{aligned} \quad (2.27)$$

We examine each term separately, creating for example a SEELEM detection probability term $P_{SEELEM}^{(s)}$ that includes only the bright state term $P_{ej}^{(s)}$ from the electron ejection probability factor. The results for each can be summed to determine the total detection probability.

2.3.1 The bright state term

We begin with the bright state term for the SEELEM detection probability:

$$\begin{aligned} P_{SEELEM}^{(s)} &= P_{ex} \times P_{surv} \times P_{ej}^{(s)} \\ &= \left(A_{ex} A_{ej}^{(s)} \right) C_s^4 \exp(-R_m C_s^2). \end{aligned} \quad (2.28)$$

As a function of C_s^2 , $P_{SEELEM}^{(s)}$ has the form of a chi-square distribution with six degrees of freedom, a fact better illustrated by making the substitution $x \equiv 2C_s^2/R_m$:

$$P_{SEELEM}^{(s)} \propto x^{6/2-1} \exp\left(-\frac{x}{2}\right). \quad (2.29)$$

To gain insight into the energy dependence of the SEELEM detection probability for an ensemble of dark states with average doorway state coupling $\langle H_{\ell m}^2 \rangle$, we evaluate the form of the SEELEM detection probability for a single eigenstate $|M\rangle$ as a function of energy. To carry this out, we note that the only energy-dependent parameter in the above equation is the fractional bright state character, C_s^2 .

The maximum of the SEELEM intensity distribution is found by taking the derivative of the SEELEM detection probability with respect to energy:

$$\frac{\partial P_{SEELEM}^{(s)}}{\partial E} = A^{(s)} P_{surv} C_s^2 \frac{\partial C_s^2}{\partial E} (2 - R_m C_s^2) \quad (2.30)$$

Setting this expression to zero, we obtain a maximum for $P_{SEELEM}^{(s)}$ where

$$C_s^2 = \frac{2}{R_m}. \quad (2.31)$$

Substituting this quantity into the SEELEM detection probability (equation 4.14), we arrive at a maximum intensity of

$$A^{(s)} \left(\frac{2}{eR_m} \right)^2. \quad (2.32)$$

This is a surprising result: the maximum SEELEM detection probability is independent of the matrix elements of the Hamiltonian!

The width of the intensity distribution does not share this invariance. To find the half width, we first make the approximation that the survival probability is approximately unity on the outer edge of the intensity distribution. Setting the total probability to half the quantity from equation 2.32 and rearranging to find C_s^2 , we get

$$C_s^2 = \frac{\sqrt{2}}{eR_m} \quad (2.33)$$

at the half maximum.

Up to this point, we have used no perturbation theory in our derivation. The results above depend only on the adopted functional form of the SEELEM detection probability. To arrive at a final expression for the width, we use perturbation theory to determine the quantity C_s^2 as a function of energy in the weak and strong coupling limits.

In the weak coupling limit, equation 2.7 from the bright state arrangement relates C_s^2 to the energy denominator $\Delta E_{\ell m}$:

$$C_s^2 = \alpha^2 \frac{H_{\ell m}^2}{\Delta E_{ms}^2}. \quad (2.34)$$

Solving for ΔE_{ms} , the FWHM of the distribution is determined to be

$$\text{FWHM} = 2|\alpha H_{\ell m} C_{\frac{1}{2}}|, \quad (2.35)$$

where $C_{\frac{1}{2}}$ is the fractional bright state character at the SEELEM half-maximum, determined in equation 2.33. The energy dependence of the intensity expression in the weak coupling limit arises only from a squared energy denominator ΔE_{ms} , thus the distribution is an even function when the energy zero is chosen to be the bright state energy E_s .

In the strong coupling limit, the energy dependence of C_s^2 is more complicated. Equation 2.4 gives the relation:

$$C_s^2 = \alpha^2(1 - \alpha^2)H_{\ell m}^2 \left\{ \frac{1}{\Delta E_{m\bar{s}}} - \frac{1}{\Delta E_{m\bar{\ell}}} \right\}^2 \quad (2.36)$$

in the mixed basis. As explained in section 2.2.1, the distribution of bright state intensity in the strong coupling limit is symmetric about the energy midpoint $\bar{E}_{\bar{s}\bar{\ell}}$ of the mixed basis states. We can remove one of the energy denominators by rewriting the equation using the energy difference $\Delta E_{\bar{s}\bar{\ell}}$. Making the substitution $\Delta E_{m\bar{\ell}} = \Delta E_{m\bar{s}} + \Delta E_{\bar{s}\bar{\ell}}$,

$$C_s^2 = \alpha^2(1 - \alpha^2)H_{\ell m}^2 \left\{ \frac{\Delta E_{\bar{s}\bar{\ell}}}{\Delta E_{m\bar{s}}(\Delta E_{m\bar{s}} + \Delta E_{\bar{s}\bar{\ell}})} \right\}^2. \quad (2.37)$$

The FWHM of the distribution around either $E_{\bar{s}}$ or $E_{\bar{\ell}}$ is given by the solutions to a quadratic equation:

$$\text{FWHM} = \left\{ 4 \left| \alpha(1 - \alpha^2)^{1/2} H_{\ell m} \Delta E_{\bar{s}\bar{\ell}} C_{\frac{1}{2}} \right| + \Delta E_{\bar{s}\bar{\ell}}^2 \right\}^{\frac{1}{2}}. \quad (2.38)$$

We have derived the widths of the bright state term of the SEELEM intensity distribution in both the weak and strong coupling limits. Along the way, a maximum of the distribution was found that depends only on the quantity R_m , which is a constant of the experiment and the molecule being studied. A value of fractional bright state character was determined for the half-maximum of the distribution, which also depends only on R_m . Since our use of perturbation theory was limited to the final steps of the derivation, most of the properties determined above depend only on the functional form of $P_{SEELEM}^{(s)}$. We turn next to the doorway term for SEELEM

detection probability, and compare its properties to those of the bright state term.

2.3.2 The doorway term

If the doorway state has sufficient vertical excitation energy, it may contribute to the electron ejection probability. We turn now to derive an intensity distribution for the doorway term

$$P_{SEELEM}^{(\ell)} = \left(A_{ex} A_{ej}^{(\ell)} \right) C_s^2 C_\ell^2 \exp(-R_m C_s^2). \quad (2.39)$$

Because the amplitudes of the bright and doorway states are squared in this equation, the relative phase of the bright vs. doorway contributions cannot lead to interference in this term. Going further, the fact that the system is doorway-mediated suggests that the doorway character be parametrized as a function of the bright state character:

$$C_\ell^2 = f(C_s^2). \quad (2.40)$$

We derive this relationship separately for the weak and strong coupling regimes.

In the weak coupling regime, we can invert the results from the embedded bright state arrangement (equation 2.7) to determine an expression for f_{weak} :

$$f_{weak}(C_s^2) = C_s^2 \frac{\Delta E_{sl}^2}{H_{sl}^2} \quad (2.41)$$

This gives a SEELEM detection probability proportional to the bright state term,

$$\begin{aligned} P_{SEELEM,weak}^{(\ell)} &= \left(A_{ex} A_{ej}^{(\ell)} \right) C_s^2 \left(C_s^2 \frac{\Delta E_{sl}^2}{H_{sl}^2} \right) \exp(-R_m C_s^2) \\ &= \frac{\Delta E_{sl}^2}{H_{sl}^2} P_{SEELEM}^{(s)}, \end{aligned} \quad (2.42)$$

the properties of which are discussed in the preceding section.

In the strong coupling regime, we begin by using the mixed basis to derive the fractional doorway state character in a nominally dark eigenstate $|M\rangle$:

$$|\langle M|\ell\rangle|^2 = H_{\ell m}^2 \left\{ \frac{\alpha^2}{\Delta E_{m\bar{s}}} + \frac{(1-\alpha^2)}{\Delta E_{m\bar{\ell}}} \right\}^2. \quad (2.43)$$

The function f_{strong} does not collapse into a simple form as it does for the weak coupling regime. We write the function instead in terms of $|\langle M|s\rangle|^2$ and $|\langle M|\ell\rangle|^2$,

$$\begin{aligned} f_{strong} &= \frac{C_s^2}{C_\ell^2} \\ &= \frac{|\langle M|s\rangle|^2}{|\langle M|\ell\rangle|^2}, \end{aligned} \tag{2.44}$$

referring the reader to the expression for $|\langle M|s\rangle|^2$ in equation 2.4. We note that the doorway~dark matrix element $H_{\ell m}$ cancels out in the function f_{strong} , since it appears to the same power in $|\langle M|s\rangle|^2$ and $|\langle M|\ell\rangle|^2$. Unlike the weak coupling regime, f_{strong} is a function of the energy differences $\Delta E_{m\bar{s}}$ and $\Delta E_{m\bar{\ell}}$. Cross terms involving these energy denominators always appear with a $(-)$ sign in the numerator and a $(+)$ sign in the denominator, so they have the effect of decreasing the SEELEM detection probability. The bright~doorway mixing amplitude α appears only to even powers in f_{strong} , so interference effects do not arise from the phase of this mixing amplitude.

We have derived the form of the doorway term for SEELEM detection probability for the weak and strong coupling limits. In the weak coupling limit, the doorway term is simply proportional to the bright state term. In the strong coupling limit, the form of the doorway term is more complicated, but does not include any interference effects arising from coupling to the bright state through the doorway state.

2.3.3 The cross term

If the doorway state has sufficient Franck-Condon overlap with low-lying vibrational levels of the ground state *and* the angle-energy integrated *total* cross section for electron ejection is affected by interference between the bright and doorway pathways, the electron ejection cross term may contribute to the intensity distribution. The form of the cross term

$$P_{SEELEM}^{(\times)} = \left(A_{ex} A_{ej}^{(\times)} \right) C_s^3 C_\ell \exp(-R_m C_s^2) \tag{2.45}$$

contains odd powers of C_s and C_ℓ , and according to their relative phase, may add or subtract from the square terms. Interference effects arising from the cross term in the SEELEM detection probability are discussed in detail by Selen Altunata [4, 3, 2]. Since we observe no such effects in the experiments described in this thesis, we do not give the cross term further consideration.

2.4 The local doorway model

We turn now to examine several model Hamiltonians for doorway-mediated systems, using the tools developed earlier in the chapter. These models are really classifications of the types of spectra that may appear for molecules exhibiting doorway-mediated coupling. Each model combines an appropriate basis set for evaluating the LIF and SEELEM intensity distributions with an assumption as to the range of states observed in the spectrum.

The basis set for a local doorway model was introduced in section 2.2, and has been used throughout the chapter. It includes a single bright basis state $|s\rangle$, a single doorway basis state $|\ell\rangle$, and a set of N pre-diagonalized dark basis states $\{|m\rangle\}$. The single bright basis state $|s\rangle$ carries all oscillator strength for the system, and thus plays a crucial role in the detectability of all states. All matrix elements between $|s\rangle$ and the bath of dark states are zero.

Upon diagonalization, the effective Hamiltonian yields a set of N nominally dark eigenstates $\{|M\rangle\}$, as well as two “special” eigenstates $|S\rangle$ and $|L\rangle$. The state $|S\rangle$ contains the greatest fractional bright state character, and likewise the state $|L\rangle$ contains the single greatest fractional doorway basis character. A cursory look at the LIF spectrum will reveal $|S\rangle$ immediately, because it carries the greatest amount of oscillator strength.

The final defining criterion for a local doorway model is that the eigenstate $|L\rangle$ is observed in the spectrum. This model does not carry in its definition any assumptions about the relative magnitudes or distributions of the remaining nonzero matrix elements in the effective Hamiltonian; it can include systems in the strong or weak

coupling limits.

We have already examined the distribution of LIF intensity in section 2.2. Likewise, we used the local doorway model as a template for deriving the width of the SEELEM intensity distribution in section 2.3. As we move on to other models, we focus on differences from the results for the local doorway model.

2.5 The distant doorway model

The distant doorway model differs from the local doorway model in that the nominal doorway state is not observed in the spectrum. In the limit that the doorway-bright energy difference becomes large compared to the width of dark state coupling in the vicinity of the bright state, statistical intensity metrics cannot distinguish a distant doorway from a system characterized by direct coupling. However, evidence for doorway-mediated coupling can still be obtained through other means, and under these circumstances the distant doorway model will provide some indication of the relative coupling magnitudes and the energy of the nominal doorway state.

Since $|\ell\rangle$ is well separated from the bright state in energy, some approximations to the dark state intensity distributions can be made. For a distant doorway, the bright state energy denominator dominates the intensity formula (equation 2.4), and

$$\begin{aligned} |\langle M|s\rangle|^2 &= \alpha^2(1 - \alpha^2)H_{\ell m}^2 \left\{ \frac{1}{\Delta E_{m\bar{s}}} + \frac{1}{\Delta E_{m\bar{\ell}}} \right\}^2 \\ &\approx \alpha^2 \frac{H_{\ell m}^2}{\Delta E_{m\bar{s}}^2}. \end{aligned} \tag{2.46}$$

In addition to eliminating one energy denominator from the above equation, we have also made the approximation that $(1 - \alpha^2) \approx 1$. This approximation is fairly good (5% error) if $|s\rangle$ and $|\ell\rangle$ are mixed to less than 25%. The SEELEM intensity distribution above is equivalent to the weak coupling formula in section 2.3.1.

If a spectrum is observed in the vicinity of the bright state and a distant doorway model is assumed, the question can be asked: what is the energy of $|L\rangle$, the nominal doorway state? The properties of the LIF and SEELEM intensity distributions in

the vicinity of the bright state do not yield the energy of $|L\rangle$ directly. However, the product $|\alpha\langle H_{\ell m}\rangle_{rms}|$ can be estimated from the width of the SEELEM spectrum, using equation 2.35. From this quantity, we parametrize α in terms of $\Delta E_{s\ell}$ and predict the LIF/SEELEM intensity of $|L\rangle$ as a function of energy separation from the bright state.

An expression for α in terms of $\Delta E_{s\ell}$ and the matrix element $H_{s\ell}$ comes from the analytical solution to the 2×2 Hamiltonian in the mixed basis:

$$\alpha^2 = \frac{(2H_{s\ell})^2}{\left(\Delta E_{s\ell} + \sqrt{\Delta E_{s\ell}^2 + 4H_{s\ell}^2}\right)^2 + 4H_{s\ell}^2} \quad (2.47)$$

$$\approx \frac{H_{s\ell}^2}{\Delta E_{s\ell}^2}.$$

The LIF intensity of $|L\rangle$ is diminished as $1/\Delta E_{s\ell}^2$. Relative to the nominal bright state intensity $(1 - \alpha^2)$, the LIF intensity of $|L\rangle$ goes as

$$\frac{\alpha^2}{1 - \alpha^2}, \quad (2.48)$$

where the energy dependence of α^2 is given above. Since the quantity $|\alpha\langle H_{\ell m}\rangle_{rms}|$ has been inferred from the spectrum in the vicinity of the bright state, an increase in energy separation $\Delta E_{s\ell}$ requires an increase in $H_{s\ell}$ or a decrease in $\langle H_{\ell m}\rangle_{rms}$ to maintain consistency with the observed properties of the spectrum.

If the spectrum has been observed within a certain range of the bright state and the nominal doorway state has not been observed in the LIF spectrum, an upper limit can be placed on α^2 , the fractional bright state character of the nominal doorway state $|L\rangle$. At small values of α^2 , the doorway state will be detectable in SEELEM but not in LIF. We evaluate the SEELEM detection probability in the weak coupling regime, recalling that, under these circumstances, any doorway contribution to the SEELEM intensity has the same form as the bright state contribution. The SEELEM detection probability scales as

$$\alpha^4 \exp(-R_m \alpha^2), \quad (2.49)$$

and is at a maximum for the doorway state when

$$\alpha^2 = \frac{2}{R_m}, \tag{2.50}$$

or when the energy difference $\Delta E_{s\ell}$ is

$$|\Delta E_{s\ell}| = |H_{s\ell}| \sqrt{\frac{2}{R_m}}. \tag{2.51}$$

Since the quantity α^2 is a function of $H_{s\ell}$, known properties of the molecule can place limits on whether the nominal doorway state appears in LIF or SEELEM spectra within a certain energy range. Thus, a distant doorway hypothesis may be tested by scanning the spectrum of a molecule within a known range. In practice, SEELEM spectra are difficult to collect over a large energy window due to time constraints, and LIF spectra provide a somewhat easier way to place an upper limit on the quantity α^2 for a particular bright state. In a later chapter, we will use the formulas above to apply the distant doorway model to several SEELEM and LIF spectra of the acetylene molecule.

2.6 The local doorway plus direct coupling model

In this section, we examine the consequences of allowing the bright state to couple weakly to the dark states in the local doorway model. We begin again by evaluating the LIF and SEELEM intensity distributions in the mixed basis. In the presence of two coupling pathways to the bright state, we separate the bright state amplitude of a nominal dark eigenstate $|M\rangle$ into a doorway term and a direct term:

$$\langle M|s\rangle = \langle M|s\rangle_{doorway} + \langle M|s\rangle_{direct} \tag{2.52}$$

The doorway term has been evaluated above (equation 2.3). The direct term arises from a matrix element H_{sm} between the dark state $|m\rangle$ and the bright state $|s\rangle$:

$$\langle M|s\rangle_{direct} = H_{sm} \left\{ \frac{(1 - \alpha^2)}{\Delta E_{\bar{s}m}} + \frac{\alpha^2}{\Delta E_{\bar{\ell}m}} \right\}, \quad (2.53)$$

leading to a square term for the direct-coupling contribution to the fractional bright state character:

$$|\langle M|s\rangle_{direct}|^2 = H_{sm}^2 \left\{ \frac{(1 - \alpha^2)^2}{\Delta E_{\bar{s}m}^2} + \frac{\alpha^4}{\Delta E_{\bar{\ell}m}^2} + \frac{2\alpha^2(1 - \alpha^2)}{\Delta E_{\bar{s}m}\Delta E_{\bar{\ell}m}} \right\} \quad (2.54)$$

The total amount of fractional bright state character in a nominal dark state includes a cross term between direct and doorway coupling:

$$\begin{aligned} |\langle M|s\rangle|^2 = & |\langle M|s\rangle_{doorway}|^2 + |\langle M|s\rangle_{direct}|^2 \\ & + 2\alpha(1 - \alpha^2)^{1/2} H_{\ell m} H_{sm} \left\{ \frac{(1 - \alpha^2)}{\Delta E_{\bar{s}m}^2} - \frac{\alpha^2}{\Delta E_{\bar{\ell}m}^2} + \frac{2\alpha^2 - 1}{\Delta E_{\bar{s}m}\Delta E_{\bar{\ell}m}} \right\}. \end{aligned} \quad (2.55)$$

Our primary concern is to evaluate possible interference patterns in the intensity distribution. To this end, we focus on factors that control the relative phase of each term. The term $|\langle M|s\rangle_{direct}|^2$ is always positive, regardless of the relative signs of α and H_{sm} . However, the last term in equation 2.55 contains the quantities α , $H_{\ell m}$, and H_{sm} to odd powers, so the overall sign of this term is determined by the product of these three quantities.

The quantity α is determined by only the zero-order bright and doorway basis states; its phase and magnitude are the same regardless of the identity of the dark state of interest, $|m\rangle$. The matrix elements H_{sm} and $H_{\ell m}$ are different for each dark state, thus the sign of the final term in equation 2.55 for one dark state compared to another is determined by the relative signs of the matrix elements H_{sm} and $H_{\ell m}$.

The question becomes: are the phases of the matrix elements H_{sm} and $H_{\ell m}$ correlated? To address this question, we consider the nature of the matrix elements in the context of spin-orbit coupling. A spin-orbit matrix element H^{SO} between two

rovibronic states can be written as a factor of an electronic matrix element and a vibrational overlap integral. Since the states $|s\rangle$ and $|\ell\rangle$ belong to different electronic surfaces their electronic factors are different. The spin-orbit matrix elements may be written as

$$H_{sm}^{SO} = \zeta_s \langle s|m\rangle \quad (2.56a)$$

$$H_{\ell m}^{SO} = \zeta_\ell \langle \ell|m\rangle. \quad (2.56b)$$

Since the phase of the electronic factor in H^{SO} is the same for all dark states in the Hamiltonian, the phase of the spin-orbit matrix element is controlled by the vibrational overlap factor alone.

Narrowing our question, are the phases of vibrational overlap factors $\langle \ell|m\rangle$ and $\langle s|m\rangle$ correlated for any dark state $|m\rangle$? The answer depends on the location of the stationary phase points of the wavefunctions $|\ell\rangle$ and $|s\rangle$ where the overlap with $|m\rangle$ occurs. Since $|\ell\rangle$ and $|s\rangle$ lie on different electronic surfaces, their points of overlap with dark state wavefunctions $|m\rangle$ are likely to occur at different geometries. The phase of a wavefunction in a highly vibrationally excited manifold will not be correlated at two disparate geometries, thus the two vibrational overlap factors $\{\langle \ell|m\rangle\}$ and $\{\langle s|m\rangle\}$ are not expected to be correlated in phase.

The local doorway plus direct coupling model lends itself naturally to a complex energy formulation. The complex energy description of dark state coupling implies a random phase approximation – the lack of correlation in the phases of H_{sm} and $H_{\ell m}$ is “built into” the formalism. The discussion of a complex-energy doorway system presented above is modified here by allowing the zero-order bright state $|s\rangle$ to have a non-vanishing width. The width of $|s\rangle$ arising from direct coupling is $2\pi|H_{sm}|^2\rho_m$. When Γ_s is nonzero, equation 2.17 is no longer valid, and $\delta\Gamma < \Gamma_\ell/2$. Other factors aside, the widths of the eigenstates will be more similar for a system that includes some direct coupling, compared to a strictly doorway-mediated system. The effective decrease of the difference in coupling widths $\delta\epsilon_{sL}$ pushes the system toward the strong coupling regime, defined by the inequality $V_{s\ell} \gg \Gamma_\ell$.

$H_{s\ell'} H_{\ell'm} / \Delta E_{sm\ell'}$:

$$|\langle M|s\rangle|^2 = |\langle M|s\rangle_{local}|^2 + |\langle M|s\rangle_{distant}|^2 + 2\alpha(1 - \alpha^2)^{1/2} H_{\ell m} \frac{H_{s\ell'} H_{\ell'm}}{\Delta E_{sm\ell'}} \left\{ \frac{(1 - \alpha^2)}{\Delta E_{\bar{s}m}^2} - \frac{\alpha^2}{\Delta E_{\bar{\ell}m}^2} + \frac{2\alpha^2 - 1}{\Delta E_{\bar{s}m} \Delta E_{\bar{\ell}m}} \right\}, \quad (2.63)$$

where the distant doorway coupling term $|\langle M|s\rangle_{distant}|^2$ is equal to

$$|\langle M|s\rangle_{distant}|^2 = \left(\frac{H_{s\ell'} H_{\ell'm}}{\Delta E_{sm\ell'}} \right)^2 \left\{ \frac{(1 - \alpha^2)}{\Delta E_{\bar{s}m}} + \frac{\alpha^2}{\Delta E_{\bar{\ell}m}} \right\}^2. \quad (2.64)$$

Interference effects arising from the local~distant doorway cross term will arise if the phases of matrix elements $H_{\ell m}$ and $H_{\ell'm}$ are correlated for a dark state $|m\rangle$. In the previous section, we argued that the matrix elements $H_{\ell m}$ and H_{sm} are not correlated in phase, because the states $|\ell\rangle$ and $|s\rangle$ belong to different electronic surfaces. However, if the local and distant doorway belong to *the same electronic state*, the vibrational overlap integrals will be coarsely determined by the shape of the same electronic surface. The Franck-Condon overlap with a dark state $|m\rangle$ is likely to occur at the same turning points for both doorway states. In this case, it is likely that the phases of $H_{\ell m}$ and $H_{\ell'm}$ will produce interference effects in the spectrum arising from the cross term in equation 2.63.

The energy dependence of the cross term will be sensitive to the relative energies of the local and distant doorway states. However, since the relative phase of the matrix elements $H_{\ell m}$ and $H_{\ell'm}$ is not known *a priori*, the sign of the energy denominator $\Delta E_{s\ell'}$ cannot be determined directly from the spectrum. *Ab initio* calculations of vibrational wavefunctions can determine the relative phase of $H_{\ell m}$ and $H_{\ell'm}$ at various turning points if the identity of the local and distant doorway states is known or can be guessed.

Chapter 3

Deconvolution of spectral data to produce a doorway-coupling model Hamiltonian

3.1 Introduction

Spectral deconvolution is a method of local deperturbation for high-resolution spectroscopy, used to determine the parameters that define a model Hamiltonian from a spectrum. The model Hamiltonian determined by spectral deconvolution contains a single zero-order bright state, which interacts with a set of pre-diagonalized dark basis states. Such a direct-coupling Hamiltonian is shown in Figure 3-1a. In its discrete formulation, spectral deconvolution returns a set of dark state energies and squared bright~dark matrix elements. In its continuous formulation, the procedure returns a zero-order spectral density function for coupling to the bright state.

Spectral deconvolution has been used to study Intramolecular Vibrational Redistribution (IVR) in many small molecules, including NO_2 , allene, and several substituted propynes [20, 123, 7, 54]. It was originally developed in the study of intersystem crossing, where it has been applied to the spectra of intermediate case molecules such as acetylene, naphthalene, and pyrazine [34, 20, 65].

The technique for deconvolution of continuous spectra was described by Berg and independently, in a more general form, by Ziv and Rhodes [10, 140]. Both methods make use of a Green's function formalism. The discrete formulation of spectral deconvolution was presented by Lawrance and Knight, and afterward simplified by Lehmann [65, 67]. Lehmann's refinement of the technique obviates the need to compute any Green's function from the spectrum – we refer to this method as Lawrance-Knight-Lehmann (LKL) deconvolution. Interestingly, the LKL method had been used in 1977 by Brand and Hoy to deperturb portions of the NO₂ spectrum [13]. That work was cited by Cable and Rhodes, who artificially re-broadened the same spectrum to demonstrate their continuous deconvolution technique [20].

The set of dark states available from LKL deconvolution loses its lustre when an interaction of interest occurs within the set of dark states. This is the case for sequential coupling among tiers of dark states, a common situation in small polyatomic molecules [124]. Although dark state~dark state interactions play a central role in the redistribution of molecular energy, the deconvolution procedure does not directly yield information pertaining to their dynamics.

To this end, several efforts have been made to investigate perturbations within the block of pre-diagonalized dark states returned by LKL deconvolution. Pate, Lehmann, and Scoles used a method of matrix rotation to obtain a qualitative explanation of a J-dependent Coriolis interaction between two dark states in their deperturbation of the trifluoropropyne spectrum [97]. Altunata and Field derived a parameter to predict the relative energy of a single “doorway” state, a unique dark state that mediates all coupling between the bright state and the remaining dark states [5]. A method to determine the energy and squared matrix element of a doorway state from the spectrum allows the construction of a new doorway-coupling model Hamiltonian. Such a Hamiltonian is shown in figure 3-1b.

The parameters in a direct-coupling Hamiltonian are uniquely determined by the spectrum; the total number of energies and intensities in the spectrum is equal to the number of free parameters in the model Hamiltonian. For a spectrum consisting of $N + 1$ transitions, the number of free parameters after normalization is $2N + 1$ ($N + 1$

energies and N normalized intensities) [65]. A direct-coupling Hamiltonian contains 1 bright state energy, N dark state energies, and N bright~dark coupling matrix elements, totaling $2N + 1$. A doorway-coupling Hamiltonian also contains $2N + 1$ free parameters: 1 bright state energy, 1 bright~doorway matrix element, 1 doorway state energy, $N - 1$ dark state energies, and $N - 1$ doorway~dark coupling matrix elements.

The equal number of parameters in the direct and doorway-coupling Hamiltonians suggests that a doorway-coupling Hamiltonian can also be derived uniquely from the experimental data. Such a technique was described for the continuous case by Ziv and Rhodes in their original paper [140]. The authors introduce the concept of a “Spectroscopic Channel Basis” to describe the multiple levels of doorway-coupling model Hamiltonians available through recursive application of spectral deconvolution. The Spectroscopic Channel Basis includes model Hamiltonians with any number of sequential doorway states, from 1 to $N - 1$.

After a brief review of the continuous and discrete forms of spectral deconvolution, we demonstrate how to use the discrete deconvolution method recursively to recover the Spectroscopic Channel Basis of Ziv and Rhodes. We provide formulas to simplify the computation of doorway state energy and matrix element, using moments of the spectral intensity. By comparison with the discrete method, we show that the continuous method produces exact results for the zero-order density function when used with Lorentzian line shapes. The usefulness of the technique is then demonstrated by application to a spectrum of the acetylene molecule. The doorway deconvolution results are shown to be consistent with other investigations of the system.

Figure 3-1: Top: Diagram of a direct-coupling model Hamiltonian. One vector of matrix elements connects a single bright state, $|s\rangle$, to a prediagonalized set of dark basis states, $\{|m\rangle\}$. Middle: Diagram of a doorway-coupling Hamiltonian. A single bright basis state, $|s\rangle$, is connected to a single doorway basis state $|\ell\rangle$, which is connected in turn to a pre-diagonalized block of dark states, $\{|m\rangle\}$. Bottom: Diagram of a doorway-coupling Hamiltonian in the embedded bright state arrangement. The form of the matrix is equivalent to the direct-coupling model, without the need for a matrix rotation. All model Hamiltonians in the figure are symmetric and real; only nonzero elements in the upper diagonal are shown.

$$\mathbf{H}_{direct} = \begin{bmatrix} E_s & H_{s1} & H_{s2} & H_{s3} & H_{s4} & \cdots \\ & E_1 & & & & \\ & & E_2 & & & \\ & & & E_3 & & \\ & & & & E_4 & \\ & & & & & \ddots \end{bmatrix}$$

(a) Direct-coupling Hamiltonian

$$\mathbf{H}_{doorway} = \begin{bmatrix} E_s & H_{s\ell} & & & & \cdots \\ & E_\ell & H_{\ell 1} & H_{\ell 2} & H_{\ell 3} & \cdots \\ & & E_1 & & & \\ & & & E_2 & & \\ & & & & E_3 & \\ & & & & & \ddots \end{bmatrix}$$

(b) Doorway-coupling Hamiltonian

$$\mathbf{H}_{doorway} = \begin{bmatrix} E_\ell & H_{\ell s} & H_{\ell 1} & H_{\ell 2} & H_{\ell 3} & \cdots \\ & E_s & & & & \\ & & E_1 & & & \\ & & & E_2 & & \\ & & & & E_3 & \\ & & & & & \ddots \end{bmatrix}$$

(c) Doorway coupling basis, rearranged

3.2 Lawrance-Knight-Lehmann deconvolution: Construction of a direct-coupling model Hamiltonian

Using the standard spectral deconvolution method, the parameters that define a direct-coupling Hamiltonian are extracted from an absorption spectrum. The basis for this Hamiltonian consists of a single bright basis state, $|s\rangle$, which is coupled to a set of N prediagonalized dark states, $\{|m\rangle\}$, through a set of bright~dark matrix elements, $\{H_{sm}\}$:

$$\mathbf{H}_{direct} = E_s |s\rangle \langle s| + \sum_{m=1}^N E_m |m\rangle \langle m| + \sum_{m=1}^N H_{sm} (|s\rangle \langle m| + |m\rangle \langle s|). \quad (3.1)$$

This Hamiltonian is illustrated in Figure 3-2a. The technique of spectral deconvolution requires a single bright state to provide all oscillator strength from the initial state for the spectrum in question, otherwise interference effects, which cannot be uniquely determined, may arise between bright states.

We briefly review the continuous formulation of spectral deconvolution, following the notation of Ziv, Cable, and Rhodes [140, 20]. The Green's function for the direct-coupling Hamiltonian,

$$\mathcal{G}_s(E) = \lim_{\gamma \rightarrow 0} [\mathbf{H}_{direct} - (E + i\gamma)\mathbf{I}]^{-1}, \quad (3.2)$$

has an imaginary component proportional to the absorption spectrum:

$$Im[\mathcal{G}_s(E)] \propto \sigma_A(E). \quad (3.3)$$

The normalization condition for the imaginary part of the Green's function is

$$-\frac{1}{\pi} \int_{-\infty}^{\infty} Im[\mathcal{G}_s(E)] = 1. \quad (3.4)$$

Dispersion relations connect the real part of the Green's function to the imaginary part. It may be derived by applying a Hilbert transformation to $Im[\mathcal{G}_s(E)]$,

$$Re[\mathcal{G}_s(E)] = \frac{1}{\pi} \mathcal{P} \int_{-\infty}^{\infty} \frac{Im[\mathcal{G}_s(E')]}{E' - E} dE', \quad (3.5)$$

where the symbol \mathcal{P} indicates the principal value of the integral.

Using projection operators, another Green's function, $\mathcal{F}_s(E)$, may be defined for the subspace of dark states in the Hamiltonian [140, 20]. It is related to the Green's function for the full Hamiltonian by

$$\mathcal{G}_s(E) = [E - E_s - \mathcal{F}_s(E)]^{-1}. \quad (3.6)$$

The imaginary part of \mathcal{F}_s ,

$$Im[\mathcal{F}_s(E)] = -Im \left[\frac{1}{\mathcal{G}_s(E)} \right], \quad (3.7)$$

is the desired zero-order density function for coupling to the bright state. This is called the “interaction density spectrum” by Ziv and Rhodes, and the “weighted density function” by Berg and others [140, 10]. The magnitude of this function is related to the local bright~dark squared matrix element $H_{sm}^2(E)$ and the density of dark states $\rho_m(E)$ by the Golden Rule [10]:

$$Im[\mathcal{F}_s(E)] = \pi H_{sm}^2(E) \rho_m(E). \quad (3.8)$$

The bright state energy E_s is obtained from the first moment of spectral intensity (the “center of gravity” of the spectrum),

$$E_s = \int E \times \sigma_A(E) dE = -\frac{1}{\pi} \int E \times Im[\mathcal{G}_s(E)] dE, \quad (3.9)$$

a result of expanding the eigenstate absorption intensities in the direct-coupling basis.

If all transitions in the spectrum are fully resolved, the procedure for deconvolution is simplified greatly. A method for deconvolution of discrete transitions was presented

by Lawrance and Knight, who modified Berg's method for the continuous case [65, 10]. A simpler and better algorithm was later put forth by Lehmann [67]. The result of discrete deconvolution is a set of zero-order dark state energies $\{E_m\}$ and squared matrix elements $\{H_{sm}^2\}$. The phases of the matrix elements are not determined by the procedure, and indeed do not affect the energy or spectral intensity of the eigenstates. Interference effects among dark states do not arise in the direct-coupling Hamiltonian because one and only one coupling pathway connects each dark state to the bright state.

We briefly review the deconvolution formulas for a discrete spectrum of transitions at frequencies $\{\nu_i\}$ with normalized intensities $\{I_i\}$, following Lehmann [67]. The bright state energy, E_s , coincides with the first moment of spectral intensity,

$$E_s = \sum_i I_i \times \nu_i, \quad (3.10)$$

as for the continuous formulation. The dark state energies, $\{E_m\}$, in the direct-coupling basis are the roots of the function

$$f_s(E) = \sum_i \frac{I_i}{\nu_i - E}, \quad (3.11)$$

which may be found numerically. After the set of dark state energies $\{E_m\}$ is obtained, the set of squared bright~dark matrix elements $\{H_{sm}^2\}$ is determined by successive substitution of each dark state energy, E_m , into the equation

$$H_{sm}^2 = \left[\sum_i \frac{I_i}{(\nu_i - E_m)^2} \right]^{-1}. \quad (3.12)$$

The sum of the squared bright~dark coupling matrix elements is equal to the second moment of spectral intensity about the mean:

$$\sum_m H_{sm}^2 = \sum_i I_i \times (\nu_i - E_s)^2. \quad (3.13)$$

This quantity, as well as the quantity in eq. 3.10, is invariant to matrix rotations, and thus is preserved for any choice of basis [67].

Because the function $f_s(E)$ has one root between each pair of consecutive eigenvalues, one dark state energy in the direct-coupling Hamiltonian is “trapped” between each pair of consecutive eigenstate energies observed in the spectrum. This effect places a limit on the degree to which coupling to a single bright state can influence the nearest-neighbor level spacings among a set of dark states [25].

3.3 Extended deconvolution: Construction of a doorway-coupling model Hamiltonian

We wish to go a step beyond the LKL deconvolution procedure and construct a Hamiltonian in which only a single dark basis state, $|\ell\rangle$, is coupled to the bright state. This doorway state mediates all coupling between the bright state and the set of remaining dark states $\{|n\rangle\}$:

$$\begin{aligned} \mathbf{H}_{doorway} = & E_s |s\rangle \langle s| + E_\ell |\ell\rangle \langle \ell| + H_{s\ell}(|s\rangle \langle \ell| + |\ell\rangle \langle s|) \\ & + \sum_{n=1}^{N-1} E_n |n\rangle \langle n| + \sum_{n=1}^{N-1} H_{\ell n}(|\ell\rangle \langle n| + |n\rangle \langle \ell|). \end{aligned} \quad (3.14)$$

A diagram of a doorway-coupling Hamiltonian is shown in Figure 3-1b.

A continuous formulation for constructing a doorway-coupling Hamiltonian from the spectrum was presented by Ziv and Rhodes [140]. They begin with the Green’s function for the subspace of dark states in the direct coupling Hamiltonian, $\mathcal{F}_s(E)$. This diagonal block of states is partitioned into a single doorway state, $|\ell\rangle$, and a new subspace of dark states, which determine the doorway-coupling Hamiltonian. The Green’s function, $\mathcal{G}_\ell(E)$, for the doorway~dark block is determined by $\mathcal{F}_s(E)$:

$$\mathcal{F}_s(E) = V_{s\ell}^2 \mathcal{G}_\ell(E) - i \Gamma_s/2, \quad (3.15)$$

where $i\Gamma_s/2$ is the width of the bright state, and $V_{s\ell}$ is the bright-doorway matrix element. The bright state is not involved in the transformation from direct to doorway-coupling Hamiltonians, thus the bright basis state is identical in both models.

Aside from a constant offset, the function, $Im[\mathcal{G}_\ell(E)]$, is proportional to the interaction density spectrum, $Im[\mathcal{F}_s(E)]$, just as the function, $Im[\mathcal{G}_s(E)]$, is proportional to the absorption spectrum. This illustrates clearly that *the problem of deriving a doorway-coupling Hamiltonian from a direct-coupling Hamiltonian is, in essence, identical to the problem of deriving a direct-coupling Hamiltonian from the spectrum*. In both cases, our task is to create, from a diagonal set of states, a new basis in which a single state carries all oscillator strength.

Following Cable and Rhodes, we proceed by rewriting equations 3.6 to 3.9 for the doorway-coupling Hamiltonian [20]. The Green's function for the subspace of dark states in the doorway-coupling Hamiltonian is

$$\mathcal{G}_\ell(E) = [E - E_s - \mathcal{F}_\ell(E)]^{-1}, \quad (3.16)$$

leading to an equation for the interaction density spectrum for coupling to the doorway state

$$Im[\mathcal{F}_\ell(E)] = -Im\left[\frac{1}{\mathcal{G}_\ell(E)}\right]. \quad (3.17)$$

The doorway state energy is the first moment of $Im[\mathcal{F}_s(E)]$, the interaction density spectrum for coupling to the bright state,

$$E_\ell = -\frac{1}{\pi} \int Im[\mathcal{F}_s(E)] \times E dE, \quad (3.18)$$

just as the bright state energy is the first moment of the absorption spectrum (an interaction density spectrum for radiative coupling to an initial state). Since the integral of $Im[\mathcal{G}_\ell(E)]$ over energy is normalized to $-\pi$, the magnitude of $V_{s\ell}$ may be obtained by integrating the energy-dependent part of the interaction density spectrum

for coupling to the bright state. Using equation 3.15,

$$V_{s\ell}^2 = -\frac{1}{\pi} \int (Im[\mathcal{F}_s(E)] + i\Gamma_s/2) dE. \quad (3.19)$$

We have derived all desired properties of the doorway-coupling Hamiltonian for the continuous case. At this point, it is clear that one could, in principle, solve the system for a second or third tier doorway. However, we choose to focus only on the single doorway-coupled Hamiltonian because that model is most readily applicable to several experimental spectra.

In the discrete case, a doorway-coupling Hamiltonian may be derived from the direct-coupling Hamiltonian by applying the LKL deconvolution procedure recursively to the pre-diagonalized block of dark states. The deconvolution algorithm de-diagonalizes this block by projecting out a single state that contains all coupling to the bright state. Dark state energies and squared bright~dark matrix elements from the direct-coupling Hamiltonian replace spectral frequencies and intensities as input to the algorithm. The doorway state energy is the first moment of the distribution of $\{H_{sm}^2\}$ in the direct-coupling Hamiltonian,

$$E_\ell = \sum_m H_{sm}^2 \times E_m. \quad (3.20)$$

The new set of dark state energies, $\{E_n\}$, for the doorway-coupling Hamiltonian is given by the roots of

$$f_\ell(E) = \sum_m \frac{H_{sm}^2}{E_m - E}, \quad (3.21)$$

which places a single E_n between each consecutive pair of dark state energies in the direct-coupling Hamiltonian. The new set of doorway~dark matrix elements is found from the dark state energies, $\{E_n\}$, by substitution into

$$H_{sn}^2 = \left[\sum_m \frac{H_{sm}^2}{(E_m - E_n)^2} \right]^{-1}. \quad (3.22)$$

The bright~doorway matrix element may be determined by considering the proper-

ties of the direct-coupling Hamiltonian. The quantity $\sum_m H_{sm}^2$ is invariant matrix rotations, and thus is conserved for any basis set that includes a single bright state [67]. Since the bright state is coupled exclusively to the doorway state in this model Hamiltonian, it follows that

$$H_{s\ell}^2 = \sum H_{sm}^2. \quad (3.23)$$

The four equations above allow calculation of all parameters in the doorway-coupling Hamiltonian.

The key parameters of the doorway-coupling model Hamiltonian (E_s , $H_{s\ell}$, and E_ℓ) may be written directly in terms of the moments of the absorption spectrum. This allows them to be derived directly from the absorption spectrum without deconvolution. Equation 3.10 equates the bright state energy and the first moment (center of gravity) of the absorption spectrum. The second central moment (variance) of the spectrum is equal to the squared bright-doorway matrix element,

$$H_{s\ell}^2 = \sum_i I_i \times (\nu_i - E_s)^2. \quad (3.24)$$

which follows (in the discrete case) from equations 3.23 and 3.13. The doorway state energy is the ratio of the third and second central moments of the absorption spectrum. In the discrete formulation, this is

$$E_\ell = \frac{\sum_i I_i \times (\nu_i - E_s)^3}{\sum_i I_i \times (\nu_i - E_s)^2}. \quad (3.25)$$

Table 3.1 summarizes the relationship between the moments of the spectrum and the parameters of the doorway-coupling Hamiltonian for both the continuous and discrete formulations.

To demonstrate the method of obtaining a doorway-coupling model Hamiltonian from a discrete spectrum, we apply our procedure to an NO_2 spectrum reported by Smalley *et. al.* [107]. Our purpose in this instance is only to demonstrate the procedure, not to address the dynamics of the NO_2 molecule. This portion of spectrum was

Table 3.1: Key parameters of the doorway-coupling model Hamiltonian may be calculated directly from the absorption spectrum without LKL deconvolution. The bright state energy, bright~doorway matrix element, and doorway state energy have simple relationships to the moments of the spectrum. For clarity, moments of the absorption spectrum are defined explicitly in the table.

Parameter	Equivalent moments of absorption spectrum	
E_s	μ	
$H_{s\ell}^2$	μ_2	
E_ℓ	μ_3/μ_2	
Moment	Continuous case	Discrete case
μ	$\int \sigma_A(E) \times E dE$	$\sum_i I_i \times \nu_i$
μ_n	$\int \sigma_A(E) \times (E - \mu)^n dE$	$\sum_i I_i \times (\nu_i - \mu)^n$

used by Cable and Rhodes to demonstrate their continuous deconvolution method, so it provides a basis for comparison with their published results [20].

Figure 3-2 displays the results of a normal LKL deconvolution to form a direct-coupling Hamiltonian. We include the original spectrum along with the zero-order energies to illustrate the level trapping phenomenon. Two eigenstates in the spectrum are nearly degenerate at about $15,000 \text{ cm}^{-1}$, trapping one of the zero-order dark states in the narrow energy range between these two eigenstates. The results of an extended deconvolution to form a doorway-coupling Hamiltonian are shown in Figure 3-3. This figure illustrates that, in the doorway-coupling model Hamiltonian, the combined set of zero-order energies plus the bright state energy are trapped between the eigenstates of the spectrum.

This property exists for the doorway-coupling Hamiltonian because it can be rearranged to have the same form as a direct-coupling Hamiltonian without a matrix rotation. Simply by re-ordering the columns such that the bright state is embedded into the manifold of dark states, the doorway-coupling Hamiltonian becomes identical in form to the direct-coupling Hamiltonian. This arrangement is shown in Figure

Figure 3-2: Thick vertical lines: Dark basis state energies and matrix elements obtained by discrete LKL deconvolution of a portion of the NO_2 spectrum reported by Smalley *et. al.* [107]. The single bright state energy obtained from deconvolution is displayed as a vertical line in the negative direction. The original absorption spectrum is shown as a set of gaussian lineshapes superimposed on the deconvolution results.

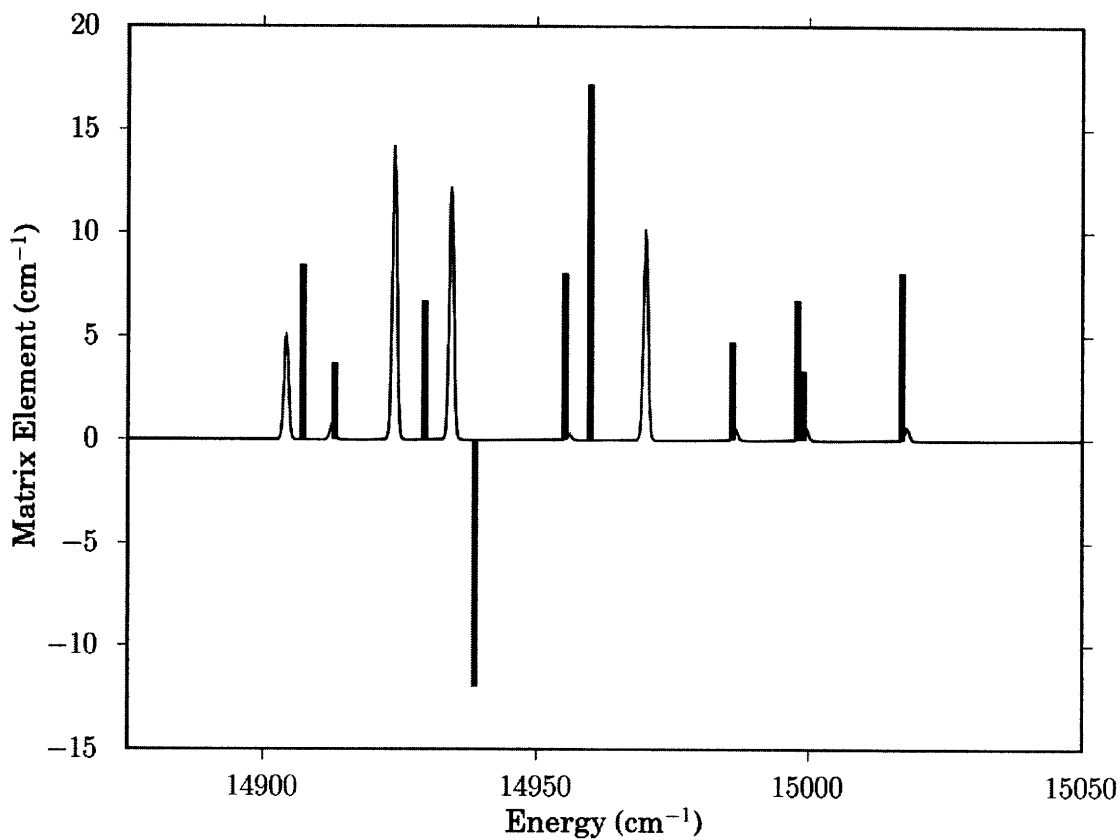
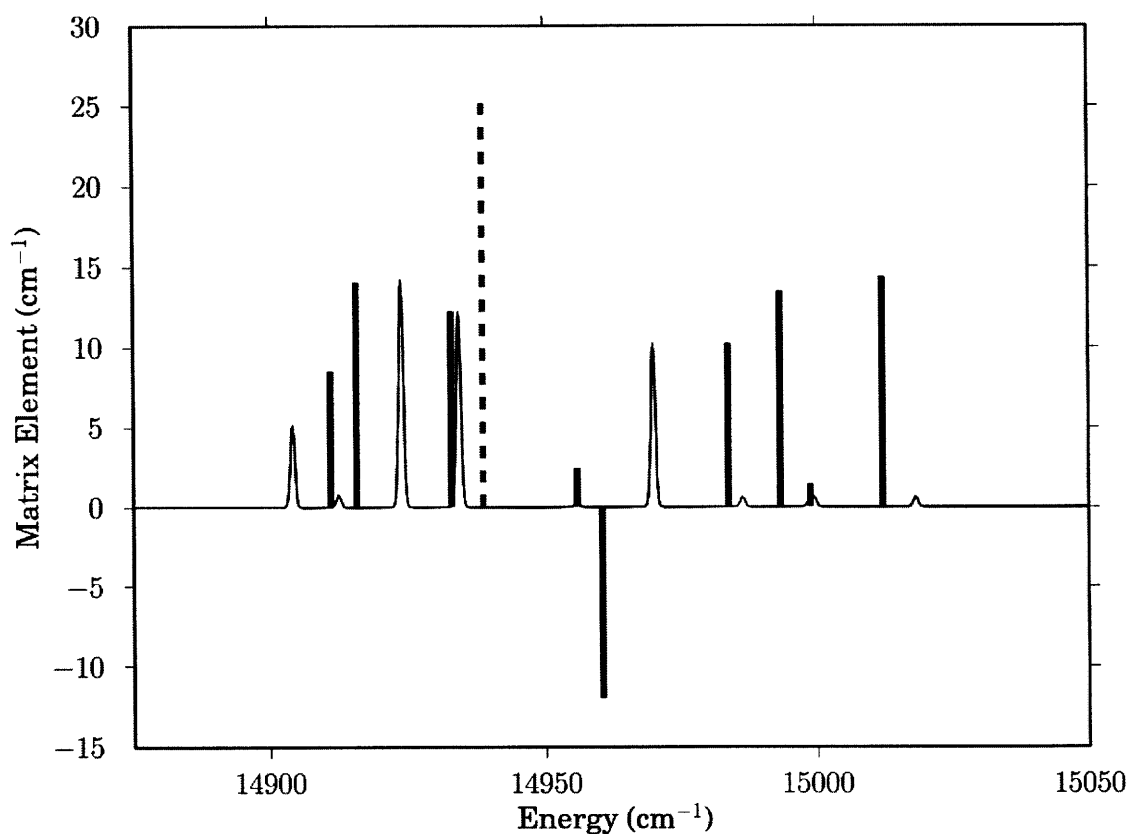


Figure 3-3: Thick vertical lines: Dark basis state energies and matrix elements obtained by an extended LKL deconvolution of a portion of the NO_2 spectrum reported by Smalley *et. al.* [107]. The bright state energy obtained from the first stage of deconvolution is displayed as a dashed vertical line in the positive direction, scaled to the bright~doorway matrix element. The energy of the single doorway state is displayed as a vertical line in the negative direction. The original absorption spectrum is shown as a set of Gaussian lineshapes superimposed on the deconvolution results. Note that the energies for the combined set of bright and dark states in the doorway-coupled basis satisfy the usual level trapping rules for dark states in a direct-coupled basis.



3-1c. With the Hamiltonian arranged in this form, it is clear that the distribution of doorway amplitude among the dark states is equivalent to the distribution of bright state amplitude in a direct-coupling model. As a consequence, the phenomenon of level trapping still applies to a doorway-coupled system, though the bright state and doorway state have swapped roles. In the doorway-coupling Hamiltonian, the zero-order bright state and the $N - 1$ zero-order dark states are trapped between the eigenstate energies, in the same manner as the N dark states of the direct-coupling Hamiltonian.

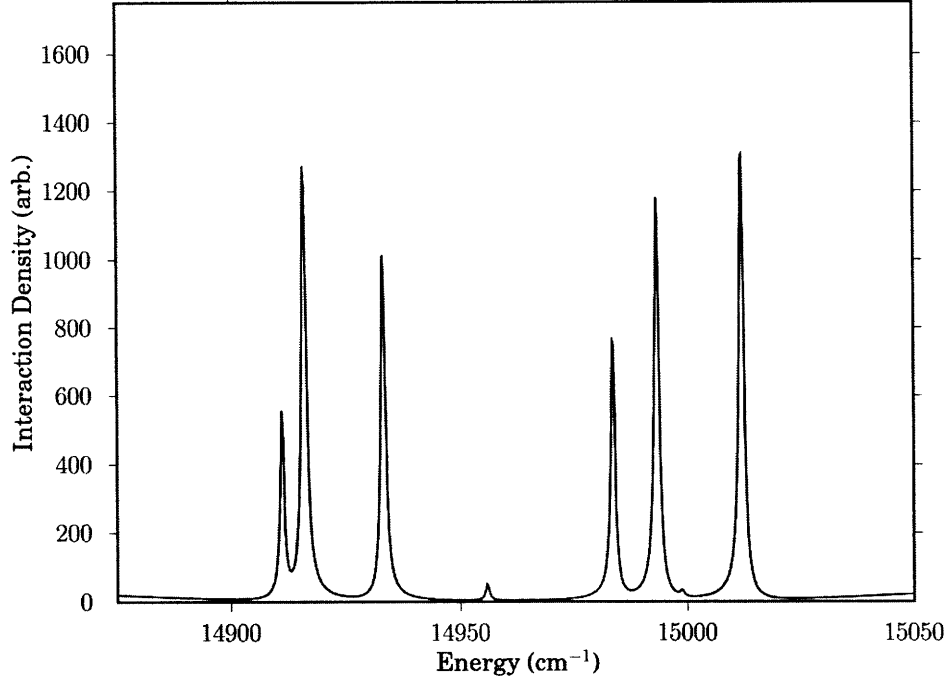
We note in passing that doorway-coupling models with two or more successive doorway states do not share this property. They require a change of basis to bring them into the form of the direct-coupling Hamiltonian. In this respect, the doorway-coupling Hamiltonian with a single doorway state is unique among the set of doorway-coupling Hamiltonians in the spectroscopic channel basis of Ziv and Rhodes.

To compare the discrete and continuous formulations, we have used the methods detailed by Cable and Rhodes to re-evaluate the interaction density spectrum for coupling to the doorway state [20]. Our results are presented in Figure 3-4; agreement with Figure 11 of reference [20] is within acceptable limits given that the previous computation involved the numerical evaluation of principal value integrals.

Figure 3-5 compares the discrete and continuous deconvolution results for the doorway-coupling Hamiltonian. The Lorentzian peaks in the interaction density spectrum coincide exactly with the dark state energies in the discrete formulation. Lorentzian lineshapes transform correctly under the Hilbert transformation of equation 3.5, producing smooth poles in the real part of the Green's function derived from the absorption spectrum.

Because the continuous formulation is exact for Lorentzian lineshapes, a continuous deconvolution of unresolved, homogeneously broadened spectral lines will have the correct functional form, although some peaks may remain unresolved in the resulting interaction density spectrum. Thus, for a spectrum with homogeneous width

Figure 3-4: Interaction density spectrum for coupling to the doorway state, computed from a portion of the NO₂ spectrum reported by Smalley *et. al.* [107]. These results are in agreement with those of Cable and Rhodes (compare to their Figure 11) [20].



γ , the interaction density spectrum, $\mathcal{F}(E)$, for the doorway state is equal to

$$\mathcal{F}_\ell(E) = \mathcal{L}_\gamma * \sum_n H_{\ell n}^2 \delta(E_n - E) \quad (3.26)$$

where the symbol $*$ denotes convolution, \mathcal{L}_γ is a Lorentzian function with FWHM γ , and the index m runs over the diagonal block of dark states coupled to K . A comparison of discrete and continuous deconvolution results is shown in Figure 3-6, where the original discrete spectrum has been convoluted with a Lorentzian function with a FWHM of 6 cm^{-1} . The rising wings of the interaction density spectrum arise from the nonzero tails of the Lorentzian peaks, which cause the inverse of the Green's function to accumulate at the edges of the computed spectrum.

In the limit of inhomogeneous broadening, the continuous form of the deconvolution fails. Gaussian lineshapes do not have the correct functional form for solutions to the Green's function of equation 3.2, and a Hilbert transformation of the spectrum

Figure 3-5: Comparison of discrete and continuous extended deconvolution results for the same spectrum. The dark state energies and squared matrix elements in the discrete formulation correspond to the peaks of the interaction density spectrum in the continuous formulation. The rising wings of the interaction density spectrum arise from the nonzero tails of the Lorentzian peaks, which cause the inverse of the Green's function to accumulate at the edges of the computed spectrum.

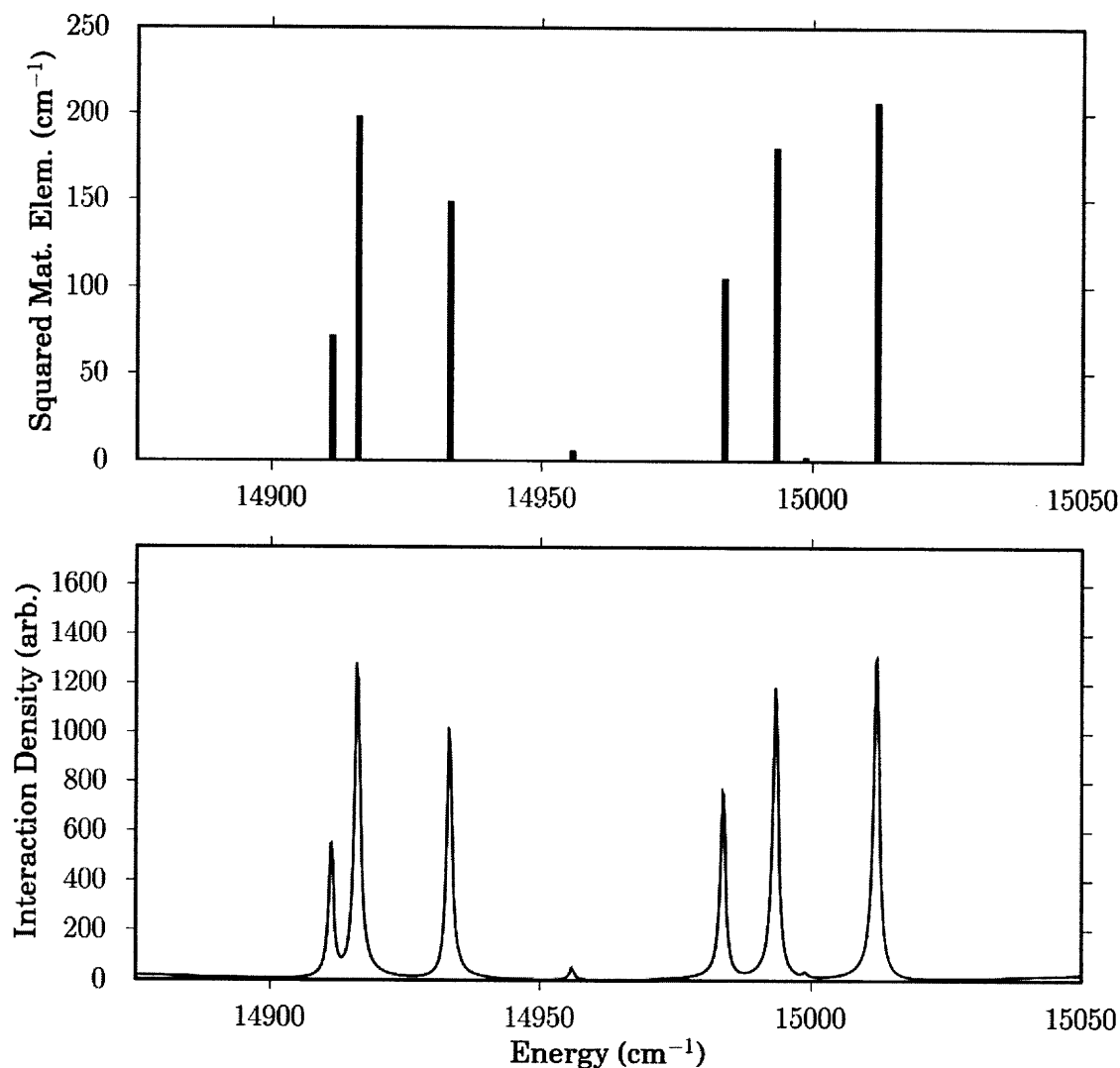
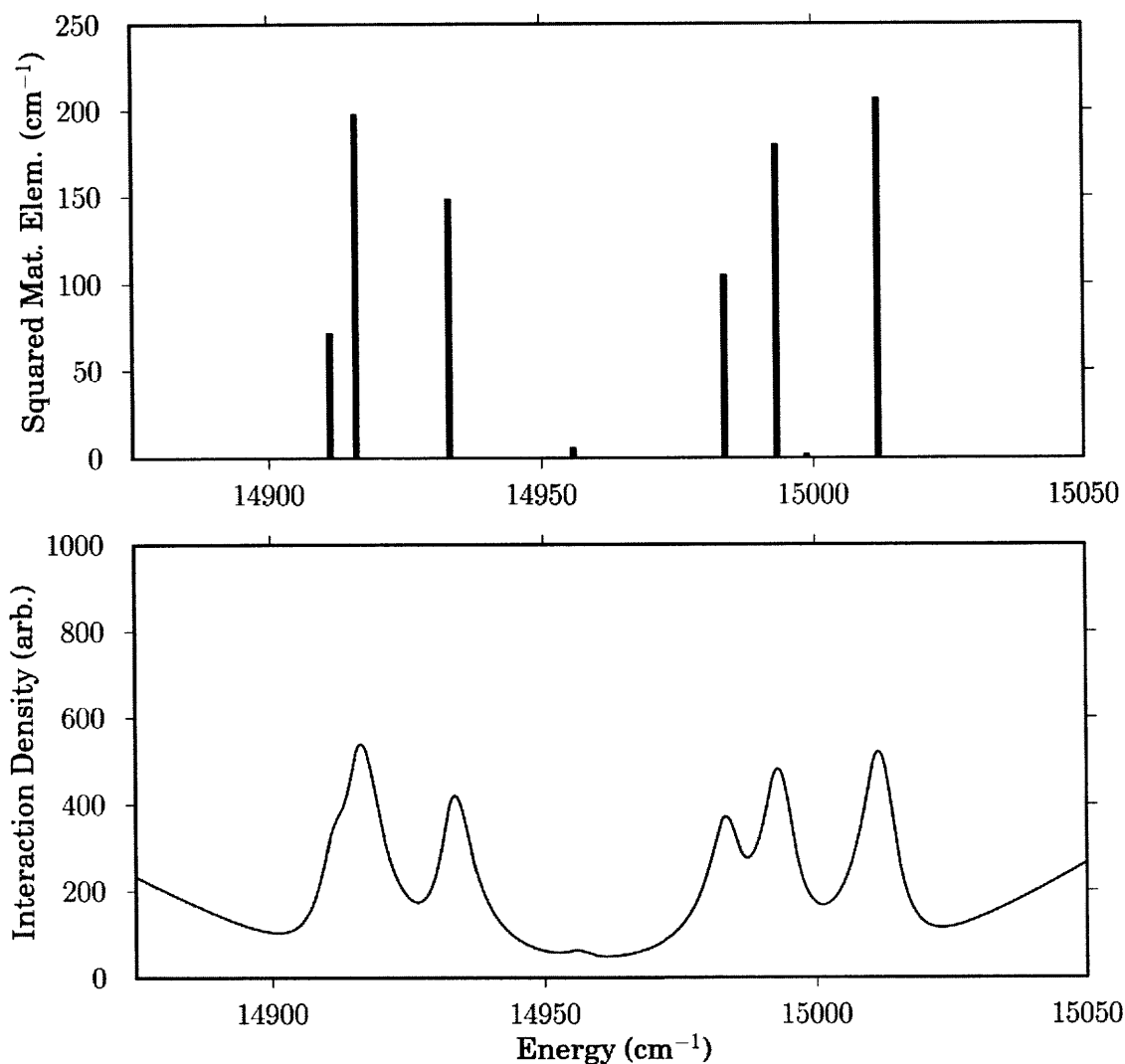


Figure 3-6: Continuous deconvolution carried out for Lorentzian broadened lineshapes of 6 cm^{-1} fwhm, corresponding to $1/2$ the average level spacing of the spectrum. The continuous deconvolution result is consistent with the discrete result to a resolution of 6 cm^{-1} . The rising wings of the interaction density spectrum arise from the nonzero tails of the Lorentzian peaks, which cause the inverse of the Green's function to accumulate at the edges of the computed spectrum.



does not produce a real function with smooth poles. If the deconvolution procedure is carried out regardless, the resulting interaction density spectrum will contain peaks at incorrect energies and intensities. In this situation, the experimentalist is faced with two choices: discretize the spectrum and miss dark state~dark state spacings smaller than the resolution, or convolve the spectrum with a Lorentzian lineshape to obtain an unresolved but functionally correct interaction density spectrum. The parameters, E_s , $H_{s\ell}^2$, and E_ℓ , because they are related to moments of the spectrum, will remain correct for any symmetric lineshape in the spectrum.

3.4 Application to high-resolution spectra of acetylene

In 1994, Drabbels *et. al.* recorded the laser-induced fluorescence (LIF) spectrum of the $3_0^3K_0^1$ vibronic subband of S_1 acetylene at a resolution of 18 MHz [34]. The authors used the LKL method to generate a set of direct-coupling matrix elements from the spectral data. However, several subsequent investigations of this band have found strong evidence that a single vibrational level of the T_3 electronic state mediates coupling between the S_1 level and the remaining levels, which are classified as high-lying vibrational levels of the T_1 and T_2 electronic states.

Using the methods described above, we have calculated the parameters of a doorway-coupling model Hamiltonian for each rotational level of $3_0^3K_0^1$ reported by Drabbels *et. al.* The results are shown in Table 3.2. Note the near-linear change in bright state - doorway state energy difference with increasing J . This result is consistent with the observation of a local T_3 vibrational level with a rotational constant slightly different that of the singlet.

This band of acetylene was also considered by Altunata and Field, who derived a parameter to predict the product $E_\ell \times H_{s\ell}^2$ [5]. The “skewness” parameter of Altunata and Field,

$$S = \sum_m I_m^2 \times (E_m - E_0), \quad (3.27)$$

is computed from the results of a single deconvolution, using the quasi-continuous

Table 3.2: Extended deconvolution results for the $3^3_0K_0^1$ vibrational subband of S_1 acetylene. The energies of the zero-order bright state, E_s , and doorway state, E_ℓ , are given, as well as the zero-order energy difference, $\Delta E_{s\ell}$, and bright~doorway matrix element, $H_{s\ell}$. All values are in units of cm^{-1} .

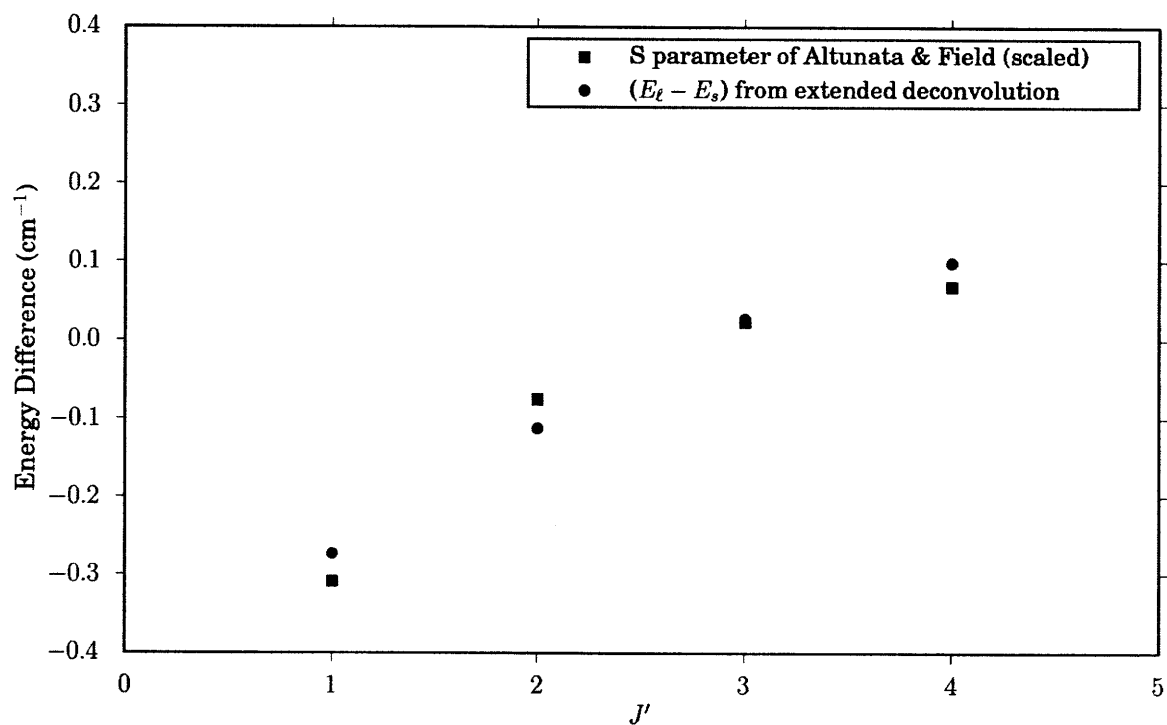
	E_s	E_ℓ	$\Delta E_{s\ell}$	$H_{s\ell}$
R(0)	45303.1255	45302.8524	-0.2731	0.1418
R(1)	45305.2210	45305.1090	-0.1120	0.1206
R(2)	45307.1738	45307.2010	0.0272	0.1188
R(3)	45308.9133	45309.0122	0.0990	0.1704
Q(1)	45300.6503	45300.6921	0.0418	0.1980
Q(2)	45300.1678	45300.1170	-0.0508	0.1245
Q(3)	45299.4414	45299.2142	-0.2272	0.1785
Q(4)	45298.4825	45298.3072	-0.1753	0.1695

formulation of Lawrance and Knight. The intensity factor I_m is proportional to the quantity H_{sm}^2 in the discrete formulation. The authors identify E_0 with the “midpoint of the energy axis of the LK output.” Because this parameter scales with energy to the first power, it is more accurately considered an expression for the center-of-gravity of the distribution of $\{H_{sm}^4\}$ in the direct-coupling Hamiltonian.

The authors of reference [5] applied their S parameter to the spectrum of $3^3_0K_0^1$ reported by Drabbels *et. al.* and reported the product $E_\ell \times H_{s\ell}^2$ for the R(0-4) transitions. We compare these results with the deconvolution method described in this work by normalizing the S parameter to the quantity $H_{s\ell}^2$, computed from the variance of the spectrum (equation 3.24). Figure 3-7 shows the doorway state energy computed from deconvolution and the normalized S parameter values reported in reference [5]. The small (0.03 cm^{-1}) discrepancies presumably result from integration of the interaction density spectrum (Lawrance and Knight’s $B(E)$) used to compute the S parameter [65].

The most complete description of the doorway level in $3^3_0K_0^1$ is given by Mishra *et. al.*, who used the complementary spectroscopic techniques of LIF and SEELEM to record the spectrum of long-lived states coupled weakly to S_1 [85]. To analyze this local T_3 perturber, they constructed reduced term value plots and fit the experimental

Figure 3-7: Comparison between Altunata and Field's S parameter and the bright state - doorway state energy difference ($E_s - E_\ell$) obtained from extended LKL deconvolution [5]. To coincide with the formula for doorway state energy, the S parameter results are scaled by the squared bright~doorway matrix element, which is equal to the variance of spectral intensity.



energies to a model Hamiltonian.

The results of the Hamiltonian fit by Mishra *et. al.* yielded a bright~doorway matrix element of $H_{s\ell} = 0.126 \text{ cm}^{-1}$ for the e -symmetry components (the authors do not give an uncertainty for this value) [85]. We compare the deconvolution results with the Hamiltonian fit by averaging the value of $H_{s\ell}$ obtained from extended deconvolution over the rotational quantum number J . The average bright~doorway matrix element from deconvolution is $\langle H_{s\ell} \rangle = 0.138 \pm 0.021 \text{ cm}^{-1}$, in agreement with the previous results. The bright state and doorway state energies obtained from deconvolution are compared to the reduced term values of reference [85] in Figure 3-8. As expected, the deperturbed energies lie between the nominal S_1 and T_3 eigenstate energies inferred from the spectrum.

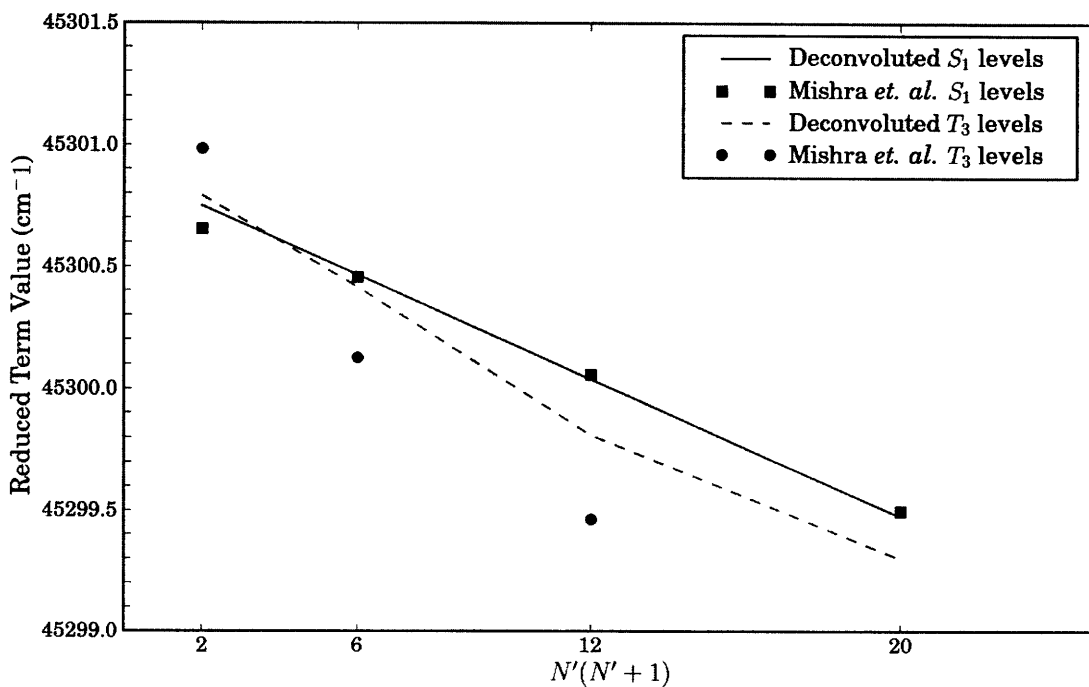
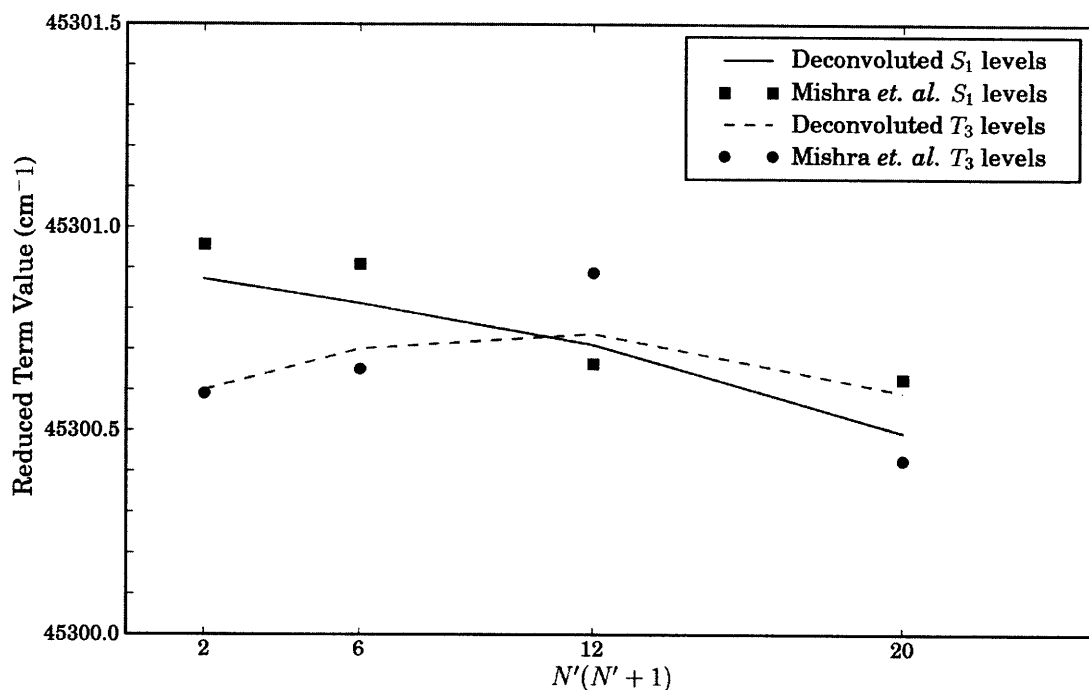
The use of LIF intensities in the deconvolution procedure instead of absorption intensities rests on the assumption that only the bright state character of an eigenstate contributes to the fluorescence intensity. This is indeed the case for the low-lying triplet basis states of acetylene, from which transitions to the ground state are spin-forbidden.

3.5 Conclusion

We have shown how to extend established methods of spectral deconvolution to uniquely determine the parameters of a doorway-coupling effective Hamiltonian. The most important parameters of the effective Hamiltonian, the doorway state energy and bright~doorway matrix element, were related to simple moments of the spectral intensity distribution. By making a correspondence to the work of Ziv and Rhodes on continuous deconvolution, we have shown how the parameters that define an effective Hamiltonian can be derived for any number of sequential doorway states.

This technique was applied to the spectrum of the $3\nu_3$ $K = 1$ vibrational level of S_1 acetylene, where a single, local, T_3 doorway level mediates coupling to the $T_{1,2}$ manifold. The deperturbed T_3 energies and matrix elements were shown to be consistent with past studies. A comparison was made to the S parameter of Altunata

Figure 3-8: The S_1 and T_3 basis state energies obtained from extended LKL deconvolution are shown together with the reduced term values of Mishra *et. al.* [85]. Top: e -symmetry basis state energies obtained from R-branch transitions. Bottom: f -symmetry basis state energies obtained from Q-branch transitions. The deperturbed energies from deconvolution lie between the nominal S_1 and T_3 eigenstate energies inferred from the spectrum, as they must.



and Field, which is equal to the product $E_\ell \times H_{s_\ell}^2$.

Chapter 4

SEELEM/LIF spectroscopy of acetylene: Spectral signatures of energetically distant doorway levels

4.1 Introduction

What are the global characteristics of doorway-mediated intersystem crossing in acetylene, C_2H_2 ? Although we have a detailed understanding of the spectroscopic patterns arising from a crossing between near-degenerate S_1 and T_3 vibrational levels [55, 4, 5, 85], we do not know quite what to anticipate in the spectrum of an S_1 sublevel which is not near-degenerate ($|\Delta E| < 2 \text{ cm}^{-1}$) with a T_3 doorway. In this study, we examine the spectra of several S_1 vibrational sublevels that fall into the latter category, and produce a comprehensive description of singlet~triplet mixing that takes into account the effects of energetically distant ($|\Delta E| > 2 \text{ cm}^{-1}$) T_3 doorway sublevels. The spectra of S_1 sublevels interacting with remote T_3 perturbors are far from uneventful, and provide an unexpected wealth of information as to the identity and rotationless energy of T_3 vibrational sublevels.

To observe the distribution of metastable, nominal $T_{1,2}$ eigenstates in the vicinity of the upper state of an allowed $S_1 \leftarrow S_0$ transition, we take advantage of two

complementary, simultaneously recorded spectroscopic detection channels: Laser-Induced Fluorescence (LIF) and Surface Electron Ejection by Laser-Excited Metastables (SEELEM). Gated LIF detection is sensitive to molecules in eigenstates with short radiative lifetimes ($\tau < 10 \mu\text{s}$), which have a high probability of fluorescence within the LIF viewing region (about 4 mm). Conversely, SEELEM detection is sensitive only to long-lived ($\tau > 300 \mu\text{s}$) molecules. To be SEELEM detectable, the vertical excitation energy of a molecule must be larger than the work function of the metal used as the detector surface. Only the S_1 and T_3 electronic states are higher in energy than the work function of gold ($\Phi = 5.1 \text{ eV}$). To be exitable from the ground state by a laser, SEELEM detectable eigenstates must have a small but nonzero amount of fractional S_1 character.

Intersystem crossing in the $\tilde{A} \ ^1A_u$ (S_1) state of acetylene is well-described by a doorway-mediated coupling model. The model is supported by observations in Zeeman anticrossing spectroscopy [41, 39, 37], LIF Zeeman quantum beat spectroscopy [93, 94, 38], high-resolution LIF spectroscopy [34, 5], simultaneous LIF and SEELEM spectroscopy [55, 4, 85], photodissociation plus H-atom action spectroscopy [138, 70, 88], and photoelectron spectroscopy [32]. Briefly, the model states that matrix elements between vibrational levels of the S_1 and $T_{1,2}$ electronic states are very nearly zero, and that all mixing between S_1 and $T_{1,2}$ levels is induced indirectly by nonzero $S_1 \sim T_3$ and $T_3 \sim T_{1,2}$ matrix elements.

The *trans*-bending mode of S_1 acetylene, ν_3 , is known to be an important promoter of $S_1 \sim T_3$ mixing. In Zeeman anticrossing experiments, Dupré and coworkers observed a rapid increase in the anticrossing density, as well as the product, $\rho_{\text{vib}} \langle H_{st} \rangle$, with energy in ν_3 [41, 37]. They also observed a single, broad singlet~triplet anticrossing in the $3\nu_3$ $K_a = 0$ level, which was in turn perturbed by many smaller couplings [38]. These observations led the authors to propose that mixing between S_1 and the dense manifold of optically dark states, including $T_{1,2}$ levels, is controlled by the magnitude of vibrational overlap factors between S_1 levels and particular doorway vibrational levels. Subsequent theoretical and experimental work identified the doorways as vibrational levels of the T_3 electronic state [126, 105, 55, 4].

The S_1 $3\nu_3$ $K'=1$ level has been heavily studied due to the presence of a near-degenerate vibrational level of T_3 , which gives rise to a rotationally assignable $S_1 \sim T_3$ level crossing at $J \approx 3$. Spectroscopic patterns in LIF and SEELEM spectra arising from the effects of the local T_3 perturber, are discussed by several authors [55, 4, 5, 85]. Using vibrational overlap integrals gained from *ab initio* calculations of the T_3 electronic surface, Thom and coauthors were able to exclude all but several candidate T_3 levels as the $3\nu_3$ local perturber [122]. However, a recent observation of increased average $T_{1,2}$ electronic character at $J' = 8 - 12$ suggests that this local T_3 perturber is not the sole, and perhaps not even the primary doorway for $3\nu_3$ $K'=1$ [32].

That an energetically distant T_3 doorway, which would be required to have a correspondingly larger spin-orbit matrix element than the local perturber, may play a role in spin-orbit mixing between S_1 $3\nu_3$ and the $T_{1,2}$ manifold, is not altogether surprising, given the energy region in question. *Ab initio* calculations are in agreement that a seam of intersection between the electronic surfaces of S_1 and T_3 states is energetically nearby [128, 122]. Such a surface crossing would allow for strong interactions with several T_3 vibrational levels in the same energy region. It should also play a role in promoting singlet~triplet coupling within other S_1 levels in the same energy region. The $4\nu_3$ level, 1000 cm^{-1} higher in energy, is also strongly perturbed by the $T_{1,2}$ manifold, although no obvious local T_3 doorway has been observed [34, 94].

We turn our attention to other vibrational levels of S_1 in the same energy region that are not near-degenerate with a mediating T_3 level at low J . In the absence of a local T_3 perturber, coupling between S_1 levels and the local manifold of $T_{1,2}$ levels is expected to be mediated by energetically distant T_3 levels. Evidence for such energetically distant, mediating T_3 levels is obtained by comparing simultaneously recorded LIF and SEELEM spectra.

We begin by deriving the energy level spacings and spin-orbit matrix elements between rovibrational levels of S_1 and T_3 . Next, we develop a new analysis technique that is sensitive to the presence of distant T_3 doorway levels. This new technique takes into account observed shifts of relative intensities in the frequency-domain LIF

spectrum as a function of delay time, which result from the time development of an incoherent ensemble of eigenstates having different radiative lifetimes. We then apply this new technique to the simultaneously recorded LIF and SEELEM spectra of four S_1 vibrational sublevels, and discuss the properties of admixed, energetically distant T_3 vibrational levels.

4.2 Theory: $S_1 \sim T_3$ rotational energy level spacing and spin-orbit matrix elements

In the S_1 (\tilde{A}^1A_u) electronic state, acetylene is a near-symmetric prolate top. Neglecting centrifugal and asymmetry terms, the rovibrational energies are approximately [131]

$$E_{S_1}(v, K, J) = T_v + [A_v - B_v]K^2 + \frac{B_v + C_v}{2} J(J + 1), \quad (4.1)$$

where J is the total angular momentum, K is the absolute value of the projection of the orbital angular momentum on the a-axis of the molecule, T_v is the rotationless energy of the vibrational level v , and A_v , B_v , and C_v ($\approx B_v$) are the rotational constants for the vibrational level. The model of a near-symmetric prolate top is also appropriate to describe the energy levels of the T_3 electronic state, although *ab initio* calculations predict that the *trans*-bent equilibrium geometry is non-planar [128, 122]. Adopting a Hund's case (*b*) basis, the rovibrational energy levels of T_3 are approximately

$$E_{T_3}(v, K, N) = T_v + [A_v - B_v]K^2 + \frac{B_v + C_v}{2} N(N + 1), \quad (4.2)$$

where the pattern-forming rotational quantum number, N , is the total angular momentum exclusive of spin. At each energy $E_{T_3}(v, K, N)$, three closely spaced spin components are present, due to the three possible values of the total angular momentum J . The components are labeled F_1 ($J = N + 1$), F_2 ($J = N$), and F_3 ($J = N - 1$). Since $S = 0$ for the S_1 electronic state, only one component $N = J$ is present for all

S_1 rotational levels.

The S_1 and T_3 electronic states are mixed by spin-orbit interaction. The total first-order spin-orbit matrix element between rovibrational states of S_1 and T_3 is the product of three factors: an electronic spin-orbit matrix element, a vibrational overlap factor, and a rotational factor that arises from angular momentum coupling. Spin-orbit matrix elements follow the rotational selection rules $\Delta J = 0$ and $\Delta P = 0$, where P is the projection of J on the a-axis of the molecule [52]. In Hund's case (b), the quantum number P is mixed among several levels with different values of K^1 , leading to the case (b) selection rule $\Delta K = 0, \pm 1$ [52, 115].

We consider the relative rotational energy differences between an S_1 vibrational sublevel, $|S\rangle$, and a T_3 vibrational sublevel, $|T\rangle$. According to the selection rule $\Delta J = 0$, a rotational level of $|S\rangle$, $|S; J = J_S\rangle$, may mix with three rotational levels of $|T\rangle$: $|T; N = J_S - 1\rangle$ (an F_1 component), $|T; N = J_S\rangle$ (an F_2 component), and $|T; N = J_S + 1\rangle$ (an F_3 component). Since the three triplet components with nonzero matrix element differ in the rotational pattern-forming quantum number, N , they have different rotational energies. Written in terms of J , these energies are

$$E_T(J) = T_{0,T} + \begin{cases} B_T (J+1)(J+2) & F_3 (\Delta N = +1), \\ B_T J(J+1) & F_2 (\Delta N = 0), \\ B_T J(J-1) & F_1 (\Delta N = -1), \end{cases} \quad (4.3)$$

where $T_{0,T}$ is the rotationless energy of the T_3 vibrational sublevel, $|T\rangle$. Subtracting the rotational energies of $|S\rangle$,

$$E_S(J) = T_{0,S} + B_S J(J+1), \quad (4.4)$$

from $E_T(J)$ yields the rotational energy differences between $|S\rangle$ and $|T\rangle$. In the approximation that the difference in rotational constants ΔB_{ST} is small compared to

¹The quantum number K is the projection of N on the top axis.

B_T , the rotational energy differences are

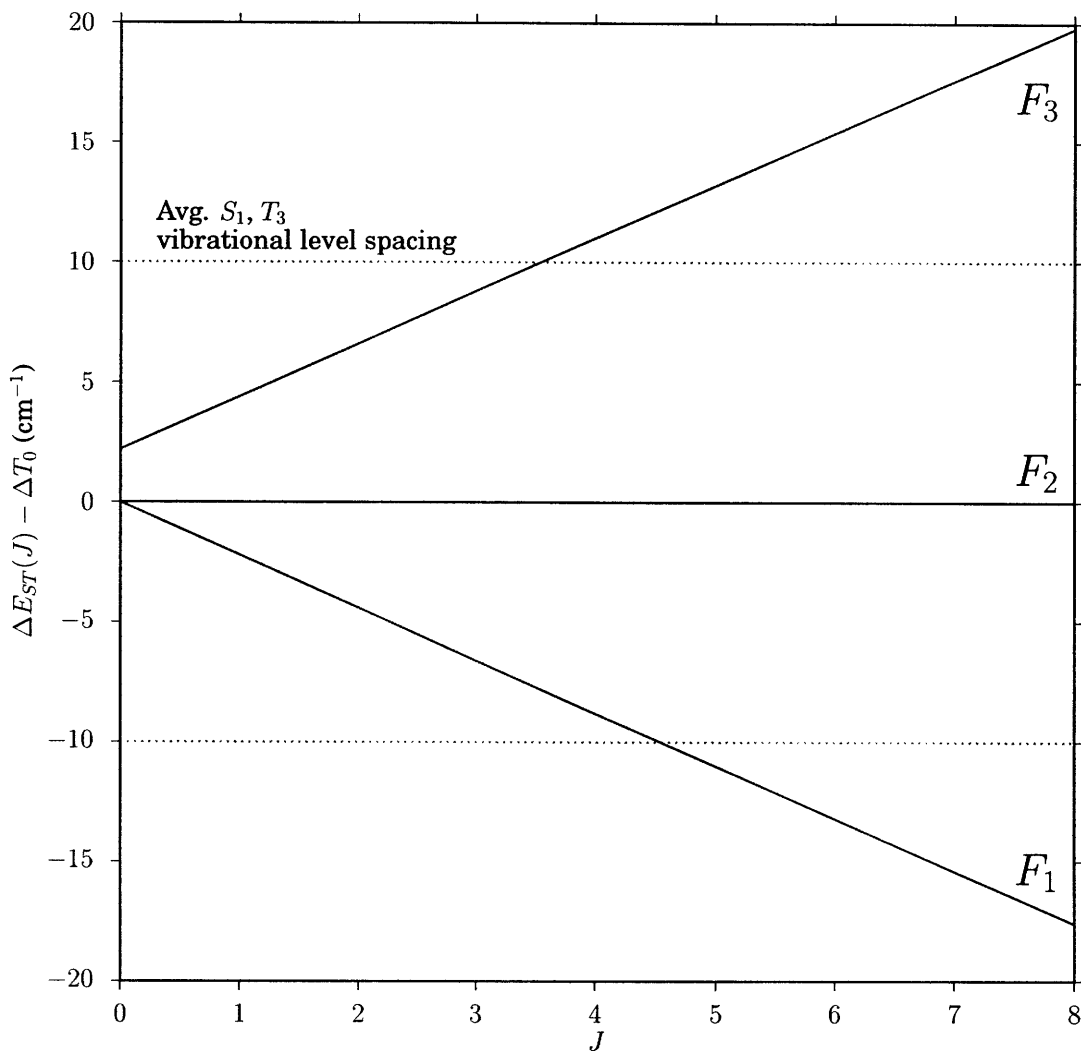
$$\Delta E_{ST}(J) = \Delta T_0 + \begin{cases} 2B_T J + 2B_T & F_3 \ (\Delta N = +1), \\ 0 & F_2 \ (\Delta N = 0), \\ -2B_T J & F_1 \ (\Delta N = -1). \end{cases} \quad (4.5)$$

The approximate energy differences $\Delta E_{ST}(J)$ are plotted as a function of J in Figure 4-1. A value of $B_T = 1.1 \text{ cm}^{-1}$ was chosen for the figure based on the rotational assignment of a T_3 perturber in the $3^3 K'=1$ sublevel of S_1 [85]. The energy of the F_2 component, relative to that of the S_1 level, has a slope of approximately zero, while the relative energies of the F_1 and F_3 components have slopes of approximately $-2B_T \approx -2 \text{ cm}^{-1}$ and $+2B_T \approx +2 \text{ cm}^{-1}$ per J , respectively. Also included on the plot is the average vibrational level spacing, $\sim 10 \text{ cm}^{-1}$ for both the S_1 and T_3 electronic states. The relative energies of the F_1 and F_2 components are 10 cm^{-1} distant from the rotationless energy separation when $J \approx 4$.

Because the F_1 and F_3 components of the triplet have large slopes in relative energy separation from a singlet level, the component of a T_3 level with which an S_1 level interacts is determined by the rotationless energy difference. The possibilities are as follows.

- When two vibrational sublevels of S_1 and T_3 are near-degenerate, $-4 \lesssim (T_{0,T} - T_{0,S}) \lesssim 2 \text{ cm}^{-1}$, the energy separation between the singlet and the F_2 component of the triplet remains close to its initial value as J increases, while the relative energy separations of the F_1 and F_3 components increase at a rate of approximately $2B_T$ per J . Energy denominators favor mixing between the singlet and the F_2 component of the triplet when $J \geq 1$.
- When a T_3 doorway level lies higher in rotationless energy than the singlet level, $(T_{0,T} - T_{0,S}) \gtrsim 2 \text{ cm}^{-1}$, energy denominators favor mixing between the singlet and the F_1 component of the triplet. The rotational energy separation between the singlet and the F_1 component of the triplet decreases at a rate of

Figure 4-1: Approximate energy separation between singlet and triplet vibrational sublevels, plotted as a function of J . The relative energy of the F_2 spin component is approximately constant. The relative energies of the F_1 and F_3 spin components change at a rate of approximately 2 cm^{-1} per J' . Dotted lines indicate the approximate average vibrational level spacing for the S_1 and T_3 electronic states in the $45,000 \text{ cm}^{-1}$ energy region.



approximately $2B_T$ per J until a level crossing occurs at $J \approx (T_{0,T} - T_{0,S})/2B_T$.

- When a T_3 doorway level lies below a singlet level in rotationless energy, $(T_{0,T} - T_{0,S}) \lesssim 4 \text{ cm}^{-1}$, energy denominators determine that the primary interaction is via the triplet F_3 component. The rotational energy separation between the singlet level and the F_3 component of the triplet decreases at a rate of $2B_T$ per J until a crossing occurs at $J \approx (T_{0,S} - T_{0,T})/2B_T - 1$.

Taken together, these trends guarantee a level crossing at $J < 8$ for any pair of S_1 and T_3 sublevels that have a rotationless energy separation of less than 20 cm^{-1} . Regardless of the sign of the rotationless energy difference, one spin component of a T_3 level always approaches the singlet at a rate of $2B_T$ per J . When a doorway is energetically distant, in other words not near-degenerate in rotationless energy, energy denominators determine that the interaction occurs via either the F_1 or F_3 component, depending on the sign of $T_{0,T} - T_{0,S}$.

To verify that the magnitude of the spin-orbit matrix elements does not dominate over energy denominator effects for the F_1 and F_3 components of a triplet level, the rotational factors for spin-orbit matrix elements are calculated from general formulas given by Stevens and Brand [115]. These factors are plotted as a function of J in Figure 4-2 for a singlet level with $K_S=1$. The rotational factors quickly approach their asymptotic limits as J is increased. Even at the lowest value of J , the rotational factor never differs from its asymptotic value by more than a factor of 2. Figure 4-3 shows the same factors for $K_S=2$, also considered in this study. The plot is essentially the same.

The overall magnitude of spin-orbit matrix elements between rovibrational levels of S_1 and T_3 is therefore not governed by J -dependent rotational factors, but by vibrational overlap factors. Franck-Condon overlaps between relatively low-lying vibrational levels of S_1 and T_3 are calculated to vary over at least three orders of magnitude [122]. The resultant wide variation in spin-orbit matrix element, arising from vibrational overlap factors, gives rise to two classes of level crossings between S_1 and T_3 levels: those where $|H_{ST}| \ll 2B_T$, and those where $|H_{ST}|$ is on the order

Figure 4-2: Rotational factors of spin-orbit matrix elements between rovibrational levels of the S_1 and T_3 electronic states, $K_S=1$ ($J \geq K_S$). The plot includes matrix elements for the F_3 ($\Delta N = +1$) and F_1 ($\Delta N = -1$) components of a T_3 sublevel with $K_T = 0, 1, 2$. In all cases, the rotational factors vary by less than a factor of 2 as a function of J .

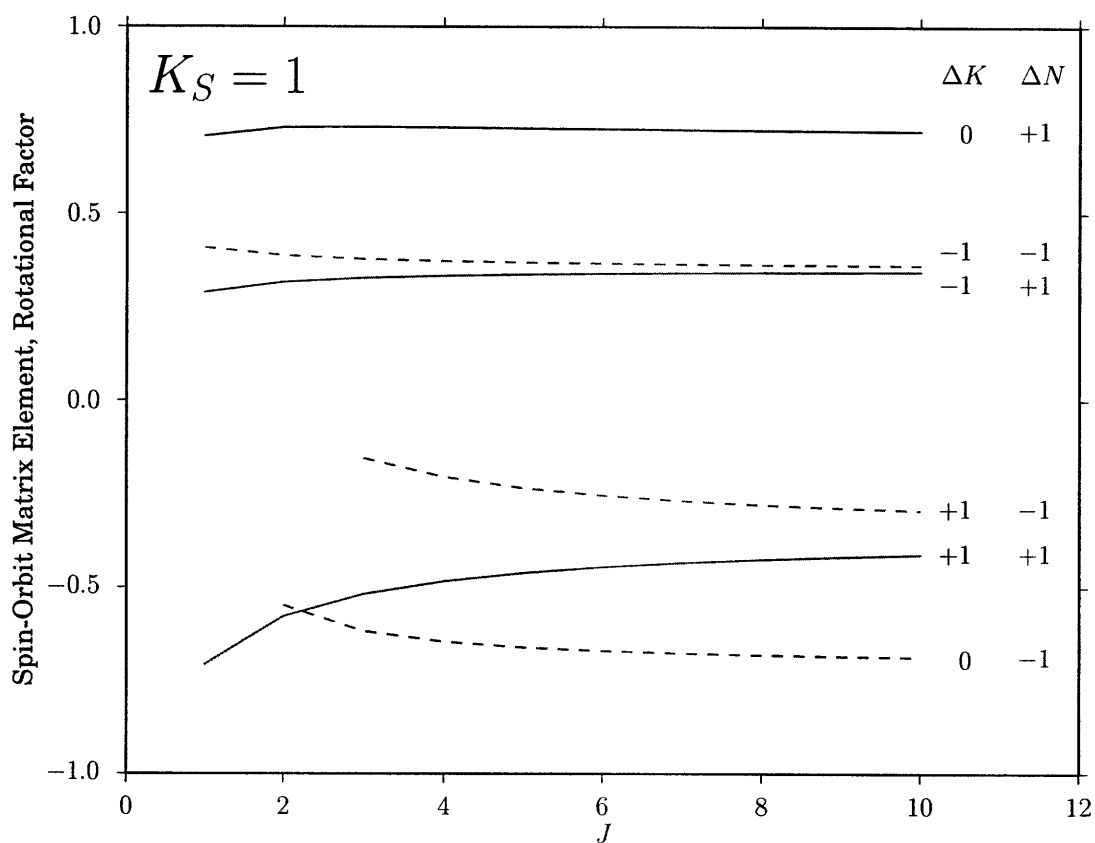
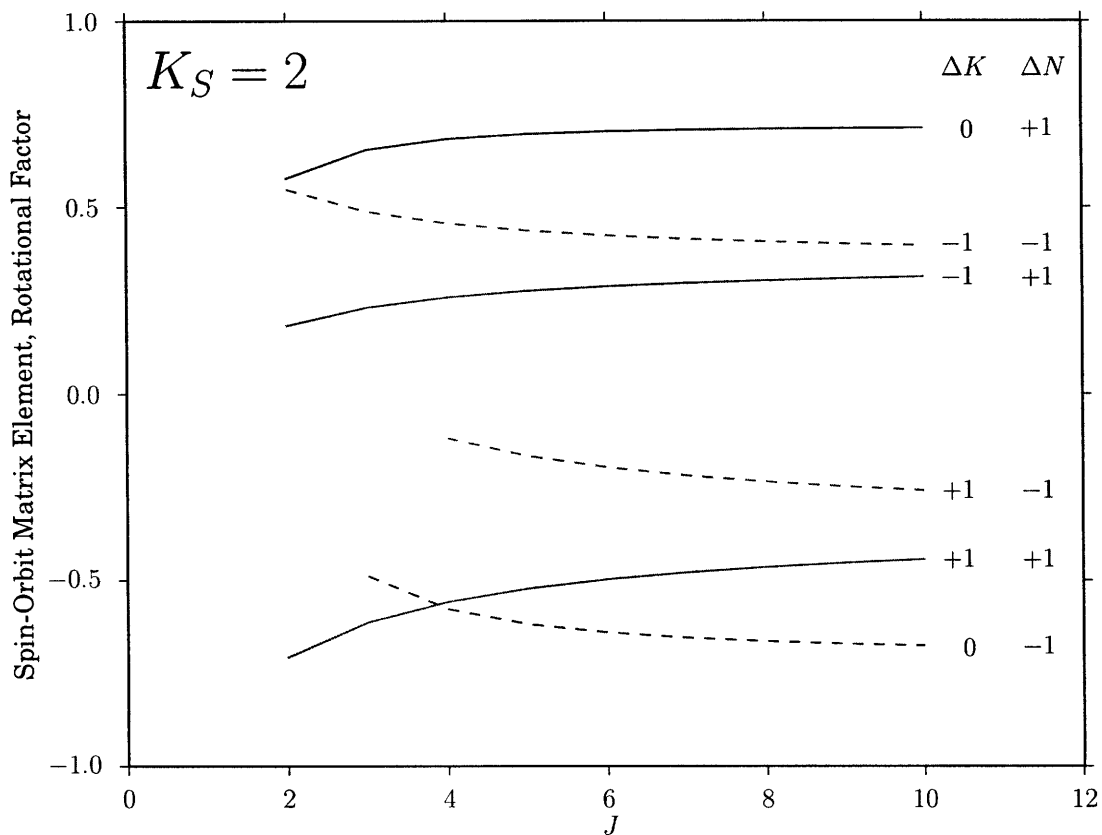


Figure 4-3: Rotational factors of spin-orbit matrix elements between rovibrational levels of the S_1 and T_3 electronic states, $K_S=2$. The plot includes matrix elements for the F_3 ($\Delta N = +1$) and F_1 ($\Delta N = -1$) components of a T_3 sublevel with $K_T = 1, 2, 3$. The rotational factors are essentially the same as those for $K_S = 1$.



of $2B_T$.

When $H_{ST}^2 \ll 2B_T$, energy denominator effects cause an $S_1 \sim T_3$ level crossing to be observable at only one J in the spectrum. However, once a triplet level with small vibrational overlap is located at a particular J , its energy above or below the perturbed singlet level may be found according to Equation 4.5. If the rotationless energy of the triplet vibrational level is higher than that of the singlet, the triplet must have $T_{0,T} \approx T_{0,S} + 2B_T J$. If the rotationless energy of the triplet vibrational level is lower than that of the singlet, the triplet must have $T_{0,T} \approx T_{0,S} - 2B_T J - 2B_T$.

When $|H_{ST}|$ is on the order of $2B_T$, significant mixing between the S_1 and T_3 levels may occur at several consecutive values of J . Such T_3 levels, having $|H_{ST}|$ on the order of $2B_T$, and lying more than $4B_T$ away in rotationless energy, are the energetically distant doorway states with which we are most concerned. By first mixing with the T_3 level, the S_1 level is permitted to mix with the local manifold of $T_{1,2}$ levels. Although a level crossing with the mediating T_3 level may occur at too high J to be observed², some T_3 -mediated $S_1 \sim T_{1,2}$ mixing is observable in the spectrum of the S_1 level. Mixing between the S_1 level and nearby $T_{1,2}$ levels is influenced by the relative energy of the doorway level: mixing is increased with $T_{1,2}$ levels that lie closer in energy to the doorway level. In the following section, we explain this effect and examine a method by which it may be observed.

4.3 Theory: Signatures of doorway-mediated intersystem crossing in delayed, incoherent fluorescence measurements

An energetically distant T_3 doorway level imprints its presence on the LIF and SEELEM spectra of the S_1 levels with which it interacts. When an S_1 level mixes with an energetically distant T_3 doorway level, the relative energy of the doorway level influences the local mixing between the S_1 level and nearby $T_{1,2}$ levels. This

²We are able to measure $J' < 9$ in pulsed jet experiments.

leads to a local energy dependence of the average fractional S_1 character in nominal $T_{1,2}$ eigenstates. This quantity may be evaluated using perturbation theory, after first pre-diagonalizing the interaction between S_1 and T_3 . Following Chapter 2, Equation 2.4, we find the energy dependence of the fractional S_1 character, $a_{S_1}^2$, of a nominal $T_{1,2}$ eigenstate to be

$$a_{S_1}^2(E) = \alpha^2(1 - \alpha^2)H_{T_3T_{1,2}}^2 \left\{ \frac{1}{E - E_{S_1}} + \frac{1}{E - E_{T_3}} \right\}^2, \quad (4.6)$$

where $\alpha = H_{S_1T_3}/(E_{S_1} - E_{T_3})$ is the mixing angle between the S_1 level and the doorway state, $H_{T_3T_{1,2}}$ is the $T_3 \sim T_{1,2}$ matrix element, E_{S_1} is the energy of the nominal S_1 eigenstate and E_{T_3} is the energy of the nominal T_3 eigenstate.

The energy dependence of average fractional S_1 character in the ensemble of nominal $T_{1,2}$ eigenstates causes their intensity-weighted center of gravity to be slightly shifted, relative to the energy of the nominal S_1 eigenstate in the LIF spectrum. The intensity-weighted center of gravity is defined as

$$E_{\text{ave}} = \int E \times I(E) dE, \quad (4.7)$$

where $I(E)$ is a unit-normalized intensity distribution. Since the total intensity of fluorescence from an eigenstate is proportional to its fractional S_1 character (see Chapter 3), the direction of the center of gravity offset may be found by combining Equations 4.6 and 4.7. Using an energy scale where $\alpha^2(1 - \alpha^2)H_{T_3T_{1,2}}^2 = 1$, and setting the zero of energy to E_{S_1} , we obtain

$$\begin{aligned} E_{\text{ave}} &\propto \int_{-1}^{+1} E \times a_{S_1}^2 dE, \\ &\propto \frac{2E_{T_3}}{E_{T_3}^2 - 1} + \log \left[\frac{E_{T_3} + 1}{E_{T_3} - 1} \right]. \end{aligned} \quad (4.8)$$

The above expression for the center of gravity is correct only in its sign, since it cannot be normalized by integrating Equation 4.6 over an energy range that includes E_{S_1} . The sign of Equation 4.8 is preserved because the normalization factor is always

positive. When the relative energy $E_{T_3} - E_{S_1}$ is positive, the center of gravity in Equation 4.8 is positive relative to E_{S_1} . When the relative energy, $E_{T_3} - E_{S_1}$, is negative, the center of gravity is negative. We have thus established that the center of gravity offset for an ensemble of nominal $T_{1,2}$ eigenstates is biased toward a T_3 doorway state, relative to E_{S_1} .

In the remainder of this section, we examine the dependence of the intensity-weighted center-of-gravity on the time delay of a gated fluorescence spectrum for an incoherent ensemble of simultaneously excited, mixed $S_1 \sim T_{1,2}$ eigenstates. Because the different eigenstates in the ensemble have different fluorescence lifetimes, their relative fluorescence intensities change as a function of time delay after excitation. Of particular concern is the relative intensity of the nominal S_1 eigenstate relative to that of the remaining, nominal $T_{1,2}$ eigenstates. Changes in relative eigenstate intensities lead to changes in the overall center of gravity, when the metric is computed from the total fluorescence intensity within a delayed time window t to $t + dt$ after excitation. Using a simple model, we show how the dependence of center of gravity on time delay reveals the energy of the doorway state, relative to that of the nominal S_1 eigenstate.

4.3.1 Characteristics of an incoherent, high-resolution fluorescence spectrum after a time delay

For a pure S_1 rovibrational level, $|s\rangle$, the time-dependent fluorescence intensity is

$$I_s(t) = \frac{1}{\tau_s} \exp\left[-\frac{t}{\tau_s}\right], \quad (4.9)$$

normalized such that $\int_0^\infty I_s(t) dt = 1$. The quantity τ_s is the radiative lifetime of the zero-order S_1 level. In acetylene, this quantity is largely independent of vibrational and rotational levels within S_1 , and is determined to be approximately 270 ns [94, 114].

We consider the case where $|s\rangle$ is admixed, through an energetically distant T_3 doorway, into $T_{1,2}$ triplet levels to create a set of singlet~triplet mixed eigenstates, $\{|m\rangle\}$, each having some fractional S_1 character, a_m^2 . If the lifetime of a pure triplet

level is much longer than τ_s , the lifetime of a mixed eigenstate $|m\rangle$ is

$$\tau_m = \tau_s/a_m^2, \quad (4.10)$$

and its time-dependent fluorescence intensity is

$$I_m(t) = \frac{a_m^4}{\tau_s} \exp\left[-\frac{a_m^2 t}{\tau_s}\right]. \quad (4.11)$$

The total integrated fluorescence intensity for a mixed state is $\int_0^\infty I_m(t) dt = a_m^2$, relative to unit intensity for a pure S_1 state. This reflects the a_m^2 times smaller probability for excitation of a mixed eigenstate, $|m\rangle$.

The relative fluorescence intensity among an incoherent ensemble of simultaneously excited, singlet~triplet mixed eigenstates is examined after a selectable time delay t . The upper limit of time delay that can be selected in our LIF experiments is determined by the field-of-view of the fluorescence detection optics. In this study, the field-of-view of the fluorescence detection optics is about 5 mm. The maximum viewing time is therefore about $5 \mu\text{s} \approx 18\tau_s$ for molecules travelling in the molecular beam with average velocity $\approx 10^3$ m/s. At a time delay longer than $18\tau_s$, no molecules remain to be seen within the fluorescence field of view.

At a chosen value of time delay, the relative fluorescence intensity among an ensemble of mixed states has a single maximum with respect to fractional S_1 character, a_m^2 . States with the largest amount of fractional S_1 character fluoresce quickly. Although fluorescence from these states begins at $t = 0$ with the greatest intensity, their relative intensity decreases rapidly as $t > 0$ with respect to longer-lived states. Eigenstates having the smallest amount of fractional bright state character, conversely, have lower intensity at $t = 0$. However, they fluoresce slowly, and as a consequence their relative intensity increases with time delay, relative to the fluorescence from other eigenstates in the ensemble.

At a given time delay, t , the fractional S_1 character resulting in the greatest relative intensity is found by setting the derivative of eigenstate intensity (Equation 4.11) with respect to fractional S_1 character, a_m^2 , equal to zero. We find that the

derivative is

$$\frac{\partial I_m}{\partial a_m^2} = \frac{a_m^2}{\tau_s} \exp \left[-\frac{a_m^2 t}{\tau_s} \right] \left(2 - \frac{a_m^2 t}{\tau_s} \right). \quad (4.12)$$

When $t \leq 2\tau_s$, the fluorescence intensity equation increases monotonically with fractional S_1 character, and is maximized when the fractional S_1 character is 1. When $t > 2\tau_s$, the fluorescence intensity equation is at a maximum when the fractional S_1 character is

$$a_m^2 = \frac{2\tau_s}{t}. \quad (4.13)$$

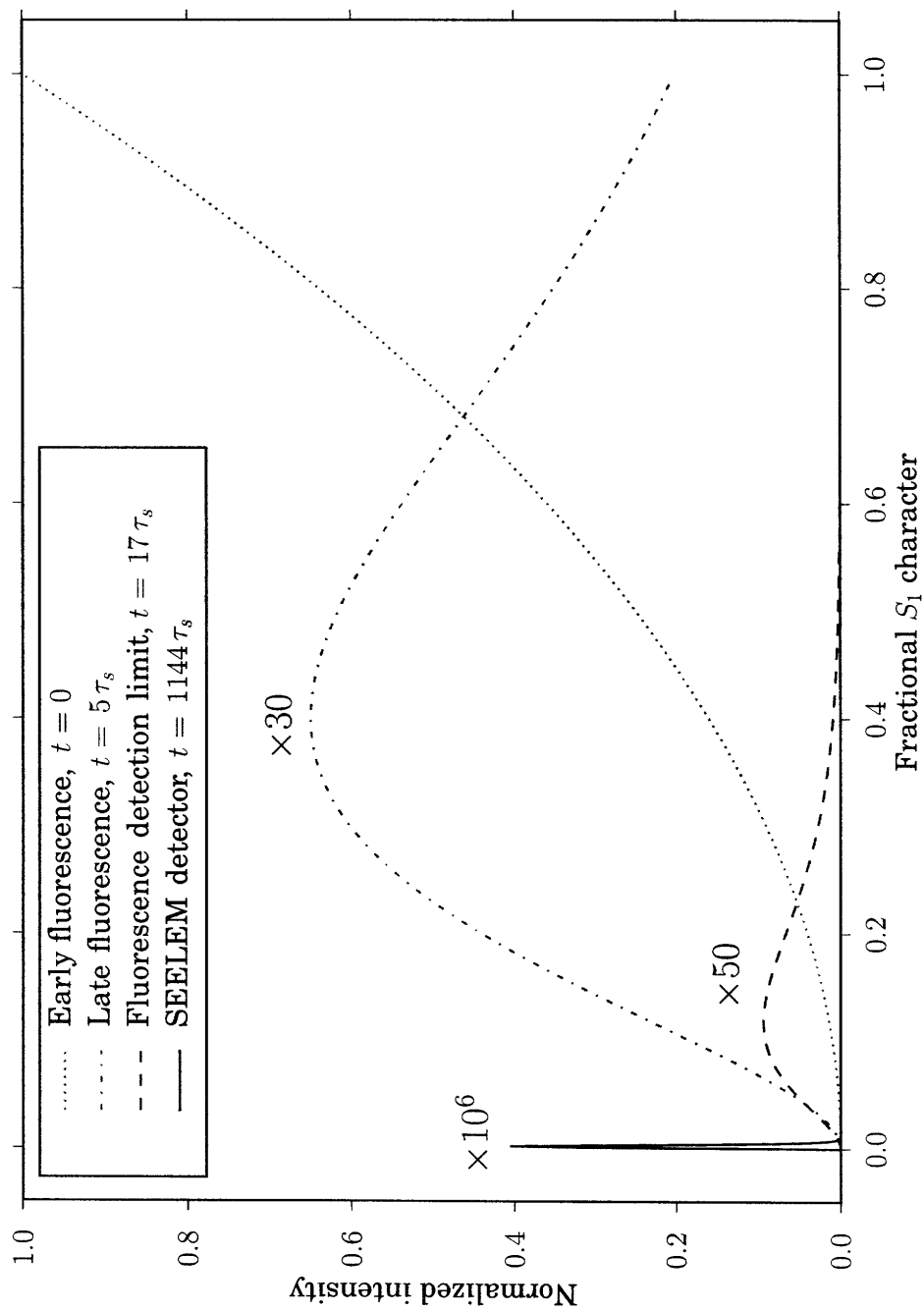
Figure 4-4 shows the dependence of fluorescence intensity on fractional S_1 character at several selectable values of time delay. When $t = 0$, the fluorescence intensity is monotonic and greatest for eigenstates that contain the largest amount of fractional S_1 character. At a delay of $t = 5\tau_s$, the fluorescence intensity equation is “tuned” to states with a fractional S_1 character of 40%. Molecules in eigenstates containing too much fractional S_1 character are discriminated against, because they have already fluoresced with high probability by a time delay of $5\tau_s$. Molecules in eigenstates with fractional S_1 character $\ll 40\%$ have a low probability of fluorescing in the time window under consideration, and are also discriminated against at this delay time. Figure 4-4 also shows the dependence of fluorescence intensity on fractional S_1 character for $t = 18\tau_s$, the maximum fluorescence time delay used in this study. At this time delay, the fluorescence intensity is at a maximum when the fractional S_1 character is approximately 22%.

The SEELEM detector used in this study detects metastable acetylene molecules after a flight time of $\tau_f = 309 \mu\text{s}$. Considering only the SEELEM electron ejection probability resulting from S_1 electronic character, the total SEELEM detection probability is (Chapter 2, equation 28):

$$P_{\text{SEELEM}} \propto a_m^4 \exp \left[-\frac{a_m^2 \tau_f}{\tau_s} \right]. \quad (4.14)$$

This is a good approximation to the total SEELEM detection probability, including electron ejection probability resulting from fractional T_3 electronic character, when a

Figure 4-4: The intensity of fluorescence from a mixed eigenstate at time $R = t/\tau_s$, plotted as a function of bright state character.



T_3 doorway state is energetically distant³ (see Chapter 2, section 2.3.2). The SEELEM detection probability, Equation 4.14, has the same functional form as the delayed LIF intensity, Equation 4.11. At a flight time of 309 μs the detection probability is at a maximum for eigenstates with 0.17% fractional S_1 character. In this approximation, the SEELEM detector may be viewed as an extreme discriminator for detecting states with small fractional S_1 character. The dependence of SEELEM detection probability on fractional S_1 character is also included in Figure 4-4.

4.3.2 Dependence of the intensity-weighted center of gravity on time delay

Our next step is to examine how the LIF intensity-weighted center of gravity metric,

$$E_{\text{ave}} = \int E \times I(E) dE, \quad (4.15)$$

changes as the time delay is increased. We model the interaction between a rovibrational level of S_1 and the local ensemble of $T_{1,2}$ rovibrational levels by first constructing a model system containing only one $T_{1,2}$ basis state.

Consider a Hamiltonian containing one S_1 level, $|s\rangle$, and one $T_{1,2}$ level, $|t\rangle$. Let us define the two mixed states $|1\rangle$ and $|2\rangle$ as

$$\begin{aligned} |1\rangle &= (1 - a^2)^{1/2} |s\rangle + a |t\rangle \\ |2\rangle &= -a |s\rangle + (1 - a^2)^{1/2} |t\rangle, \end{aligned} \quad (4.16)$$

where a is the mixing angle between $|s\rangle$ and $|t\rangle$, $0 \leq |a| \leq 0.5$. The fractional S_1 character of $|2\rangle$ is a^2 , and that of $|1\rangle$ is $(1 - a^2)$. The normalized fluorescence intensities

³The term “energetically distant” has a slightly different meaning in this context. The magnitude of T_3 electronic character will be approximately proportional to the magnitude of S_1 electronic character if the energy denominator $E_m - E_{T_3}$ is approximately constant with respect to the energy denominator $E_m - E_{S_1}$.

of the mixed states are

$$\begin{aligned} I_1(t) &= \frac{(1-a^2)^2}{\tau_s} \exp\left[-\frac{(1-a^2)t}{\tau_s}\right] \\ I_2(t) &= \frac{a^4}{\tau_s} \exp\left[-\frac{a^2 t}{\tau_s}\right]. \end{aligned} \quad (4.17)$$

The ratio of the fluorescence intensities, $I_1(t)/I_2(t)$, has the following time dependence:

$$\frac{I_1(t)}{I_2(t)} = \left(\frac{1-a^2}{a^2}\right)^2 \exp\left[-\frac{(1-2a^2)t}{\tau_s}\right]. \quad (4.18)$$

The intensity ratio at $t = 0$ is determined by the prefactor $((1-a^2)/a^2)^2$. In the limit of long time delay, $I_1(t)/I_2(t)$ always approaches zero, because the lifetime of $|2\rangle$ is always longer than that of $|1\rangle$, by definition.

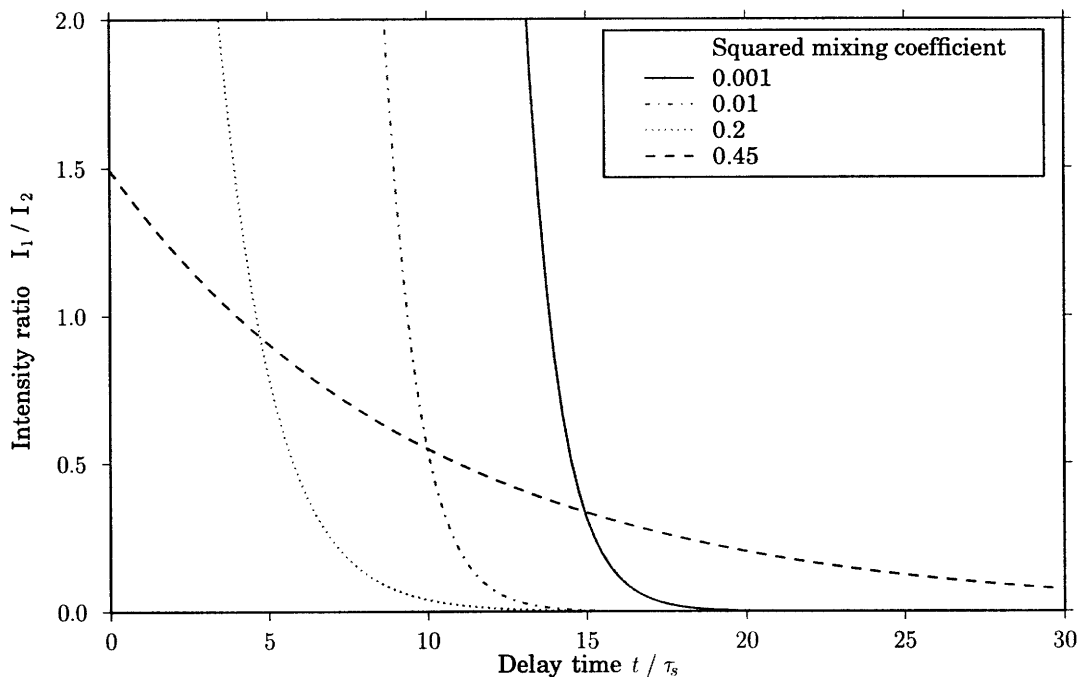
The intensity ratio I_1/I_2 is plotted as a function of time in Figure 4-5, using several values of the mixing fraction, a^2 . At small values of the mixing fraction, $0.001 \leq a^2 \leq 0.2$, the intensity ratio changes rapidly at a time delay between $5\tau_s$ and $15\tau_s$. When the mixing fraction approaches its limiting value of 0.5, the prefactor $((1-a^2)/a^2)^2$ causes the intensities I_1 and I_2 to be of comparable magnitude at $t = 0$. As the time delay is increased, the intensity ratio changes slowly, because the states $|1\rangle$ and $|2\rangle$ have similar lifetimes.

The intensity-weighted center of gravity of the model system may be written as a sum of two terms,

$$E_{\text{ave}}(t) = E_1 \times I_1(t) + E_2 \times I_2(t), \quad (4.19)$$

where E_1 and E_2 are the energies of $|1\rangle$ and $|2\rangle$, respectively. The intensity-weighted center of gravity is plotted as a function of time delay in Figure 4-6. The main features of the plot are similar to those of Figure 4-5. At small values of the mixing fraction, $0.001 \leq a^2 \leq 0.2$, the intensity-weighted center of gravity changes rapidly from E_1 to E_2 at a time delay between $5\tau_s$ and $15\tau_s$. When the mixing fraction is nearly 0.5, the initial center of gravity at $t = 0$ is midway between E_1 and E_2 , because $|1\rangle$ and $|2\rangle$ have similar intensities at $t = 0$. In this case of near-50:50 mixing, the center of gravity changes slowly as a function of time. The quantity still approaches E_2 in the

Figure 4-5: Dependence of the intensity ratio I_1/I_2 on time delay for a model two-state system.

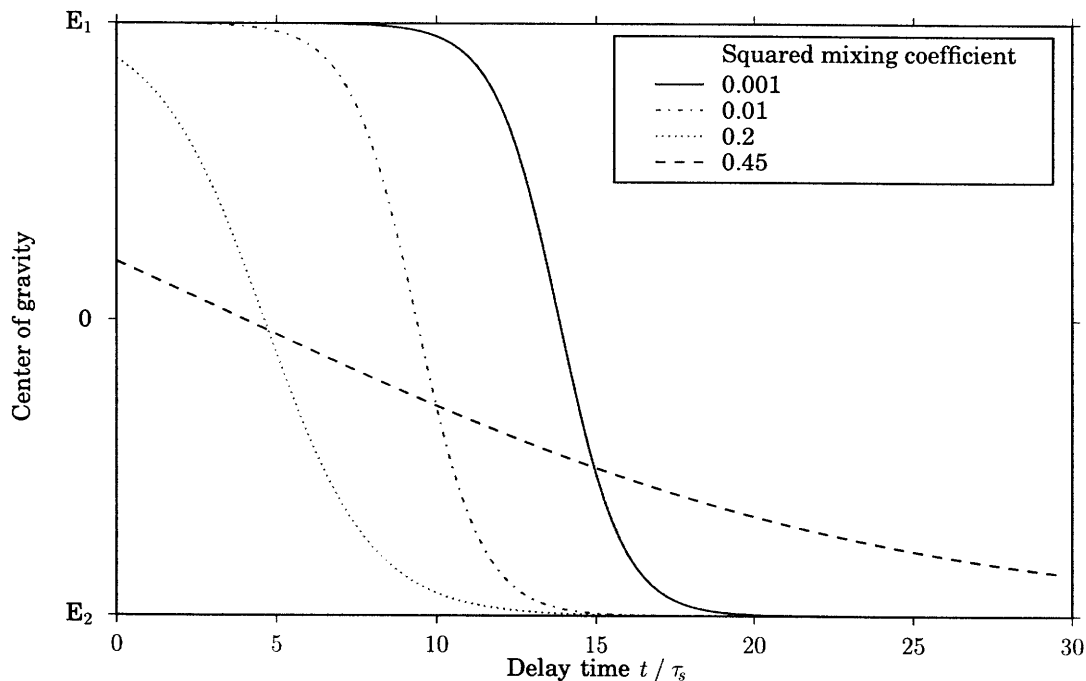


limit of long time delay, because the lifetime of $|2\rangle$ is always longer than that of $|1\rangle$. The total magnitude of change in center of gravity is decreased, due to the greater relative intensity of $|2\rangle$ at $t = 0$.

A characteristic feature in the plot of center of gravity vs. time is the presence and location of a rapid (within several τ_s) shift in center of gravity from E_1 to E_2 . If a rapid shift is observed, its location may be used to infer the mixing fraction, a^2 . The location of the shift is determined by the point of inflection for the center of gravity function, where $I_1 = I_2$. The dependence of mixing fraction on the location of a center of gravity shift is plotted in Figure 4-7. Rapid center of gravity shifts, located between $t = 5.5\tau_s$ and $t = 14\tau_s$, are the result of mixing fractions between 0.1 and 0.001, respectively.

The presence of a rapid shift in center of gravity vs. time indicates that the intensity ratio I_1/I_2 changes rapidly. For this to occur, the fluorescence decay rates of $|1\rangle$ and $|2\rangle$ must be appreciably different. For a system containing many $T_{1,2}$ levels, the qualitative features of the center of gravity function will be determined

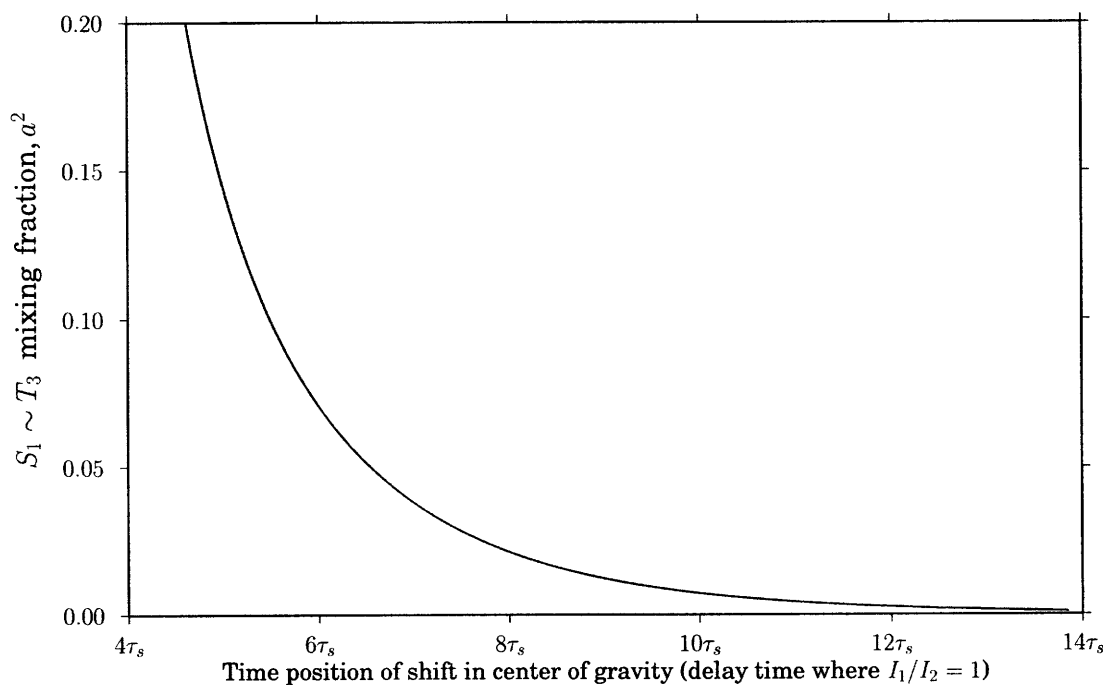
Figure 4-6: Time development of the center of gravity for a model system containing two basis states.



by the subset of nominal $T_{1,2}$ eigenstates with the largest fractional S_1 character. These states will have the largest intensities, and therefore the greatest impact on the behavior of the center of gravity vs. time. Therefore, the presence of a rapid shift in center of gravity vs. time indicates that no $T_{1,2}$ level is mixed to more than 20% with the S_1 level.

We have examined the dependence of the intensity-weighted center of gravity on time delay in the LIF spectrum of an incoherent ensemble of simultaneously excited, singlet~triplet mixed molecular eigenstates. A model system was constructed, containing one S_1 level and one $T_{1,2}$ level. The initial ($t = 0$) position of the center of gravity for the model system is influenced by the total $S_1 \sim T_{1,2}$ mixing fraction. As the time delay is increased, the center of gravity shifts from its initial position to a final position, which is determined solely by the energy and fractional S_1 character of nominal $T_{1,2}$ eigenstates. Small $S_1 \sim T_{1,2}$ mixing fractions lead to a rapid, characteristic shift in the center of gravity with time delay. Large mixing fractions lead to a gradual change in the center of gravity with time delay. In this case, the change in

Figure 4-7: The location of a rapid shift in center of gravity (within several units of $\tau_s = 270$ ns) may be used to infer the $S_1 \sim T_3$ mixing fraction. The characteristic time of the shift is defined by the value of delay time where the relative intensities of the nominal S_1 eigenstate and the nominal $T_{1,2}$ eigenstates are equal. The mixing fraction is plotted here as a function of the location of a rapid shift in center of gravity, defined as the delay time where $I_1 = I_2$.



center of gravity not only occurs more slowly, but the total magnitude of the shift is decreased, due to the larger relative intensity of nominal triplet states at $t = 0$.

The behavior of the LIF center of gravity with time delay will be used as a primary tool to examine the spectra of various vibrational sublevels in acetylene \tilde{A}^1A_u . To analyze the local $S_1 \sim T_{1,2}$ mixing around a single rotationally-resolved $S_1 \leftarrow S_0$ transition, relative intensities are compared over a very small energy range, about 1 cm^{-1} . This has the effect of minimizing relative intensity errors, which arise in LIF experiments mostly from slowly drifting laser power and baseline effects. Unlike measurements of fluorescence lifetime, the center of gravity metric is not biased by molecules leaving the LIF detection area. Laser excitation of molecules is instantaneous with respect to the position of a molecule in a molecular beam, and has no affect on molecular velocities. When the excitation laser is perpendicular to the jet axis, the molecular velocity along the jet axis has no bearing on the excitation probability. Although the total signal is decreased as molecules exit the LIF detection region, relative excitation probabilities are conserved among the subset of molecules that remain in the observation region. The center of gravity is determined only by the *relative* fluorescence among the set of molecules which remain within the field-of-view of the LIF detection optics.

4.4 Experiment

In the SEELEM experiment, a molecular beam of acetylene is excited by a $\sim 5 \text{ ns}$ FWHM pulsed tunable laser into spin-rotation-vibration eigenstates of metastable electronic states via weak, nominally forbidden transitions. After excitation, the long-lived species must travel 35 cm before colliding with an Au metal detector surface, where an electron is ejected in the de-excitation process. Two criteria must be met for electron ejection by a metastable species. First, the vertical electronic energy of the metastable state of the particle approaching the surface must exceed the work function of the metal ($\Phi_{\text{Au}} = 5.1 \text{ eV}$). Second, the radiative lifetime of the detected metastable eigenstate (τ_{rad}) must exceed the flight time from the point of laser excitation to the

SEELEM surface ($\Delta t=300 \mu s$).

A sample of acetylene (BOC gases) at a backing pressure of one atmosphere is pulsed through a 0.5 mm diameter nozzle (Jordan Valve), operating at 10 Hz, into a diffusion pumped vacuum chamber at $\sim 5 \times 10^{-5}$ Torr. An Nd:YAG pumped (Spectra Physics GCR-270), frequency-doubled dye laser (Lambda Physik FL3002, 220 nm) excites the acetylene molecules in the pulsed jet expansion 2 cm downstream from the nozzle orifice.

UV-LIF is detected in a direction perpendicular to the plane defined by the intersection of the pulsed molecular and laser beams using f/1.2 collection optics, a fluorescence filter (UG-11) to reduce scattered laser light, and a PMT (Hamamatsu model R375). The time-varying UV-LIF signal was averaged on a digital oscilloscope (LeCroy) at each laser frequency. The resulting oscilloscope trace, recorded over a 5 μs timespan (time bins of 10 ns), was transferred to a PC for analysis.

Simultaneous SEELEM detection took place in a separate, differentially pumped vacuum chamber. Following laser excitation, molecules in the pulsed expansion passed through a conical skimmer (3mm diameter), forming a collimated molecular beam in the SEELEM detection chamber. The detector chamber was diffusion pumped (Varian 600) to maintain a pressure of $\sim 4 \times 10^{-7}$ torr during operation. The SEELEM detector surface, a 2.5 cm diameter region of heated (300° C) Au foil, was located 35 cm downstream from the point of laser excitation. The SEELEM detector was identical to that used in the previously described apparatus with Au foil ($\Phi_{Au} = 5.1$ eV) as the detector surface.

Electron signals from the SEELEM detector were collected using pulse counting techniques. Electrons ejected from the metal surface were detected by a nearby electron multiplier (ETP, SGE Instruments, Model 14831H). The collection plate of the multiplier was biased at +100V to attract electrons. The electron multiplier signal was sent to a discriminator (EG&G/Ortec Model 9301), and then to a PC-operated multichannel scalar (Oxford Tennelec Nucleus Inc. MCS-II v2.091), where the total number of electrons was summed. The typical signal level for SEELEM detection of acetylene was 2-20 counts per laser pulse.

Both SEELEM and LIF signals were averaged over 100 laser shots at each laser frequency. The frequency increment step size was typically $\sim 0.015 \text{ cm}^{-1}$ in the doubled output, although several detailed spectra were recorded with a $4\times$ smaller frequency step size.

4.5 SEELEM/LIF spectroscopy of four S_1 vibrational levels located at higher energy than the minimum of the $S_1 \sim T_3$ seam of intersection

The choice of S_1 vibrational levels in this study was guided by two considerations: the energetic accessibility of T_3 vibrational levels [28, 122] and absence of predissociation effects. The minimum of the $S_1 \sim T_3$ electronic seam of intersection, located near $3^3 K'=1$, $T_0 \simeq 45300 \text{ cm}^{-1}$, provides a lower energy bound for the Franck-Condon accessibility of T_3 vibrational levels from the S_1 electronic surface [28]. Above this energy, it is possible for levels of S_1 to have large vibrational overlaps with levels of T_3 . The first dissociation limit, located near $3^4 K'=1$, $T_0 \simeq 46300 \text{ cm}^{-1}$, provides an upper energy bound for this study [88]. Below this dissociation limit, predissociation pathways are not energetically accessible, and do not complicate the study of $S_1 \sim T_3$ interactions.

We consider four S_1 sublevels in the energy region of $45300\text{--}46300 \text{ cm}^{-1}$, observed in the $\tilde{A}^1A_u \leftarrow \tilde{X}^1\Sigma_g^+$ spectrum of acetylene. The sublevels are listed with their total (rotationless) vibronic energy, T_{v0} , in Table 4.1. Included in the table is an order-of-magnitude estimate of the SEELEM:LIF intensity ratio observed in the spectrum. To determine this quantity, the relative LIF intensities of $2^23^1 K'=1$, $3^24^2 K'=1$, and $2^13^2 K'=1$ were estimated from a low resolution jet spectrum reported by Merer and coworkers [82]. The LIF intensity of the $3^3 K'=2$ subband was compared to that of $3^3 K'=1$ in our own experiments. The absolute SEELEM intensity was then divided by the estimated LIF intensity, and normalized to the largest SEELEM:LIF ratio.

We observe that the highest energy state in our study has the lowest SEELEM:LIF

Table 4.1: The four acetylene S_1 vibrational levels considered in this study, listed here, have total vibronic energies in the critical region above the minimum of the $S_1 \sim T_3$ electronic seam of intersection ($\simeq 45300 \text{ cm}^{-1}$) and below the first dissociation barrier ($\simeq 46300 \text{ cm}^{-1}$) [88]. An order-of-magnitude estimate of the observed SEELEM:LIF intensity ratio is included.

Subband		$T_0 \text{ (cm}^{-1}\text{)}$	SEELEM:LIF
2^23^1	$K'=1 \leftarrow 0_0$	46009	10^{-2}
3^24^2	$K'=1 \leftarrow 0_0$	45812	10^{-1}
2^13^2	$K'=1 \leftarrow 0_0$	45677	10^{-1}
3^3	$K'=2 \leftarrow 4_1$	45352	1

intensity ratio. Rather than total energy, the SEELEM:LIF intensity ratio is determined by the number of quanta in mode 3. This observation is in agreement with previous estimates of SEELEM:LIF intensity ratios in acetylene \tilde{A}^1A_u [55]. Measurements of the Zeeman anticrossing density show the same exponential dependence on the number of quanta in ν_3 [41]. Because the intensity ratio is determined by vibrational basis state character and not by total energy, it must be a reflection of the vibrational overlap factors contained in the spin-orbit matrix elements, rather than due to the slowly increasing density of $T_{1,2}$ states [41, 37].

The presence of local T_3 perturbers is ruled out, because we observe no telltale, systematic splittings that would have indicated a crossing with a triplet F_2 spin component, as in 3^3 $K'=1$ [85]. Evidence of energetically distant T_3 doorway levels is found, however, in both the SEELEM and LIF spectra of these sublevels. To characterize the spectral signatures of energetically distant doorway levels, we discuss the SEELEM/LIF spectrum of each sublevel individually.

4.5.1 The 3^24^2 $K'=1$ sublevel: evidence for an energetically distant T_3 doorway level plus a localized T_3 level crossing

The 3^24^2 level is the upper member of the 3^2B^2 polyad of the acetylene \tilde{A}^1A_u state, where $B \equiv \nu_4 + \nu_6$. The ν_4 and ν_6 vibrations are strongly mixed by a-type Coriolis

Figure 4-8: Simultaneously recorded SEELEM (upper trace) and LIF (lower trace) spectra of the $3^2 4^2 K'=1$ sublevel of the $\tilde{A}^1 A_u$ state of C_2H_2 . The LIF spectrum is integrated in two time regions: an early time window ($0.5\tau_s - 2\tau_s$, solid trace) and a delayed time window ($10\tau_s - 18\tau_s$, dashed trace). The peak positions are blueshifted in the delayed fluorescence spectrum for all transitions, with the exception of Q(2). Interactions with a remote perturber level of slightly lower energy than the nominal S_1 level are apparent in the delayed fluorescence spectrum of the Q(2) and R(1) transitions.

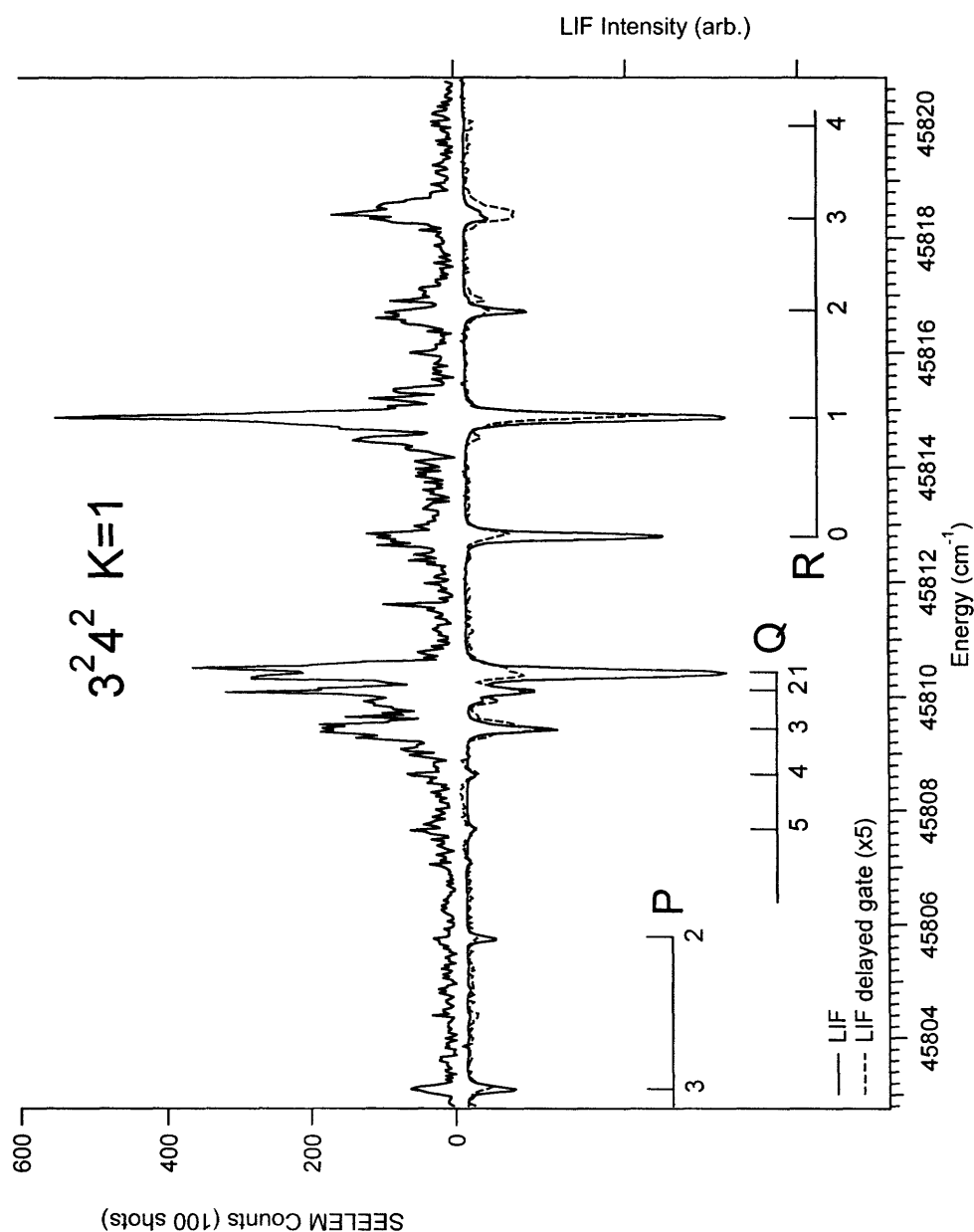
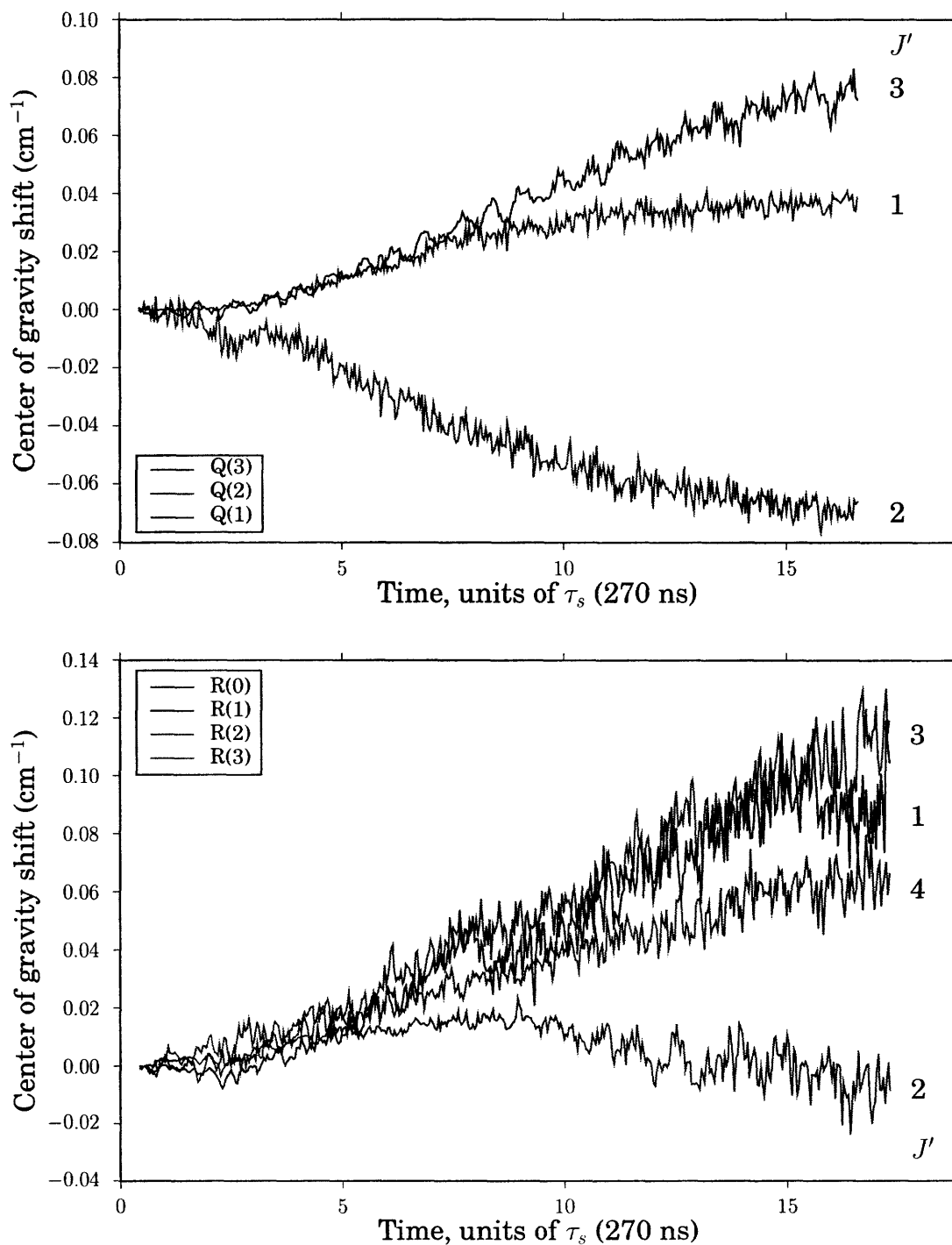


Figure 4-9: Dependence of the intensity-weighted center of gravity on delay for a series of individually resolved transitions, Q(1–3) (top), and R(0–3) (bottom), in the LIF spectrum of 3^24^2 $K'=1$. Local perturbations in the Q(2) and R(1) transitions cause the behavior of the center of gravity to be different from those of the other transitions as the delay time is increased.



and Darling-Dennison anharmonic resonances [83]. As a result, the nominal 3^24^2 level is expected to contain essentially a 50:50 mixture of mode 4 (4^2) and mode 6 (6^2) basis character [83, 129].

The simultaneously recorded SEELEM/LIF spectrum of the $3^24^2 K'=1 \leftarrow 0_0$ sub-band of the $\tilde{A}^1A_u \leftarrow \tilde{X}^1\Sigma_g^+$ electronic spectrum is shown in Figure 4-8. To highlight the dependence of the LIF spectrum on delay time, two integration regions are used. An early-LIF fluorescence spectrum is generated by gating the fluorescence signal between $0.5\tau_s$ and $2\tau_s$. A second, delayed-LIF spectrum is generated by integrating over the time window $10\tau_s - 18\tau_s$. The line positions of several transitions are clearly blueshifted in the delayed-LIF spectrum relative to the early-LIF. Line offsets in the R(0), R(1), and R(4) transitions are approximately 0.08 cm^{-1} .

To more closely examine the dependence of the LIF spectrum on time delay, the intensity-weighted center of gravity (Equation 4.15) is plotted for each transition as a function of delay time. The plot for Q-branch transitions was generated from another dataset, not shown here, sampled at approximately $4\times$ more closely spaced energy intervals, resulting in increased signal to noise. With the exception of the R(1) and Q(2) transitions, the center of gravity increases by $0.04\text{-}0.12 \text{ cm}^{-1}$ over the delay range $0.5\tau_s - 18\tau_s$. Such a consistent increase in center of gravity with delay time indicates the presence of a non-local T_3 doorway level that lies higher in energy, according to Equation 4.8.

A line splitting is present in the LIF spectrum of two transitions, Q(2) and R(1). In the delayed fluorescence spectrum, the extra lines appear with larger relative intensity than the main component of the transition. Their increased relative intensity in the delayed fluorescence spectrum indicates that the extra lines arise from levels with longer zero-order fluorescence lifetimes than that of the nominal singlet level. The extra component of R(1) is observable only in the delayed-LIF spectrum, where its relative intensity increase causes it to emerge from under the red wing of the main line. The extra line in the R(1) transition, with upper state quantum number $J' = 2$, is located at an energy of -0.33 cm^{-1} below the main component at 45814.87 cm^{-1} . The $J' = 2$ perturber of opposite parity appears in Q(2). It is located at an energy of

-0.17 cm⁻¹ relative to the strong, nominally singlet LIF transition at 45810.08 cm⁻¹.

The presence of two local perturbations at the same J' (but opposite parities), arising from levels with a long zero-order lifetime, and not appearing in transitions with adjacent values of J' , can be explained by the presence of a level crossing involving the F_1 or F_3 component of a T_3 level that has a small spin-orbit matrix element with the S_1 level. According to Equation 4.3, the relative energy of a T_3 level in this case is $\pm 2B \simeq \pm 2$ cm⁻¹ at $J' = 1$ and 3.

At $J' = 2$, the singlet and its triplet perturber are not 50:50 mixed, thus the matrix element must be appreciably smaller than half the energy separation. This places an upper bound on the matrix elements of about 0.01 cm⁻¹. At $J' = 1$ or 3, the increase in energy denominator from 0.2 cm⁻¹ to 2 cm⁻¹ would make the intensity of the perturber 100 times weaker than for $J' = 2$, precluding its observation in LIF.

A lone SEELEM peak is observed in the band gap at 45811.6 cm⁻¹, at approximately 2 cm⁻¹ higher frequency than the Q(3) transition at 45809.5 cm⁻¹. It is possible that this peak arises from the same weakly perturbing T_3 vibrational level. Unfortunately, it is impossible to search for the other parity component of this perturber in the spectrum, because the appropriate energy region is overlapped by an R-branch transition. However, if we assign the transition in the band gap as $J' = 3$, it must also be assigned as the F_3 component of the triplet level, $N_T = J' + 1 = 4$, in order to be located at +2 cm⁻¹ instead of -2 cm⁻¹. As a consequence, the triplet level must have a rotationless vibronic energy of $45811 - 6B \simeq 45804$ cm⁻¹.

We have examined a singlet sublevel, $3^2 4^2 K'=1$, which shows evidence of interaction with an energetically distant T_3 doorway level at higher energy. An extra line with a small matrix element was observed at $J' = 2$ in both parity components of the singlet level, and was assigned as a level of T_3 based on its zero-order lifetime. An assignment of $\Delta N = +1$ was suggested for the perturbing level based on the observation of a weak transition in the SEELEM spectrum, which was assigned as $J' = 3$, $N_T = 4$ because the observed frequency is +2 cm⁻¹ relative to the singlet Q(3) transition. The assignment of N_T determines that the rotationless energy of the perturbing triplet level is -6 cm⁻¹ relative to the singlet.

Local, weak perturbations by T_3 levels are common in the spectrum of \tilde{A}^1A_u acetylene, as we will see in the following examples. In cases where N_T or K_T of the perturber can be assigned, the relative energies of weak transitions into locally perturbing vibrational levels can be determined exactly. In cases where N_T or K_T can be assigned for energetically distant T_3 doorway levels ($|H_{ST}|$ is on the order of $2B_T$), the relative rotationless energy is determined to be either positive or negative. This can then be checked against the dependence of the intensity-weighted LIF center of gravity on time delay.

4.5.2 The 2^13^2 $K'=1$ sublevel: assignment of K_a for an energetically distant T_3 doorway level

We turn next to an S_1 sublevel which also contains two quanta of the ν_3 vibration, 2^13^2 $K'=1$. The overall SEELEM:LIF intensity ratio observed in the spectrum of this sublevel is similar to that of 3^24^2 $K'=1$, indicating a similar overall mixing angle with T_3 doorway levels.

The SEELEM/LIF spectrum of the 2^13^2 $K'=1 \leftarrow 0_0$ subband of the $\tilde{A}^1A_u \leftarrow \tilde{X}^1\Sigma_g^+$ transition is shown in Figure 4-10. The LIF spectrum is integrated in early and delayed time windows, using time limits of $0.5\tau_s - 2\tau_s$ and $10\tau_s - 18\tau_s$. The spectrum contains six Q-branch transitions (upper states of f -symmetry, $J' = 1 - 6$) and one P-branch transition (upper state of e -symmetry, $J' = 1$). The delayed LIF peak position is redshifted by -0.08 cm^{-1} relative to the early LIF peak position for two transitions terminating in f -symmetry states, Q(1) and Q(2). The sole e -symmetry state observed in the spectrum, via the P(2) transition, is also redshifted by -0.12 cm^{-1} in the delayed fluorescence spectrum. The remaining transitions, Q(3,4,5,6), have the same peak position in the early and delayed-LIF spectra. The Q(3) transition appears anomalously weak. This issue is addressed later in this section.

The dependence of the intensity-weighted center of gravity for all transitions in the Q-branch is shown in Figure 4-11. The center of gravity for the Q(1) and Q(2) transitions changes from the zero-delay position by approximately -0.07 cm^{-1} at a

Figure 4-10: Simultaneously recorded SEELEM (upper trace) and LIF (lower trace) spectra of the 2^13^2 $K'=1$ sublevel of the \tilde{A}^1A_u state of C_2H_2 . The LIF spectrum is integrated in two time regions: an early time window ($0.5\tau_s - 2\tau_s$, solid trace) and a delayed time window ($10\tau_s - 18\tau_s$, dashed trace). The Q(1) and Q(2) transitions are redshifted in the delayed fluorescence spectrum, in contrast to the Q(3,4,5,6) transitions. The upper states of the P(2) and Q(1) transitions, with the same J' but opposite parity, show similar redshifts in the delayed fluorescence spectrum.

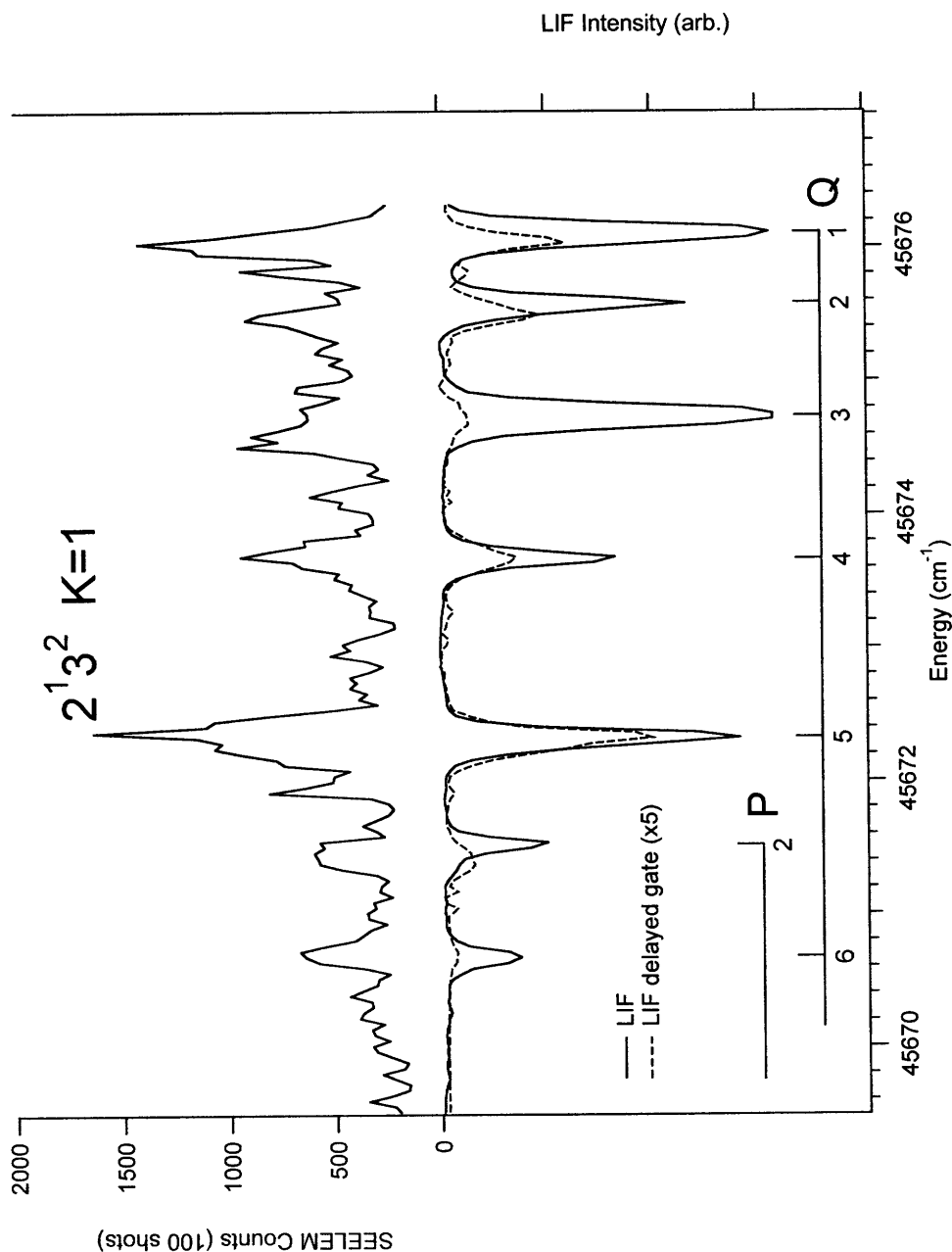
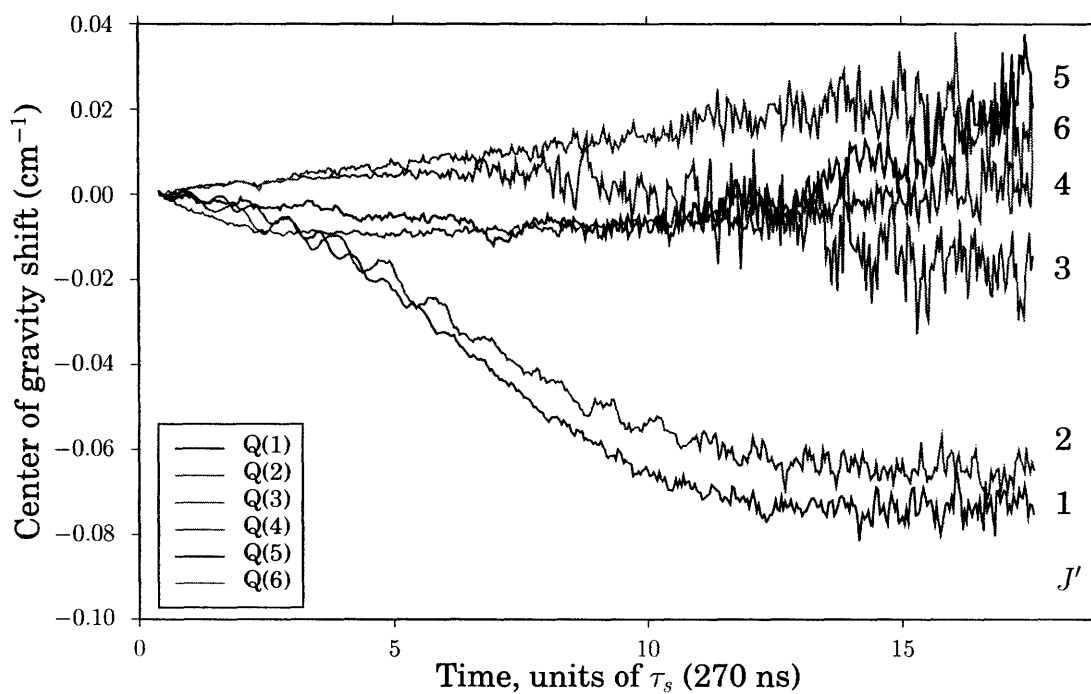


Figure 4-11: Dependence of the intensity-weighted center of gravity on delay for a series of individually resolved rotational transitions, Q(1–6), in the LIF spectrum of 2^13^2 $K'=1$. The center of gravity of the Q(1) and Q(2) transitions is identical to the peak positions in the SEELEM spectrum at delay $> 15\tau_s$.



time delay of $15\tau_s$, in accord with the observation of delay-dependent peak positions in the LIF spectrum. The centers of gravity for the Q(3,4,5,6) transitions do not shift by more than 0.02 cm^{-1} from their initial positions.

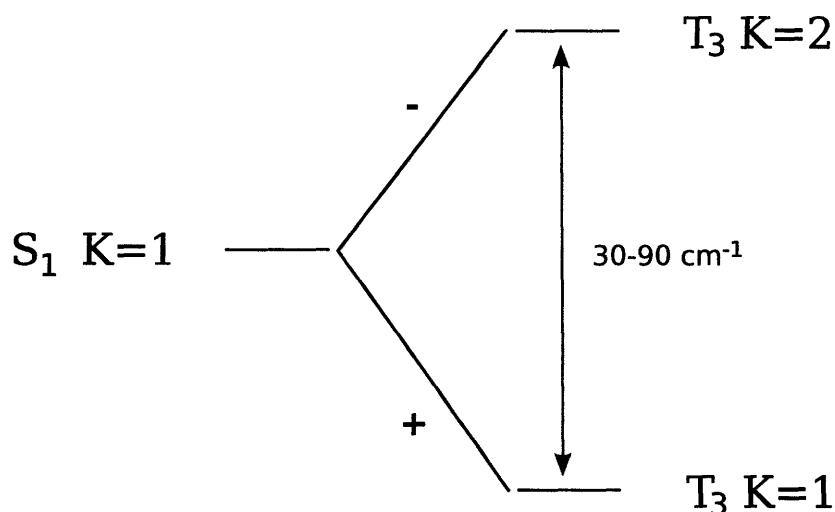
We showed in the preceding section that a monotonic shift in center of gravity with delay indicates the presence of an energetically distant T_3 doorway level. It is puzzling that, in the present case, such an interaction abruptly ceases at $J' \geq 3$. However, this behavior can be explained by the presence of a *second* T_3 doorway level, located at higher energy than the singlet level. An interaction with a second T_3 doorway level could cause the delayed center of gravity to behave differently for the Q(3,4,5,6) transitions, if the interaction with the second doorway level were to *begin* at $J' = 3$.

The existence of such an interaction leads to an assignment of K_T for the second doorway level. The spin-orbit selection rule, $\Delta K = 0, \pm 1$, restricts possible assignments to $K_T = 0, 1$, and 2. A level with $K_T = 2$ has rotational levels that begin with $N_T = 2$. An $S_1 \sim T_3$ interaction with the F_1 component of such a level follows the selection rule $\Delta N = -1$, and would first turn on at $J' = N_S \geq 3$, as observed in the spectrum. All other combinations of ΔK and ΔN lead to $S_1 \sim T_3$ interactions starting at $J' \geq 1$ or 2. Thus, we can assign $K_T = 2$ for the second T_3 doorway level.

For the F_1 component of a triplet level, the energy of the triplet relative to the singlet has a negative slope with respect to J' (see Figure 4-1). At $J' = 3$, where the interaction with the second doorway level begins, the F_1 component is $6B \simeq 6 \text{ cm}^{-1}$ lower in energy than the F_2 component. As J' increases, the relative energy of the F_1 component decreases by $2B$ per J' . Since the interaction must occur through an F_1 component in order to turn on at $J' = 3$, and since the relative energy of the F_1 component is appreciably lower than that of the other two components, we must conclude from the assignment of K_T that the second T_3 doorway level lies at higher energy than the singlet level.

The assignment of $K_T = 2$ for the second doorway state has additional consequences. The $K_T = 2$ doorway level, higher in energy than the singlet level, must be accompanied by a $K_T = 1$ doorway level at lower energy. A diagram of the relevant

Figure 4-12: Energy level diagram of the $K_T = 1, 2$ sublevels of a possible T_3 doorway state. In this possible scenario, which is ruled out for the $S_1 2^13^2 K'=1$ sublevel, a $K_S = 1$ sublevel is perturbed by both the $K_T = 1$ and $K_T = 2$ sublevels of the same T_3 vibrational level. The T_3 sublevels are separated by an energy of $30-90 \text{ cm}^{-1}$. For two sublevels of the same vibrational level, the relative sign of the spin-orbit matrix element is determined only by a rotational factor. In this case, one rotational factor is positive, and the other is negative.



energy level structure is given in Figure 4-12. The energy separation between the $K = 1$ and 2 sublevels of the same vibrational level is $3(A_T - B_T)$, where A_T is the a-axis rotational constant for the triplet level in question. According to *ab initio* calculations, the A_T rotational constants for T_3 vibrational levels vary between 10 and 30 cm^{-1} [122]. This places the $K_T = 1$ sublevel about $30-90 \text{ cm}^{-1}$ lower in energy than the second $K_T = 2$ doorway level.

Spin-orbit matrix elements between S_1 and T_3 are limited by vibrational overlap factors to a magnitude of approximately $\lesssim 1 \text{ cm}^{-1}$. Therefore, the rotationless energy of the second ($K_T = 2$) doorway cannot be more than about 20 cm^{-1} above the singlet sublevel, for appreciable mixing to occur. It follows that the rotationless energy of the $K_T = 1$ doorway must be lower than the singlet level. Furthermore, the vibrational overlap factors for two sublevels of the same vibrational level are identical, and the

relative spin-orbit matrix elements are determined only by rotational factors. Using the rotational factors calculated in Section 4.2, we find that the $K_T = 1$ sublevel of the same vibrational level as the second doorway has matrix elements about 5 times larger than those of the $K_T = 2$ sublevel, and have opposite sign [115]. Because the energy denominators between the singlet sublevel and the $K_T = 1, 2$ sublevels also have opposite phase, the spin orbit matrix elements connecting these two sublevels to the singlet must have the same phase.

However, we observe that the overall fluorescence lifetime is at a minimum in the LIF spectrum at $J' = 3$. This is indicated by the low intensity of the Q(3) transition in the delayed-LIF spectrum. A short fluorescence lifetime indicates less mixing between the S_1 rotational level and the doorway state, resulting from a smaller total $S_1 \sim T_3$ matrix element at $J' = 3$. For the interaction with the second doorway level to cause a decrease in the total $S_1 \sim T_3$ matrix element, the mixing amplitude of the second doorway level must interfere *destructively* with that of the first doorway level. Since the mixing amplitudes of the $K_T = 1$ and $K_T = 2$ sublevels of the second doorway interfere constructively, we must conclude that the first doorway belongs to another T_3 vibrational level.

Analysis of the LIF spectrum vs. time delay has led to the determination of the relative energy and K -assignments of two energetically distant T_3 doorway sublevels in the $2^13^2 K'=1 \leftarrow 0_0$ spectrum of acetylene \tilde{A}^1A_u . Such a conclusion is further supported by the general appearance of the SEELEM spectrum of this vibronic transition, which is strikingly similar to the delayed fluorescence spectrum. Peak positions in the delayed fluorescence spectrum are matched in the SEELEM spectrum, even for weak lines, for instance at 45675.9 cm^{-1} and 45671.9 cm^{-1} .

4.5.3 The $2^23^1 K'=1$ sublevel: a local T_3 perturbation in the presence of small $S_1 \sim T_3$ matrix elements

Although the $2^23^1 K'=1$ sublevel has the highest energy of the four sublevels discussed in this study, it interacts most weakly with the local manifold of $T_{1,2}$ levels. This

Figure 4-13: Simultaneously recorded SEELEM (upper trace) and LIF (lower trace) spectra of the 2^23^1 $K'=1$ sublevel of the \tilde{A}^1A_u state of C_2H_2 . The LIF spectrum is integrated in two time regions: an early time window ($0.5\tau_s - 2\tau_s$, solid trace) and a delayed time window ($8\tau_s - 12\tau_s$, dashed trace). The upper states of the Q(1) and R(0) transitions, which have the same quantum number $J' = 1$ but opposite parities, are shifted in opposite directions in the delayed fluorescence spectrum.

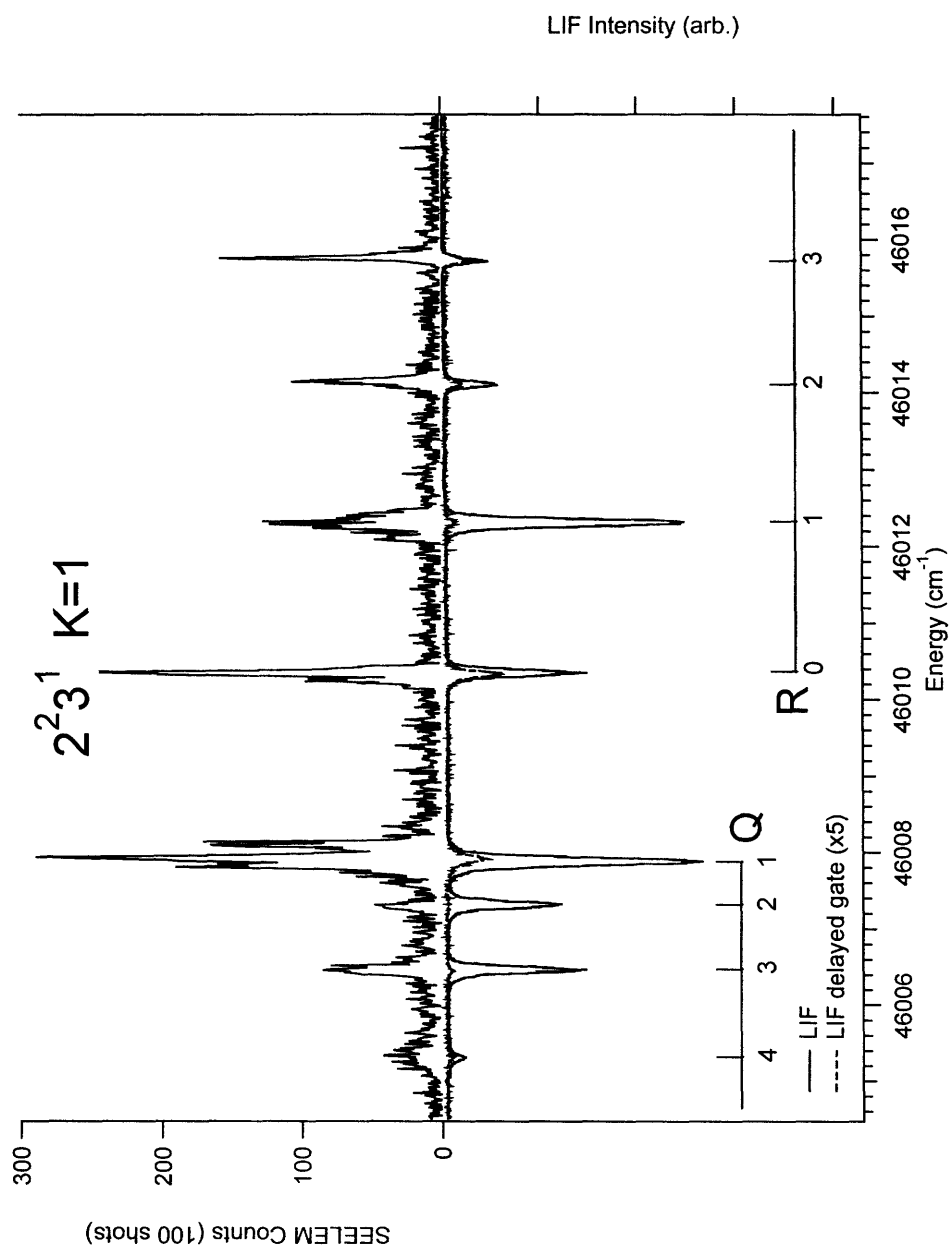
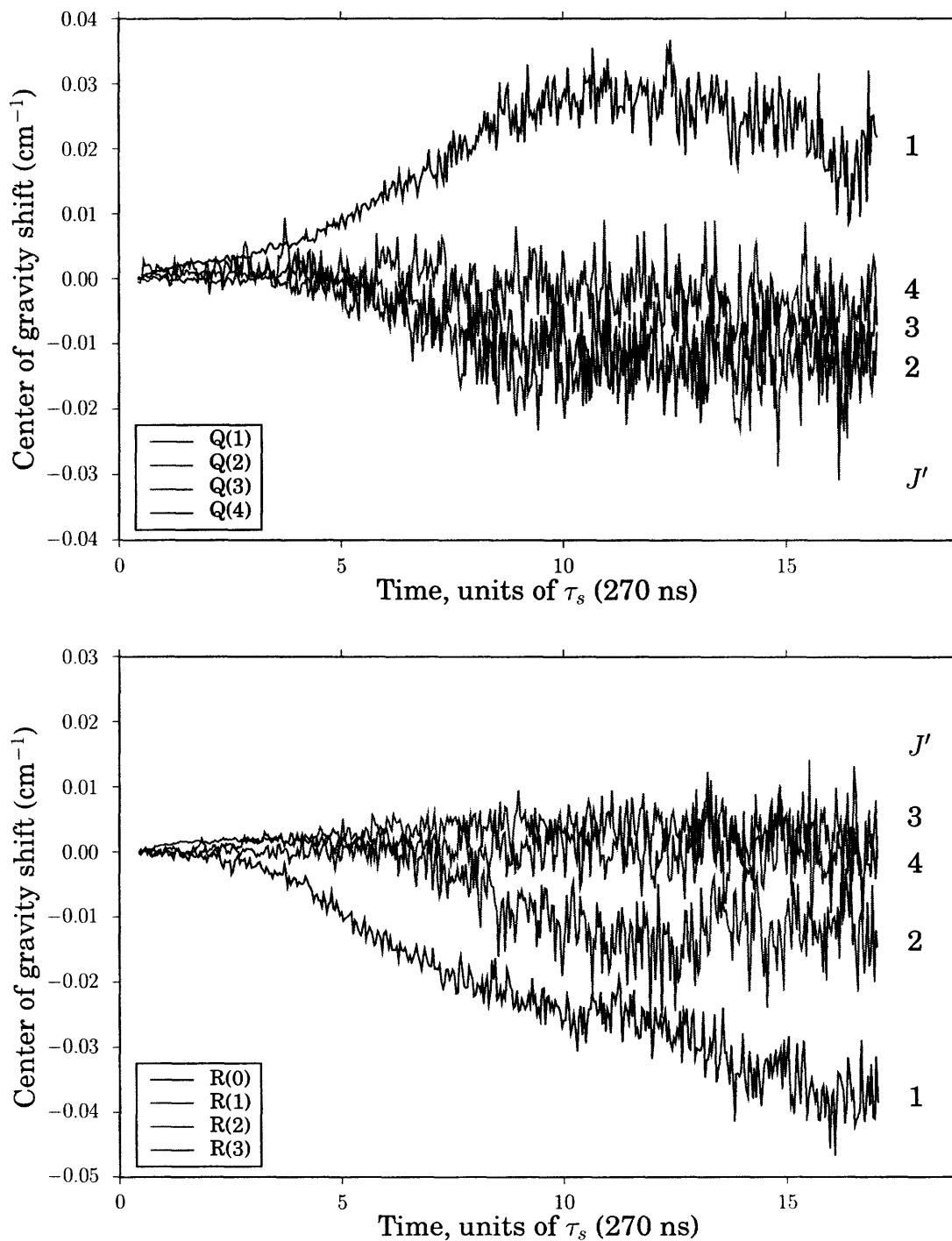


Figure 4-14: Dependence of the intensity-weighted center of gravity on delay for a series of rovibronic transitions, Q(1–4) (top), and R(0–3) (bottom), in the LIF spectrum of $2^23^1 K'=1$. As delay increases, the center of gravity for the Q(1) transition rapidly increases to its final value, where it matches the peak of the SEELEM distribution at $46007.87+0.03 \text{ cm}^{-1}$. For the R(0) transition, the center of gravity decreases to $46010.35-0.3 \text{ cm}^{-1}$ at a delay of $18\tau_s$.



results from having only one quantum of the ν_3 vibration, which controls the overall magnitude of $S_1 \sim T_3$ doorway matrix elements.

The spectrum of the $2^23^1 K' = 1 \leftarrow 0_0$ subband is shown in Figure 4-13. In addition to the overall SEELEM:LIF intensity ratio, the small magnitude of $S_1 \sim T_3$ doorway matrix elements is indicated by the width of the SEELEM intensity envelope surrounding each singlet transition. This topic is discussed at length in Chapter 2. Briefly, the width of the SEELEM spectrum is a measure of the energy range over which the singlet level, through interaction with T_3 doorways, is able to lend approximately 0.25% fractional singlet character to eigenstates within the local manifold of $T_{1,2}$ levels. In the case of $2^23^1 K'=1$, the width of the SEELEM envelope surrounding each singlet transition is on the order of 0.4 cm^{-1} , much narrower than the average spacing between rotational lines. In the next section, we will contrast this with the observed width of SEELEM intensity envelopes in a strongly interacting subband.

The dependence of the intensity-weighted center of gravity for each transition terminating in $2^23^1 K'=1$ is shown in Figure 4-14. With the exception of the Q(1) and R(0) transitions, the center of gravity does not shift by more than 0.02 cm^{-1} from its initial position. For a singlet level with such a small spin-orbit matrix element with a doorway state, any small change in center of gravity, which might arise from the effects of an energetically distant T_3 level, is not expected to appear until delay times in excess of $15\tau_s$.

The anomalous behaviour of the center of gravity for the Q(1) and R(0) transitions is once again evidence of a weak, local T_3 perturbation at $J' = 1$. The upper states of the Q(1) and R(0) transitions have the same J' , but opposite parity (f - and e -symmetry, respectively). The energy difference between the e - and f -symmetry components is $\Delta E_{e-f} = +0.13 \text{ cm}^{-1}$. The perturbation in the e -symmetry singlet transition, R(1), results in a shift to lower frequency, with a magnitude of approximately -0.03 cm^{-1} , while the perturbation shifts the f -symmetry singlet level to higher frequency, with a magnitude of approximately $+0.03 \text{ cm}^{-1}$. The splitting between the asymmetry components of the T_3 perturber is therefore less than

$0.13 - 0.03 - 0.03 = 0.07 \text{ cm}^{-1}$ at $J' = 1$. An asymmetry splitting of this magnitude would be unusually small for a T_3 level with $K_T = 1$. As a result, we conclude that the perturber is likely a level with $K_T = 2$. Only one component of a $K_T = 2$ level may interact with a singlet level at $J' = 1$, and that is the F_3 component, where $N_T = J + 1$. An interaction with the F_1 or F_2 components would require N_T to be 0 or 1; these levels cannot exist when $K_T = 2$. Because the interaction occurs via the F_3 component of the triplet level at $J' = 1$, the rotationless energy of the triplet level must be located approximately $4B \simeq 4 \text{ cm}^{-1}$ below the singlet level.

Again, the assignment of the K_a quantum number for a T_3 level observed in the spectrum has allowed us to infer its energy relative to the singlet. At $J' = 2$, the nearest component of this weak T_3 perturber lies $2B \simeq 2 \text{ cm}^{-1}$ above the singlet level. The resultant increase in squared energy denominator makes the extra line $(2.0/0.03)^2 \simeq 4500$ times weaker at $J' = 2$, thus it is not observed.

4.5.4 The $3^3 K'=2$ sublevel: spectral patterns in the presence of large $S_1 \sim T_3$ matrix elements

The $3^3 K'=2$ sublevel is the higher-energy sibling of $3^3 K'=1$, which has been studied in great detail due to a perturbation by a T_3 doorway level with matrix element $\simeq 0.1 \text{ cm}^{-1}$. The T_3 perturber observed in $3^3 K'=1$ has been assigned as the F_2 component of $K_T = 1$. Because its energy relative to S_1 tunes slowly with J' , it interacts with both parities of the singlet, and the perturbation is present at $J' = 1$ [85]. It has been suggested that the $K_T = 0$ sublevel of this perturber is responsible for the large Zeeman anticrossing observed in $3^3 K'=0$ [122, 38]. To account for this, the A -rotational constant of the perturbing T_3 level would have to closely match the A -rotational constant for the singlet level. However, it is unlikely that an energetic near match in the $K = 0$ and 1 sublevels, separated by $1A \simeq 15 \text{ cm}^{-1}$, will extend to $K = 2$, which would be $3A \simeq 45 \text{ cm}^{-1}$ higher in energy. In the absence of a local T_3 perturbation, the $3^3 K'=2$ sublevel provides an excellent opportunity to examine a singlet sublevel which is known to be capable of large vibrational overlap with T_3

Figure 4-15: Simultaneously recorded SEELEM (upper trace) and LIF (lower trace) spectra of the $3^3 K'=2$ sublevel of the \tilde{A}^1A_u state of C_2H_2 . The LIF spectrum is integrated in two time regions: an early time window ($0.5\tau_s - 2\tau_s$, solid trace) and a delayed time window ($10\tau_s - 18\tau_s$, dashed trace). The individual transitions each split into at least two strongly mixed components. Although the energy splitting between the components is on the order of the experimental resolution, the splitting is discernible because the nominal singlet and triplet components have different relative intensities in the early and delayed-LIF spectra. One splitting in the R(4) transition is barely resolved in this spectrum.

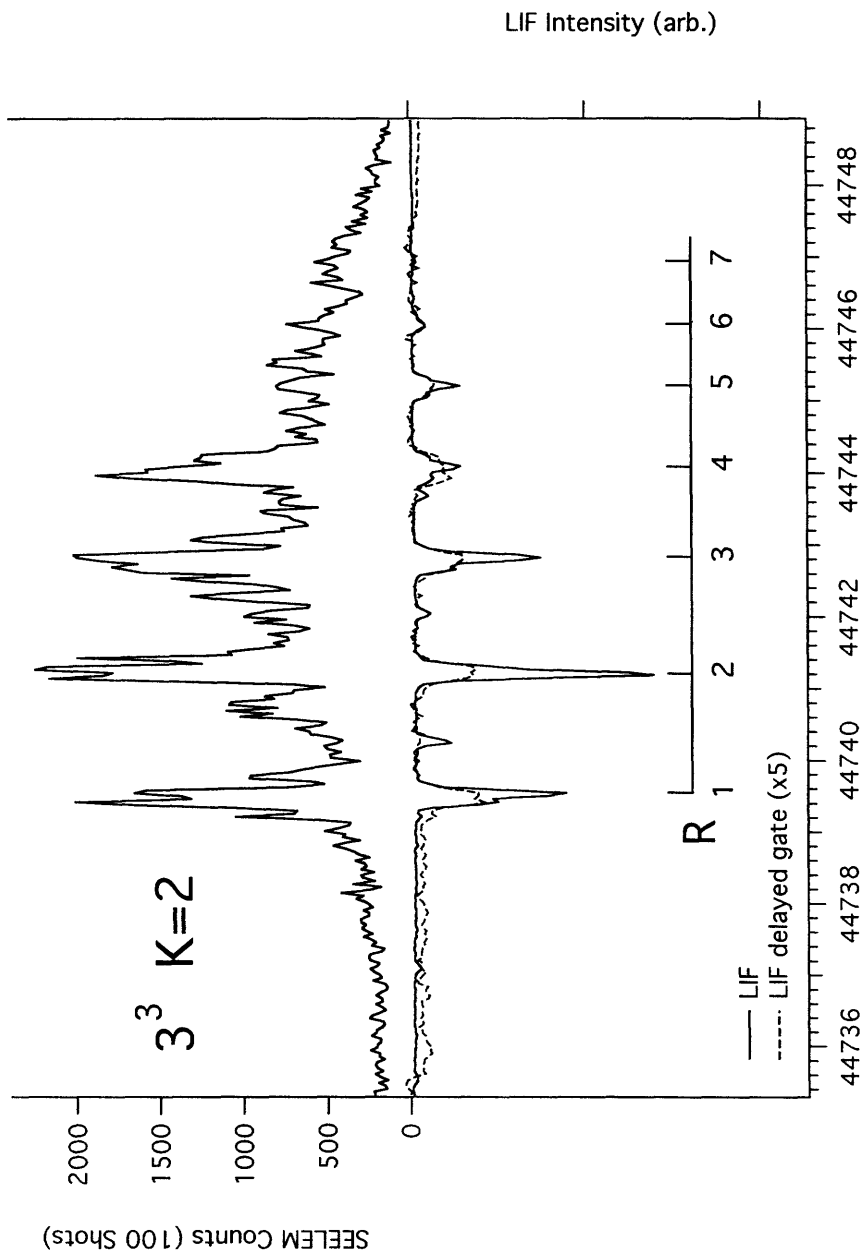
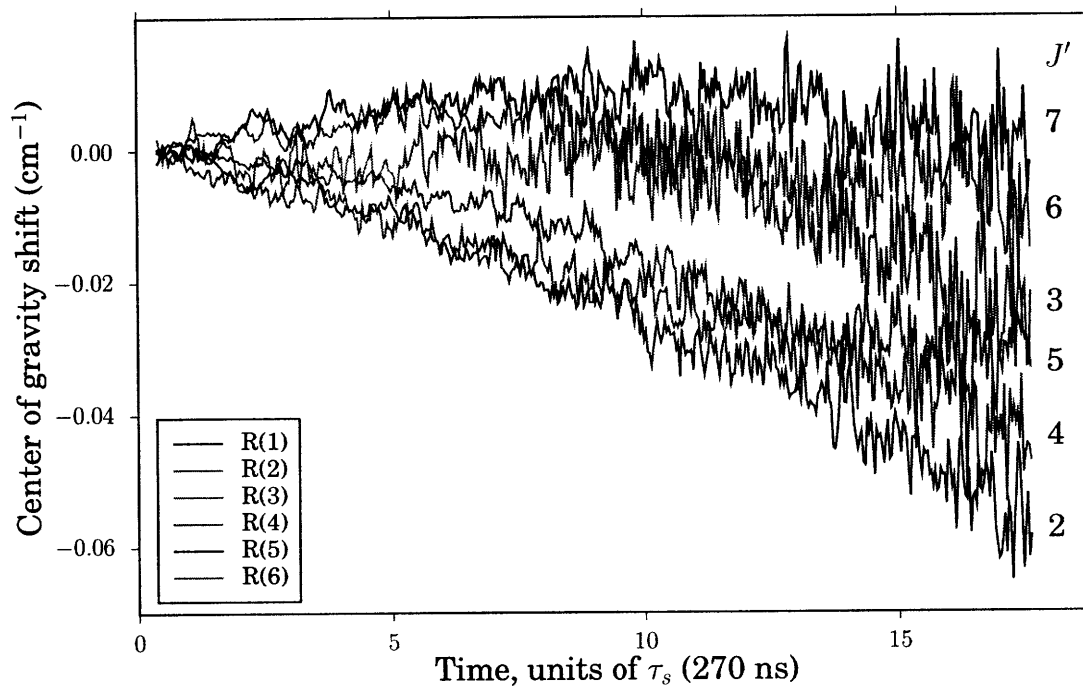


Figure 4-16: Dependence of the intensity-weighted center of gravity on delay for a series of individually resolved transitions, R(1–7), in the LIF spectrum of the $3^3 K'=2$ sublevel. The individual transitions have an overall bias toward lower energies at long delay times, indicating an interaction with a T_3 doorway level at lower energy than the S_1 level.



levels.

The $3^3 K'=2$ sublevel is not accessible from the ground state of acetylene due to $K' - \ell'' = \pm 1$ selection rules. However, the spectrum of the $3^3 K'=2 \leftarrow 4_1$ hot band transition was observed in our apparatus without heating the nozzle. The simultaneously recorded SEELEM/LIF spectrum of the R-branch of this transition is shown in Figure 4-15. Another interloping band⁴ is present in the spectrum with low intensity, giving rise to the weak lines at 44740.3, 44742.2, and 44743.6 cm^{-1} . No intensity alternation is present in the rotational series, consistent with expectations for a band that originates from the 4_1 vibrational level of the ground electronic state.

Evidence of strong mixing with the local manifold of $T_{1,2}$ levels is present in both the SEELEM and LIF detection channels. The SEELEM intensity envelope surrounding each singlet transition exceeds the spacing between adjacent rotational lines, about 1.5 cm^{-1} at low J' . This is at least 4 times the width observed for the transitions in $2^2 3^1 K'=1$, which contains only one quantum of excitation in ν_3 . The increased width of the local SEELEM intensity envelope has the effect of creating an envelope of SEELEM intensity that extends across the entire spectrum. This effect is also observed in the $3^3 K'=1 \leftarrow 0_0$ spectrum (see reference [55], for example).

However, we observe no large, systematic splittings at adjacent rotational levels of $3^3 K'=2$, which would result from a level crossing with the F_2 component of a near-degenerate T_3 doorway vibrational level, as in $3^3 K'=1$ [85]. Instead, narrow line splittings on the order of 0.05 cm^{-1} are evident in the LIF spectrum of each transition, even in the early time-gated LIF spectrum. Although most of the line splittings are slightly smaller than the laser resolution, the individual components have different fractional S_1 characters, and hence different lifetimes. This produces different relative intensities in the early and delayed-LIF spectra, which permits the splittings to be determined by comparing the spectra. Two of three strong components are barely resolved in the early-time LIF spectrum of the R(4) transition. In contrast to this strongly $S_1 \sim T_3$ mixed sublevel, the weakly mixed $2^2 3^1 K'=1$ sublevel contains no

⁴This band is currently unassigned because it is too broadly overlapped by other strong bands. The lines referenced here possibly belong to a hot band with a Q-head near 44736 cm^{-1} . Another possible assignment is to the second highest $K=2$ sublevel of the B^4 polyad [81].

such splittings.

The dependence of the intensity-weighted center of gravity for each transition in $3^3 K' = 2$ is shown in Figure 4-16. The transitions display an overall bias toward lower energy, indicating the presence of a T_3 doorway level to lower energy. The F_3 components of such a doorway level would approach the singlet level from below at a rate of $2B$ per J' , while the F_2 components would remain energetically distant and the F_1 components would rapidly tune away. That no crossing is observed by at least $J' = 6$ means that the doorway must lie at least $6 \times 2B + 2B \simeq 14 \text{ cm}^{-1}$ lower in energy than the singlet level.

The center of gravity generally decreases as a function of time delay for the transitions in the spectrum. The dependence is most pronounced for the $J' = 2$ rotational level, and the magnitude of shift is diminished as J' is increased. However, if the F_3 component of the doorway level is rapidly approaching the singlet, the overall mixing angle is expected to increase in magnitude. Why does the magnitude of the change in center of gravity not also increase? This paradox is explained by the large fractional singlet character in nominal $T_{1,2}$ levels, which is induced by strong mixing with the doorway level. As several states of nominal $T_{1,2}$ electronic character borrow more intensity, their lifetime decreases. As the nominal singlet level lends out more fractional character, its lifetime increases. The result is a lack of contrast between the intensities of the nominal singlet and nominal triplet eigenstates as a function of delay time, resulting in smaller changes in the intensity-weighted center of gravity.

4.6 Conclusion

The mechanism of doorway-mediated interaction by an energetically distant T_3 level skews the SEELEM spectrum of nearby, nominal $T_{1,2}$ eigenstates, resulting in a center of gravity shift between the LIF and SEELEM spectra. Additionally, when viewed in successive time windows, the center of gravity of the LIF spectrum exhibits evolution toward the limiting behavior exhibited in the SEELEM spectrum. A simple model can be used to show that strong mixing between the singlet level and the mediating

T_3 level causes a gradual shift in the center of gravity, while weak mixing with the doorway level induces a more delayed and rapid shift in the center of gravity, with respect to the S_1 lifetime.

Rotational selection rules for $S_1 \sim T_3$ spin-orbit interaction give rise to J -dependent effects in the LIF/SEELEM spectrum. As J increases, the F_1 or F_3 component of every distant T_3 level approaches the singlet at a rate $d\Delta E/dJ$ of approximately $2B_T$ ($\sim 2 \text{ cm}^{-1}$ per J). In the spectrum, the result is a shift in the LIF-SEELEM center of gravity when integrated across an entire branch of transitions. The effect not only leads to strong J -dependent changes in the patterns of T_3 -mediated coupling, but also ensures detection and assignment of $S_1 \sim T_3$ level crossings at relatively low values of J .

For every S_1 vibrational level, one spin component of a T_3 doorway level is rapidly approaching with J . Because of this, further LIF/SEELEM spectroscopy of the acetylene $\tilde{A}^1A_u \leftarrow \tilde{X}^1\Sigma_g^+$ transition will be fruitful and informative. We highlight some candidates for future investigation:

1. any levels which exhibit long lifetimes or quantum beats in the LIF spectrum,
2. levels with unassigned perturbations or splittings ($3^24^2 K'=1 J' = 5-10, K'=1$ sublevel of second B^4 polyad member),
3. other 3^2B^2 polyad members ($3^26^2 K'=1, 3^24^16^1 K'=1$), and
4. other K -sublevels of the Franck-Condon active levels studied here ($3^3 K'=3, 2^13^2 K'=2$).

The appearance of population quantum beats in the spectrum indicates a splitting on the order of 80 MHz or less. Quantum beat waveforms follow a well-defined analytical expression, and an analysis of quantum beats determines both the matrix element and zero-order energy spacing of the levels involved. The matrix elements gained from an analysis of zero-field quantum beats in the acetylene spectrum can serve as probes of the magnitude of local matrix elements between the nominal S_1 bright state and neighboring $T_{1,2}$ dark states. Furthermore, the study of Zeeman

quantum beats at low magnetic fields can provide a method for distinguishing between triplet perturbations and perturbations from other singlet levels, such as S_1 levels which are localized in the *cis* geometry of the \tilde{A}^1A_u state, because singlet states do not tune in a magnetic field.

Chapter 5

IR-UV double resonance

LIF/SEELEM spectroscopy of the $3^3_4^1$ $K'=0$ and $3^3_6^1$ $K'=0$ vibrational sublevels of S_1 acetylene

5.1 Introduction

The $\tilde{A} \ ^1A_u \leftarrow \tilde{X} \ ^1\Sigma_g^+$ spectrum of acetylene, C_2H_2 , provides a paradigm for an electronic transition accompanied by a change in geometry. The acetylene molecule is linear in the ground state (S_0), but has a planar *trans*-bent geometry in the $\tilde{A} \ ^1A_u$ state (S_1) [59, 56, 57]. *Ab initio* calculations are in agreement that the T_1 and T_2 electronic excited states also have a planar *trans*-bent equilibrium geometry [33, 68, 137, 105, 76, 128]. The third triplet state, T_3 , has a non-planar equilibrium geometry, twisted approximately 75° out of plane from the *trans* configuration [27, 128, 122].

Experiment and theory have shown that vibrational levels of the T_3 electronic state play a crucial role in allowing mixing between S_1 levels and the dense manifold of optically dark $T_{1,2}$ levels [55, 4, 38, 28, 122, 128]. The fundamental premise of the

model is that spin-orbit matrix elements between S_1 and $T_{1,2}$ levels are much smaller than those between levels of T_3 and $T_{1,2}$. In the doorway model, mixing between S_1 and $T_{1,2}$ levels occurs as a second-order effect; a level of T_3 must mix with S_1 , which, in turn, permits mixing with the manifold of $T_{1,2}$ levels.

The magnitude of $S_1 \sim T_3$ spin-orbit matrix elements is controlled principally by vibrational overlap factors, resulting in vibrational specificity for $S_1 \sim T_3$ mixing. To date, most studies have addressed the role of the symmetric *trans*-bending mode, partially because the levels containing this Franck-Condon-active vibration are well understood and appear with great intensity in the $\tilde{A} \ ^1A_u \leftarrow \tilde{X} \ ^1\Sigma_g^+$ spectrum. Many studies have observed an increase in T_3 -mediated $S_1 \sim T_{1,2}$ mixing with increased excitation in the ν_3 (*trans*-bend) vibrational mode of $\tilde{A} \ ^1A_u$ acetylene [41, 94, 55].

The role of the non-symmetric bending modes, ν_4 (torsion) and ν_6 (antisymmetric in-plane bend), is much less clear. Since the geometry change from in-plane to out-of-plane occurs along the torsional coordinate, a naïve Franck-Condon model would suggest that increased excitation in the torsional mode (ν_4) would lead to increased $S_1 \sim T_3$ vibrational overlap. However, the current experimental evidence and theoretical calculations disagree with this naïve model. Mizoguchi *et. al.* observe large splittings in the spectrum of $3^36^1 \ K'=1$, but not in the spectrum of $3^34^1 \ K'=1$ [87]. Yamakita and coworkers observe Zeeman quantum beats in several rotational lines in the spectrum of $3^36^1 \ K'=1$, but none in the spectrum of $3^34^1 \ K'=1$ [139]. These authors cite agreement with the calculations of Cui and Morokuma, who predict a half-linear geometry for the minimum of the seam of intersection between the S_1 and T_3 electronic surfaces [27]. Such a half-linear geometry is accessible via a combination of the ν_3 and ν_6 vibrations.

We are left without explanation as to the small magnitude vibrational overlap integrals upon excitation in mode 4, relative to mode 6. In an effort to address this problem, Virgo and coworkers recently published a comparison of the simultaneously recorded SEELEM/LIF spectrum of the $2^13^14^2 \ K'=1$ and $2^13^16^2 \ K'=1$ sublevels [129]. They observe that the SEELEM:LIF intensity ratio is three times larger for $2^13^14^2 \ K'=1$ than for $2^13^16^2 \ K'=1$. In order to characterize the experimental results

in terms of $2^13^14^2$ and $2^13^16^2$ basis character, they present a tentative deperturbation of the $2^13^1B^2$ polyad, which consists of the $2^13^14^2$ (a_g), $2^13^16^2$ (a_g), and $2^13^14^16^1$ (b_g) levels [83, 129]. They note that $2^13^14^2$ and $2^13^16^2$ basis character is essentially evenly distributed between the two $K'=1$ sublevels observed in the experiment. The difference in SEELEM:LIF intensity ratio is ascribed instead to be the result of an interference effect which cancels out almost all $2^13^14^16^1$ (b_g) basis character in one of the levels.

The interference effect is due to two separate, strong interactions between the ν_4 and ν_6 vibrations. The first interaction is a strong Darling-Dennison resonance, which connects vibrations by exchanging two quanta of ν_4 for two quanta of ν_6 , or vice versa. Levels with only one quantum of modes 4 or 6, such as those studied by Mizoguchi, are immune to this effect. The second interaction is the a -axis Coriolis coupling, which exchanges one quantum of mode 4 for one quantum of mode 6. The matrix element for a -axis Coriolis coupling includes a factor of K , thus sublevels with $K = 0$ are immune to this effect.

In this study, we use SEELEM/LIF spectroscopy to address separately the role of modes 4 and 6 in promoting vibrational overlap with T_3 levels. To avoid the Darling-Dennison resonance, we select a polyad with only one quantum of non-symmetric bend. To avoid a -type Coriolis coupling, we examine the $K = 0$ sublevels of the polyad members. To investigate the effects of ν_4 and ν_6 near the crucial half-linear and twisted geometries, we select the particular combination levels 3^34^1 $K'=0$ and 3^36^1 $K'=0$ of S_1 acetylene.

5.2 Experiment

Vibrational levels of \tilde{A}^1A_u acetylene with *ungerade* symmetry are inaccessible via one-photon transitions from the ground state, according to g/u selection rules. To access the 3^34^1 (a_u) and 3^36^1 (b_u) levels, we employed an IR-UV double resonance scheme. The $v_3'' + v_4''$ level of the $\tilde{X}^1\Sigma_g^+$ state was chosen as an intermediate state for laser excitation. According to the selection rule $K' - \ell'' = \pm 1$, the $K' = 0$ sublevels

of 3^34^1 and 3^36^1 are accessible from this $\ell'' = 1$ ground state intermediate.

IR laser radiation in the region of 3900 cm^{-1} was generated by difference frequency mixing (DFM) followed by optical parametric amplification (OPA). The second harmonic output of an Nd:YAG injection-seeded laser (Spectra Physics PRO-270) was used to pump a tunable dye laser (Lambda Physik FL2002), operating with LDS 751 laser dye. The dye laser output was mixed in a lithium niobate (LiNbO_3) crystal with a portion of the 1064 nm Nd:YAG fundamental beam. The IR output was amplified in another LiNbO_3 crystal, using the remaining 1064 nm radiation. The amplified IR laser radiation had a typical power of 3 mJ and an incoherent linewidth of 0.15 cm^{-1} . A photoacoustic cell containing approximately 100 mTorr of acetylene was used for frequency calibration of the IR radiation.

The UV laser radiation used in the second step of the double resonance was generated from the output of a second dye laser (Lambda Physik FL3002), operating with Coumarin 480, pumped by the third harmonic of the Nd:YAG laser described above. The dye laser output was frequency doubled using a BBO crystal. The UV laser radiation was frequency calibrated by recording the absorption spectrum of $^{130}\text{Te}_2$ using the fundamental frequency output of the dye laser. The frequency step size of the UV laser was approximately 0.047 cm^{-1} (frequency doubled output) in this study.

The IR and UV beams were positioned in an overlapping, colinear geometry inside the SEELEM/LIF apparatus. The UV laser pulse was delayed by 10 ns relative to the IR pulse by using several UV reflectors to create an optical delay line. A dichroic mirror, transparent in the IR, was used to combine the IR and UV beams. Except where noted, both beams were p -polarized, relative to the plane defined by the direction of laser propagation and the molecular beam axis of the apparatus.

The SEELEM/LIF apparatus, in its current arrangement, has been described previously [29, 2, 3, 85]. Briefly, the apparatus consists of two differentially pumped vacuum chambers, a source chamber and a SEELEM detection chamber. In the source chamber, a supersonic jet of acetylene gas (Matheson) is expanded from a 10 Hz pulsed valve (Jordan) through a 0.5 mm diameter nozzle. The source chamber is pumped by

a 6 inch diffusion pump (Varian), and has a typical operating pressure of 10^{-4} Torr. Approximately 2 cm downstream from the nozzle, the molecules are excited by the overlapping UV and IR laser beams, which intersect the axis of the jet at a 90° angle. The laser-induced molecular fluorescence is collected by $f/4$ optics along an axis normal to the plane defined by the lasers and the jet axis. The fluorescence passes through a filter (UG-11) and is detected by a photomultiplier tube (Hamamatsu R375). The time-varying photomultiplier output signal is averaged at each laser frequency on a digital oscilloscope (LeCroy) and recorded on a PC.

Approximately 5 cm from the region of excitation, molecules in the supersonic expansion pass through a 3 mm diameter skimmer and enter the SEELEM detection chamber. The detection chamber is also pumped by a 6 inch diffusion pump (Varian), and has a typical operating pressure of 10^{-6} Torr. The SEELEM detector is positioned along the molecular beam axis, approximately 35 cm downstream of the excitation region. The design of the SEELEM detector used in these experiments has been described by several authors [29, 2]. In the SEELEM detector, electrons ejected from a grounded metal surface are detected by an electron multiplier (ETP). The electron multiplier output is sent to a fast amplifier/discriminator (EG&G/Ortec), and the resulting pulses are acquired by PC-operated multichannel scalar hardware.

To eject an electron from the metal surface of the SEELEM detector, an excited molecule must have a vertical electronic excitation energy larger than the work function of the metal. In this study, a gold surface was used, with a work function of approximately 5.1 eV. Among the low-lying electronically excited states of acetylene, only S_1 and T_3 have sufficient energy to be detectable on gold.

5.3 Results

The spectra in this study were collected using two double resonance strategies: a survey method and an “individual line” method. In the survey method, the IR laser was tuned to the Q-branch head of the $v_3'' + v_4''$ level in the ground electronic state. The Q-branch of this band is very compact, and the incoherent linewidth of the IR

laser is sufficient to excite the rotational levels $J = 1f - 5f$ at a single laser frequency. From the f -symmetry rotational levels populated in the first excitation step, Q-branch transitions in the UV are permitted to the $3^34^1 K'=0$ sublevel, and P or R-branch transitions are permitted to the $3^36^1 K'=0$ sublevel. A diagram of the energy levels and the allowed transitions is shown in Figure 5-1.

In the individual line method, the IR laser was tuned to individual lines in the P or R-branch of the $v_3'' + v_4''$ level in the ground electronic state. Using this strategy, only a single e -symmetry rotational level of $v_3'' + v_4''$ is populated by the IR laser at a given frequency. From the intermediate state, only a single Q-branch transition to the $3^36^1 K'=0$ sublevel of the \tilde{A}^1A_u state is permitted in the UV. The $3^34^1 K'=0$ sublevel of the \tilde{A}^1A_u state is accessible through P or R-branch transitions from the intermediate state, as shown in Figure 5-1.

Figures 5-2-5-6 show the simultaneously recorded SEELEM (plotted upward) and LIF (plotted downward) spectra of the $J' = 1-5$ rotational levels of $\tilde{A}^1A_u 3^36^1 K'=1$, recorded using the individual line method. The SEELEM:LIF intensity ratio was on the same order of magnitude as that of the $3^3 K'=1$ sublevel, reported previously [85]. Figures 5-2-5-6 each contain a magnified view of the SEELEM spectrum, showing a large number of transitions to long-lived eigenstates over each energy range scanned by our UV laser. Unlike previous experiments, each spectrum in Figures 5-2-5-6 contains eigenstates belonging to only one value of the rotational quantum number, J' . Using the individual line double resonance method, the full envelope of metastable eigenstates drawing intensity from each singlet basis state is viewed without overlap from neighboring J' transitions.

The LIF spectra in Figures 5-2-5-6 are integrated in two time regions: an early time window ($0.5\tau_s - 2\tau_s$, solid trace) and a delayed time window ($10\tau_s - 18\tau_s$, dashed trace). The quantity τ_s is the characteristic fluorescence lifetime of the \tilde{A}^1A_u state, determined to be 270 ns [94]. Line splittings are resolved in the early and delayed LIF spectra of the $J' = 1-4$ rotational levels. The frequency separation of the components in the splittings varies between 0.06 and 0.2 cm^{-1} . In each figure, the line with greatest intensity in the early-time LIF spectrum is marked with a solid indicator. Additional

lines, appearing with greater intensity in the delayed LIF spectrum, are marked with dashed indicators.

In the spectra under consideration, all oscillator strength is provided by a single, optically bright S_1 basis state. Optically dark basis states, triplet in character, may mix with the bright state by spin-orbit interaction, according to the selection rule $\Delta J = 0$. The fluorescence lifetime of the resultant eigenstates is inversely proportional to the fractional S_1 electronic character, as detailed in Chapter 4, Section 2. The eigenstate that has the largest amount of fractional S_1 character is labeled as the nominal bright state. This eigenstate has the shortest lifetime among the ensemble of mixed eigenstates. Levels with less fractional S_1 character have longer lifetimes and greater intensity in the delayed LIF spectrum, relative to the early LIF spectrum. Consequently, for each spectrum we label the single highest-intensity line in the early LIF channel with a solid marker, indicating its status as the nominal bright state.

The spectrum of the $J' = 0$ rotational level of $3^36^1 K'=0$ cannot be recorded using the individual line double resonance method, since the method permits only Q-branch transitions to appear in the UV spectrum, and Q(0) transitions are strictly forbidden. Instead, the spectrum of $3^36^1 K'=0 J' = 0$ was recorded in the region of the P(1) transition by the survey method, using two relative polarization geometries for the IR and UV laser beams. Because selection rules for M_J make the P(1) transition forbidden in one geometry, a “baseline” spectrum can be recorded in the region of the P(1) transition, and $J' = 0$ levels can be distinguished from neighboring $J' = 1$ levels. To evaluate the M_J selection rules for the two-step excitation, we choose to adopt a laboratory-fixed axis system where the z -axis is the polarization axis of the IR laser, and the y -axis is the direction of the colinear IR and UV laser propagation. The reader is free to choose another laboratory-fixed axis system under which to evaluate the selection rules. The M_J selection rules are equally valid for all orientations of the laboratory-fixed axes; our choice is determined by convenience and ease of explanation.

When the colinear IR and UV beams are perpedicularly polarized, the P(1) transition, terminating on $J' = 0$, is permitted in the UV. The IR excitation step proceeds

Figure 5-2: Simultaneously recorded SEELEM (upper trace) and LIF (lower trace) spectra of the $3^36^1 K'=0$ sublevel of the \tilde{A}^1A_u state of C_2H_2 . The $P(2)$ line of the $X^1\Sigma_g^+ v_3''+v_4''$ level is used as an intermediate state in the experiment, so only the $Q(1)$ line is observed, according to Figure 5-1. The LIF spectrum is integrated in two time regions: an early time window ($0.5\tau_s - 2\tau_s$, solid trace) and a delayed time window ($10\tau_s - 18\tau_s$, dashed trace). Two additional lines, labeled with dashed markers, are observed in the delayed LIF spectrum on either side of the nominally singlet eigenstate. The intensity envelope of the delayed LIF spectrum closely resembles that of the SEELEM spectrum – this effect is echoed in Figures 5-3 to 5-6.

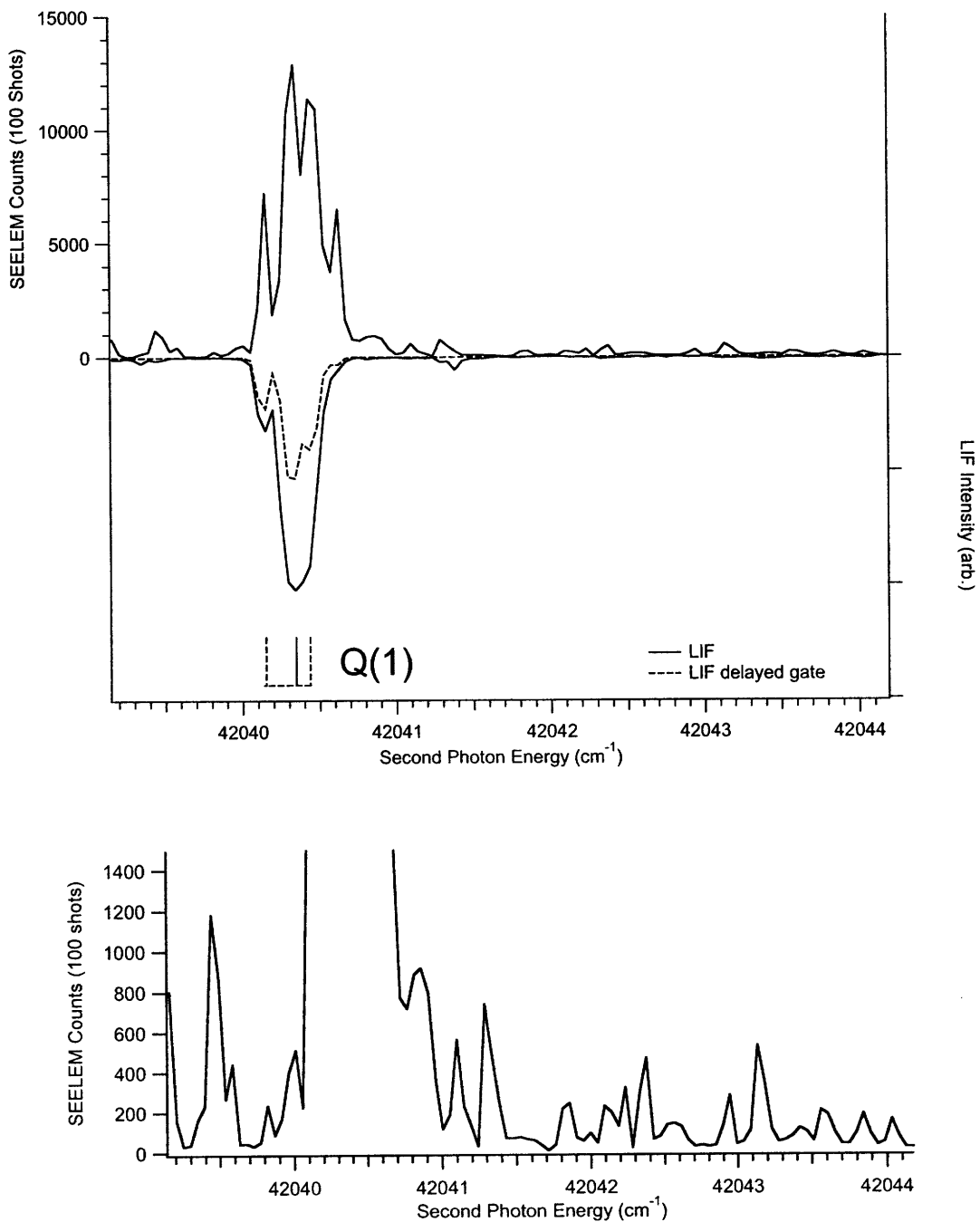


Figure 5-3: Simultaneously recorded SEELEM (upper trace) and LIF (lower trace) spectra of the $3^36^1 K'=0$ sublevel of the \tilde{A}^1A_u state of C_2H_2 . The P(3) line of the $\tilde{X}^1\Sigma_g^+ v_3'' + v_4''$ level is used as an intermediate state in the experiment, so only the Q(2) line is observed, according to Figure 5-1. The LIF spectrum is integrated in two time regions: an early time window ($0.5\tau_s - 2\tau_s$, solid trace) and a delayed time window ($10\tau_s - 18\tau_s$, dashed trace). A line splitting of $\sim 2 \text{ cm}^{-1}$ is observed in the LIF spectrum, with the longer-lifetime (nominally triplet) component located at higher energy.

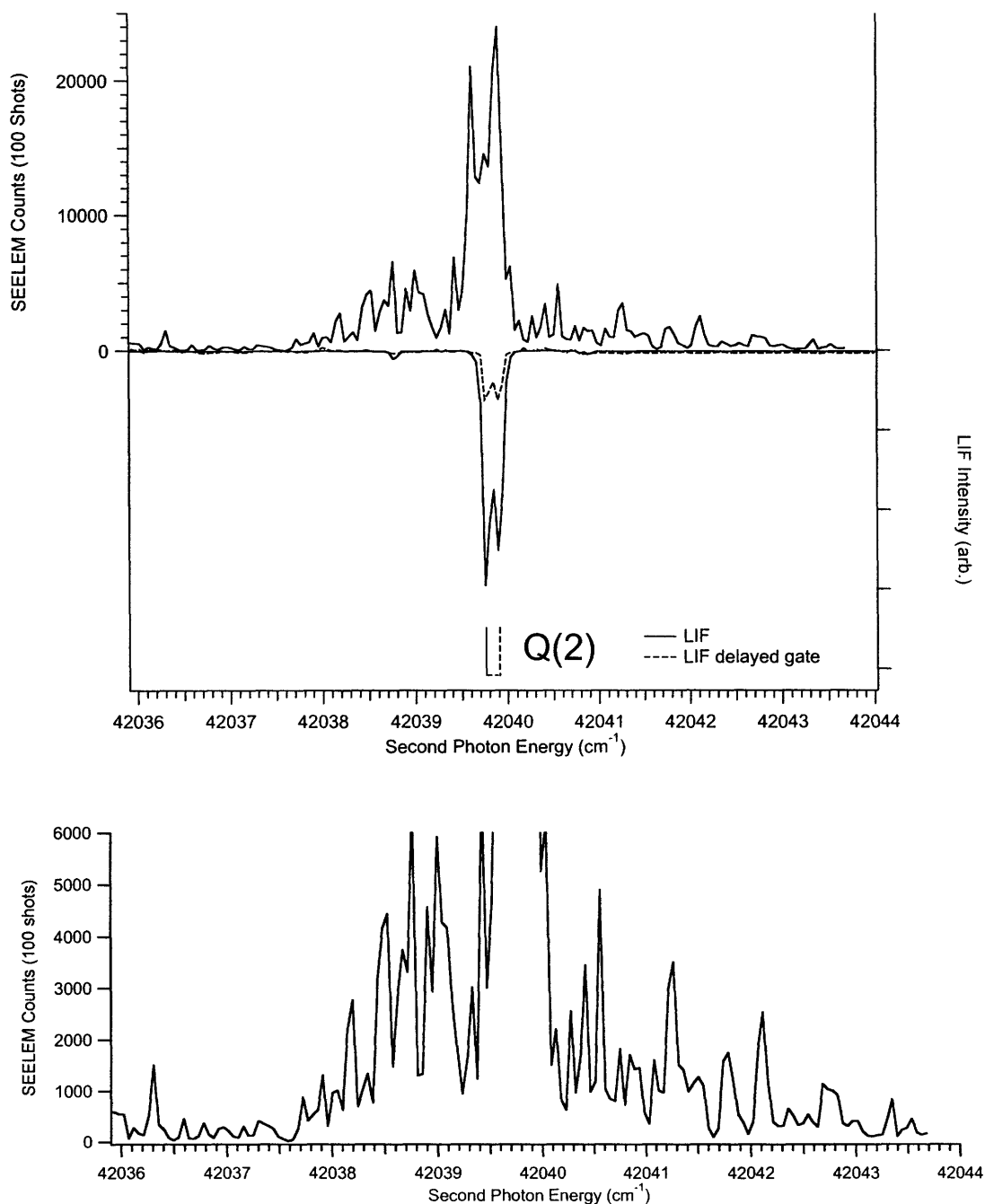


Figure 5-4: Simultaneously recorded SEELEM (upper trace) and LIF (lower trace) spectra of the 3^36^1 $K'=0$ sublevel of the \tilde{A}^1A_u state of C_2H_2 . The P(4) line of the $\tilde{X}^1\Sigma_g^+$ $v_3''+v_4''$ level is used as an intermediate state in the experiment, so only the Q(3) line is observed, according to Figure 5-1. The LIF spectrum is integrated in two time regions: an early time window ($0.5\tau_s - 2\tau_s$, solid trace) and a delayed time window ($10\tau_s - 18\tau_s$, dashed trace). The transition at 42038.3 cm^{-1} has a short lifetime, and belongs to an unassigned singlet sublevel. A small line splitting of less than 0.05 cm^{-1} is apparent from the shifted peak position in the delayed LIF spectrum relative to the early LIF spectrum. The longer-lifetime (nominally triplet) component is located to higher energy.

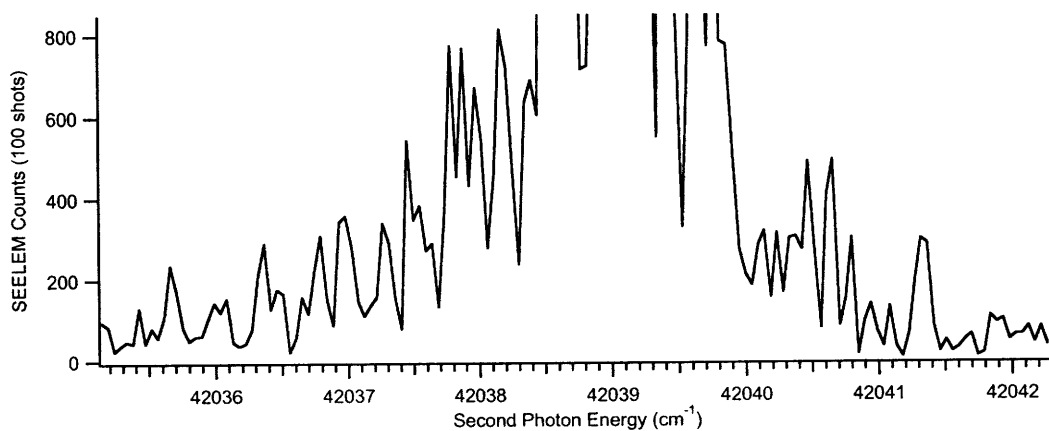
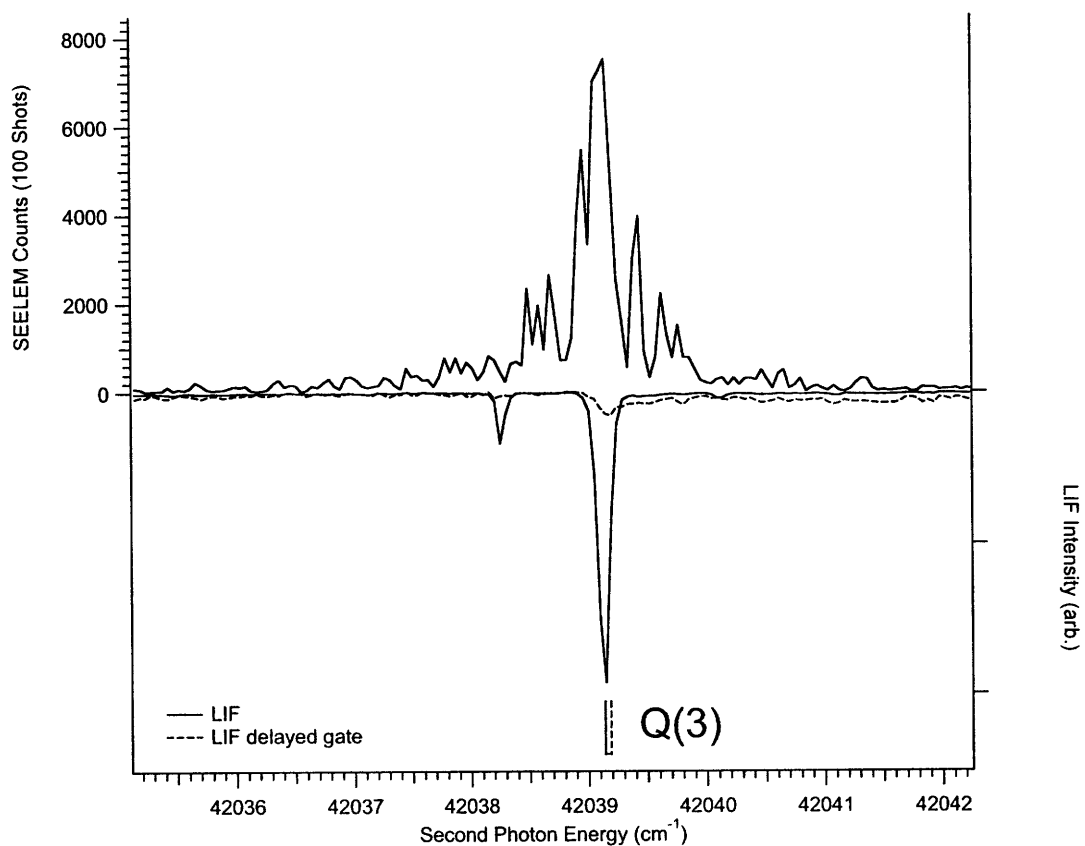


Figure 5-5: Simultaneously recorded SEELEM (upper trace) and LIF (lower trace) spectra of the 3^36^1 $K'=0$ sublevel of the \tilde{A}^1A_u state of C_2H_2 . The R(3) line of the $\tilde{X}^1\Sigma_g^+$ $v_3'' + v_4''$ level is used as an intermediate state in the experiment, so only the Q(4) line is observed, according to Figure 5-1. The LIF spectrum is integrated in two time regions: an early time window ($0.5\tau_s - 2\tau_s$, solid trace) and a delayed time window ($10\tau_s - 18\tau_s$, dashed trace). A line splitting of ~ 0.2 cm^{-1} is observed in the LIF spectrum, with the longer-lifetime (nominally triplet) component located at higher energy.

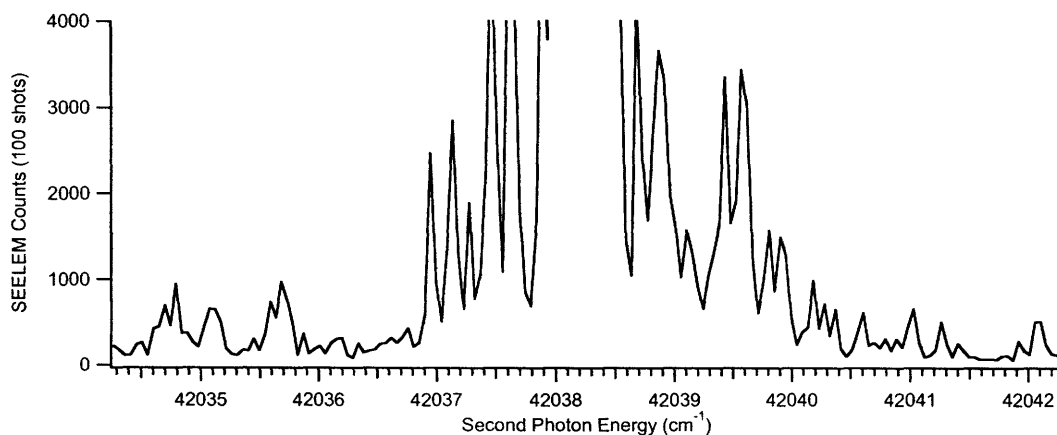
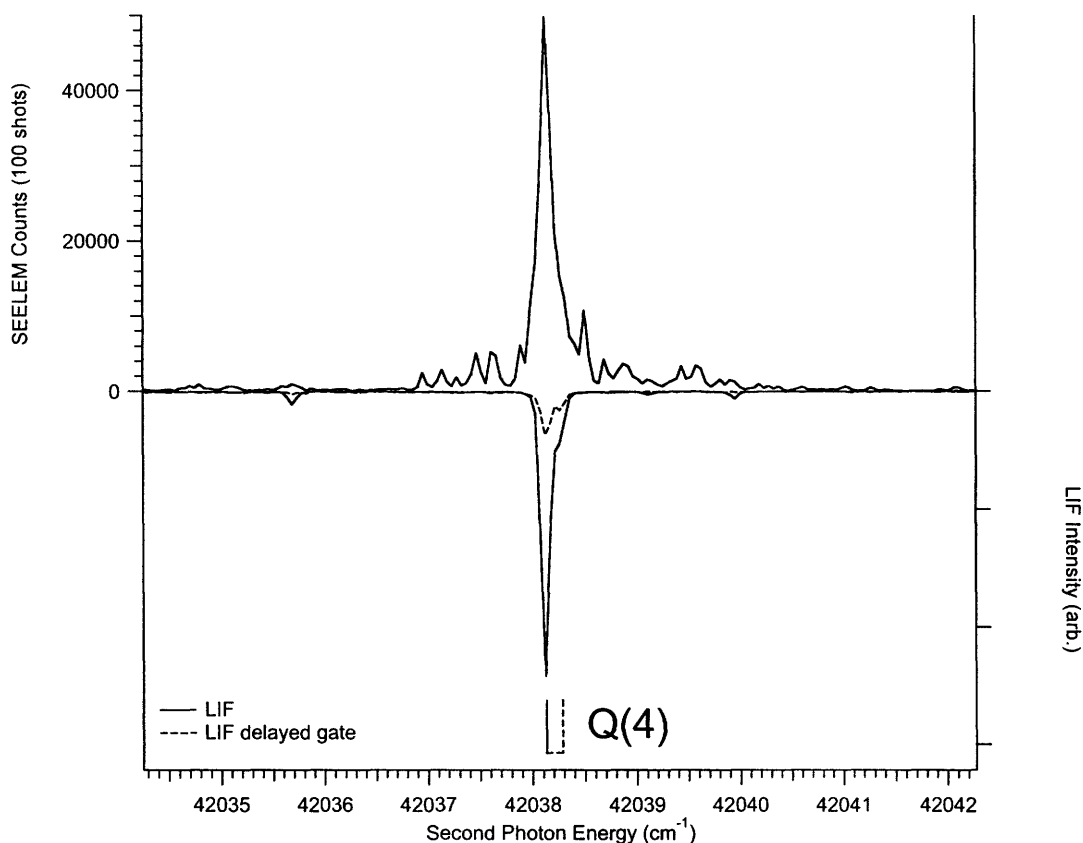
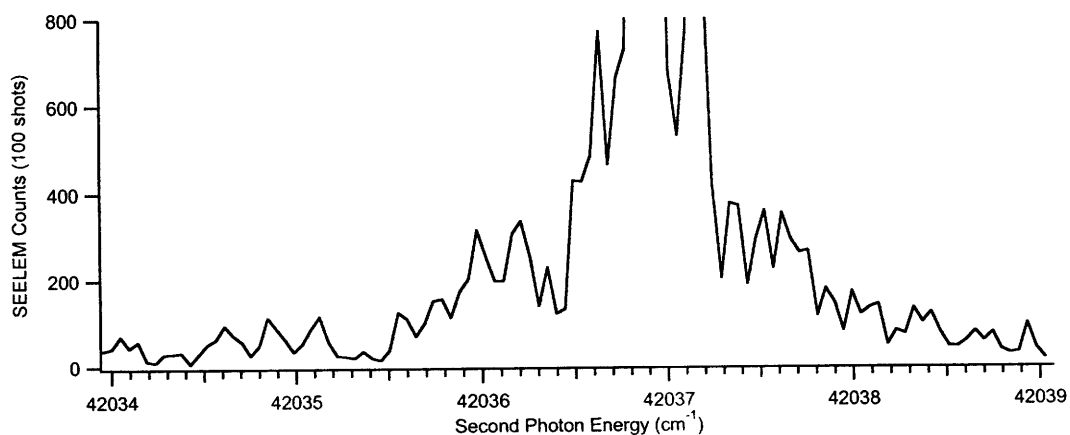
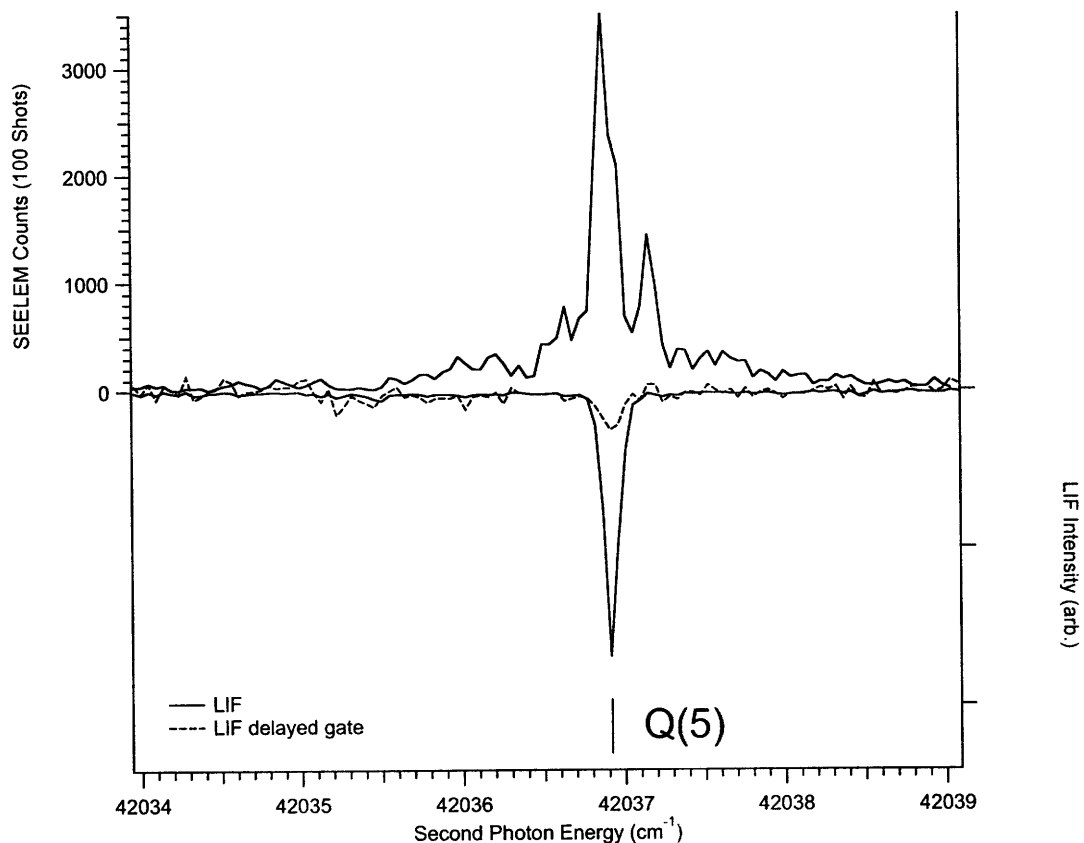


Figure 5-6: Simultaneously recorded SEELEM (upper trace) and LIF (lower trace) spectra of the $3^36^1 K'=0$ sublevel of the \tilde{A}^1A_u state of C_2H_2 . The R(4) line of the $\tilde{X}^1\Sigma_g^+ v_3'' + v_4''$ level is used as an intermediate state in the experiment, so only the Q(5) line is observed, according to Figure 5-1. The LIF spectrum is integrated in two time regions: an early time window ($0.5\tau_s - 2\tau_s$, solid trace) and a delayed time window ($10\tau_s - 18\tau_s$, dashed trace). No line splittings are observed in the LIF spectrum.



according to the selection rule $\Delta M_J = 0$. Magnetic sublevels in the intermediate state with $M_J = 1$ are populated from $M_J = 1$ sublevels of the ground state. In the second excitation step, when the UV laser beam is perpedicularly polarized relative to the IR beam, $\Delta M_J = \pm 1$ transitions are permitted to the upper state $J' = 0$ rotational level, which has only one M_J component, $M_J = 0$. Figure 5-7 illustrates the permitted transitions among M_J sublevels as solid arrows.

When the colinear IR and UV laser beams are polarized in parallel, the selection rules for ΔM_J do not allow any transitions that terminate in the upper state $J' = 0$ rotational level. Since the IR and UV beams are both linearly polarized along the z -axis, $\Delta M_J = 0$ in the IR and UV excitation steps. The upper state has no sublevels with $M_J = \pm 1$, so transitions beginning in the $M_J = \pm 1$ sublevels of the ground state cannot occur to the excited state. A two-step excitation could possibly terminate in the $M_J = 0$ level of the excited state, if it were to start from $M_J = 0$ in the ground state. However, such a transition is forbidden in the first step, according to the selection rule that $M_J = 0 \leftrightarrow M_J = 0$ for $\Delta J = 0$ (Q-branch) transitions [47]. The forbidden transition is illustrated with dashed arrows in Figure 5-7.

Simultaneously recorded SEELEM/LIF spectra in the region of the $3^36^1 K'=0$ P(1) transition are shown in Figure 5-8, for perpendicular (solid trace) and parallel (dashed trace) laser polarization. Since the transition to $J' = 0$ is forbidden in the parallel geometry, the dashed trace serves as a null spectrum in this region. At UV frequencies between 42036.0 and 42041.3 cm^{-1} , essentially all peaks in the SEELEM spectrum are due to intensity borrowing from the $J' = 0$ level of $3^36^1 K'=0$. This particular region is shown with more detail in Figure 5-9. The delayed LIF spectrum is also included as a dashed trace in this figure. A line splitting is resolved in the delayed LIF spectrum, with the long-lifetime component lying to higher frequency.

The SEELEM/LIF spectrum of $3^34^1 K'=0$, recorded by the survey method, is shown in Figure 5-10. The LIF spectrum is integrated in both early ($0.5\tau_s - 2\tau_s$, solid trace) and delayed ($10\tau_s - 18\tau_s$, dashed trace) time windows. Due to saturation of the photomultiplier tube at early time intervals, the early LIF spectrum shown in the figure was recorded and calibrated in a separate scan. The delayed LIF spectrum and

Figure 5-7: Diagram of transitions among M_J sublevels terminating in the $J' = 0$ rotational level of $3^36^1 K' = 0$. When the IR and UV lasers are polarized in a perpendicular geometry, transitions terminating in the $J' = 0$ rotational level of the excited state are permitted according to the selection rules $\Delta M_J = 0$ (first step), $\Delta M_J = \pm 1$ (second step). When the IR and UV lasers are polarized in a parallel geometry, transitions terminating in the $J' = 0$ rotational level of the excited state are forbidden according to the selection rule $M_J = 0 \leftrightarrow M_J = 0$ when $\Delta J = 0$.

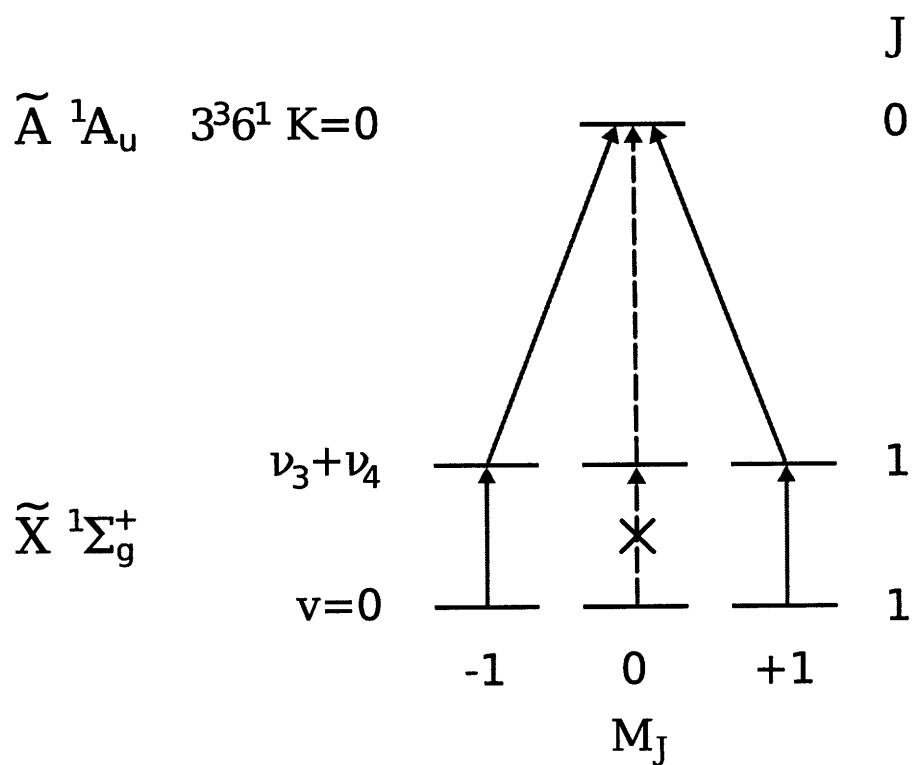


Figure 5-8: Simultaneously recorded SEELEM (upper trace) and LIF (lower trace) spectra of the $3^36^1 K'=0$ sublevel of the \tilde{A}^1A_u state of C_2H_2 . The Q-branch of the $\tilde{X}^1\Sigma_g^+ v_3'' + v_4''$ level is used as an intermediate transition in the experiment. As a result, P- and R-branch lines are observed into the upper state, according to Figure 5-1. The P(1) transition to the upper state is forbidden in a parallel IR-UV laser polarization geometry. A spectrum recorded with this laser geometry is shown as a dashed line. Lines appearing unambiguously in the SEELEM spectrum are indicated by solid arrows. Lines indicated by dashed arrows are more uncertain.

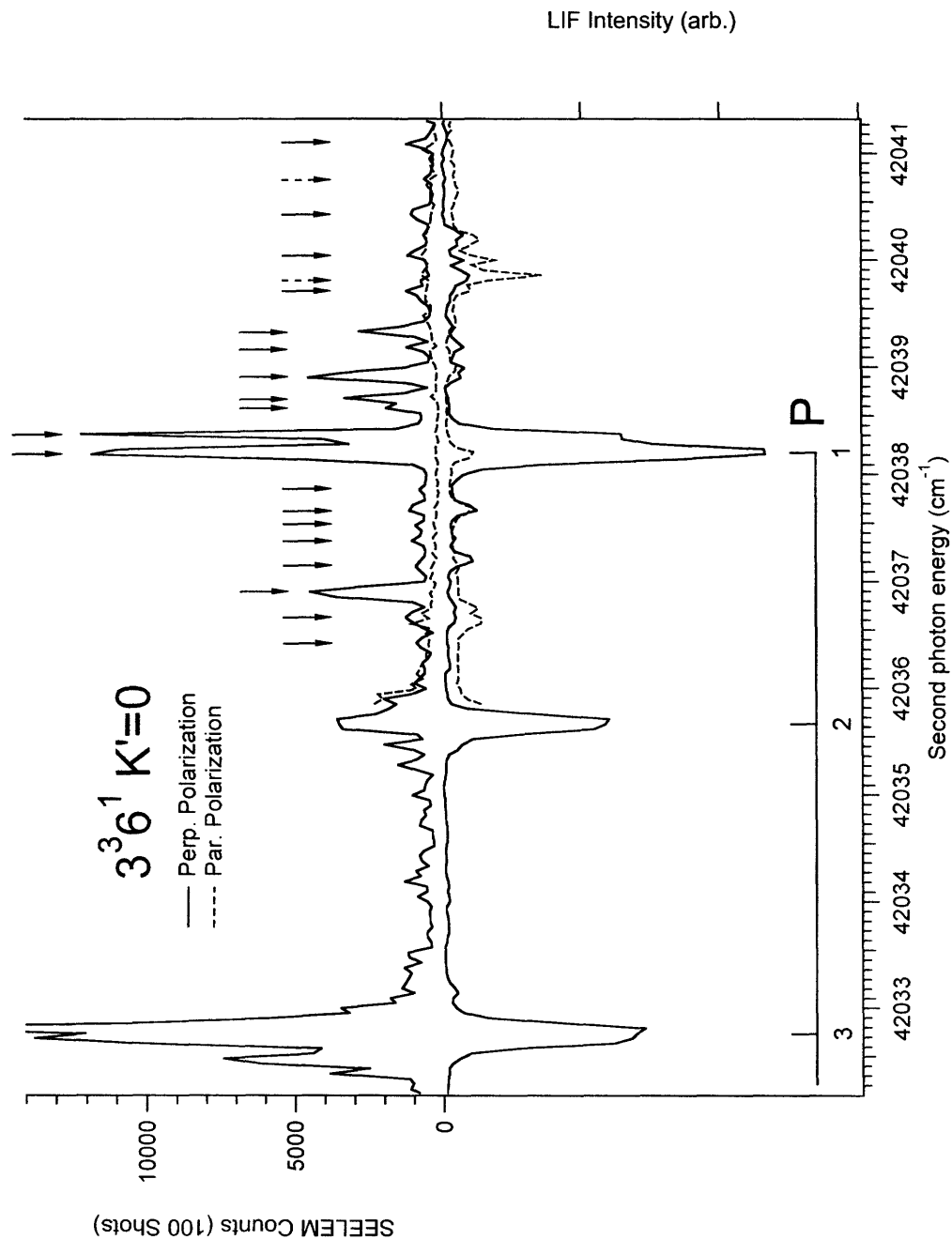
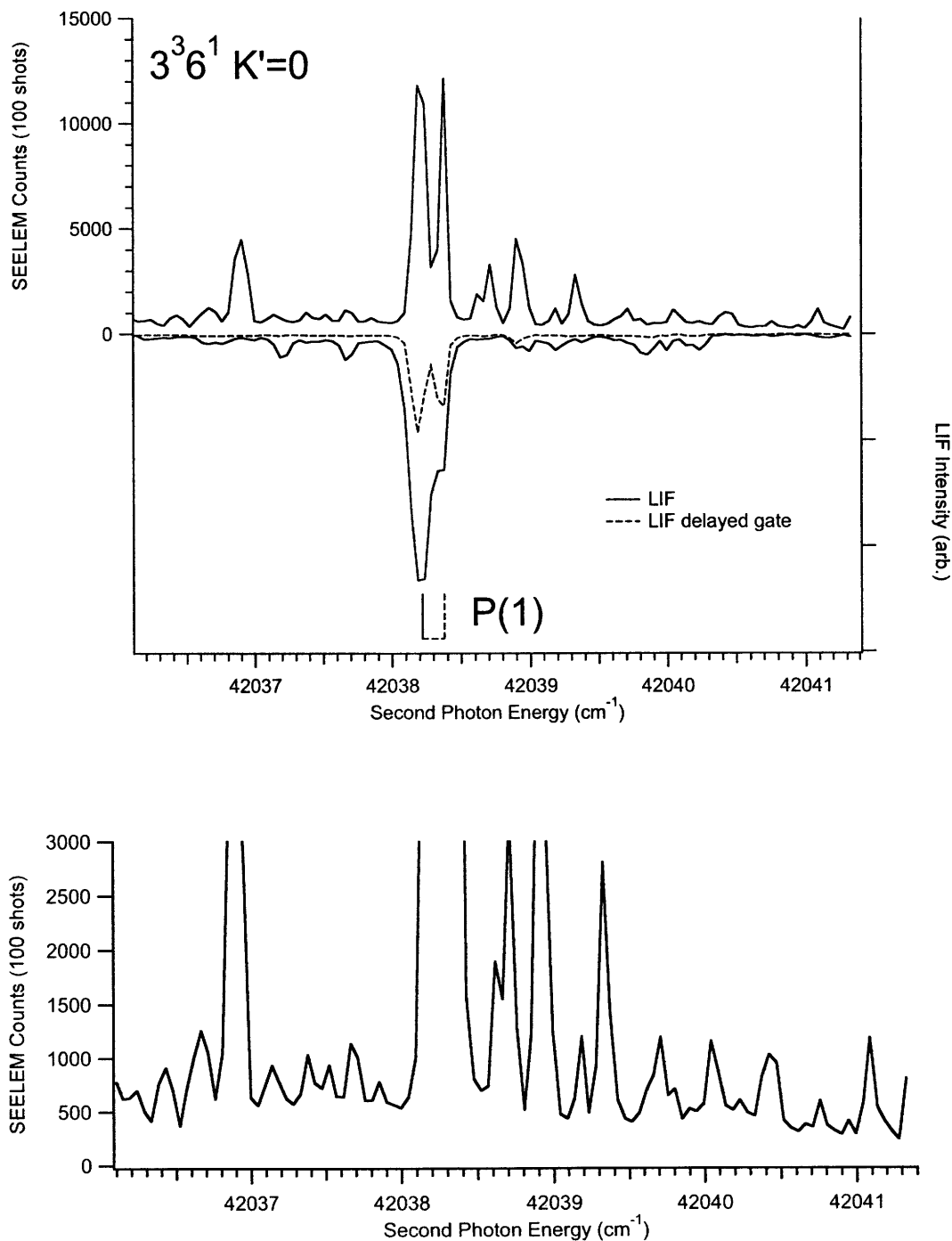


Figure 5-9: Simultaneously recorded SEELEM (upper trace) and LIF (lower trace) spectra of the $3^36^1 K'=0$ sublevel of the \tilde{A}^1A_u state of C_2H_2 . The Q-branch of the $\tilde{X}^1\Sigma_g^+ v_3'' + v_4''$ level is used as an intermediate transition in the experiment. As a result, P- and R-branch lines are observed into the upper state, according to Figure 5-1. The LIF spectrum is integrated in two time regions: an early time window ($0.5\tau_s - 2\tau_s$, solid trace) and a delayed time window ($10\tau_s - 18\tau_s$, dashed trace). A line splitting of $\sim 2\text{ cm}^{-1}$ is observed in the LIF spectrum, with the longer-lifetime (nominally triplet) component located at higher energy.



the SEELEM spectrum were recorded simultaneously. The integrated SEELEM:LIF intensity ratio is observed to be on the same order of magnitude as that of the 3^36^1 $K'=0$ level.

Line splittings appear in the delayed LIF spectrum of every transition to the 3^34^1 $K'=0$ sublevel. The splittings span a frequency range of $0.06 - 0.3 \text{ cm}^{-1}$. The average frequency difference between components of the same J' is slightly larger than that of 3^36^1 $K'=0$, and in general the splittings are more pronounced in the early LIF spectrum. Presumably the line splittings in 3^34^1 $K'=0$ were too small to be detected by Mizoguchi and coworkers, who recorded and assigned the LIF spectrum of this level previously, and cite a UV laser resolution of 0.1 cm^{-1} [87]. Line splittings reported in that reference, observed in another sublevel, are an order of magnitude larger than those observed in this spectrum.

The line splitting in Q(1) could not be assigned directly from the survey spectrum, because the long-lifetime component appears at a frequency halfway between the Q(1) and Q(2) transitions. To assign the long-lifetime component, the spectrum of the P(2) transition in 3^34^1 $K'=0$ was recorded using the individual line method, via the P(3) transition from the ground state. This spectrum is shown in Figure 5-11. A line splitting of -0.2 cm^{-1} is observed in the LIF spectrum, confirming the assignment of the long-lifetime component in Q(1) (Figure 5-10).

5.4 Analysis

5.4.1 LIF Spectrum:

Characterization of mediating T_3 levels

Line splittings on the order of 0.2 cm^{-1} were observed in the LIF spectrum of both S_1 sublevels, 3^36^1 $K'=0$ and 3^34^1 $K'=0$. Because the extra lines appear with greater intensity in the delayed LIF spectrum relative to the early LIF spectrum, they are attributed to mixing between the S_1 sublevel and nearby triplet levels. Three triplet electronic states are energetically accessible: T_1 , T_2 , and T_3 . According to the doorway

Figure 5-10: Simultaneously recorded SEELEM (upper trace) and LIF (lower trace) spectra of the $3^3 4^1 K'=0$ sublevel of the $\tilde{A}^1 A_u$ state of C_2H_2 . The Q-branch of the $\tilde{X}^1 \Sigma_g^+ v_3'' + v_4''$ level is used as an intermediate transition in the experiment. As a result, Q-branch lines are observed into the upper state, according to Figure 5-1. The LIF spectrum is integrated in two time regions: an early time window ($0.5\tau_s - 2\tau_s$, solid trace) and a delayed time window ($10\tau_s - 18\tau_s$, dashed trace). Line splittings ranging from 0.06 to 0.3 cm^{-1} are observed in the delayed LIF spectrum of all rotational lines. With one exception, the longer-lifetime (nominally triplet) components are located at lower energy than the shortest-lifetime (nominally singlet) component.

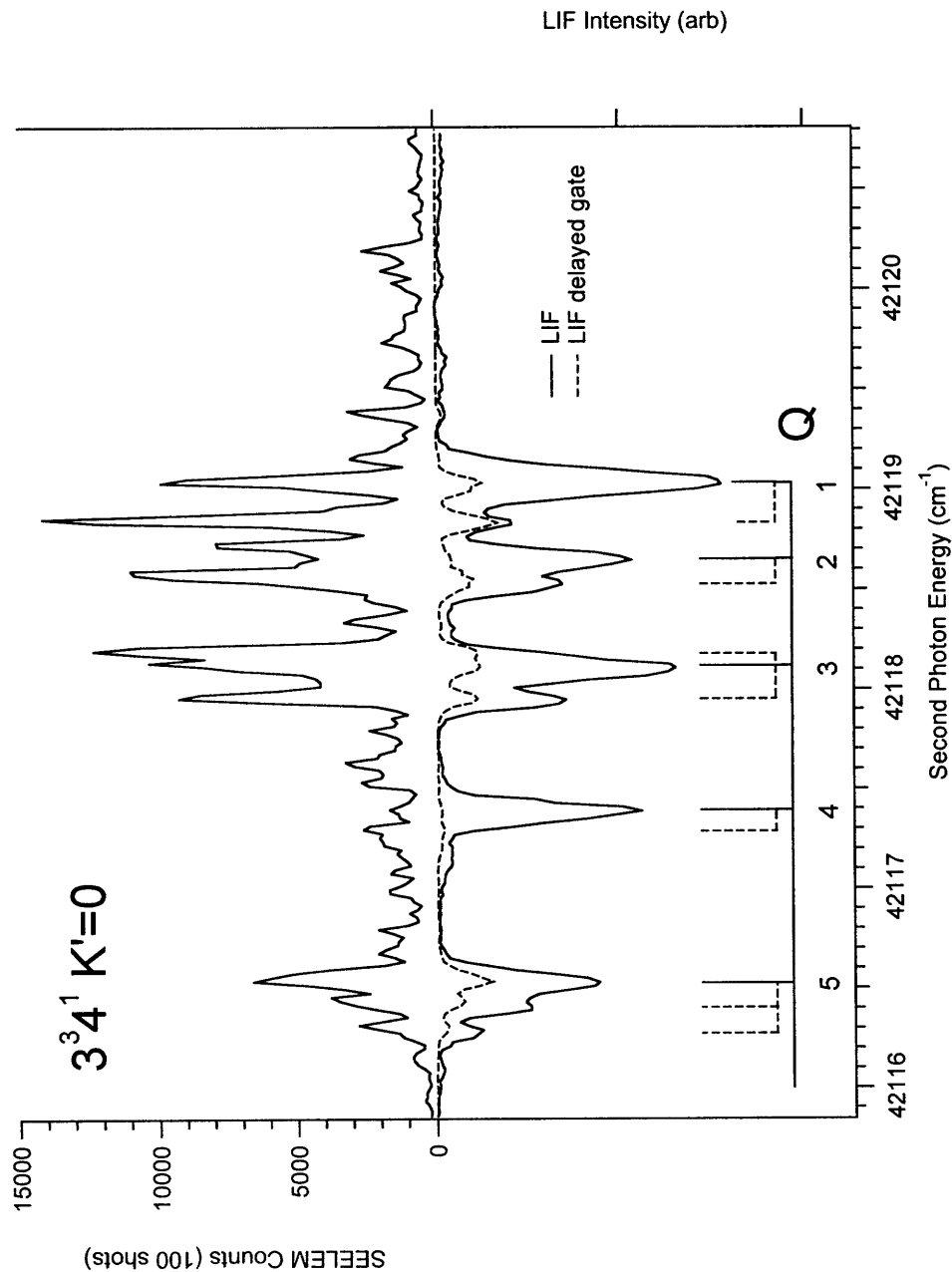
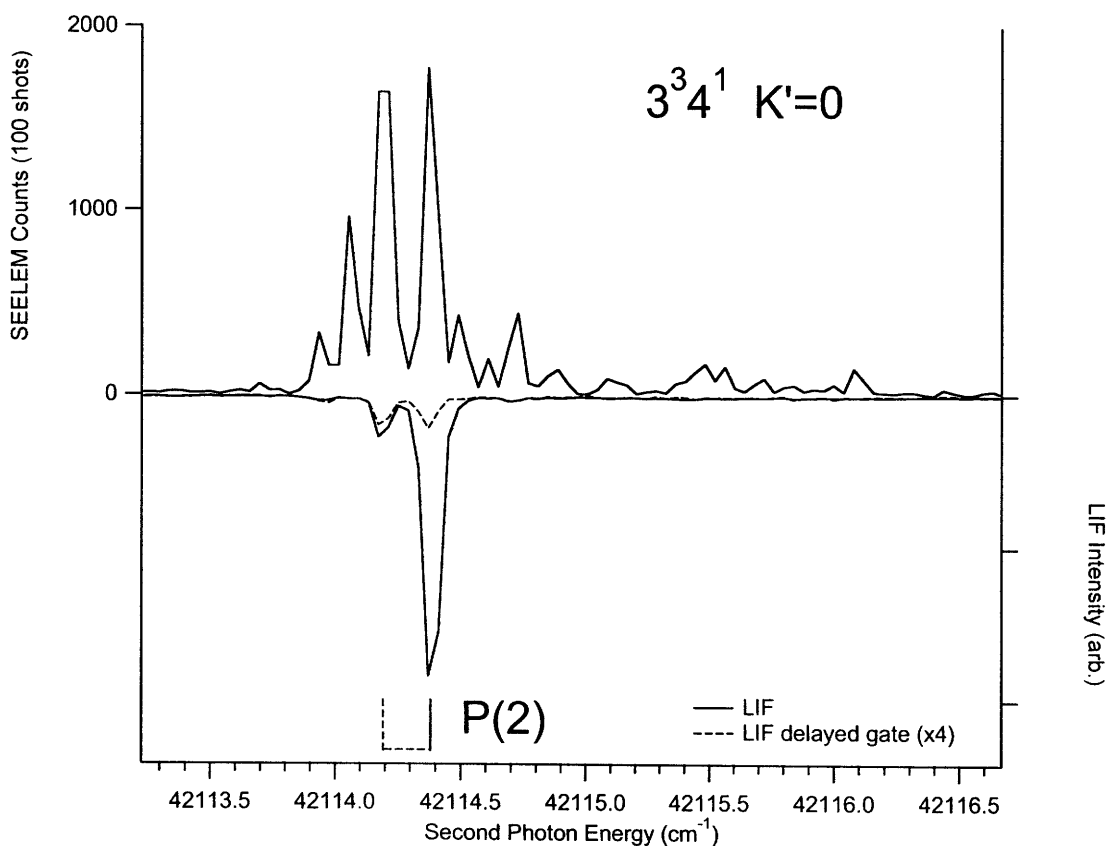


Figure 5-11: Simultaneously recorded SEELEM (upper trace) and LIF (lower trace) spectra of the $3^3 4^1 K'=0$ sublevel of the $\tilde{A}^1 A_u$ state of C_2H_2 . The P(3) line of the $\tilde{X}^1 \Sigma_g^+ v_3'' + v_4''$ level is used as an intermediate state in the experiment, so only the P(2) line is observed into the upper state, according to Figure 5-1. The LIF spectrum is integrated in two time regions: an early time window ($0.5\tau_s - 2\tau_s$, solid trace) and a delayed time window ($10\tau_s - 18\tau_s$, dashed trace). A line splitting of -0.2 cm^{-1} is observed in the delayed fluorescence, confirming the assignment of the low-energy component as $J' = 1$.



model for acetylene, mixing between S_1 levels and the manifold of $T_{1,2}$ triplet levels is mediated by specific vibrational levels of the T_3 electronic state [41, 39, 37, 55, 4, 85]. The average vibrational level spacing of T_3 is on the order of 10 cm^{-1} , similar to that of S_1 [122]. In the majority of cases, the T_3 levels, which mediate $S_1 \sim T_{1,2}$ mixing, do not appear in the spectrum of an S_1 transition. However, a spectrum may still contain signatures of remote T_3 doorway levels ($S_1 \sim T_3$ energy separation greater than 2 cm^{-1}), primarily as a result of the J' -dependence of $S_1 \sim T_3$ energy denominators. Four examples of this behavior are discussed in Chapter 4.

An analysis of the early vs. delayed LIF spectrum is our primary tool for characterizing such distant doorway states. In Chapter 4.3, it was shown that a remote T_3 doorway level may give rise to a dependence of the LIF center of gravity,

$$E_{\text{ave}} = \int E \times I_t(E) dE, \quad (5.1)$$

on time delay, t . This effect results from drastically shorter fluorescence lifetime for the nominal S_1 eigenstate relative to the cluster of nearby, nominally triplet eigenstates. The contrast in fluorescence lifetimes leads to changes in relative fluorescence intensity from different eigenstates as a function of time: at early times, the center of gravity is dominated by the nominal S_1 state, while at longer delay times, the center of gravity is dominated by nominally triplet eigenstates. However, if the nominal S_1 eigenstate acquires more triplet character, the contrast in fluorescence lifetimes is reduced, decreasing the rate of change in center of gravity vs. time delay.

The relatively large line splittings observed in the spectrum of $3^36^1 K'=0$ and $3^34^1 K'=0$ levels indicate that nominal S_1 eigenstates in these levels are appreciably singlet-triplet mixed. To make matters more complicated, the LIF spectra in this experiment suffer from some saturation of the fluorescence signal at early time delays, when the relative fluorescence intensity of the nominal S_1 state is at a maximum. We are thus precluded from using the center of gravity vs. time as a diagnostic of the relative T_3 doorway energy, as we were able to do with the spectrum of $3^3 K'=2$, Chapter 4.5.4.

We rely, instead, on the positions and relative intensities of resolved, long-lifetime lines as indicators of the relative T_3 doorway state energy. In the spectrum of $3^3 4^1 K'=0$, all long-lived components are *redshifted* from the energy of the nominal S_1 state, with one exception. The exception, occurring in the Q(3) transition, warrants further examination. The two observed line splittings, indicated in Figure 5-10 by dashed frequency markers, have frequencies of approximately $+0.1$ and -0.2 cm^{-1} relative to the nominal S_1 state (solid frequency marker). The intensities of both nominal triplet components are roughly equivalent in the delayed LIF spectrum, indicating that the fractional S_1 character of both states is approximately equal.

The ratio of fractional S_1 character may be used to estimate the relative matrix elements for the two levels involved in the line splitting. Indirect mixing between S_1 and $T_{1,2}$ levels can be evaluated by working in a mixed $S_1 \sim T_3$ basis, described in Chapter 2.2.1. In the mixed basis, the $S_1 \sim T_3$ spin-orbit interaction is prediagonalized, resulting in a doorway-mixed S_1 state, $|\tilde{s}\rangle$, and an S_1 -mixed doorway state, $|\tilde{\ell}\rangle$. Following Chapter 2, the ratio of S_1 and T_3 amplitudes in $|\tilde{s}\rangle$ is determined by the mixing angle α between the pure S_1 basis state, $|s\rangle$, and the T_3 doorway, $|\ell\rangle$:

$$|\tilde{s}\rangle = (1 - \alpha^2)^{1/2} |s\rangle + \alpha |\ell\rangle. \quad (5.2)$$

The basis states are defined such that $\alpha^2 \leq 0.5$. The fractional S_1 character of a nominal $T_{1,2}$ eigenstate, $|m\rangle$, may be evaluated using perturbation theory:

$$\begin{aligned} |\langle m|s\rangle|^2 &= \alpha^2(1 - \alpha^2) H_{\ell m}^2 \left\{ \frac{1}{\Delta E_{m\tilde{s}}} + \frac{1}{\Delta E_{m\tilde{\ell}}} \right\}^2 \\ &\approx \alpha^2(1 - \alpha^2) H_{\ell m}^2 \frac{1}{\Delta E_{m\tilde{s}}^2}. \end{aligned} \quad (5.3)$$

The approximate expression applies to remote doorway states, where the energy separation $\Delta E_{m\tilde{s}}$ is much smaller than the energy separation $\Delta E_{m\tilde{\ell}}$.

Both triplet components observed in the vicinity of the Q(3) transition interact with the same mixed- S_1 basis state, so the s, ℓ mixing angle α is identical for both components, and $|\langle m|s\rangle|^2 \propto H_{\ell m}^2 / \Delta E_{m\tilde{s}}^2$. In Chapter 3 we showed that a doorway-

mediated effective Hamiltonian with one doorway state contains no interference pathways, and as a result, the phases of all matrix elements may be taken to be real and positive. According to this property, the relative magnitudes of the matrix elements, $H_{\ell m}$, for two triplet levels that appear in the delayed LIF spectrum of the same S_1 transition may be determined using the expression

$$H_{\ell m} \propto \sqrt{\Delta E_{m\bar{s}}^2 |\langle m|s\rangle|^2} \quad (5.4)$$

For the Q(3) transition of $3^3 4^1$ $K'=0$, the component that appears at lower frequency must have approximately twice the matrix element with the doorway state as the component that appears at higher frequency.

The pattern of line splittings is reversed in the delayed LIF spectrum of $3^3 6^1$ $K'=0$, shown in Figures 5-2–5-6 and Figure 5-9. For this sublevel, all observed line splittings in the delayed LIF spectrum are *blueshifted* from the frequency of the transition into the nominal S_1 state, with one exception. This exception occurs in the Q(1) transition, shown in Figure 5-2. Two additional lines are observed in the delayed LIF spectrum, at frequencies of approximately $+0.10$ and -0.18 cm^{-1} , relative to the frequency of the nominal S_1 eigenstate. The ratio of line intensities (blueshifted:redshifted) is approximately 2:1 in the delayed LIF spectrum, indicating that the fractional S_1 character of the higher frequency state is approximately twice as large as that of the lower frequency state. The ratio of matrix elements $H_{\ell m}$ may be determined in the same manner as previously. For this transition, the state that appears at higher frequency must have a matrix element with the doorway state approximately 0.78 times as large as that of the state that appears at lower frequency. With the one exception just outlined, we find that the long-lived states observed in the LIF spectrum of $3^3 6^1$ $K'=0$ are blueshifted relative to the nominal S_1 state energy.

The $S_1 \sim T_3$ mixing angle, α , is determined by the matrix element and energy separation between the bright state and the doorway state,

$$\alpha = \frac{H_{s\ell}}{\Delta E_{s\ell}}. \quad (5.5)$$

The matrix element, $H_{s\ell}$, can be estimated from the variance of the LIF spectrum. In Chapter 3, we showed that, for a doorway-mediated Hamiltonian, the variance of the integrated LIF spectrum,

$$\sigma^2 = \int (E - E_s)^2 \times I(E) dE, \quad (5.6)$$

is equal to the squared matrix element between the bright state and the doorway state. Consequently, the $S_1 \sim T_3$ matrix element may be determined by taking the square root of the variance,

$$H_{s\ell} = \sqrt{\sigma_{LIF}^2}, \quad (5.7)$$

under the condition that all LIF intensity supplied by the bright state is observed in the spectrum. When the doorway level is not observed in the spectrum, this condition is not met, but the variance of the LIF spectrum will certainly be smaller than the variance calculated when the doorway level is included. Therefore, in the event that the doorway is not observed in the spectrum, the variance of the LIF spectrum may be used as a *lower bound* estimate for $H_{s\ell}^2$.

The approximate lower bound for the matrix element, $H_{s\ell}$, was determined from the variance of each LIF transition, calculated from the integrated $(0.5\tau_s - 18\tau_s)$ LIF spectrum. Our results are summarized in Table 5.1. The average lower bound values of $H_{s\ell}$ for the $3^36^1 K'=0$ and $3^34^1 K'=0$ sublevels are on the order of 0.1 cm^{-1} . To make a comparison, the matrix element for the local T_3 doorway level ($\Delta E_{s\ell} < 0.3 \text{ cm}^{-1}$) observed in $S_1 3^3 K'=1$ was determined to be approximately 0.1 cm^{-1} [85]. However, no local doorway state is observed in the $3^36^1 K'=0$ and $3^34^1 K'=0$ sublevels, so $\Delta E_{s\ell} > 2 \text{ cm}^{-1}$. This indicates that the $S_1 \sim T_3$ matrix elements for the $3^36^1 K'=0$ and $3^34^1 K'=0$ sublevels must be larger than that observed for the $3^3 K'=1$ sublevel.

The observed patterns of splitting indicate that, if the local singlet-triplet mixing is mediated by a non-local T_3 doorway, the relative energy of the doorway is likely to be positive for the $3^36^1 K'=0$ sublevel and negative for the $3^34^1 K'=0$ sublevel. This places both T_3 doorway states at a total energy between 45937.8 cm^{-1} and 46017.57

Table 5.1: Variance of the integrated LIF spectrum for each transition observed in the S_1 3^34^1 $K'=0$ and 3^36^1 $K'=0$ sublevels. The quantity $\sqrt{\sigma_{LIF}^2}$ is a lower bound for the $S_1 \sim T_3$ doorway matrix element, H_{sl} . Also shown is the time-integrated center of gravity for each transition, E_{ave} , as well as the integration region used in the analysis. All values are in units of cm^{-1} .

	E_{ave}	$\sqrt{\sigma_{LIF}^2}$	Integration region
3^36^1 $K'=0$			
P(1)	42038.24	0.097	42037.85–42038.60
Q(1)	42040.35	0.118	42039.50–42041.00
Q(2)	42039.84	0.089	42039.20–42040.50
Q(3)	42039.14	0.085	42038.50–42039.50
Q(4)	42038.15	0.083	42037.50–42038.80
Q(5)	42036.93	0.095	42036.50–42037.50
3^34^1 $K'=0$			
Q(1)	42118.99	0.106	42118.76–42119.29
Q(2)	42118.61	0.071	42118.36–42118.77
Q(3)	42118.09	0.088	42117.74–42118.33
Q(4)	42117.37	0.080	42117.00–42117.70
Q(5)	42116.49	0.094	42116.13–42116.80

cm^{-1} . The $3^3 4^1 K'=0$ and $3^3 6^1 K'=0$ sublevels are separated by about 80 cm^{-1} in total energy. The spin-orbit matrix element between either of these S_1 sublevels and a T_3 doorway state is on the order of 1 cm^{-1} . If $3^3 6^1 K'=0$ and $3^3 4^1 K'=0$ were to mix primarily with the same doorway state, the energy denominator would be at least 40 cm^{-1} , and the $S_1 \sim T_3$ mixing angle would be limited to $|\alpha| < 0.025$.

A brief discussion of selection rules for spin-orbit perturbations lends some insight as to the possible identity of candidate T_3 doorway levels. Selection rules for spin-orbit perturbations in polyatomic molecules are given by Stevens and Brand, and have been reformulated by other authors [115, 53, 40]. The total first-order spin-orbit matrix element between rovibrational states of S_1 and T_3 is the product of three factors: an electronic spin-orbit matrix element, a vibrational overlap factor, and a rotational factor arising from angular momentum coupling. Spin-orbit matrix elements follow the rotational selection rules $\Delta J = 0$ and $\Delta P = 0$, where P is the projection of J on the top axis (a -axis) of the molecule [52]. In Hund's case (b), the quantum number P is mixed among several states with different values of K , leading to the case (b) selection rule $\Delta K = 0, \pm 1$ [52, 115].

We express selection rules for spin-orbit perturbations in the molecular symmetry group of the T_3 state, C_2 , rather than the symmetry group of S_1 , C_{2h} . The correspondence between the C_{2h} and C_2 symmetry groups can be made by simply removing all g/u labels from C_{2h} irreducible representations. One potential complication arises, due to the possible reversal of the b and c inertial axes of a near-prolate top in C_2 symmetry. However, the vibration-rotation spin-orbit matrix elements are the same for both cases, because the symmetry axis of twofold rotation remains perpendicular to the inertial a -axis, regardless of the relative orientation of the b and c axes [52].

The three molecule-fixed spin functions, Γ_σ , transform as rotations in the molecular symmetry group [52, 115]. The symmetries of these functions, $\Gamma_\sigma(J_a)$, $\Gamma_\sigma(J_b)$, and $\Gamma_\sigma(J_c)$, determine the selection rules for ΔK . Mixing according to $\Delta K = 0$ is permitted when the vibronic symmetry of the S_1 and T_3 levels transforms as a rotation about the top axis (a -axis), ${}^{ev}\Gamma_S \times {}^{ev}\Gamma_T = \Gamma_\sigma(J_a)$ [115]. In the C_2 molecular symmetry group, a rotation about the a -axis is of species B [18].

Table 5.2: Spin-orbit perturbation selection rules between the S_1 3^34^1 , 3^36^1 vibrational levels and vibrational levels of the T_3 electronic state. Matrix elements for spin-orbit interaction may be nonzero when the vibronic symmetry of the singlet and triplet levels transforms as the appropriate molecule-fixed spin function, Γ_σ . When $\Delta K = 0$, singlet sublevels may only mix with T_3 sublevels of the same vibrational symmetry. The restriction is lifted when $\Delta K = 1$.

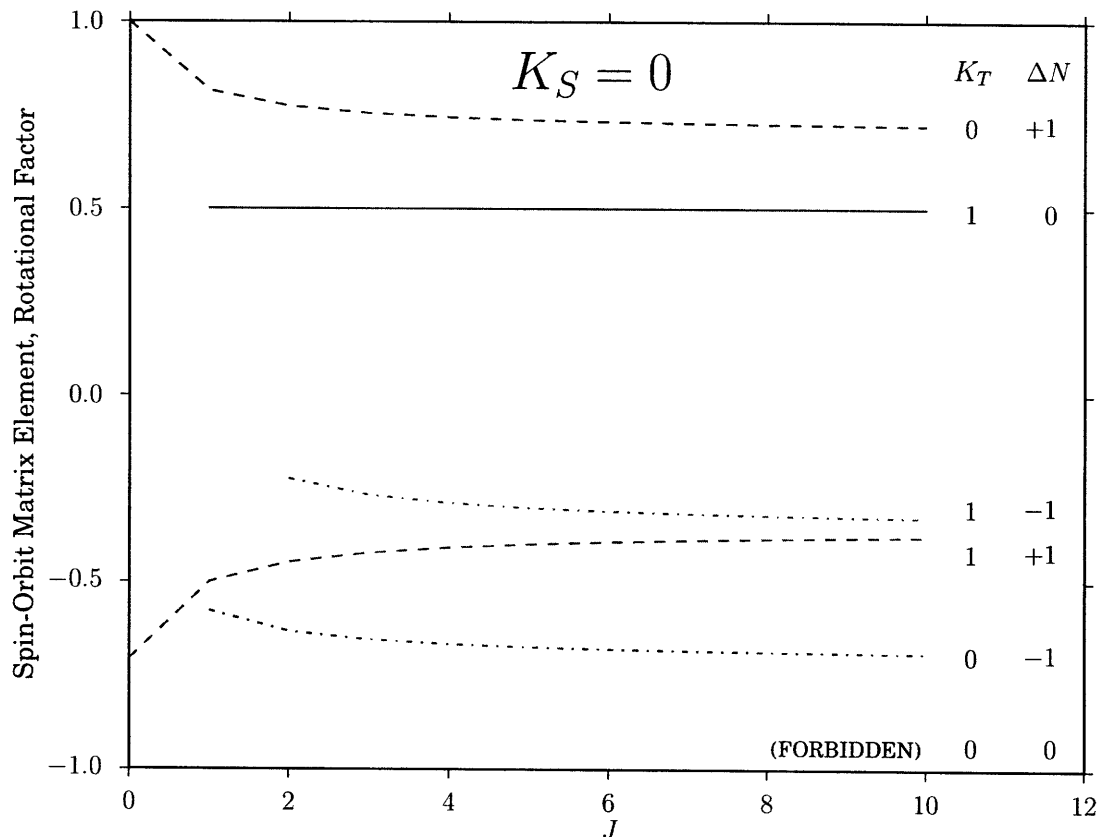
S_1 Level	${}^v\Gamma_S$	${}^{ev}\Gamma_S$	Γ_σ	ΔK	${}^v\Gamma_T$
3^36^1	b	1B	B	0	b
			A, B	± 1	a, b
3^34^1	a	1A	B	0	a
			A, B	± 1	a, b

C_2 symmetry, ${}^e\Gamma_T = {}^3B$

Taking into account the electronic symmetry of the T_3 state and the vibronic symmetry of the S_1 3^36^1 and 3^34^1 levels, the vibrational symmetry of an admixed T_3 sublevel may be inferred. Table 5.2 shows the relevant spin and vibronic symmetries necessary to determine the T_3 vibrational symmetry. We introduce the subscripted quantum numbers K_T and K_S to denote the value of K for the singlet (S_1) and triplet (T_3) vibronic sublevels of interest. A sublevel with $K_T = 0$ must have a vibrational symmetry of b to mix with S_1 3^36^1 $K_S = 0$. Conversely, to mix with S_1 3^34^1 $K_S = 0$, a $K_T = 0$ sublevel must have a vibrational symmetry of a . Therefore, a $K_T = 0$ sublevel may mix with either 3^36^1 and 3^34^1 $K_S = 0$, but not both. Mixing according to $\Delta K = 0$ is permitted when the vibronic symmetry of the S_1 and T_3 levels transforms as a rotation about the b or c axes, ${}^{ev}\Gamma_S \times {}^{ev}\Gamma_T \supset \Gamma_\sigma(J_b)$ or $\Gamma_\sigma(J_c)$ [115]. Thus, a $K_T = 1$ vibrational sublevel of any symmetry may mix with a $K_S = 0$ sublevel of any symmetry.

The rotational factors for spin-orbit matrix elements are approximately independent of J' . However, as discussed in Chapter 4, the relative phases of rotational factors between two sublevels of the same vibrational level may result in interference effects. Figure 5-12 shows the magnitudes and relative phases of the rotational factors for spin-orbit matrix elements. The energy separation between $K_T = 0$ and $K_T = 1$ sublevels of the same T_3 vibrational level is on the order of 15–20 cm^{-1} [122]. The

Figure 5-12: Rotational factors of spin-orbit matrix elements between rovibrational levels of the S_1 and T_3 electronic states, where $K_S=0$. A $K_S=0$ level may mix with T_3 levels with $K_T = 0, 1$. Spin orbit perturbations are forbidden according to parity when $\Delta K = \Delta N = 0$.



total spin-orbit matrix element between vibrational levels of S_1 and T_3 may be as large as approximately 1 cm^{-1} [122]. To mix appreciably with both $K_T = 0$ and 1 sublevels of the same T_3 vibration, a sublevel of S_1 must have a total energy which is midway between the $K' = 0$ and $K' = 1$ triplet sublevels.

The nonzero rotational factors for spin-orbit matrix elements are illustrated on energy level diagrams in Figure 5-13 for $K_T = 0$ sublevels, and in Figure 5-14 for $K_T = 1$ sublevels. Figure 5-13 shows that the 3^36^1 and 3^34^1 $K_S = 0$ sublevels may only mix with $K_T = 0$ sublevels of the same vibrational symmetry. Mixing with the F_2 component of a $K_T = 0$ sublevel is forbidden, because the triplet rotational level is of opposite parity. Figure 5-14 illustrates that triplet sublevels with $K_T = 1$ contain

Table 5.3: The vibrational normal modes of the S_1 and T_3 electronic states. The mode number of the torsional mode is changed in T_3 relative to S_1 , because g/u symmetry operations are not present in the C_2 molecular symmetry group of T_3 .

S_1	
ν_1 (a_g)	symmetric CH stretch
ν_2 (a_g)	CC stretch
ν_3 (a_g)	<i>trans</i> -bend
ν_4 (a_u)	torsion
ν_5 (b_u)	antisymmetric CH stretch
ν_6 (b_u)	<i>cis</i> -bend
T_3	
ν_1 (a)	symmetric CH stretch
ν_2 (a)	torsion
ν_3 (a)	CC stretch
ν_4 (a)	<i>trans</i> -bend
ν_5 (b)	antisymmetric CH stretch
ν_6 (b)	<i>cis</i> -bend

levels of both parities for each value of J and N , therefore spin-rotation levels of both parities are available for mixing with a $K_S = 0$ singlet rotational level.

Having surveyed the vibronic symmetry restrictions and rotational selection rules for spin-orbit perturbations, we investigate the propensities of vibrational overlap integrals between vibrational levels of S_1 and T_3 . Harmonic frequencies for the T_3 electronic surface have been reported by Bryan Wong, who carried out a high-level *ab initio* calculation of the S_1 and T_3 electronic surfaces [136]. A significant challenge in that work was the diabatization of the T_2 and T_3 electronic surfaces along two strongly coupled modes, the antisymmetric CH stretch and the *cis*-bend [122]. The vibrational modes of S_1 and T_3 are numbered differently, since the equilibrium geometry of the T_3 electronic state has C_2 symmetry. The vibrations of both electronic states are identified in Table 5.3. The frequency of the T_3 torsional vibration, ν_2 , is twice as large as the corresponding S_1 vibration, ν_4 . Conversely, the frequencies of the T_3 *trans* and *cis*-bending vibrations, ν_4 and ν_6 , are significantly smaller than those in S_1 .

Using the results of this *ab initio* calculation, Thom and coworkers reported vibra-

Figure 5-13: Diagram of spin-orbit rotational selection rules between the S_1 $3^3 4^1$, $3^3 6^1$ $K'=0$ sublevels and T_3 sublevels with $K_T = 0$. When $K_T = K_S = 0$, each singlet sublevel may only mix with zero-order triplet sublevels of the same vibrational symmetry.

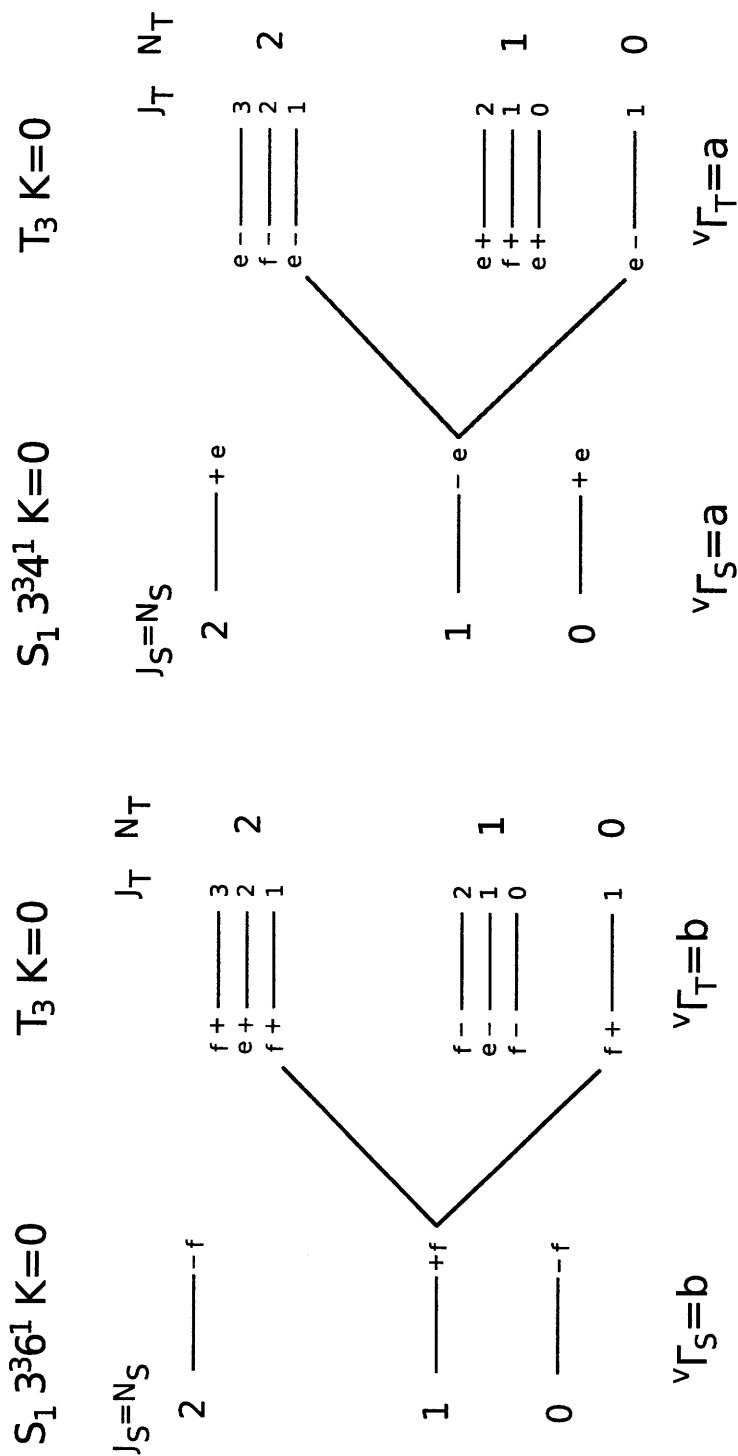
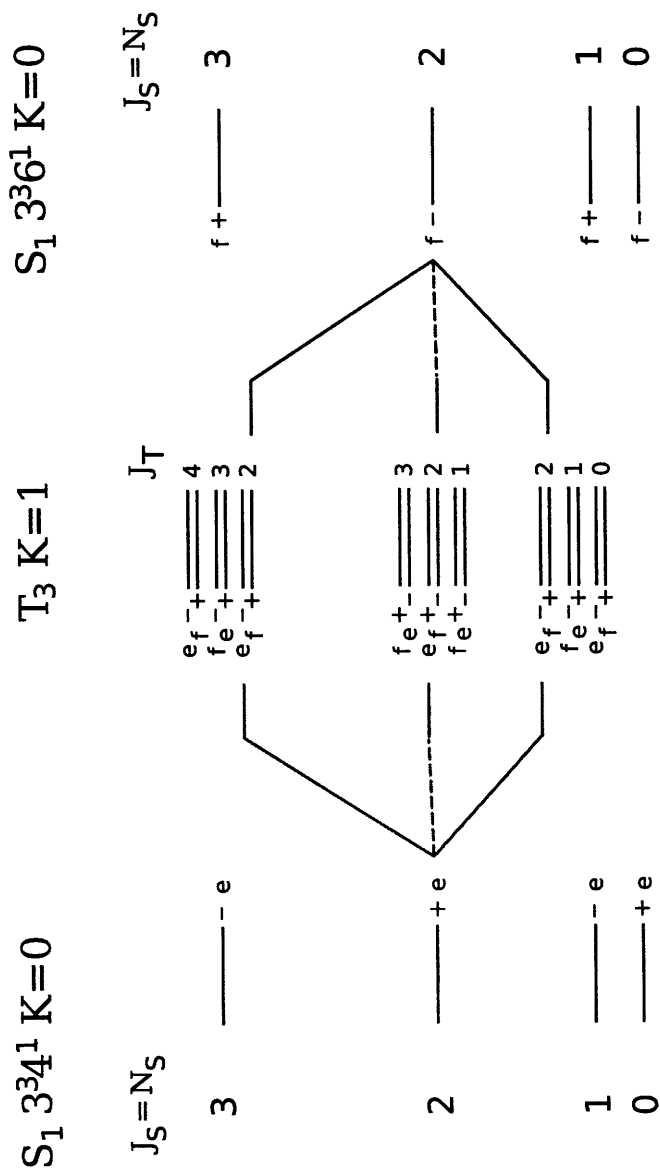


Figure 5-14: Diagram of spin-orbit rotational selection rules between the S_1 $3^3 4^1$, $3^3 6^1$ $K'=0$ sublevels and T_3 sublevels with $K_T = 1$. In this case, the singlet sublevels are permitted to mix with a zero-order triplet sublevel of any vibrational symmetry.



tional overlap integrals between $S_1\ 3\nu_3$ and nearby levels of T_3 [122]. The harmonic approximation of Sharp and Rosenstock was used to calculate the overlap integrals, which is sufficiently accurate to give a general idea of the magnitude of vibrational overlap [104]. Using the programs published by Bryan Wong in his thesis, we have carried out an identical calculation for the $S_1\ 3\nu_3 + \nu_4$ and $3\nu_3 + \nu_6$ levels [136]. Our results are summarized in Tables 5.4 and 5.5.

For both S_1 levels, we find at least one vibrational level of T_3 within 300 cm^{-1} that has an extremely large (~ 0.1) overlap integral. When levels with the largest absolute overlap integrals are considered, we observe that both the T_3 *trans*-bending vibration (ν_4) and torsional vibration (ν_2) are observed to promote vibrational overlap with $S_1\ 3\nu_3 + \nu_4$. For $S_1\ 3\nu_3 + \nu_6$, the T_3 levels with the five largest absolute vibrational overlap integrals contain quanta in both the *trans* and *cis*-bending vibrations (ν_4 and ν_6).

Although specific T_3 doorway levels cannot be identified from our spectra, the relative energy of T_3 doorways is determined from line splittings that appear in the delayed LIF spectra of $S_1\ 3^36^1\ K'=0$ and $3^34^1\ K'=0$. The magnitudes of the spin-orbit matrix element between the S_1 level and the doorway level are estimated from the variance of the LIF spectrum. Additionally, the allowed vibrational symmetries of T_3 doorway states are discussed above in terms of spin-orbit selection rules for ΔK . To investigate the possible identity of T_3 doorway levels, we use the previously reported programs of Bryan Wong to calculate vibrational overlap integrals. The vibrational overlap integral calculations indicate that the T_3 *trans*-bending vibration (ν_4) and torsional vibration (ν_2) both separately have a propensity to increase vibrational overlap with $S_1\ 3\nu_3 + \nu_4$, while a combination of the T_3 *trans* and *cis*-bending (ν_6) vibrations is observed to increase vibrational overlap with $S_1\ 3\nu_3 + \nu_6$.

Table 5.4: Calculated vibrational overlap integrals between S_1 $3v_3 + v_4$ and levels of diabaticized T_3 within an energy separation of 300 cm^{-1} . The energies and vibrational overlap integrals are calculated in the harmonic approximation, according to the methods outlined by Thom and coworkers [122]. Integrals with an absolute magnitude of less than 1×10^{-6} are not shown, including those that are zero by symmetry. The five vibrational levels of T_3 with the largest absolute vibrational overlap integrals are marked with a (\triangleright). One T_3 level, containing 6 quanta of the *trans*-bending vibration (ν_4), is calculated to have an extremely large vibrational overlap integral (~ 0.1) with S_1 $3v_3 + v_4$. Overall, the T_3 *trans*-bending vibration and torsional vibration (ν_2) are observed to promote vibrational overlap. The mean and median of the absolute values of the T_3 vibrational overlap integrals for S_1 $3v_3 + v_4$ are shown below the table.

T_3 vibrational level	$E - E(S_1 \ 3v_3 + v_4)$ (cm^{-1})	Overlap integral
$v_1 + v_4$	-294	0.0022
\triangleright $2v_2 + v_4$	-267	0.037
\triangleright $6v_4$	-255	0.12
$10v_6$	-198	-0.0002
$v_2 + 6v_6$	-161	-0.0002
$v_1 + 2v_6$	-152	0.0002
$v_3 + 4v_4$	-149	-0.027
$2v_2 + 2v_6$	-124	0.0032
$5v_4 + 2v_6$	-113	0.011
$v_4 + v_5 + v_6$	-86	-0.014
$2v_3 + 2v_4$	-43	-0.025
$v_3 + 3v_4 + 2v_6$	-7	0.0081
\triangleright $4v_4 + 4v_6$	29	-0.028
$v_5 + 3v_6$	56	-0.0021
$3v_3$	62	-0.0013
\triangleright $v_2 + 4v_4$	66	0.080
$2v_3 + v_4 + 2v_6$	99	-0.0047
$v_3 + 2v_4 + 4v_6$	135	-0.0025
$3v_4 + 6v_6$	171	0.0059
\triangleright $v_2 + v_3 + 2v_4$	172	0.056
$v_2 + 3v_4 + 2v_6$	208	-0.023
$2v_3 + 4v_6$	241	-0.0004
$v_3 + v_4 + 6v_6$	277	-0.0004
$v_2 + 2v_3$	277	0.0047
Mean overlap integral (abs. val.):		0.019
Median overlap integral (abs. val.):		0.0053

Table 5.5: Calculated vibrational overlap integrals between S_1 $3v_3 + v_6$ and levels of diabaticized T_3 within an energy separation of 300 cm^{-1} . The energies and vibrational overlap integrals are calculated in the harmonic approximation, according to the methods outlined by Thom and coworkers [122]. Integrals with an absolute magnitude of less than 1×10^{-6} are not shown, including those that are zero by symmetry. The five vibrational levels of T_3 with the largest absolute vibrational overlap integrals are marked with a (\triangleright). One T_3 level, containing 3 quanta of the *trans*-bending vibration (ν_4) and one quantum of the *cis*-bending vibration (ν_6), is calculated to have an extremely large vibrational overlap integral (~ 0.2) with S_1 $3v_3 + v_6$. All five T_3 levels with the largest absolute vibrational overlap factors contain a combination of the T_3 *trans* and *cis*-bending vibrations (ν_4 and ν_6). The mean and median of the absolute values of the vibrational overlap integrals for S_1 $3v_3 + v_6$ are larger than those for S_1 $3v_3 + v_4$ by less than a factor of two.

T_3 vibrational level	$E - E(S_1 \ 3v_3 + v_6)$ (cm^{-1})	Overlap integral
\triangleright $v_2 + 3v_4 + v_6$	-281	-0.21
$2v_3 + 3v_6$	-248	0.0007
$v_3 + v_4 + 5v_6$	-212	0.0085
$2v_4 + 7v_6$	-175	0.010
$v_2 + v_3 + v_4 + v_6$	-175	-0.040
$v_2 + 2v_4 + 3v_6$	-139	-0.039
$v_3 + 7v_6$	-69	0.0007
$v_4 + 9v_6$	-33	0.0039
$v_2 + v_3 + 3v_6$	-33	-0.0025
$v_2 + v_4 + 5v_6$	3	-0.017
$v_1 + v_4 + v_6$	12	-0.0039
\triangleright $2v_2 + v_4 + v_6$	40	0.057
\triangleright $6v_4 + v_6$	52	-0.084
$2v_4 + v_5$	78	-0.027
$11v_6$	109	0.0005
$v_2 + 7v_6$	146	-0.0015
$v_1 + 3v_6$	154	-0.0006
\triangleright $v_3 + 4v_4 + v_6$	157	0.090
$2v_2 + 3v_6$	182	0.0040
$v_3 + v_5$	184	-0.0018
$5v_4 + 3v_6$	194	0.0095
$v_4 + v_5 + 2v_6$	220	0.0085
$2v_3 + 2v_4 + v_6$	263	-0.0061
\triangleright $v_3 + 3v_4 + 3v_6$	299	-0.051
	Mean overlap integral (abs. val.):	0.028
	Median overlap integral (abs. val.):	0.0085

5.4.2 SEELEM Spectrum:

Characterization of the local manifold of $T_{1,2}$ levels

The SEELEM spectrum shows the distribution of nominal $T_{1,2}$ eigenstates that have approximately 0.25% fractional S_1 character. This specificity in SEELEM detection probability, discussed in Chapter 4.3.1, arises from the competing effects of excitation probability, electron ejection probability and survival probability. When the T_3 doorway level is energetically distant ($\Delta E > 1 \text{ cm}^{-1}$), the envelope of SEELEM-detectable states is not expected to exhibit large interference effects, as observed in S_1 3^3 $K'=1$. Interference effects in the SEELEM spectrum result from a cross term in the equation for SEELEM detection probability, described in Chapter 2.3.3.

Levels of the T_1 and T_2 electronic states are observed to be extensively mixed in this energy region, evidenced by the widely varying Landé g -factors observed in Zeeman Anticrossing (ZAC) spectra [39]. (Although many of the states observed in the ZAC experiments are nominally S_0 , the authors rule out extensive $S_0 \sim T_{1,2}$ mixing as the underlying cause for the widely varying g -factors. Such mixing would cause the average g -factor to be approximately zero as discussed in Section 5.1 of [39].)

We adopt a simple model, based on the classic work of Bixon and Jortner, to address $T_3 \sim T_{1,2}$ mixing [11]. Mixing between a bright state and an ensemble of equally spaced dark states with identical matrix elements results in a Lorentzian distribution of fractional bright state character, α^2 . The full width at half maximum of the distribution is

$$\Gamma = 2\pi v^2 \rho_m, \quad (5.8)$$

where v is the bright~dark matrix element (held constant in the model), and ρ_m is the density of dark states. Since the S_1 level is only indirectly coupled to the manifold of $T_{1,2}$ levels, the parameter v in equation 5.8 must be related to the matrix elements of a doorway-mediated effective Hamiltonian. In equation 5.3, it can be seen that the effective squared matrix element between a $T_{1,2}$ level and the S_1 level is $\alpha^2(1-\alpha^2)H_{\ell m}^2$. When $\alpha < 0.25$, the product $\alpha^2(1-\alpha^2) \approx \alpha^2$. The Lorentzian parameter v is thus

related to the doorway-mediated Hamiltonian model as $v^2 \approx \alpha^2 H_{\ell m}^2$.

Another challenge is that the SEELEM signal is not proportional to fractional bright state character. The SEELEM detection probability is a function of fractional S_1 and T_3 character, and includes factors for laser excitation, survival probability, and electron ejection probability [55]. In Chapter 2, we showed that if the doorway state is remote ($\Delta E_{se} > 2 \text{ cm}^{-1}$), the fractional T_3 character follows an approximate proportionality to the fractional S_1 character. Under these circumstances, the SEELEM intensity equation simplifies to

$$P_{\text{SEELEM}} \propto a^4 \times \exp(-R a^2), \quad (5.9)$$

where R is the ratio of the SEELEM detector flight time (309 μs) to the fluorescence lifetime of the S_1 electronic state (270 ns), approximately equal to 1144 in this study. The factor of a^4 is the product of laser excitation and electron ejection probabilities, and the exponential factor represents the probability that a molecule will not fluoresce before arriving at the SEELEM detector surface (see Chapter 2, Section 3). The combination of the two factors results in a maximum of SEELEM detection probability when the fractional S_1 character is approximately $2/R_m \approx 0.0017$, less than one percent.

On the outer edge of the SEELEM intensity distribution, we assume that the fractional S_1 character of the SEELEM-detectable eigenstates approaches zero. In this limit, the SEELEM detection probability is dominated by the polynomial factor, and is proportional to the fractional bright state character squared. Surprisingly, this causes a *narrowing* effect on the outer edge of the SEELEM intensity distribution, relative to the Lorentzian distribution of fractional bright state character. The fundamental cause of this effect is the sampling of a non-time-integrated intensity. Because the SEELEM detector samples the population of metastable molecules only at a particular time, the normalization conditions for conservation of fractional bright state character result in a squared Lorentzian distribution. The full width of a squared Lorentzian distribution is approximately 0.64 times the full width of a

standard Lorentzian.

The SEELEM spectra recorded with the individual line method were fit to Lorentzian envelopes. To carry out the fit, the SEELEM spectrum was first smoothed to approximately twice the average level spacing, using a Hamming window function for convolution. A Lorentzian profile was fit to the smoothed spectrum using a non-linear least-squares regression. Figure 5-15 shows the best-fit Lorentzian profiles obtained for the $J' = 1 - 5$ rotational levels of $3^3 6^1 K'=0$. The Lorentzian FWHM, Γ , varies between 0.39 and 0.59 cm^{-1} . From these values, the product $v^2 \rho_m$ is determined to be approximately $\Gamma/(2\pi) \approx 0.078 \text{ cm}^{-1}$.

The density of states is determined by direct count. The simple formula

$$\rho_m = \frac{n}{\Delta E} \quad (5.10)$$

was used, where n is the number of lines in the SEELEM spectrum, and ΔE is the energy difference between the lowest and highest energy line. Lines in the SEELEM spectrum were identified simply by finding local maxima. State densities for the spectra in Figure 5-15 are listed in Table 5.6. It is likely that a direct count underestimates the number of nominal $T_{1,2}$ eigenstates, since the incoherent laser linewidth is only a factor of three smaller than the average line spacing. Drabbels and co-workers reported density of states measurements for the $3^3 K'=1$ sublevel using a high-resolution (18 MHz) laser [34]. Their estimates, spanning a smaller frequency range, exceed our observation by a factor of 1 to 4 times.

From the density of states measurement, we may estimate the parameter $v^2 \approx (0.0134 \text{ cm}^{-1})^2$. Following the relation $v^2 \approx \alpha^2 H_{\ell m}^2$, we estimate the product $\alpha H_{\ell m}$ as 0.116 cm^{-1} . The final formula for this important molecular property, according to the simple model, is

$$\alpha H_{\ell m} = \sqrt{\frac{\Gamma}{f 2\pi \rho_m}}, \quad (5.11)$$

where f is a factor describing the change in the width of the intensity distribution resulting from a non-time-integrated measurement, described above. According to

Table 5.6: Estimation of the product $\alpha H_{\ell m}$ from the SEELEM spectra of five transitions in S_1 3^36^1 $K'=0$. The quantity α represents the $S_1 \sim T_3$ mixing angle in a single doorway-mediated effective Hamiltonian, and the $H_{\ell m}$ represents the doorway $\sim T_{1,2}$ matrix element (held constant) in a simple statistical coupling model. The fitted Lorentzian width for the SEELEM spectrum, Γ_{SEELEM} , and the directly-counted density of $T_{1,2}$ states, ρ_m , are used to determine $\alpha H_{\ell m}$.

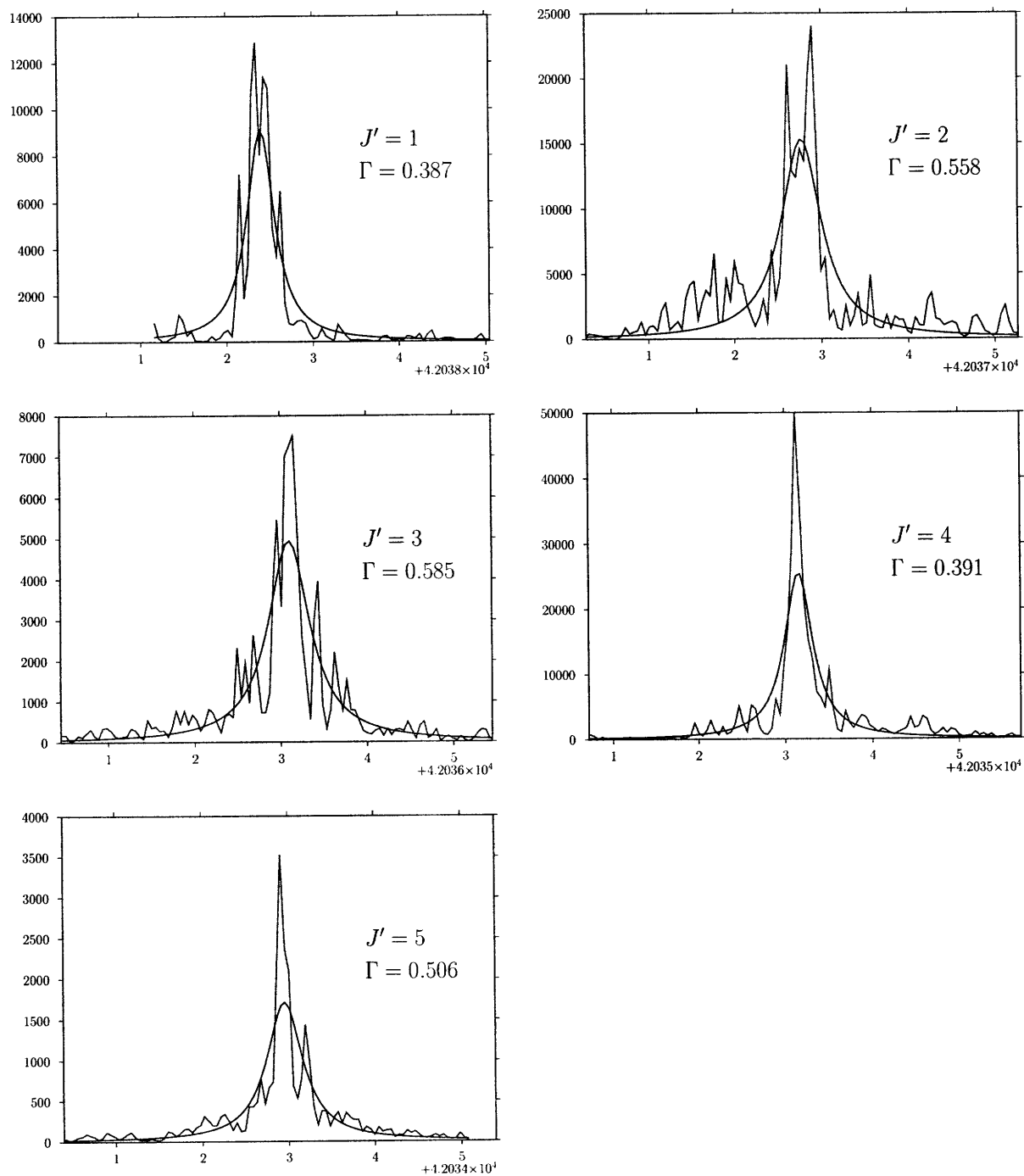
Transition	Γ_{SEELEM} (cm ⁻¹)	ρ_m (states / cm ⁻¹)	$\alpha H_{\ell m}$ (cm ⁻¹)
Q(1)	0.387	5.66	0.104
Q(2)	0.558	5.66	0.125
Q(3)	0.585	6.24	0.122
Q(4)	0.391	5.66	0.105
Q(5)	0.506	5.93	0.116
	0.49(8)	5.8(2)	0.114(8)

this formula, a possible underestimation of the state density would cause the estimate of $\alpha H_{\ell m}$ to be larger than the true value. Potential narrowing effects caused by the sampling a non-time-integrated spectrum would cause the estimate of $\alpha H_{\ell m}$ to be slightly smaller than its true value. Our estimates of $\alpha H_{\ell m}$ are shown in Table 5.6, for the five transitions in 3^36^1 $K'=1$ recorded via the individual line method.

To further examine the properties of the local manifold of nominal $T_{1,2}$ eigenstates, a modified reduced term value plot is prepared for the 3^36^1 $K'=0$ level of S_1 acetylene. To construct this plot, S_1 basis state rotational energies were approximated from the intensity-weighted center of gravity of the early LIF spectrum. The total energy of each state was reduced by an approximate rotational term energy, $1.04J'(J'+1)$. The resultant S_1 rotational energies are shown as large square markers in Figure 5-16. The energies of nominal triplet $T_{1,2}$ levels observed in the SEELEM spectrum are shown in the plot with small markers.

For each SEELEM transition, a horizontal bar denotes the approximate magnitude of the matrix element $H_{\ell m}$, according to equation 5.4. The total magnitude of the horizontal bars is normalized separately at each value of J' . The energy spacing and matrix elements show a remarkable uniformity, in agreement with our proposed simple model for the $T_3 \sim T_{1,2}$ interactions. The conclusions drawn from such a figure

Figure 5-15: Lorentzian fitting results for the $J' = 1 - 5$ SEELEM spectra of the $3^36^1 K'=0$ sublevel. The parameter Γ , equal to the half-width at half-maximum of the distribution, is proportional to the product of the $S_1 \sim T_3$ mixing angle and the average $T_3 \sim T_{1,2}$ matrix element. The value of Γ is given in units of cm^{-1} .

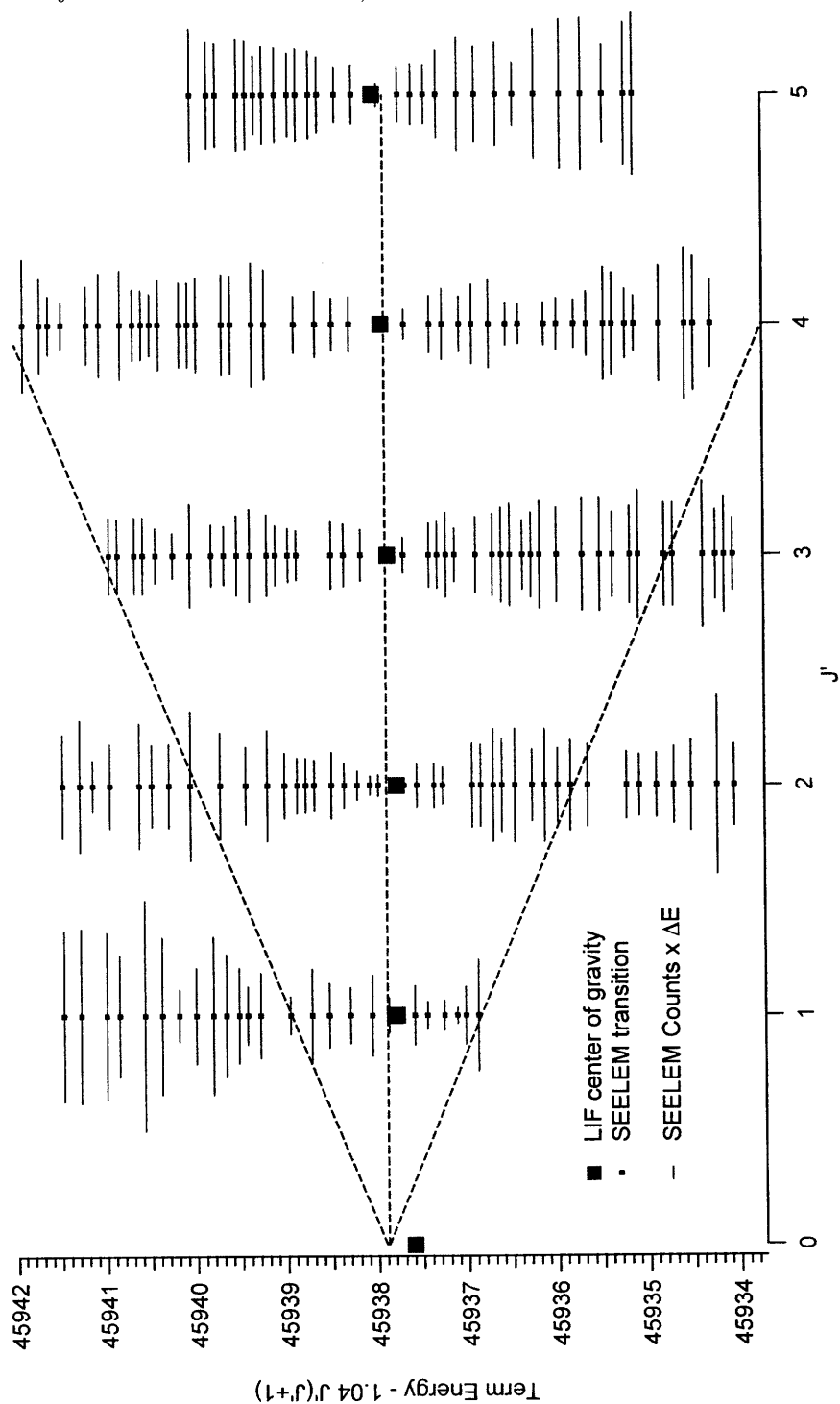


should be treated with caution, however, because nominal $T_{1,2}$ states with small matrix elements may be obscured by others with strong intensity in the SEELEM spectrum. Without a better idea of the intrinsic $T_3 \sim T_{1,2}$ dynamics, we have no way of knowing what lurks beneath the lines in our SEELEM spectra.

Three dotted lines are superimposed on the figure to serve as guides for the approximate rotational energy dependence of the three spin components F_1 , F_2 , and F_3 . The reduced term energies of the three triplet components have slopes of approximately $-2B$, 0 , and $+2B$ when plotted against J' (not $J'(J'+1)$). For a $K_T = 1$ sublevel, any of the three components may appear, while for a $K_T = 0$ sublevel, spin-orbit mixing is allowed only with the F_1 or F_3 components. The absence of any apparent rotational structure in the ensemble of SEELEM-detectable states justifies our statistical treatment of $T_3 \sim T_{1,2}$ mixing. The reader is challenged to find any series of SEELEM detectable states that fit unambiguously to the slope of the dotted lines.

The observation of a $J' = 0$ rotational level in the spectrum of $3^3 6^1 K'=0$ affords us a unique opportunity to estimate the local triplet level density. For a triplet vibrational sublevel with $K_T = 0$ or 1 , only a single spin component, F_3 , is present to mix with a $J' = 0$ singlet. The vibrational symmetry of the triplet is restricted ($\Gamma_T = b$) when $K_T = 0$, but unrestricted when $K_T = 1$ ($\Gamma_T = a$ or b), thus we expect to observe that the ratio of $K_T = 1$ sublevels to $K_T = 0$ sublevels is 2:1. (If Coriolis-induced mixing is complete within the manifold of $T_{1,2}$ levels, the ratio becomes 1:1, and the state density is decreased by approximately 24%.) Over an energy range of approximately 5 cm^{-1} , we observe approximately 26 total lines in the SEELEM and LIF spectrum. Of these, one must be subtracted as the nominal S_1 bright state. The 25 lines that remain are partitioned among triplets with $K_T = 0$ and 1 . Counting only the expected fraction of those with $K_T = 1$, we are left with 16.6 levels over a range of 5 cm^{-1} , or an observed triplet level density of $\rho_{T_{1,2}} = 3.3 \text{ per cm}^{-1}$. The triplet level density inferred from this observation is in general agreement with the high-resolution results of Drabbels and coworkers, who inferred a level density of approximately 4.9 per cm^{-1} from the highly fractionated LIF spectrum of the $3^3 K'=1$ and $3^4 K'=1$

Figure 5-16: Modified reduced term value plot for the $3^36^1 K'=0$ level of S_1 acetylene. An approximate term energy $1.04 J'(J'+1)$ is subtracted from the total S_1 rotational energies (large markers) and the energies of nominal triplet eigenstates observed in the SEELEM spectrum (small markers). For each SEELEM-detectable state, a horizontal bar denotes the relative magnitude of the spin-orbit matrix element $H_{\ell m}$. The width of the horizontal bars is normalized separately for each value of J' . The energy spacing and matrix elements show a remarkable uniformity, which is expected from an extensively mixed manifold of $T_{1,2}$ levels.



sublevels [34]. In their observations, any of the three spin components of a triplet sublevel with either $K_T = 0, 1$ or 2 may appear in the spectrum. It is natural that their triplet level count should be slightly larger and somewhat more uncertain than ours.

5.5 Discussion

The SEELEM and LIF spectra of two acetylene S_1 sublevels, $3^36^1 K'=0$ and $3^34^1 K'=0$, are compared in order to address the effects of the non-symmetric bending vibrations, ν_4 and ν_6 , on $S_1 \sim T_3$ vibrational overlap integrals. The sublevel involving torsional motion, $3^34^1 K'=0$, is found to have triplet-induced line splittings on the same order of magnitude as the sublevel involving the antisymmetric in-plane bending motion, $3^36^1 K'=0$. This result is in contrast to other experimental observations involving the two motions, which have found perturbations only in levels involving ν_6 [87, 139]. A measurement of the spectral variance is used to place a lower bound on the $S_1 \sim T_3$ doorway state matrix element. A lower bound of approximately 0.1 cm^{-1} is obtained for both sublevels. To be consistent with the required energy separation of a distant doorway level from the singlet, the actual $S_1 \sim T_3$ matrix element must be larger than this lower bound.

To address the identity of T_3 vibrational sublevels responsible for mediating the $S_1 \sim T_{1,2}$ mixing, we considered the vibronic and rotational selection rules for spin-orbit perturbations in acetylene. A calculation of vibrational overlap integrals between S_1 and T_3 , based on recent *ab initio* calculations of the potential energy surfaces, reveals a propensity for particular vibrational modes of T_3 to promote overlap with S_1 $3\nu_3 + \nu_4$ and $3\nu_3 + \nu_6$. The T_3 *trans*-bending vibration (ν_4) and torsional vibration (ν_2) are found to increase vibrational overlap with S_1 $3\nu_3 + \nu_4$, while a combination of the T_3 *trans* and *cis*-bending (ν_6) vibrations is observed to increase vibrational overlap with S_1 $3\nu_3 + \nu_6$.

In terms of vibrational overlap and spin-orbit mixing, two questions must be addressed: where are the relevant stationary phase points at which the vibrational

overlap integrals accumulate, and are the electronic seams of intersection accessible at these points? We first consider the $S_1 \ 3\nu_3 + \nu_6$ level. It has been suggested in the literature that $S_1 \sim T_3$ vibrational overlap may accumulate at a half-linear turning point geometry [87]. Recent calculations carried out by Josh Baraban indicate that the $S_1 \ 3\nu_3 + \nu_6$ level has appreciable amplitude in this region of phase space, particularly in comparison to the $S_1 \ 3\nu_3$ level [8]. The calculation of vibrational overlap integrals indicates a similar picture for the diabaticized T_3 surface, where the critical half-linear geometry is accessible in a combination of the $T_3 \ trans$ (ν_4) and *cis*-bending (ν_6) vibrations. The calculations of Ventura and coworkers indicate that the seam of $S_1 \sim T_3$ intersection passes through the half-linear region of phase space at a CCH bending angle of approximately 140° (linear is 180° , see their figure 5b) [128]. We conclude that our explanation for the T_3 perturbations in $S_1 \ 3^3 6^1 \ K'=0$ is in accord with previous research.

The characterization of stationary phase points for the $S_1 \ 3\nu_3 + \nu_4$ level is more of a challenge. Calculated wavefunctions for S_1 are not available along the torsional coordinate. However, our calculations of T_3 vibrational overlap integrals support the general Franck-Condon argument that excitation in the $T_3 \ trans$ -bending vibration (ν_4) and torsional vibration (ν_2) increase the magnitude of vibrational overlap. However, the seam of $S_1 \sim T_3$ intersection is generally inaccessible along the torsional coordinate. The *ab initio* calculations of Ventura and coworkers predict that the $S_1 \sim T_3$ seam of intersection in the torsional coordinate occurs on the **opposite side** of the torsional well from S_1 (see their Figure 6), at angles between 90 and 140° [128]. The seam of intersection is most accessible along the torsional coordinate at near-linear geometries. It should also be noted that the seam of intersection is located at lower energies along the torsional coordinate.

One possible explanation for the observed mixing in $3^3 4^1 \ K'=0$ is that this sublevel gains T_3 character through *b*-axis Coriolis coupling with the $K'=1$ sublevel of $3^3 6^1 \ K'=1$. The $3^3 6^1 \ K'=1$ sublevel is known to be strongly perturbed by a level of T_3 . The matrix element for *b*-axis Coriolis interaction between $3^3 4^1 \ K'=0$ and $3^3 6^1 \ K'=1$ is approximately 1.4 cm^{-1} . The energy separation between the $3^3 4^1 \ K'=0$ level and

the $3^36^1 K'=1$ sublevel is approximately 42 cm^{-1} . This leads to a mixing angle of about 0.03. The observed splitting in $3^36^1 K'=1$ is approximately 1 cm^{-1} , indicating what is probably a local T_3 perturber with a matrix element of 0.5 cm^{-1} . Coriolis mixing with $3^36^1 K'=1$ would lead to a second-order spin-orbit interaction with the T_3 perturber on the order of $0.5 \times 0.03 = 0.015 \text{ cm}^{-1}$, which is not sufficient to satisfy the lower bound condition of 0.1 cm^{-1} for the $S_1 \sim T_3$ matrix element. The observed spin-orbit matrix element for $3^34^1 K'=0$ cannot be attributed to mixing with the $3^36^1 K'=1$ sublevel.

The technique of IR-UV double resonance excitation allows, in contrast to previous one-photon studies, the observation of the full SEELEM intensity envelope surrounding each rovibronic transition in an S_1 sublevel. The cluster of nominal $T_{1,2}$ eigenstates appearing in the spectrum is fit to a Lorentzian distribution, following a simple statistical coupling model. The product $\alpha H_{\ell m}$ is determined by the fit results to be on the order of 0.1 cm^{-1} .

One may ask: do we observe *too many* doorway states in the spectrum of C_2H_2 ? The answer lies in the definition of a doorway state, and is inherent to the doorway model. The doorway model is based on the more general tier model of energy levels [117, 118]. If the zeroth tier is the bright state, the S_1 sublevel assigned in the LIF spectrum, then the first tier contains all the vibrational sublevels of T_3 , and the second contains the sublevels of $T_{1,2}$. The tier model simplifies to the doorway model in the limit of small level density in the first tier. In this limit, the effect of energy denominators is to select, in most cases, one state of T_3 to dominate the mixing. However, there is nothing inherent to the model that prevents more than one doorway state from being active for a particular S_1 vibrational level. Our zero-order assumption of a single doorway is based only on a propensity that results from the effects of energy denominators and the local density of T_3 levels.

One of the stated goals of this research project has been to observe an acetylene T_3 level “in the wild,” that is, at an energy separation of more than 2 cm^{-1} from the S_1 level from which it borrows intensity. To date, this goal remains elusive. We speculate here on the prospects for direct observation of a lone T_3 level, in light of

our current results.

1. A T_3 doorway state is fractionated among the manifold of $T_{1,2}$ levels with a full width of $2\pi(1-\alpha^2)^2 H_{\ell m} \rho_m$. An accurate determination of the average $T_3 \sim T_{1,2}$ matrix element is therefore crucial for the estimation of this width.
2. The primary interaction for a distant T_3 doorway state is via the F_1 or F_3 spin components. The term energy of these components changes by approximately $\pm 2 \text{ cm}^{-1}$ per J' , causing consecutive rotational transitions to be widely spaced in frequency.

The prospect of recording weak, highly fractionated transitions over large frequency ranges seems daunting. An accurate estimate of the average $T_3 \sim T_{1,2}$ matrix element would allow the experimentalist an appropriate frequency step size to use in a search for a lone T_3 level. The average $T_3 \sim T_{1,2}$ matrix element also determines the maximum intensity of the transition to the T_3 level, since the peak intensity of a Lorentzian lineshape function is inversely proportional to the spectral width.

5.6 Conclusion

The SEELEM/LIF spectra of two acetylene S_1 sublevels, $3^36^1 K'=0$ and $3^34^1 K'=0$, are recorded in an IR-UV double resonance experiment. The spectra were analyzed in terms of a doorway model, where specific vibrational levels of the T_3 electronic state mediate $S_1 \sim T_{1,2}$ mixing. An analysis of the LIF spectrum indicates that the S_1 $3^36^1 K'=0$ and $3^34^1 K'=0$ sublevels are triplet-mixed to about the same degree. A calculation of vibrational overlap integrals, based on recent *ab initio* results, is in accord with this observation. A simple statistical mixing model is used in the analysis of the SEELEM spectrum for $3^36^1 K'=0$. The model allows us to determine the product of the $S_1 \sim T_3$ mixing angle and the $T_3 \sim T_{1,2}$ matrix element.

Chapter 6

A pulsed supersonic jet source of molecules in long-lived, electronically excited states

6.1 Introduction

It is our goal to develop a supersonic jet source of molecules in long-lived, electronically excited states. Although molecular triplet states are hard to populate optically, they are easily generated in collisions with other electronically excited species. Such methods are familiar to photochemists, who use the process of mercury photosensitization to create free radicals and other reactive species [17, 16, 26, 30, 98, 116]. A common technique is to place mercury and reactants in a heated reaction vessel, and irradiate with 254 nm light from a mercury resonance lamp [15].

The process of mercury photosensitization was used in the first and second experimental detections of acetylene triplet states [19, 132]. Later, Kanamori and coworkers used mercury photosensitization to study the $cis-T_2 \leftarrow cis-T_1$ absorption spectrum of acetylene [58] in the near IR spectral region.

The main drawback to the use of a traditional mercury photosensitization technique with acetylene is polymer formation [106, 102]. Another problem with tradi-

tional techniques of mercury photosensitization is the complicated dynamics of radiation trapping and energy pooling [80, 46, 74, 75].

The rate of polymer formation could be kept to a minimum if the number density of mercury atoms could be carefully controlled. In addition, we would like to design a method where the particular atomic metastable state could be selected based on the desired electronic energy. Furthermore, we wish to carry out experiments in a molecular beam, so that rotational and vibrational cooling can concentrate the population of triplet molecules into a relatively small number of rovibronic states.

We describe a method to generate large numbers of metastable atoms in the early stages of a supersonic expansion, without polymer formation. The metastable atoms are populated by a technique of optical pumping via two-photon transitions. We first discuss the details of two-photon transitions in atoms, and weigh the various options for optical pumping. A simple curve-crossing model is described for atom*-molecule collisional excitation transfer. We demonstrate the general principles of the technique for the $\text{Xe}^* + \text{N}_2$ system, and then report progress on $\text{Hg}^* + \text{C}_2\text{H}_2$.

6.2 Theory: Optical pumping of atomic metastables via two-photon transitions

Our initial goal is to populate metastable excited states of mercury and xenon atoms. The lowest-energy excited state term of both atoms is $^1,^3P$. The $^1,^3P$ term contains two metastable levels, 3P_0 and 3P_2 . In this section, we examine the level structure of mercury, formulate methods to populate the metastable 3P_0 and 3P_2 levels, and calculate transition probabilities for the proposed excitation schemes.

Excitation of one electron into a $6p$ orbital gives rise to four energy levels in mercury: 6^3P_0 , 6^3P_1 , 6^3P_2 , and 6^1P_1 . For brevity, we hereafter omit the principal quantum number from the mercury $6^1,^3P$ levels. The matrix of spin-orbit interaction

within the $1,3P$ term is

$$H^{SO} = \begin{matrix} & \begin{matrix} {}^3P_2 & {}^3P_1 & {}^1P_1 & {}^3P_0 \end{matrix} \\ \begin{matrix} {}^3P_2 \\ {}^3P_1 \\ {}^1P_1 \\ {}^3P_0 \end{matrix} & \begin{bmatrix} 1 & 0 & 0 & 0 \\ 0 & -1 & \sqrt{2} & 0 \\ 0 & \sqrt{2} & 0 & 0 \\ 0 & 0 & 0 & -2 \end{bmatrix} \end{matrix} \cdot \zeta_{6s6p}/2 \quad (6.1)$$

where the spin-orbit constant, ζ_{6s6p} , is approximately 4265 cm^{-1} [66]. The 3P_1 state is contaminated with singlet character, giving it a relatively short lifetime of ~ 125 ns. The 3P_2 and 3P_0 levels have no spin-orbit interaction pathway to the singlet, and are metastable. The lifetimes of the 3P_0 and 3P_2 states are so excessively long that experimental measurement is difficult [134]. Theoretical predictions for the lifetimes of the 3P_0 and 3P_2 states in odd isotopes are on the order of 1.0 and 0.5 s, respectively [84].

The metastable triplet levels may be populated by spontaneous radiative decay from singlet-triplet mixed levels at higher energy. We examine a series of potential two-photon excitation schemes, which result in population of one or both metastable levels, 3P_0 and 3P_2 . Many of the high-lying atomic levels which radiate directly to 3P_0 and 3P_2 have been carefully studied, and accurate branching ratios are available [9]. Two especially promising candidates are $6 {}^3D_2$ and $7 {}^3S_1$. The $6 {}^3D_2$ level has a branching ratio of approximately 3:1:1 among the 3P_1 , 3P_2 , and 1P_1 levels [9]. Thus, it is suitable to populate the higher-energy metastable level, 3P_2 . The $7 {}^3S_1$ level radiates only to levels within the 3P multiplet, with a branching ratio of 1:2:2 among the 3P_0 , 3P_1 , and 3P_2 levels [9]. Both metastable levels may be populated via radiative decay from $7 {}^3S_1$.

A general formula for the calculation of two-photon transition probabilities is derived by Bonin and McIlrath [12]. Starting from the atomic ground state, $|i\rangle$, the

two-photon transition probability to a final state $|f\rangle$ is given by

$$P_{f \leftarrow i} = \frac{2\pi}{\hbar^4} \left| \sum_a \frac{\langle f | \hat{\epsilon}_1 \cdot \bar{D} | a \rangle \langle a | \hat{\epsilon}_2 \cdot \bar{D} | f \rangle}{\omega_{ai} - \omega_2 + i\Gamma_a/2} + \frac{\langle f | \hat{\epsilon}_2 \cdot \bar{D} | a \rangle \langle a | \hat{\epsilon}_1 \cdot \bar{D} | f \rangle}{\omega_{ai} - \omega_1 + i\Gamma_a/2} \right|^2 \quad (6.2)$$

$$\times \frac{1}{\pi} \frac{\Gamma_f/2}{(\omega_1 + \omega_2 - \omega_{fi})^2 + (\Gamma_f/2)^2} \frac{\omega_1 \omega_2}{4\epsilon_0^2 c^4 k_1 k_2} \bar{I}_1 \bar{I}_2,$$

where the index a runs over all intermediate states [12, 43]. In the formula above, $\omega_n = E_n/\hbar$ is the energy of $|n\rangle$ in units of radians/s, $\omega_{nm} = (E_n - E_m)/\hbar$ is the energy difference between $|n\rangle$ and $|m\rangle$ in units of radians/s, Γ_n is the natural width of $|n\rangle$, $\hat{\epsilon}_{1,2}$ is the unit polarization vector for each photon, $k_{1,2}$ is the wave-vector magnitude of each photon, and $\bar{I}_{1,2}$ is the intensity of each beam.

The following two-photon optical pumping schemes were investigated:

- (a) one color TPA to 7^3S_1 ,
- (b) two color TPA to 7^3S_1 , with one laser tuned to the $7^3S_1 \rightarrow 6^3P_0$ downward transition,
- (c) two color TPA to 7^3S_1 , using the 3rd harmonic Nd:YAG laser output at 355 nm,
- (d) one color TPA to 6^3D_2 , and
- (e) two color TPA to 6^3D_2 , with one laser tuned to the $6^3D_2 \rightarrow 6^3P_2$ downward transition.

Figure 6-1 shows the various optical pumping schemes on an energy level diagram for the mercury atom. For each scheme, the total transition probability for TPA was calculated using Equation 6.2. The two-photon transition probability scales with the square of the laser intensity, therefore we give the probabilities in units of $(\text{W/m}^2)^{-2}\text{s}^{-1}$.

The calculated transition probabilities for each scheme are displayed in Table 6.1. The one-color, two-photon transition to the 6^3D_2 level, item (d), has the greatest transition probability among all the two-photon schemes considered. The two color

Figure 6-1: Diagram of possible two-photon excitation schemes for population of the 6^3P_0 and 6^3P_2 metastable excited states of Hg. Excitation to the 7^3S_1 level is followed by spontaneous decay to both metastable levels, while excitation to the 6^3D_2 is followed by spontaneous decay to only one of the metastable levels, 6^3P_2 . The various schemes, labeled (a)-(e), are described in the text. A dashed arrow is used to indicate two-photon excitation schemes that utilize photons of two different frequencies.

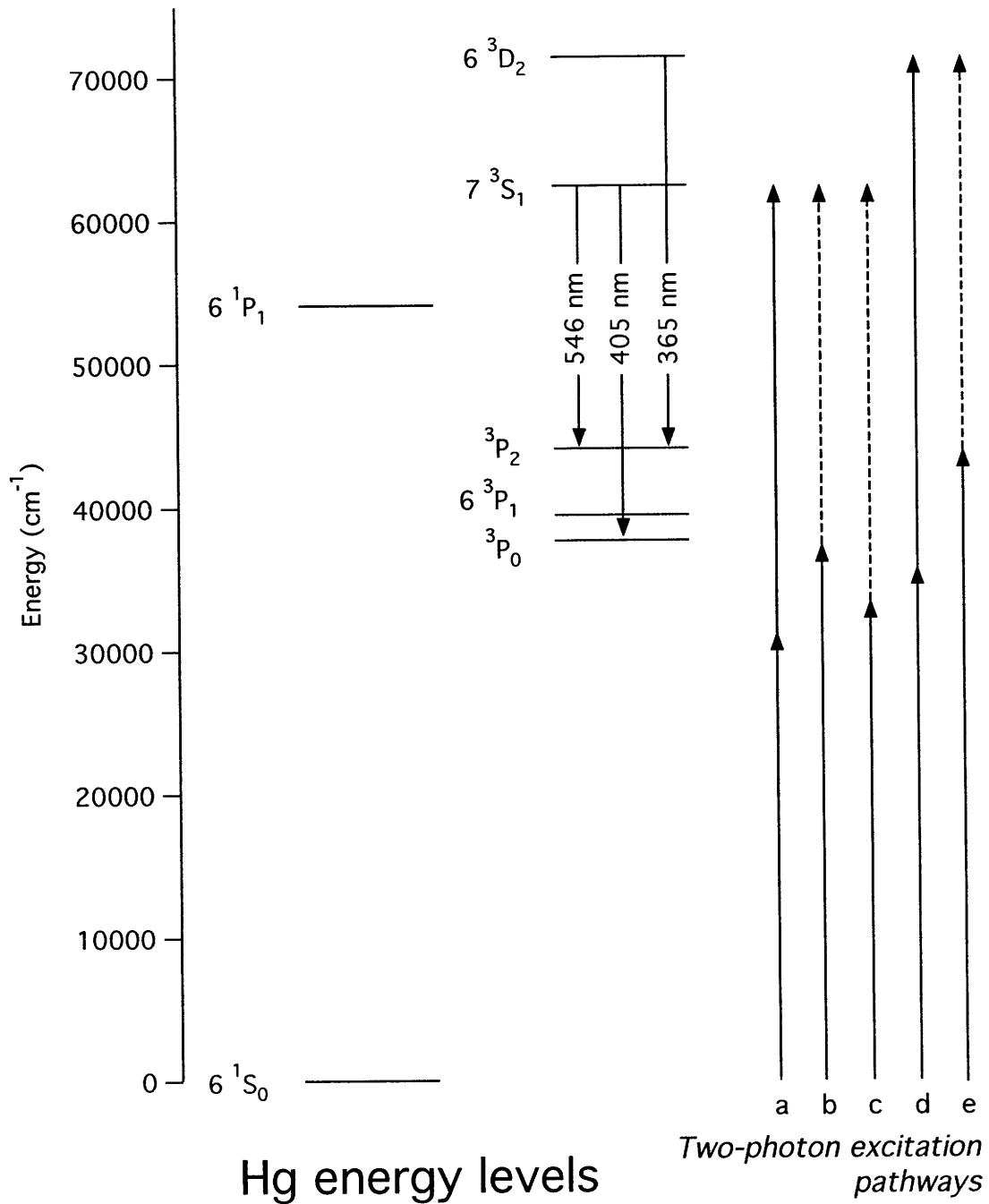


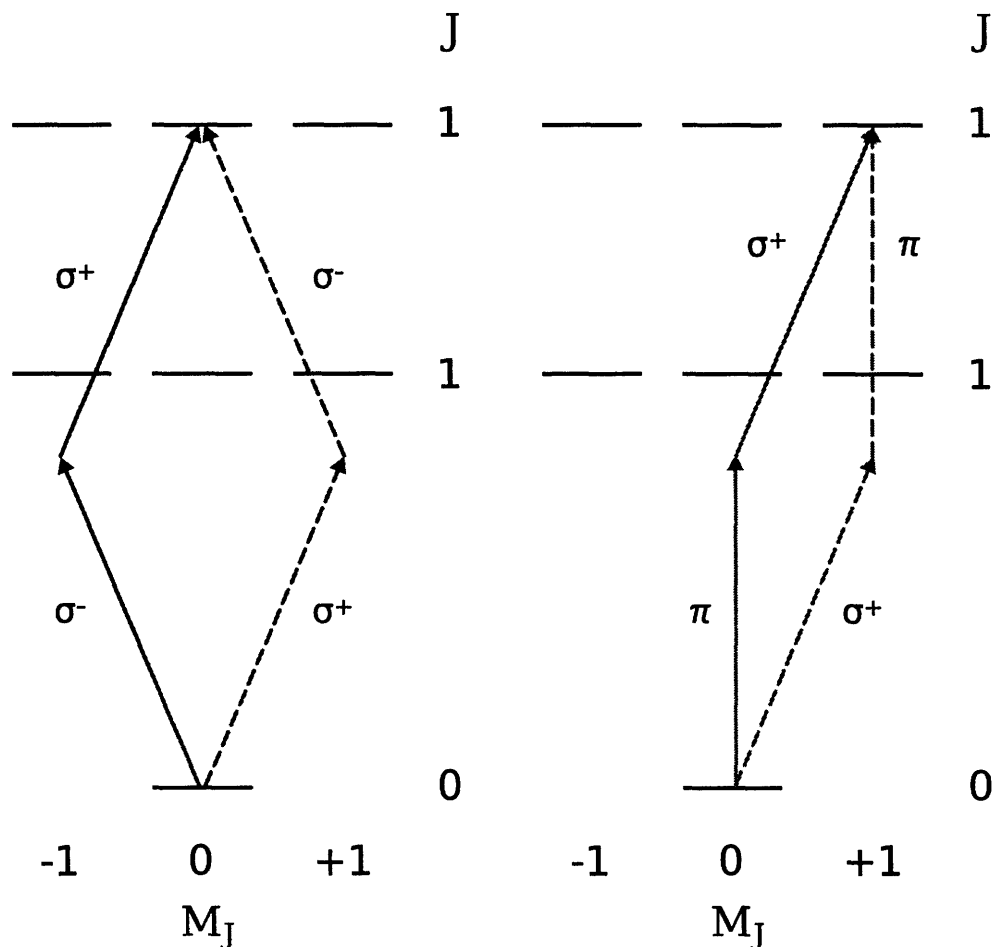
Table 6.1: Calculated two-photon transition probabilities for the five excitation schemes discussed in the text. The calculation indicates that one color TPA to $\text{Hg}^*(7\ ^3S_1)$ is exactly zero. Transition probabilities for excitation to the $\text{Hg}^*(6\ ^3D_2)$ level are two orders of magnitude larger than the weakly allowed two-color, two-photon transition probabilities for excitation to $\text{Hg}^*(7\ ^3S_1)$.

Hg transition	Two-photon transition probability, $10^{-15} (\text{W}/\text{m}^2)^{-2}\text{s}^{-1}$
$7\ ^3S_1 \leftarrow\leftarrow 6\ ^1S_0$ one color	0
$7\ ^3S_1 \leftarrow\leftarrow 6\ ^1S_0$ two color, tuned to 3P_0	3.19
$7\ ^3S_1 \leftarrow\leftarrow 6\ ^1S_0$ two color (355 + 292 nm)	2.29
$6\ ^3D_2 \leftarrow\leftarrow 6\ ^1S_0$ one color	466
$6\ ^3D_2 \leftarrow\leftarrow 6\ ^1S_0$ two color, tuned to 3P_2	106

transition to $6\ ^3D_2$, item (e), is slightly weaker. The two color, two-photon excitation schemes to the $7\ ^3S_1$ level, items (b) and (c), are an order of magnitude weaker yet, and the one color, two-photon excitation to $7\ ^3S_1$, item (a), is rigorously forbidden.

The $\text{Hg}^*(7\ ^3S_1) \leftarrow\leftarrow \text{Hg}(6\ ^1S_0)$ two-photon transition is rigorously forbidden according to the selection rule $J = 1 \leftrightarrow J = 0$ for photons of equal frequency and any relative polarization [12]. The rule may be rationalized by considering the interference between quantum mechanical pathways leading from the initial to final state [12, 43]. Figure 6-2 shows several of the possible pathways, as well as their relative phases according to Equation 6.2. It can be seen that the amplitudes for the two different orderings of photon absorption are equal and opposite. In fact, experimental verification of this two-photon selection rule is proposed as a test for the validity of some fundamental principles of quantum field theory [48].

Figure 6-2: Diagram of the interfering excitation pathways in $J' = 1 \leftarrow J'' = 0$ two-photon transitions with equal frequency photons. Any choice of polarization results in equal but opposite amplitudes and for the two possible photon orderings. Since amplitudes for both orderings of the photons are summed and then squared in Equation 6.2, two-photon transition probability is rigorously cancelled by interference between alternate excitation pathways. The figure on the left illustrates the pathways for left and right circularly polarized photons, while the figure to the right illustrates the pathways for z -polarized and right circularly polarized photons. The phase of each transition amplitude is indicated by either a solid or dashed arrow.



6.3 Experiments: Xe* + N₂

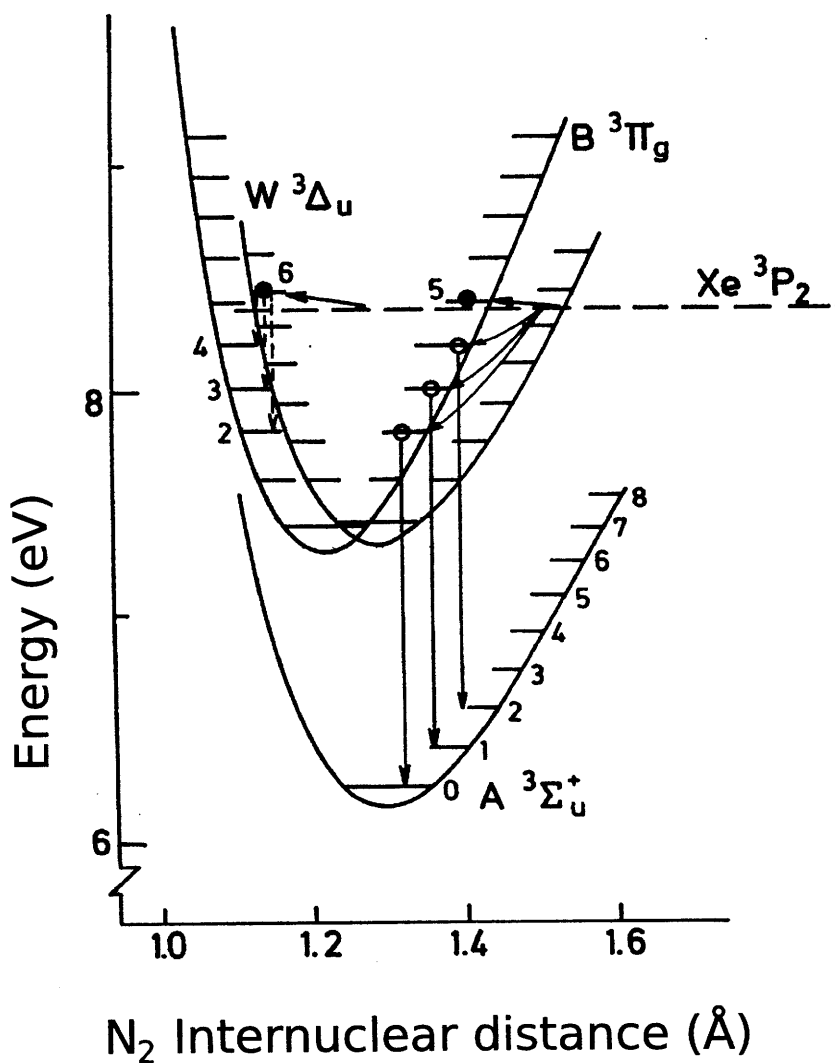
We investigate the Xe* + N₂ system as a precursor to our experiments with mercury and acetylene. The xenon-nitrogen system has the advantage of high excitation energies. The lowest excited state of xenon, ³P₂, lies 8.3 eV above the ground state [103]. The lowest triplet state of nitrogen, A ³Σ_u⁺, while far below Xe*(³P₂), lies 6.2 eV above the ground state [71]. (Triplet electronic states of nitrogen are labeled with uppercase letters for historical reasons.) The energies of Xe*(³P₂) and N₂*(A ³Σ_u⁺) far exceed the work function of gold, and both species are extremely metastable [84, 71].

Metastable xenon in the ³P₂ state transfers electronic energy selectively into the v'=5 level of N₂*(B ³Π_g) [62, 63, 96, 1]. The fluorescence lifetime of B ³Π_g → A ³Σ_u⁺ emission is on the order of 10 μs [71]. The A ³Σ_u⁺ state is metastable, with a fluorescence lifetime on the order of 1 s [71]. Thus, visible fluorescence (400–500 nm) may be measured to observe absolute quantum yield of the preparation of metastable N₂.

The potential energy curves and vibrational levels of the three “lowest” energy triplet electronic states of nitrogen are shown in Figure 6-3 (adapted from [62]). The W ³Δ_u electronic state is near-degenerate with the B ³Π_g state. Less is known about electronic energy transfer from Xe into the W ³Δ_u state of nitrogen, however, the ultimate decay route is unchanged. Molecules in the W ³Δ_u state decay slowly to the near-degenerate B ³Π_g electronic state via the emission of IR fluorescence. Shown in the figure for reference is the energy of the xenon ³P₂ state. Open and closed circles indicate possible channels for electronic energy transfer, and arrows indicate the principal fluorescence components [62].

One-color TPA to the ³D₂ state is used to populate metastable xenon (³P₂). The ³D₂ state decays spontaneously to ³P₁ and ³P₂ with a branching ratio of 1:2 [21]. The two-photon transition probability for Xe ³D₂ ←← ¹S₀ is calculated in the same manner as the Hg transitions. A total transition probability of 3.35×10⁻¹⁴ (W/m²)⁻²s⁻¹ is obtained for the one-color TPA. The magnitude of the xenon two-photon transition probability is approximately 1/10th that of the analogous transition

Figure 6-3: Potential energy curves and vibrational levels of the three lowest energy triplet electronic states of nitrogen, N_2 . The $A^3\Sigma_u^+$ state is metastable, with a fluorescence lifetime in the hundreds of microseconds. Molecules in the $W^3\Delta_u$ state decay slowly to the near-degenerate $B^3\Pi_g$ electronic state via IR fluorescence. The fluorescence lifetime for $B^3\Pi_g \rightarrow A^3\Sigma_u^+$ emission is several μs . It is this 400–500 nm fluorescence that we measure to observe the preparation of metastable N_2 . Also shown in the figure is the energy of the xenon 3P_2 state, which is known to populate the $v'=5$ level of the nitrogen $B^3\Pi_g$ state in gas-phase collisions [62]. Less is known about electronic energy transfer from Xe into the $W^3\Delta_u$ state of nitrogen. The figure is adapted from Reference [61].



in Hg.

The LIF spectrum of the xenon ${}^3D_2 \leftarrow \leftarrow {}^1S_0$ two-photon transition was recorded first in a static cell (Figure 6-4) and then in a molecular beam (Figure 6-5). The ${}^3D_2 \rightarrow {}^3P_2$ fluorescence emission at 823 nm was passed through a colored glass filter and collected by a Hamamatsu R375 photomultiplier tube. Emission to the 3P_1 state at 895 nm was outside the wavelength response range of the photomultiplier. The fluorescence decay, plotted in the bottom of Figure 6-5, is consistent with the fluorescence lifetime of $\tau = 28$ ns reported in the literature [21].

Electronic energy transfer to nitrogen molecules was measured first under static cell conditions. The excitation chamber of the SEELEM apparatus was sealed and filled with 210 mTorr of a 50:50 Xe/N₂ gas mixture. The laser was held fixed on the Xe ${}^3D_2 \leftarrow \leftarrow {}^1S_0$ two-photon transition. The intensity of collision-induced N₂ $B {}^3\Pi_g \rightarrow A {}^3\Sigma_u^+$ emission in the visible region of the spectrum is plotted in Figure 6-6 as a function of time. Our observation is consistent with the reported fluorescence lifetime of N₂ $B {}^3\Pi_g \rightarrow A {}^3\Sigma_u^+$ emission, which is on the order of 10 μ s.

To carry out the excitation in the early stages of a supersonic expansion, a short nozzle extension was constructed. The extension piece consisted of a cylinder of stainless steel, 2 cm in length, with a 1 mm diameter bore. The piece was tapered at the end to maximize the exposure at the tip of the orifice to laser radiation. The nozzle extension allowed the laser radiation to intersect the free jet in the high pressure region immediately in front of the nozzle orifice.

The two-photon excitation to Xe (3D_2) was carried out in the high-pressure region of a supersonic expansion with a 50:50 gas mixture of Xe and N₂. The time dependence of Xe $6 {}^3D_2 \rightarrow 6 {}^3P_2$ and N₂ $B {}^3\Pi_g \rightarrow A {}^3\Sigma_u^+$ emission is plotted in Figure 6-7. Xenon fluorescence (823 nm, $\tau = 28$ ns) is emitted when the optically excited state decays spontaneously to the metastable $6 {}^3P_2$ state. Nitrogen molecules are electronically excited during the expansion process as a result of collisions with metastable xenon atoms. Near-resonant vibrational levels of the nitrogen $B {}^3\Pi_g$ state decay spontaneously to the metastable $A {}^3\Sigma_u^+$ state ($\tau = 20$ μ s), accompanied by fluorescence in the visible region of the spectrum.

Figure 6-4: Laser-Induced Fluorescence (LIF) spectrum of the one-color, two-photon transition $\text{Xe } ^3D_2 \leftarrow \leftarrow ^1S_0$, recorded under static cell conditions. The LIF signal results from spontaneous emission to the metastable 3P_2 state at 823 nm.

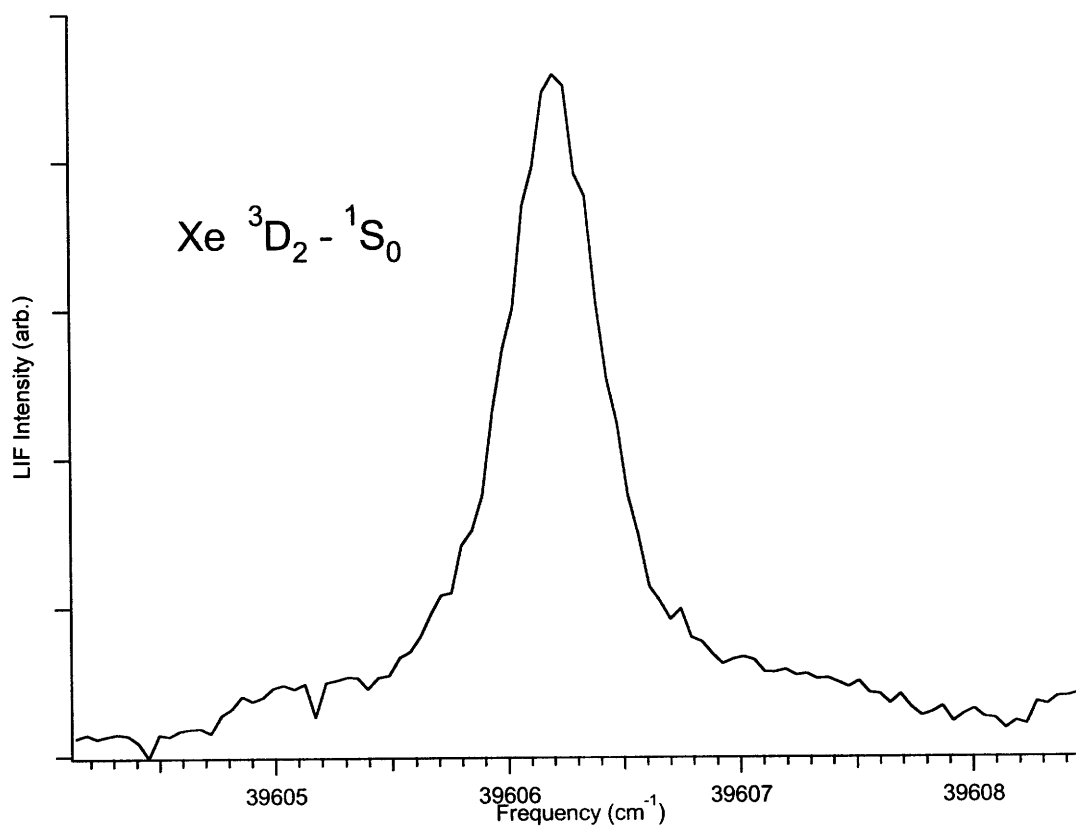


Figure 6-5: (Top) Laser-Induced Fluorescence (LIF) spectrum of the one-color, two-photon transition $\text{Xe } ^3D_2 \leftarrow \leftarrow ^1S_0$, recorded in a supersonic expansion. (Bottom) Time dependence of $\text{Xe } ^3D_2 \rightarrow ^3P_2$ emission (solid trace), compared to a signal that results from scattered laser light (dashed trace, normalized to intensity of Xe fluorescence). The fluorescence signal results from spontaneous emission to the metastable 3P_2 state at 823 nm ($\tau = 28$ ns).

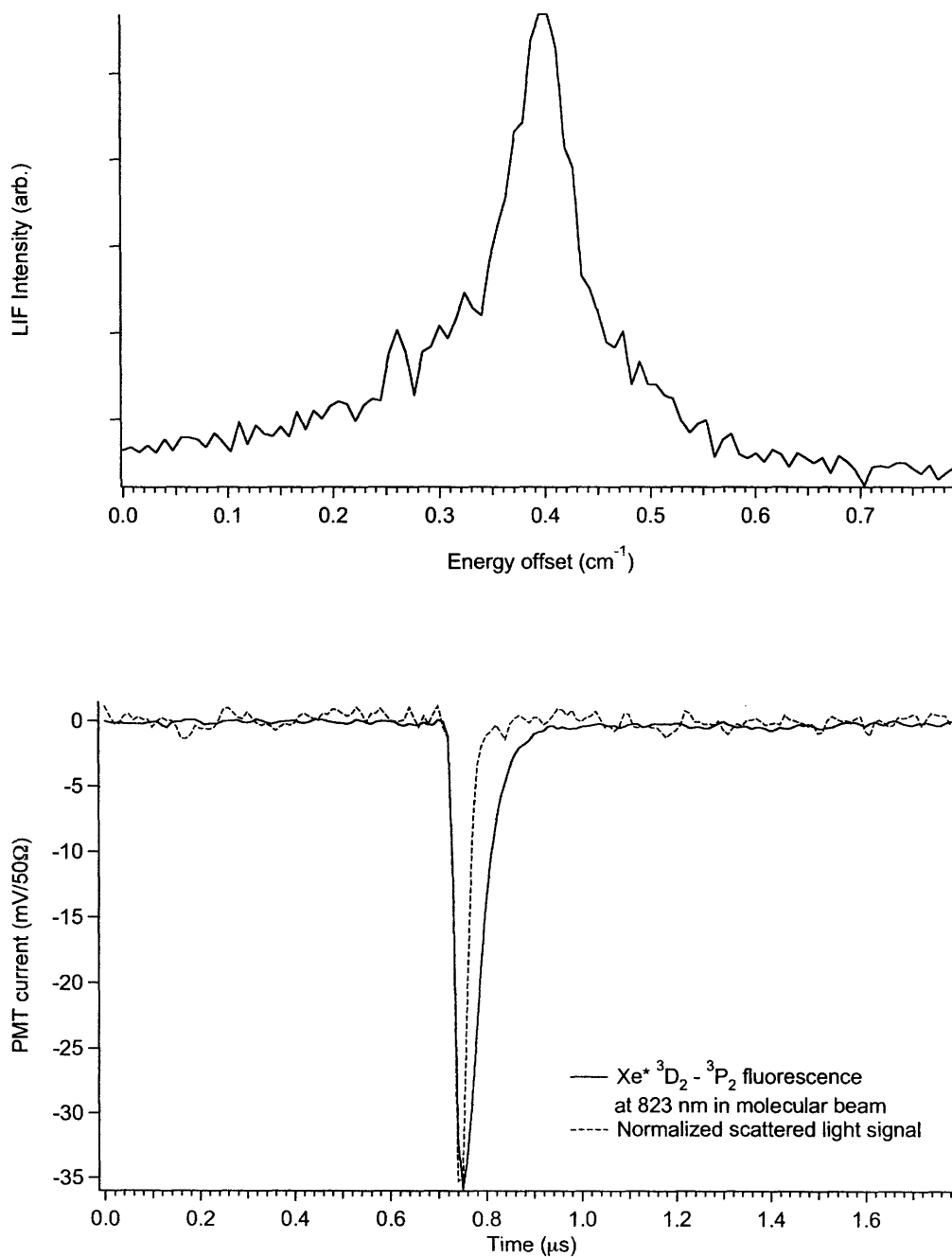


Figure 6-6: Time dependence of $N_2 B \ ^3\Pi_g \rightarrow A \ ^3\Sigma_u^+$ emission, induced by collisions with metastable $Xe^* ({}^3P_2)$. The excitation chamber of the SEELEM apparatus was sealed and filled with a 50:50 mixture of Xe and N_2 , to a total pressure of 210 mTorr. Metastable $Xe^* ({}^3P_2)$ was populated by spontaneous emission, following the $6 \ ^3D_2 \leftarrow \leftarrow 6 \ ^1S_0$ two-photon transition.

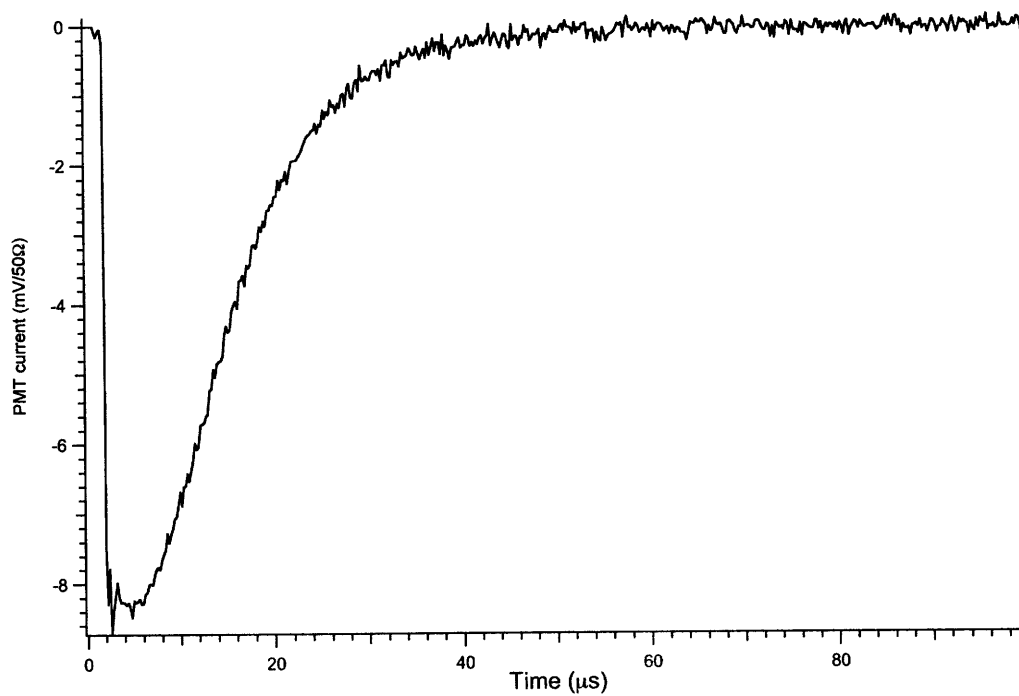
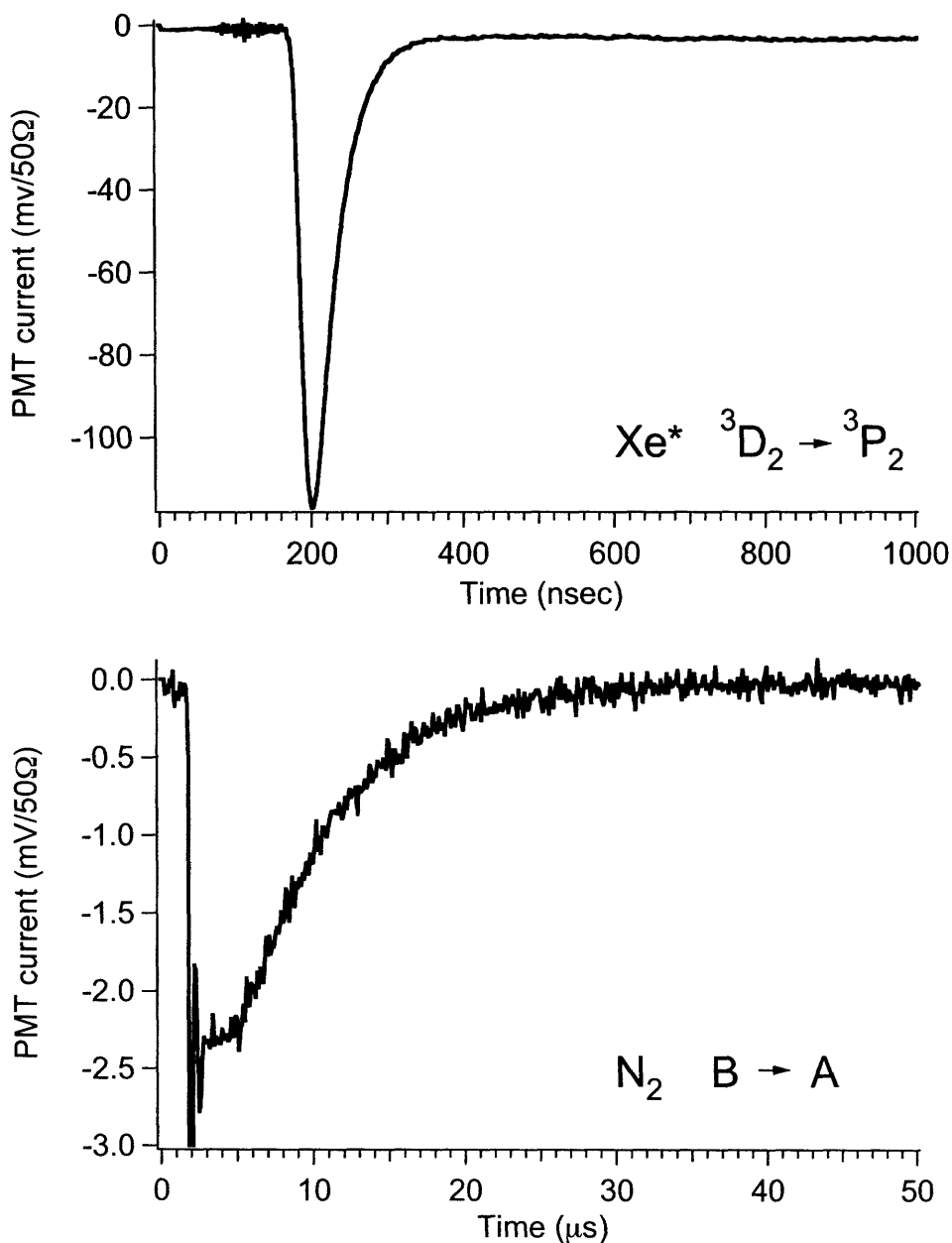


Figure 6-7: Time dependence of Xe $6\ ^3D_2 \rightarrow 6\ ^3P_2$ (top plot) and N₂ $B\ ^3\Pi_g \rightarrow A\ ^3\Sigma_u^+$ (bottom plot) emission, following the two-photon excitation of Xe (3D_2) in a supersonic expansion. The xenon and nitrogen emission signals occur on vastly different timescales. Xenon fluorescence (823 nm, $\tau = 28$ ns) is emitted when the optically excited state decays spontaneously to the metastable $6\ ^3P_2$ state. Nitrogen molecules are electronically excited during the expansion process by collisions with metastable xenon atoms. Near-resonant vibrational levels of the nitrogen $B\ ^3\Pi_g$ state decay spontaneously to the metastable $A\ ^3\Sigma_u^+$ state ($\tau \approx 10\ \mu\text{s}$), accompanied by 600–800 nm fluorescence.



6.4 Experiments: $\text{Hg}^* + \text{C}_2\text{H}_2$

The production of Hg^* -sensitized metastable molecules in a molecular beam is more of a challenge than sensitization by Xe^* . Firstly, the lowest metastable state of Hg, 3P_0 , is too low in energy to eject an electron from a gold surface. Secondly, the only allowed triplet-triplet transition in acetylene is in the infrared, and the upper state of the transition, T_1 , is not detectable even on a medium-work function metal such as Yttrium.

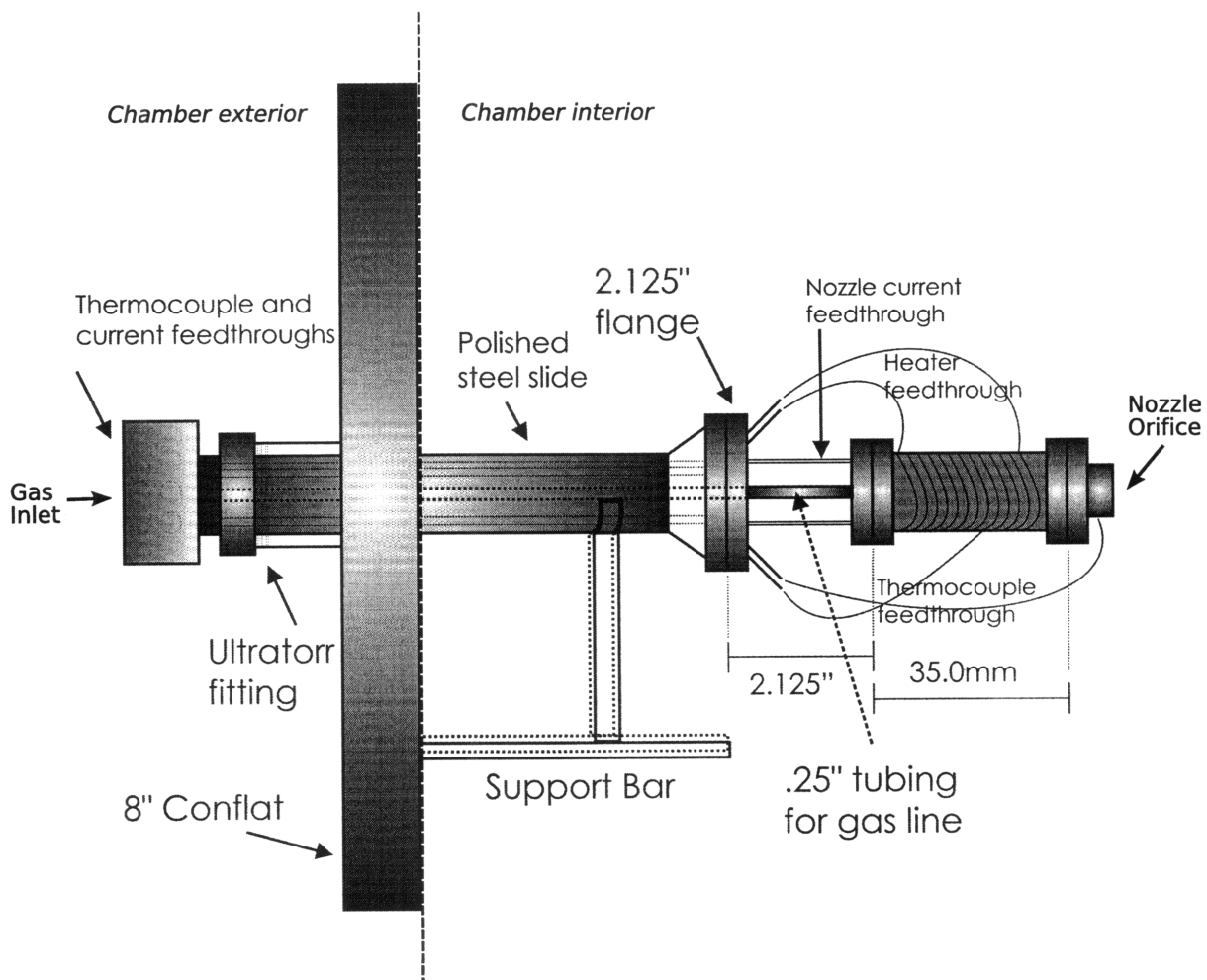
Another challenge is the generation of large number densities of mercury in the pulsed nozzle. The Jordan valve, normally used for SEELEM experiments, may only be heated to 100°C , corresponding to a mercury vapor pressure of 281 mTorr. Another nozzle design, capable of higher temperatures, was needed to achieve larger partial pressures of Hg inside the nozzle. Heated continuous beam sources of $\text{Hg}^*(^3P_0)$ are reported in the literature [44, 92]. Nitrogen backing gas is first bubbled through a mercury oven, and the resulting gas mixture is expanded through a heated nozzle, next to an embedded Hg resonance lamp. However, we require a pulsed design, due to pump speed limitations.

A new pulsed valve was designed by Wilton Virgo in 2007 to meet our demands for heated mercury. The design is based on a pulsed valve used by the Leutwyler research group at the University of Bern, Switzerland [120, 91]. The valve can be heated to 250°C , corresponding to a mercury vapor pressure of 75 Torr. A diagram of the “Bern Valve” is shown in Figure 6-8.

We attempted to populate the 3P_0 level of mercury via collisional intramultiplet relaxation by N_2 molecules. Nitrogen is known to efficiently quench $\text{Hg}^*(^3P_1)$ to $\text{Hg}^*(^3P_0)$, because the $^3P_1 - ^3P_0$ energy difference is about the same as the vibrational level spacing in N_2 [23, 50, 86]. Bras and coworkers measured the energy transfer dynamics of mercury in N_2 buffer gas, and determined that $\text{Hg}(^3P_0)$ may be efficiently produced by two-photon excitation to the $7\ ^1S_0$ level, followed by radiative $7\ ^1S_0 \rightarrow ^3P_1$ decay and collisional $^3P_1 \rightarrow 6\ ^3P_0$ quenching [14].

The relatively strong one-color, two-photon transition $\text{Hg}\ 7\ ^1S_0 \leftarrow\leftarrow 6\ ^1S_0$ was

Figure 6-8: Diagram of the heated pulsed valve developed for experiments with mercury. The “Bern Valve” can be safely heated to 250° C. A small vial of mercury is housed in the heated region, close to the nozzle orifice (far right).



recorded under static cell conditions. However, the excitation energy of $\text{Hg}^*(^3P_0)$ is below the work function of gold. A yttrium surface was tested in an effort to develop a lower work function SEELEM detector. In a collaborative project with Trevor Sears, we installed a commercially available sample (Alfa Aesar) of yttrium foil on our SEELEM detector, and measured the SEELEM-TOF spectra of metastable phenylacetylene molecules [49]. SEELEM-TOF spectra were recorded for several vibrational bands of the phenylacetylene \tilde{A} state. Most of the bands, labeled here according to their approximate frequency above the \tilde{A} state origin, have been assigned by Powers and coworkers [99]. The SEELEM-TOF spectra of phenylacetylene levels are plotted together in Figure 6-9. Unfortunately, we were not able to maintain the detector in a reliable state of operation with a yttrium surface, due to degradation of the electron multiplier front plate surface. We turned to methods for creating $\text{Hg}(^3P_2)$.

Following our success with xenon, we attempted to use the $6\ ^3D_2 \leftarrow\leftarrow 6\ ^1S_0$ one-color, two-photon transition to create mercury atoms in the 3P_2 state. The LIF spectrum of this transition, recorded in a static cell, is plotted in Figure 6-10. An interference filter was used to record only the $6\ ^3D_2 \rightarrow\ ^3P_2$ fluorescence at 365 nm. The experiment was attempted in a supersonic expansion, prior to the time that the Bern valve was manufactured. We were unable to achieve a sufficient number density of Hg atoms to measure a signal in the free jet.

Direct excitation to the 3P_2 state was also attempted as a method for triplet formation. This transition, while forbidden in the solitary molecule, is made allowed in collision complexes with a variety of gases [64, 6]. Also, we note that weak $^3P_2 \rightarrow 6\ ^1S_0$ emission was observed in pre-laser experiments [90]. Figure 6-11 shows the SEELEM-TOF spectrum of mercury excited to directly to the $6\ ^3P_2$ level. The signal level is sufficiently low that it is checked against a repeated experiment with the pulsed valve turned off, shown for comparison in Figure 6-12. While it is clear that we do register a SEELEM signal from the direct excitation of $\text{Hg}^*(6\ ^3P_2)$, we were not able to increase the gas density sufficiently at the point of excitation to make this an efficient process for the population of acetylene metastables.

Figure 6-9: SEELEM-TOF spectra of several vibrational bands of \tilde{A} phenylacetylene. Yttrium was used as a low work function surface in the experiment. The excitation laser was tuned to the frequency of highest intensity in each band. The bands are labeled according to their frequency above the \tilde{A} state origin.

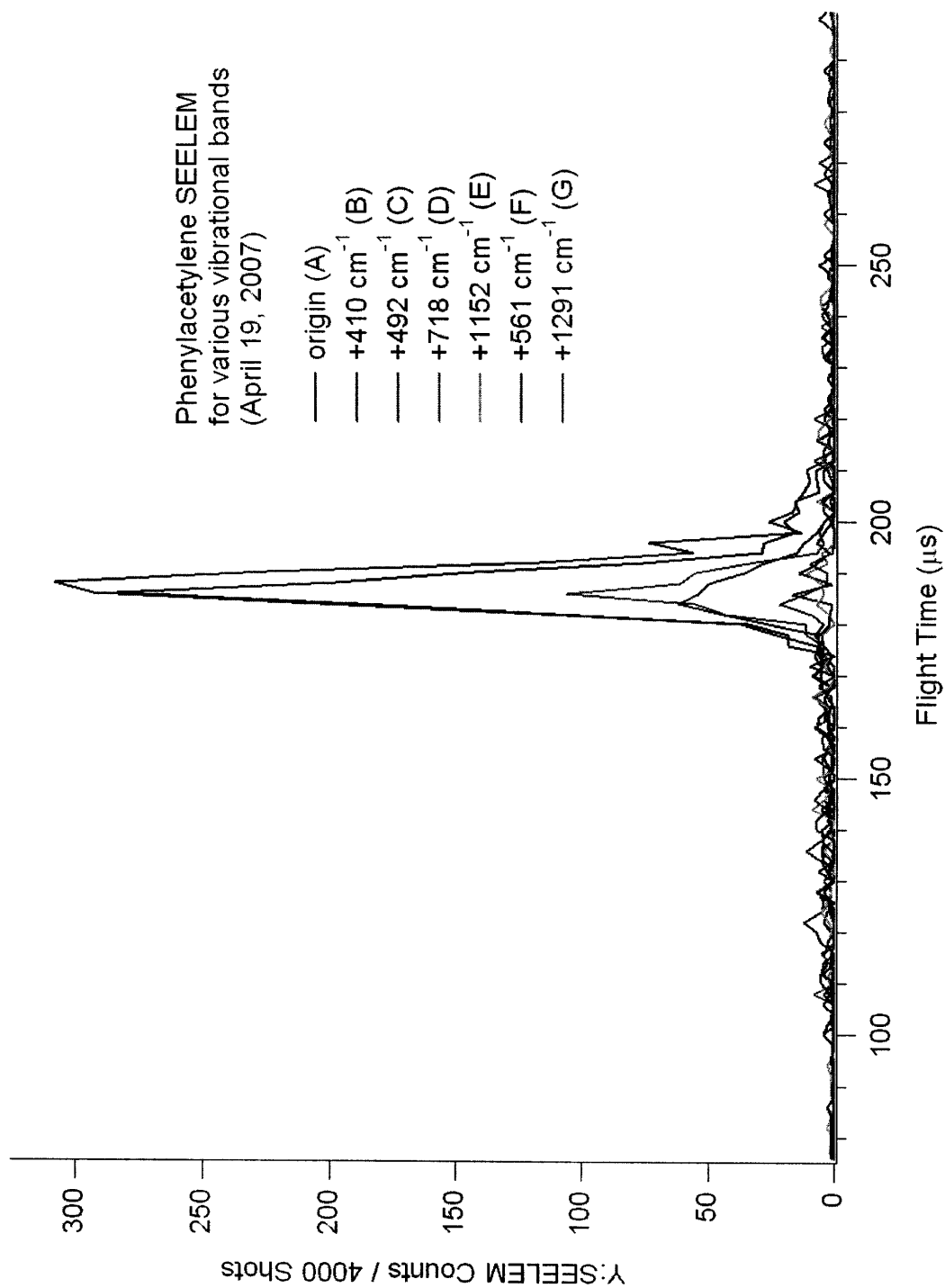


Figure 6-10: Laser-Induced Fluorescence (LIF) spectrum of the one-color, two-photon transition $\text{Hg } 6^3D_2 \leftarrow \leftarrow 6^1S_0$, recorded under static cell conditions. The LIF signal results from spontaneous emission to the metastable 6^3P_2 state at 365 nm.

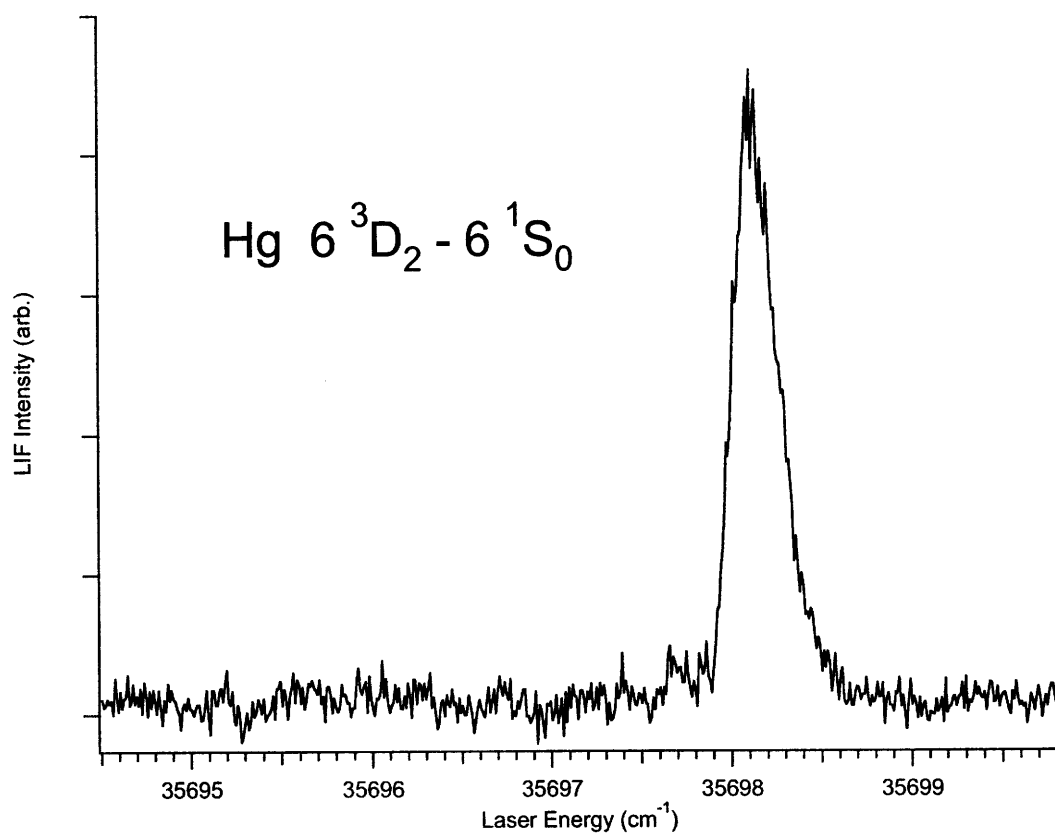


Figure 6-11: SEELEM time of flight (TOF) detection of metastable mercury produced via the direct excitation $\text{Hg}^*(6^3P_2) \leftarrow \text{Hg}(6^1S_0)$ at 44042.98 cm^{-1} . The pulsed valve was heated to 250° C to increase the number density of mercury. The two traces are recorded in repeated experiments.

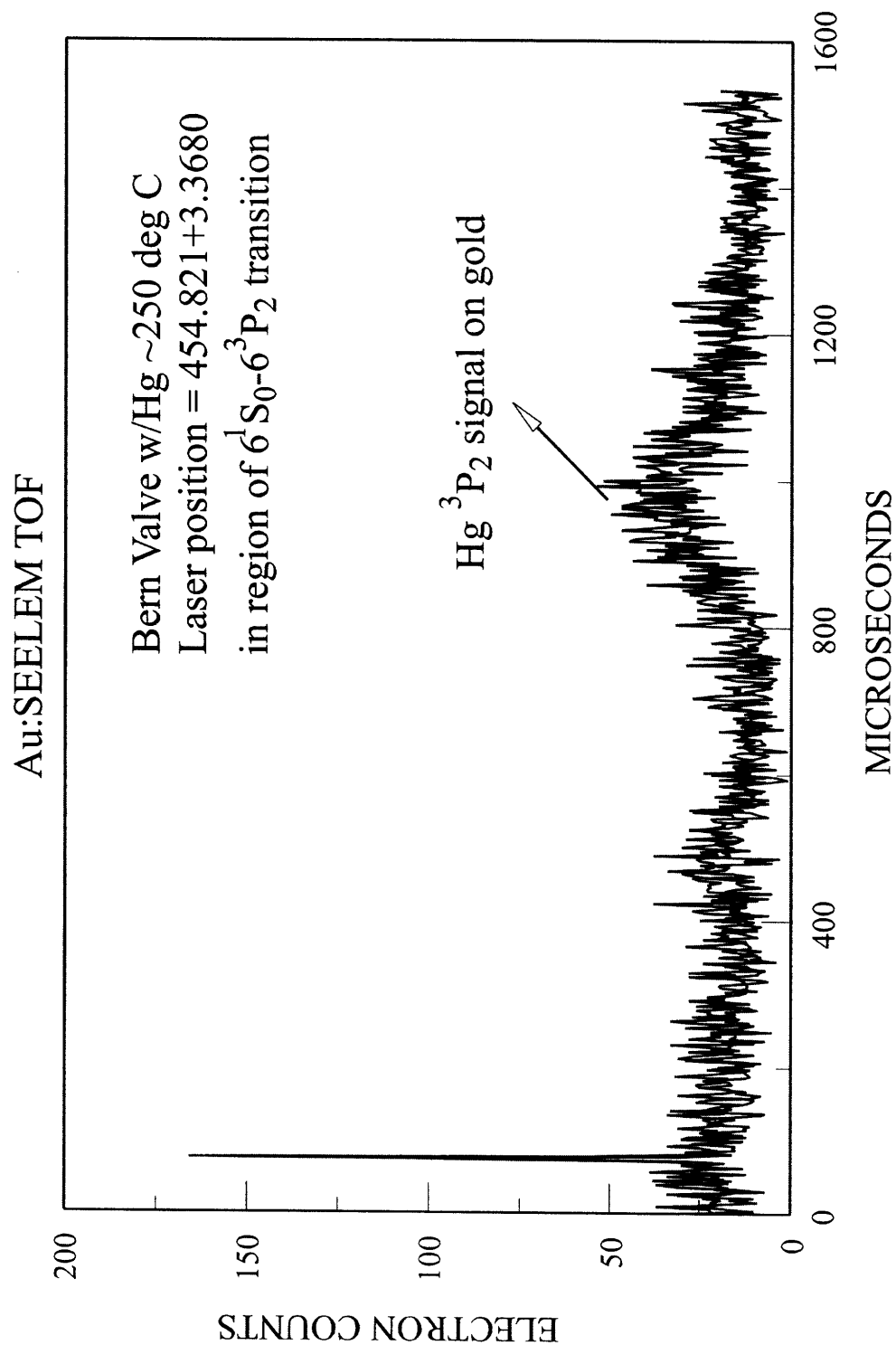
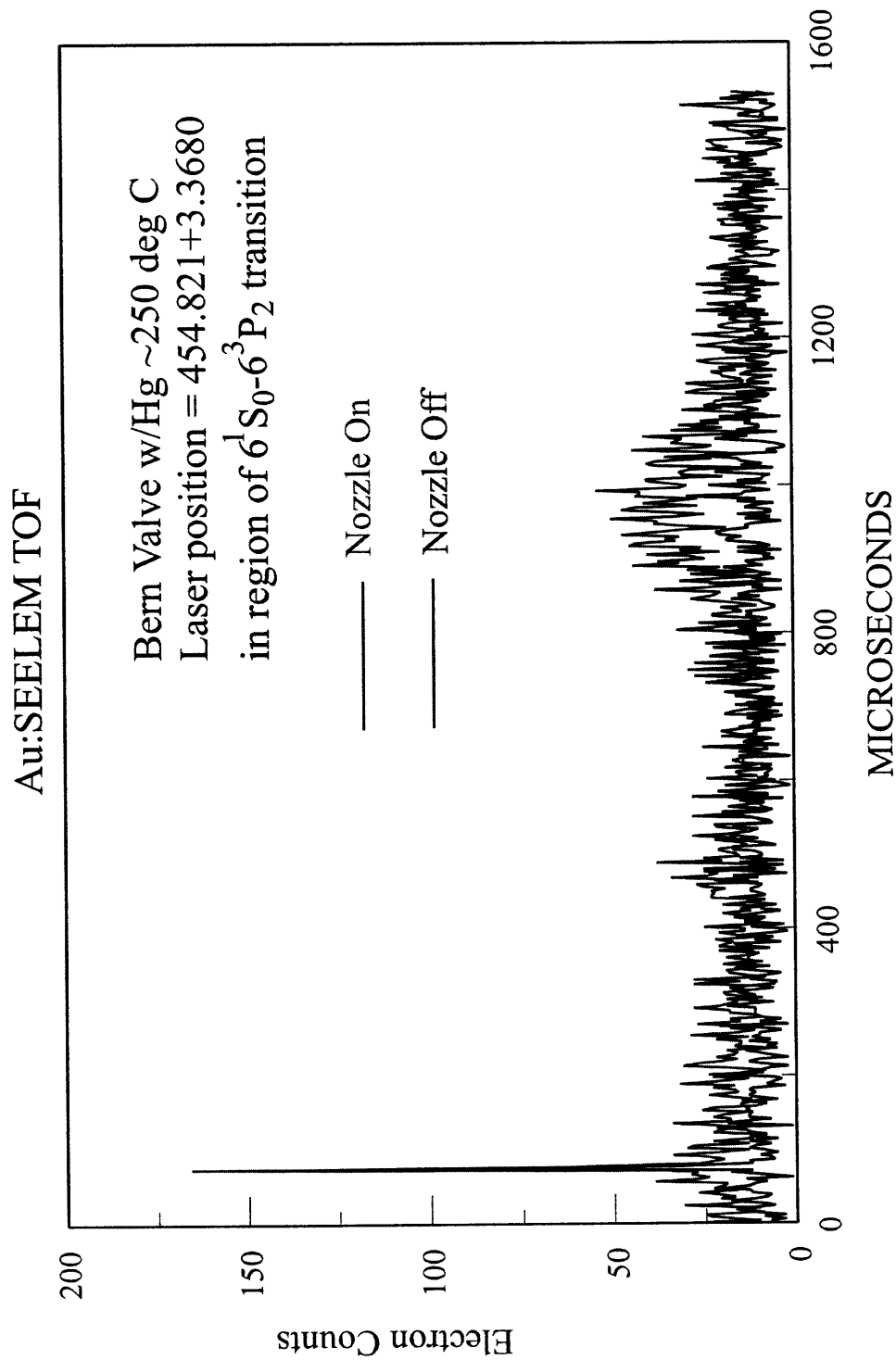


Figure 6-12: Comparison of signal to background in the SEELEM time of flight (TOF) detection of metastable mercury produced via the direct excitation $\text{Hg}^*(6^3P_2) \leftarrow \text{Hg}(6^1S_0)$ at 44042.98 cm^{-1} . The lighter trace is recorded with the pulsed valve on, and the black trace is recorded with the valve off.



We found that the most efficient method for the population of $\text{Hg}^*(^3P_2)$ was a simple, two step excitation to $7\ ^3S_1$ via the 3P_1 level. Figure 6-13 shows a simultaneously recorded LIF and SEELEM spectrum for mercury seeded in xenon gas. The frequency of one laser was fixed to the $\text{Hg } 7\ ^3S_1 \leftarrow ^3P_1$ atomic transition, while another was scanned in the region of the $^3P_1 \leftarrow ^1S_0$ transition. An interference filter was used to record only $7\ ^3S_1 \rightarrow ^3P_2$ emission, which results in the population of metastable Hg atoms. The SEELEM spectrum detects the metastables that survive a $700\ \mu\text{s}$ flight time. The hyperfine structure of several Hg isotopes is apparent from the lineshape in the spectrum.

After the observation of metastable $\text{Hg}^*(^3P_2)$ formed in the two-step excitation, the measurement was repeated, using acetylene as the buffer gas. The resulting SEELEM spectrum of the two-color, stepwise excitation of $\text{Hg}(^3S_1)$ via the 3P_1 level is plotted in Figure 6-14. The lower-intensity spectrum shows mercury seeded in Xe gas, while the upper spectrum shows mercury seeded in acetylene. We attribute the larger overall signal level for the mercury/acetylene mixture to electronic excitation transfer between $\text{Hg}(^3P_2)$ and $\text{C}_2\text{H}_2(T_3)$.

6.5 Future Work

We propose a new experiment, building on the success of our previous work with the $\text{Xe}^* + \text{N}_2$ system. The experiment would study the rotational and vibrational dependence of collision-induced intersystem crossing from the $a'\ ^1\Sigma_u^-$ and $a\ ^1\Pi_g$ states to the $B\ ^3\Pi_g$ state of nitrogen. Nitrogen may be excited to the $a\ ^1\Pi_g$ state via two-photon transitions [127]. Collisions between N_2 molecules facilitate energy transfer between the $a\ ^1\Pi_g$ and $a'\ ^1\Sigma_u^-$ electronic states [77]. The $a\ ^1\Pi_g \leftrightarrow a'\ ^1\Sigma_u^-$ processes may be studied using “traditional” LIF/SEELEM spectroscopy, perhaps with a longer pathlength for the SEELEM detector. The fluorescence lifetime of the $a\ ^1\Pi_g$ state is on the order of 10^{-4} s – this fluorescence may be viewed directly, using a long time window. The lifetime of $a'\ ^1\Sigma_u^-$ is on the order of 10^{-2} s – molecules in this electronic state may be detected in the SEELEM channel.

Figure 6-13: Simultaneously recorded LIF and SEELEM spectra for the two-color, stepwise excitation of $\text{Hg}(^3S_1)$ via the 3P_1 level. An interference filter was used to record only $\text{Hg}(^3S_1) \rightarrow \text{Hg}(^3P_2)$ emission, which results in the population of metastable Hg atoms. The SEELEM spectrum shows the intensity of metastables that survive a $700 \mu\text{s}$ flight time. The structure in the atomic lineshape is the result of hyperfine splittings in mercury.

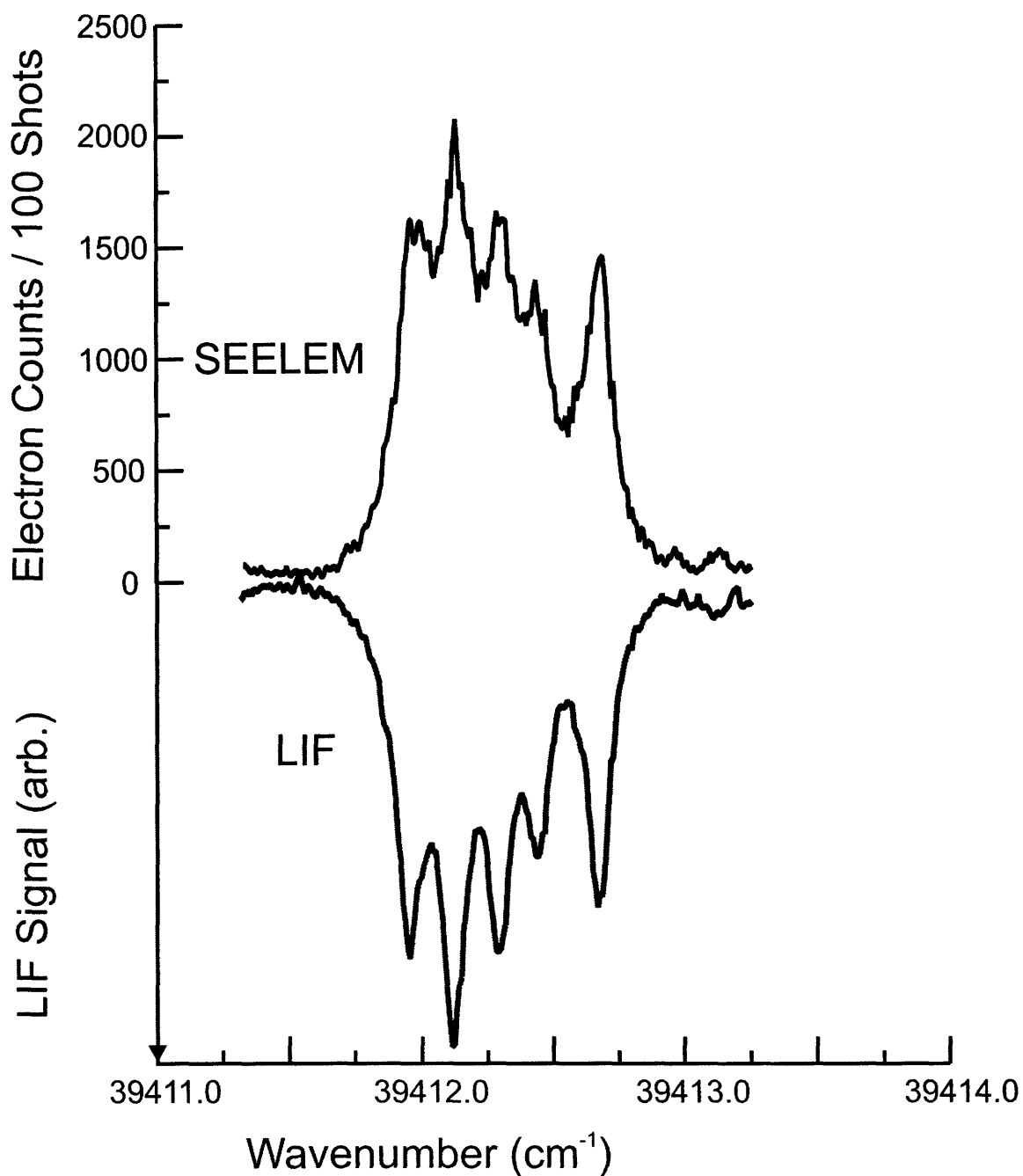
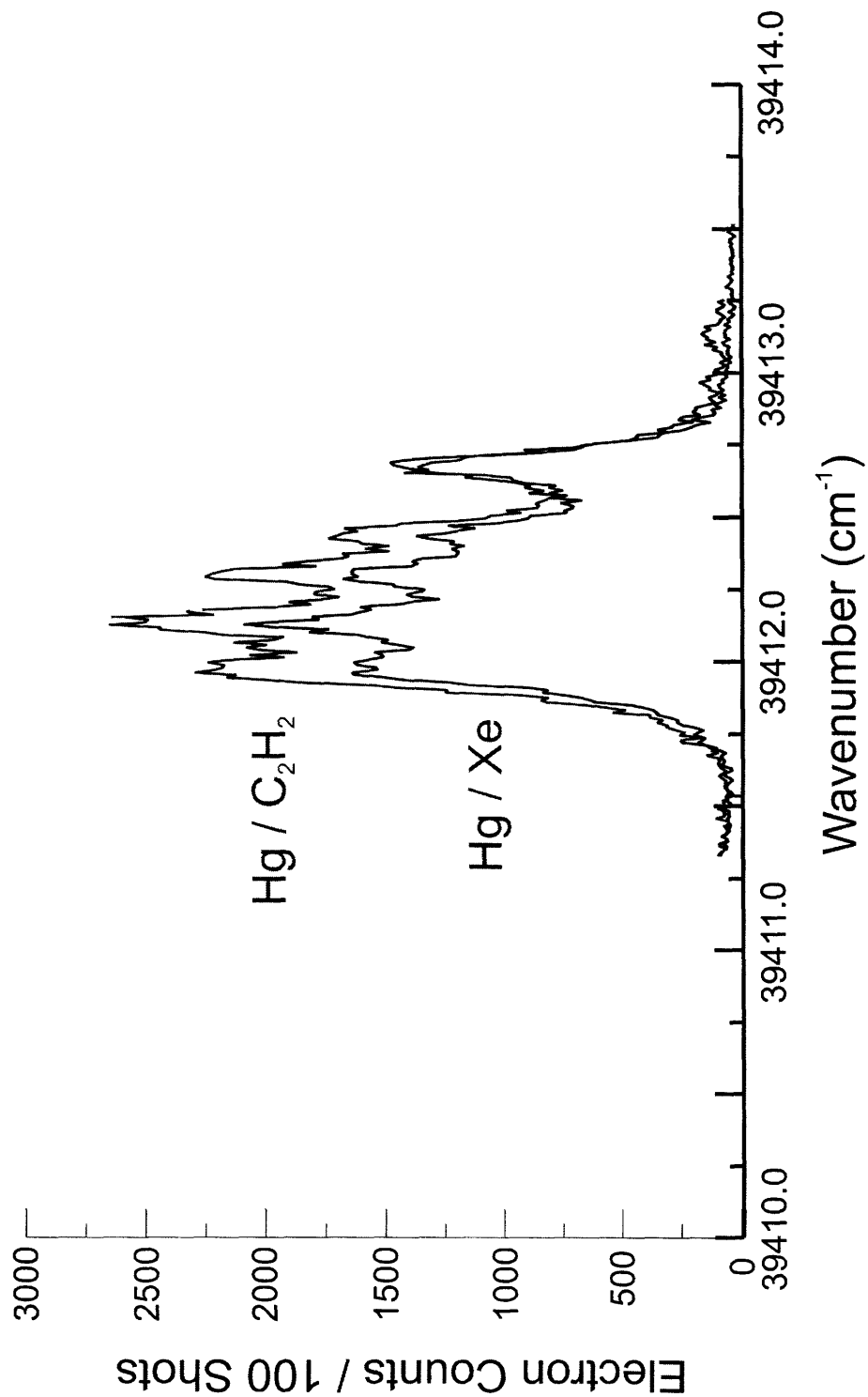


Figure 6-14: SEELEM spectrum of the two-color, stepwise excitation of $\text{Hg}(^3S_1)$ via the 3P_1 level. The lower spectrum shows mercury seeded in Xe gas, while the upper spectrum shows mercury seeded in acetylene. The larger overall signal level in the mercury/acetylene mixture is the result of electronic excitation transfer between $\text{Hg}(^3P_2)$ and $\text{C}_2\text{H}_2(T_3)$. The bern nozzle was used for both measurements, heated to 250°C .



Xenon-nitrogen collisions are observed to facilitate the process of collisional $a' \ ^1\Sigma_u^- \rightarrow B \ ^3\Pi_g$ intersystem crossing, although the rotational and vibrational dependences of this process are uncertain [125]. The intersystem crossing process would be readily observable via $B \ ^3\Pi_g \rightarrow A \ ^3\Sigma_u^+$ fluorescence in the visible region of the spectrum.

In separate experiments, Ottinger has observed collision-induced “gateway” intersystem crossing, which is attributed to an accidental near-degeneracy between $a' \ ^1\Sigma_u^-, v = 16, J = 14$ and $C \ ^3\Pi_u, v = 0, J = 14$ [95]. The gateway process is *quenched* in collisions with Xe atoms. Ottinger proposes that the energy of the $a' \ ^1\Sigma_u^-, v = 16$ state is high enough that the quenching reaction proceeds according to a harpooning mechanism, which efficiently produces Xe^* [95].

A rapid change in the chemistry of $\text{Xe} + \text{N}_2(a' \ ^1\Sigma_u^-)$ collisions as the vibrational level is changed from $v = 0$ to $v = 14$ makes this experiment an exciting proposition. Two-photon laser excitation of N_2 will allow rotational and vibrational effects in nitrogen to be studied selectively. Furthermore, a range of detection options are available in the current apparatus for the reaction products Xe^* and N_2^* .

6.6 Conclusions

We demonstrate the production of metastable acetylene and nitrogen molecules in a molecular beam by the method of collisional electronic excitation. Metastable atoms, populated by two-photon transitions followed by spontaneous emission, are used as the energy-carrying collision partners.

Chapter 7

Conclusions

A theory of the spectral signatures of doorway-mediated intersystem crossing is developed. The problem is formulated under three distinct frameworks, and the relationships between the frameworks are described. Four model Hamiltonians are discussed: the local doorway model, the distant doorway model, the local doorway plus direct coupling model, and the double doorway model. Using the theory developed in this thesis, the relative statistical properties of LIF and SEELEM intensity distributions are derived for each class of model Hamiltonian.

The parameters that define a local doorway model Hamiltonian are determined uniquely by the absorption spectrum. This discrete spectral inversion process is carried out by a recursive application of the standard Lawrance-Knight-Lehmann deconvolution method. The statistical moments of the spectrum are shown to be related, by simple equations, to the important parameters of the model Hamiltonian. The technique of “doorway deconvolution” is demonstrated using examples from NO_2 and acetylene spectra.

The experimental method of simultaneous SEELEM/LIF spectroscopy is used to investigate singlet~triplet mixing in the acetylene molecule. New experimental results are reported for a number of S_1 vibrational levels, looking beyond the frequently studied $v'_3 = 0 - 4$ levels. New methods are developed to analyze the spectra, which allow the detailed structure of the spectrum to be related back to the doorway model.

The impact of torsional (ν'_4) and antisymmetric in-plane bending (ν'_6) vibrations on

singlet-triplet mixing is investigated by IR-UV double resonance LIF/SEELEM spectroscopy. The effects of Darling-Dennison resonance and a -type Coriolis interaction, which plagued earlier studies, are excluded by an appropriate choice of vibrational sublevels. The roles of the ν'_4 and ν'_6 modes in promoting vibrational overlap with T_3 levels are discussed.

The understanding of “distant doorway” interactions in S_1 acetylene paints an optimistic picture for future study, using the standard experimental techniques of LIF/SEELEM spectroscopy. Specifically, the crucial finding is that one spin component of a distant doorway level rapidly approaches a perturbed singlet level as J' is increased. Not only does this explain many rotational effects at low values of J' , but it also means that more perturbations are likely to be observable in the range $5 \lesssim J' \lesssim 15$.

Methods are developed for the production of metastable molecules in a molecular beam. Two-photon transitions are used to generate metastable atoms, and the molecules are excited via collisional excitation transfer from the atoms. The selection rules and transition probabilities for two-photon excitation of the atoms are discussed in detail for mercury. SEELEM and LIF spectroscopy are used to demonstrate the production of metastable acetylene and nitrogen molecules in a molecular beam by the method of collisional electronic excitation transfer.

Building on the success of our experiments with $\text{Xe}^* + \text{N}_2$, we propose a new experiment to study collisional intersystem crossing in the $\text{N}_2^* + \text{Xe}$ system. The proposal is motivated by the ability to selectively excite many metastable rovibronic transitions in N_2 , and by our ability to selectively detect the various products in the current apparatus.

Bibliography

- [1] T. G. Aardema, E. J. van Nignatten, and H. C. W. Beijerinck. Excitation transfer for $\text{Xe}^*(^3P_2) + \text{N}_2$ in the eV energy range: double potential crossing for $\text{N}_2(B, v' = 5)$. *Chem. Phys.*, 184:273, 1994.
- [2] S. Altunata. *Intersystem crossing in acetylene: A mechanistic study*. PhD thesis, Massachusetts Institute of Technology, 2001.
- [3] S. Altunata, K. L. Cunningham, M. Canagaratna, R. Thom, and R. W. Field. The mechanism of surface electron ejection by laser-excited metastable molecules. *J. Phys. Chem. A*, 106(7):1122, 2002.
- [4] S. Altunata and R. W. Field. A statistical approach for the study of singlet-triplet interactions in small polyatomic molecules. *J. Chem. Phys.*, 113(16):6640, 2000.
- [5] S. Altunata and R. W. Field. An assumption-violating application of the Lawrance-Knight deconvolution procedure: A retrieval of electronic coupling mechanisms underlying complex spectra. *J. Chem. Phys.*, 114:6557, 2001.
- [6] K. Amano, K. Ohmori, T. Kurosawa, H. Chiba, M. Okunishi, K. Ueda, Y. Sato, A. Z. Devdariani, and E. E. Nikitin. $c \leftarrow X$ laser excitation spectrum of the Hg-Ar vdW complex. *J. Chem. Phys.*, 108(19):8110, 1998.
- [7] A. M. Andrews, G. T. Fraser, and B. H. Pate. Molecular-beam infrared infrared double-resonance spectroscopy study of the vibrational dynamics of the acetylenic CH stretch of propargyl amine. *J. Chem. Phys.*, 109(11):4290, 1998.
- [8] J. Baraban. DVR calculation of acetylene S_1 wavefunctions. Private communication, 2008.
- [9] E. C. Benck, J. E. Lawler, and J. T. Dakin. Lifetimes, branching ratios, and absolute transition probabilities in Hg I. *J. Opt. Soc. Am. B*, 6(1):11, 1989.
- [10] J. O. Berg. Extraction of vibronic information from tangled spectra. *Chem. Phys. Lett.*, 41:547, 1976.
- [11] M. Bixon and J. Jortner. Intramolecular radiationless transitions. *J. Chem. Phys.*, 48(2):715, 1968.

- [12] K. D. Bonin and T. J. McIlrath. Two-photon electric dipole selection rules. *J. Opt. Soc. Am. B*, 1(1):52, 1984.
- [13] J. C. D. Brand and A. R. Hoy. A deconvolution of the $\tilde{A} - \tilde{X}$ band system of nitrogen dioxide. *J. Mol. Spec.*, 65:75, 1977.
- [14] N. Bras, J. C. Jeannet, and D. Perrin. Energy transfer in mercury vapour following laser excitation of the 7^1S_0 state by two-photon absorption. *J. Phys. B: At. Mol. Opt. Phys.*, 26:2289, 1993.
- [15] S. H. Brown and R. H. Crabtree. A novel route to alkanes, alcohols, and ethers by dehydrodimerization. *Tet. Lett.*, 28(46):5599, 1987.
- [16] S. H. Brown and R. H. Crabtree. Alkane activation by mercury vapor. *J. Chem. Ed.*, 65(4):290, 1988.
- [17] S. H. Brown and R. H. Crabtree. Making mercury-photosensitized dehydrodimerization into an organic synthetic method: Vapor pressure selectivity and the behavior of functionalized substrates. *J. Am. Chem. Soc.*, 111:2935, 1989.
- [18] P. R. Bunker and P. Jensen. *Molecular Symmetry and Spectroscopy*. National Research Council of Canada, Ottawa, Canada, second edition, 1998.
- [19] C. S. Burton and H. E. Hunziker. Triplet state of acetylene: Biacetyl emission from the mercury photosensitized reaction. *J. Chem. Phys.*, 57(1):339, 1972.
- [20] R. Cable and W. Rhodes. Theoretical analysis of spectral structure: Doorway state coupling schemes. *J. Chem. Phys.*, 73:4736, 1980.
- [21] J. A. Cabrera, M. Ortiz, and J. Campos. Transition Probabilities of $6s - 6p$ lines and lifetimes of $6p$ configuration levels of XeI. *Physica*, 104C:416, 1981.
- [22] G. Cairo and J. Franck. Über zerlegung von wasserstoffmolekülen durch angeregte quecksilberatome. *Z. Phys.*, 11:161, 1922.
- [23] A. B. Callear and G. J. Williams. Cross-sections for deactivation of $Hg(6^3P_0)$. *Trans. Faraday Soc.*, 60:2158, 1970.
- [24] J. G. Calvert and J. N. Pitts. *Photochemistry*. Wiley, 1966.
- [25] S. L. Coy and K. K. Lehmann. Energy-level statistics for a relaxation hamiltonian. *Phys. Rev. A*, 36:404, 1987.
- [26] R. H. Crabtree, S. H. Brown, C. A. Muedas, P. Krajnik, and R. R. Ferguson. Recent advances in mercury photosensitized reactions. *J. Mol. Catal.*, 74:85, 1992.

- [27] Q. Cui and K. Morokuma. Ab initio MO studies on the photodissociation of C_2H_2 from the S_1 (1A_u) state. I. Non-adiabatic effects and S-T interaction. *Chem. Phys. Lett.*, 263:46, 1996.
- [28] Q. Cui and K. Morokuma. Ab initio MO studies on the photodissociation of C_2H_2 from the S_1 (1A_u) state. II. Mechanism involving triplet states. *Chem. Phys. Lett.*, 272:319, 1997.
- [29] K. L. Cunningham. *The surface ejection of electrons by laser-excited metastables spectroscopy of acetylene*. PhD thesis, Massachusetts Institute of Technology, 2000.
- [30] R. J. Cvetanović. Mercury photosensitized reactions. *Prog. React. Kinet.*, 2:39, 1964.
- [31] M. Dallos, H. Lischka, E. Ventura, M. Hirsch, and W. Quapp. Determination of energy minima and saddle points using multireference configuration interaction methods in combination with reduced gradient following: The S_0 surface of H_2CO and the T_1 and T_2 surfaces of acetylene. *J. Comput. Chem.*, 23:576, 2002.
- [32] M. DeGroot. *High-resolution spectroscopy as a probe for electronic coupling*. PhD thesis, University of Amsterdam, 2007.
- [33] D. Demoulin. The shapes of some excited states of acetylene. *Chem. Phys.*, 11:329, 1975.
- [34] M. Drabbels, J. Heinze, and W. L. Meerts. A study of the singlet-triplet perturbations in the \tilde{A}^1A_u state of acetylene by high resolution ultraviolet spectroscopy. *J. Chem. Phys.*, 100:165, 1994.
- [35] Marcel Drabbels, C. G. Morgan, and A. M. Wodtke. The spin-forbidden $a^4\Pi(\nu = 1315)$ and $b^4\Sigma^-(\nu = 3) \leftarrow X^2\Pi(\nu = 0)$ bands of nitric oxide: A new scheme for quantum state-specific high-resolution kinetic energy measurements. *J. Chem. Phys.*, 103:7700, 1995.
- [36] R. Dressler and M. Allan. A dissociative electron attachment, electron transmission, and electron energy-loss study of the temporary negative ion of acetylene. *J. Chem. Phys.*, 87:4510, 1987.
- [37] P. Dupré. Study of Zeeman anticrossing spectra of the \tilde{A}^1A_u state of the acetylene molecule (C_2H_2) by Fourier transform: product $\rho_{\text{vib}} \langle V \rangle$ and the isomerization barrier. *Chem. Phys.*, 196:239, 1995.
- [38] P. Dupré and P. G. Green. Characterization of a large singlet-triplet coupling in the \tilde{A} state of the acetylene molecule. *Chem. Phys. Lett.*, 212(6):555, 1993.

- [39] P. Dupré, P. G. Green, and R. W. Field. Quantum beat spectroscopic studies of Zeeman anticrossings in the \tilde{A}^1A_u state of the acetylene molecule (C_2H_2). *Chem. Phys.*, 196:211, 1995.
- [40] P. Dupre, R. Jost, and M. Lombardi. Study of singlet-triplet coupling in glyoxal by level anticrossing spectroscopy. V. Nature of singlet-triplet interaction. *Chem. Phys.*, 91:355, 1984.
- [41] P. Dupré, R. Jost, M. Lombardi, P. G. Green, E. Abramson, and R. W. Field. Anomalous behavior of the anticrossing density as a function of excitation energy in the C_2H_2 molecule. *Chem. Phys.*, 152:293, 1991.
- [42] K. F. Freed. *Radiationless Processes in Molecules and Condensed Phases*, chapter 2. Energy Dependence of Electronic Relaxation Processes in Polyatomic Molecules, page 23. Springer-Verlag, 1976.
- [43] G. Grynberg and B. Cagnac. Doppler-free multiphotonic spectroscopy. *Rep. Prog. Phys.*, 40:791, 1977.
- [44] J. A. Haberman, B. E. Wilcomb, F. J. Van Itallie, and R. B. Bernstein. Formation of supersonic beams of metastable mercury, $hg(6^3p_0)$. kinetics of photoexcitation and intramultiplet quenching in a nozzle. *J. Chem. Phys.*, 62(11):4466, 1975.
- [45] J. C. Hemminger, B. G. Wicke, and W. Klemperer. Delocalization of electronic energy in the lowest triplet states of molecules. *J. Chem. Phys.*, 65(7):2798, 1976.
- [46] M. T. Herd, J. E. Lawler, and K. L. Menningen. Radiation trapping of the Hg 254 nm resonance line. *J. Appl. Phys. D: Appl. Phys.*, 38:3304, 2005.
- [47] G. Herzberg. *Molecular Spectra and Molecular Structure III. Electronic Spectra and Electronic Structure of Polyatomic Molecules*. D. Van Nostrand Company, Princeton, NJ, 1966.
- [48] R. C. Hilborn. Analysis of an atomic $J = 0$ to $J = 1$ two-photon transition as a test of the spin-statistics connection for photons. *Phys. Rev. A*, 65:032104, 2002.
- [49] J. Hofstein, H. Xu, T. Sears, and P. Johnson. Fate of excited states in jet-cooled aromatic molecules: Bifurcating pathways and very long lived species from the S_1 excitation of phenylacetylene and benzonitrile. *J. Phys. Chem. A*, 112(6):1195, 2008.
- [50] H. Horiguchi and S. Tsuchiya. Spectroscopic determination of quenching cross sections of excited mercury atoms ($6^3p_1, 6^3p_0$) in molecular collisions. *Bull. Chem. Soc. Japan*, 44:1213, 1971.

- [51] H. Hotop. Detection of metastable atoms and molecules. *Exp. Meth. Phys. Sci.*, 29B:191, 1996.
- [52] J. T. Hougen. Rotational structure of singlet-triplet transitions in near symmetric tops. *Can. J. Phys.*, 42:433, 1964.
- [53] W. E. Howard and E. W. Schlang. Rotational selection rules for nonradiative processes. *J. Chem. Phys.*, 68(6):2679, 1978.
- [54] E. Hudspeth, D. A. McWhorter, and B. H. Pate. Intramolecular vibrational energy redistribution in the acetylenic CH and hydroxyl stretches of propynol. *J. Chem. Phys.*, 109(11):4316, 1998.
- [55] S. J. Humphrey, C. G. Morgan, Wodke A. M., K. L. Cunningham, S. Drucker, and R. W. Field. Laser-excited metastable states of acetylene in the 5.5-5.7 eV region. *J. Chem. Phys.*, 107(1):49, 1997.
- [56] C. K. Ingold and G. W. King. Excited states of acetylene. Part I. Possibilities of interaction between σ -bond hybridisation and π -electron excitation with resulting changes of shape during transitions. *J. Chem. Soc.*, page 2702, 1953.
- [57] K. K. Innes. Analysis of the near ultraviolet absorption spectrum of acetylene. *J. Chem. Phys.*, 22:863, 1954.
- [58] H. Kanamori. Triplet acetylene at T. I. Tech. Private Communication, 2007.
- [59] G. W. King and C. K. Ingold. The bent excited state of acetylene. *Nature*, 169:1101, 1952.
- [60] J. Kommandeur, W. A. Majewski, W. L. Meerts, and D. L. Pratt. Pyrazine: An "exact" solution to the problem of radiationless transitions. *Ann. Rev. Phys. Chem.*, 38:433, 1987.
- [61] T. Krümpelmann. *Spektroskopische Untersuchung der Energieübertragung beim Stoß metastabiler Xe-Atome auf N₂ und CO Moleküle*. PhD thesis, Max-Planck Institute, Göttingen, 1987.
- [62] T. Krümpelmann and Ch. Ottinger. Vibrationally selective electronic energy transfer from metastable Xe atoms to N₂ and CO molecules. *Chem. Phys. Lett.*, 140(2):142, 1987.
- [63] T. Krümpelmann and Ch. Ottinger. Spin-orbit state selectivity in Xe* + N₂, CO electronic energy transfer. *J. Chem. Phys.*, 88(8):5245, 1988.
- [64] T. Kurosawa, K. Ohmori, H. Chiba, M. Okunishi, K. Ukeda, Y. Sato, A. Z. Devdariani, and E. E. Nikitin. Collision induced absorption in mercury-rare-gas collisions. *J. Chem. Phys.*, 108(19):8101, 1998.

- [65] W. D. Lawrance and A. E. W. Knight. Direct deconvolution of extensively perturbed spectra: The singlet-triplet molecular eigenstate spectrum of pyrazine. *J. Phys. Chem.*, 89:917, 1985.
- [66] H. Lefebvre-Brion and R. W. Field. *The Spectra and Dynamics of Diatomic Molecules*. Elsevier, 2004.
- [67] K. K. Lehmann. Comment on direct deconvolution of extensively perturbed spectra: The singlet-triplet molecular eigenstate spectrum of pyrazine. *J. Phys. Chem.*, 95:7556, 1991.
- [68] H. Lischka and A. Karpfen. Ab initio calculations on the excited states of π -systems. I. Valence excitations in acetylene. *Chem. Phys.*, 102:77, 1986.
- [69] J. M. Lisy and W. Klemperer. Electric deflection studies of metastable acetylene. *J. Chem. Phys.*, 72(7):3880, 1980.
- [70] P. Löffler, E. Wrede, L. Schnieder, J. B. Halpern, W. M. Jackson, and K. H. Welge. Dissociation dynamics of acetylene Rydberg states as a function of excited state lifetime. *J. Chem. Phys.*, 109(13):5231, 1998.
- [71] A. Lofthus and P. H. Krupenie. The spectrum of molecular nitrogen. *J. Phys. Chem. Ref. Data*, 6(1):113, 1977.
- [72] M. Lombardi. Singlet-triplet coupling in small organic molecules by anticrossing, quantum beat, and magnetic resonance spectroscopy. In E. C. Lim and K. K. Innes, editors, *Excited States*, volume 7, page 163. Academic Press, 1988.
- [73] J. K. Lundberg, R. W. Field, Sherrill C. D., E. T. Seidl, Y. Xie, and H. F. Schaefer III. Acetylene: Synergy between theory and experiment. *J. Chem. Phys.*, 98(11):8384, 1993.
- [74] S. Majetich, E. M. Boczar, and J. R. Wiesenfeld. Energy pooling and associative ionization following laser excitation of mercury vapor. *J. Appl. Phys.*, 66(2):475, 1989.
- [75] S. Majetich, C. A. Tomczyk, and J. R. Wiesenfeld. Associative ionization and dissociative recombination in mercury vapor. *J. Appl. Phys.*, 69(2):563, 1991.
- [76] K. Malsch, R. Rebentisch, P. Swiderek, and G. Hohlneicher. Excited states of acetylene: a CASPT2 study. *Theor. Chem. Acc.*, 100:171, 1998.
- [77] W. J. Marinelli, B. D. Green, M. A. DeFaccio, and W. M. A. Blumberg. Vibrational relaxation and intersystem crossing in $N_2(a^1\Pi_g)$. *J. Phys. Chem.*, 92:3429, 1988.
- [78] S. P. McGlynn, T. Azumi, and M. Kinoshita. *Molecular Spectroscopy of the Triplet State*. Prentice-Hall, 1969.

- [79] E. S. Medvedev and V. I. Osherov. *Radiationless transitions in polyatomic molecules*. Springer-Verlag, 1995.
- [80] K. L. Menningen and J. E. Lawler. Radiation trapping of the hg 185 nm resonance line. *J. Appl. Phys.*, 88(6):3190, 2000.
- [81] A. J. Merer. Some feedback from a "triplet reader". Private communication, 2008.
- [82] A. J. Merer, N. Yamakita, S. Tsuchiya, J. F. Stanton, Z. Duan, and R. W. Field. New vibrational assignments in the $\tilde{A}^1A_u \leftarrow \tilde{X}^1\Sigma_g^+$ electronic transition of acetylene, C_2H_2 : the ν'_1 frequency. *Mol. Phys.*, 101(4-5):663, 2003.
- [83] A. J. Merer, N. Yamakita, S. Tsuchiya, A. H. Steeves, H. A. Bechtel, and R. W. Field. Darling-Dennison resonance and Coriolis coupling in the bending overtones of the \tilde{A}^1A_u state of acetylene, C_2H_2 . *J. Chem. Phys.*, 129:054304, 2008.
- [84] A. P. Mishra and T. K. Balasubramanian. Radiative lifetimes of the first excited $^3P_{2,0}^o$ metastable levels in Kr I, Xe I, Yb I and Hg-like atoms. *J. Quant. Spec. Rad. Trans.*, 69:769, 2001.
- [85] A. P. Mishra, R. L. Thom, and R. W. Field. New S_1 State Vibrational and $T_{3,2,1}$ Spin-Rotational Assignments in the Vicinity of the Acetylene $\tilde{A}^1A_u - \tilde{X}^1\Sigma_g^+ V_0^3K_0^1$ Band. *J. Mol. Spec.*, 228:565, 2004.
- [86] A. C. G. Mitchell and M. W. Zemansky. *Resonance Radiation and Excited Atoms*. Cambridge University, Cambridge, 1961.
- [87] M. Mizoguchi, N. Yamakita, S. Tsuchiya, A. Iwasaki, K. Hoshina, and K. Yamanouchi. IR-UV double resonance spectroscopy of acetylene in the \tilde{A}^1A_u $n\nu'_3 + \nu'_4$ and $n\nu'_3 + \nu'_6$ ($n = 2, 3$) ungerade vibrational states. *J. Phys. Chem. A*, 104(45):10212, 2000.
- [88] D. H. Mordaunt, M. N. R. Ashfold, R. N. Dixon, P. Löffler, L. Schnieder, and K. H. Welge. Near threshold photodissociation of acetylene. *J. Chem. Phys.*, 108(2):519, 1998.
- [89] C. G. Morgan, M. Drabbels, and A. M. Wodtke. The correlated product state distribution of ketene photodissociation at 308 nm. *J. Chem. Phys.*, 104:7460, 1996.
- [90] S. Mrozowski. Forbidden lines $\lambda 2967.5$ and $\lambda 2269.8$ of mercury HgI. *Phys. Rev.*, 67:161, 1945.
- [91] A. Mueller. *Model Nucleobase Pairs: Gas Phase Structures, Energetics and Vibrational Dynamics*. PhD thesis, University of Bern, 1999.

- [92] K. Obi, Y. Matsumi, Y. Takeda, S. Mayama, H. Watanabe, and S. Tsuchiya. Fluorescence lifetimes and excitation spectra of the jet-cooled HNO radical. *Chem. Phys. Lett.*, 95(6):520, 1983.
- [93] N. Ochi and S. Tsuchiya. Quantum beat spectroscopy of zeeman splitting and level anticrossing of rotationally selected acetylene ($\tilde{A}^1A_u\ 3\nu_3$) under weak magnetic fields. *Chem. Phys. Lett.*, 140(1):20, 1987.
- [94] N. Ochi and S. Tsuchiya. Rovibronic level structure of electronically excited acetylene (\tilde{A}^1A_u) in a supersonic jet by laser-induced fluorescence and Zeeman quantum beat spectroscopy. *Chem. Phys.*, 152:319, 1991.
- [95] Ch. Ottinger and G. Shen. Molecular beam study of gateway-coupling $N_2(C\ ^3\Pi_u/a'\ ^1\Sigma_u^-)$ and chemical quenching of the metastable $N_2(a')$ state. *J. Chem. Phys.*, 108(5):1997, 1998.
- [96] Ch. Ottinger, A. V. Vilesov, and D. D. Xu. High-resolution study of the luminescent electronic energy transfer reaction of $Xe(^3P_{0,2})$ with $^{14}N_2$ and $^{15}N_2$. *Chem. Phys.*, 192:49, 1995.
- [97] B. H. Pate, K. K. Lehmann, and G. Scoles. The onset of intramolecular vibrational energy redistribution and its intermediate case: The ν_1 and ν_2 molecular beam, optothermal spectra of trifluoropropyne. *J. Chem. Phys.*, 95:3891, 1991.
- [98] L. F. Phillips. Mercury photosensitized luminescence. *Acc. Chem. Res.*, 7:135, 1974.
- [99] D. E. Powers, J. B. Hopkins, and R. E. Smalley. Vibrational relaxation in jet-cooled phenylalkynes. *J. Chem. Phys.*, 74(11):5971, 1981.
- [100] J. M. Price, A. Ludviksson, M. Nooney, M. Xu, Martin R. M., and A. M. Wodtke. Time-of-flight measurements of single rovibrational states of carbon monoxide. *J. Chem. Phys.*, 96(3):1854, 1992.
- [101] G. W. Robinson. Intersystem crossing in gaseous molecules. *J. Chem. Phys.*, 47:1967, 1967.
- [102] D. J. Le Roy and E. W. R. Steacie. The mercury-sensitized polymerization of acetylene. *J. Chem. Phys.*, 12(4):117, 1944.
- [103] E. E. Saloman. Energy levels and observed spectral lines of xenon, XeI through XeLIV. *J. Phys. Chem. Ref. Data*, 33(3):765, 2004.
- [104] T. E. Sharp and H. M. Rosenstock. Franck-Condon factors for polyatomic molecules. *J. Chem. Phys.*, 41:3453, 1964.
- [105] C. D. Sherrill, G. Vacek, Y. Yamaguchi, H. F. Schaefer III, J. F. Stanton, and J. Gauss. The \tilde{A}^1A_u state and the T_2 potential surface of acetylene: Implications for triplet perturbations in the fluorescence spectra of the \tilde{A} state. *J. Chem. Phys.*, 104(21):8507, 1996.

- [106] S. Shida, Z. Kuri, and T. Furuoya. Mercury sensitized polymerization of acetylene. *J. Chem. Phys.*, 28(1):131, 1958.
- [107] R. E. Smalley, L. Wharton, and D. H. Levy. The fluorescence excitation spectrum of rotationally cooled NO_2 . *J. Chem. Phys.*, 63:4977, 1975.
- [108] O. Sneh, A. Amirav, and O. Cheshnovsky. The branching of nonradiative processes in isoquiniline. *J. Chem. Phys.*, 91(6):3532, 1989.
- [109] O. Sneh and O. Cheshnovsky. Surface ejection of electrons by laser-excited metastables of anthracene derivatives. *Chem. Phys. Lett.*, 130:53, 1986.
- [110] O. Sneh and O. Cheshnovsky. Triplet selectivity in surface ejection of electrons by laser-excited metastables of aniline. *Chem. Phys. Lett.*, 146:216, 1988.
- [111] O. Sneh and O. J. Cheshnovsky. Dynamics of triplet states in beam-isolated benzaldehyde. *J. Phys. Chem.*, 95(19):7154, 1991.
- [112] O. Sneh, D. Dünn-Kittenplon, and O. Cheshnovsky. The decay of triplet pyrazine in supersonic jets. *The Journal of Chemical Physics*, 91(12):7331, 1989.
- [113] A. H. Steeves, A. J. Merer, H. A. Bechtel, A. R. Beck, and R. W. Field. Direct observation of the symmetric stretching modes of \tilde{A}^1A_u acetylene by pulsed supersonic jet laser induced fluorescence. *submitted, Mol. Phys.*, 2008.
- [114] J. C. Stephenson, J. A. Blazy, and D. S. King. Spectroscopy and collisional quenching rates of $\tilde{A}^1C_2H_2$ ($\nu'_3 = 0, 1, 2$). *Chem. Phys.*, 85(1):31, 1984.
- [115] C. G. Stevens and J. C. D. Brand. Angular momentum dependence of first- and second-order singlet-triplet interactions in polyatomic molecules. *J. Chem. Phys.*, 58(8):3324, 1973.
- [116] O. P. Strausz, R. J. Norstrom, D. Salahub, R. K. Gosavi, H. E. Gunning, and I. G. Csizmadia. Mercury $6(^3P_1)$ photosensitization of mono- and difluoroethylenes. Correlation of mechanism with calculated molecular orbital energy levels. *J. Am. Chem. Soc.*, 92(22):6395, 1970.
- [117] A. A. Stuchebrukhov and R. A. Marcus. Theoretical study of intramolecular vibrational relaxation of acetylenic CH vibration for $\nu = 1$ and 2 in large polyatomic molecules $(\text{CX}_3)_3\text{YCCH}$, where $\text{X}=\text{H}$ or D and $\text{Y}=\text{C}$ or Si . *J. Chem. Phys.*, 98:6044, 1993.
- [118] A. A. Stuchebrukhov, A. Mehta, and R. A. Marcus. Vibrational superexchange mechanism of intramolecular vibrational relaxation in $(\text{CH}_3)_3\text{CCCH}$ molecules. *J. Phys. Chem.*, 97:12491, 1993.
- [119] P. Swiderek, M. Michaud, and L. Sanche. Condensed phase electron-energy-loss spectroscopy of the low-lying triplet states of acetylene. *J. Chem. Phys.*, 106(23):9403, 1997.

- [120] C. Tanner, M. Thut, A. Steinlin, C. Manca, and S. Leutwyler. Excited-state hydrogen-atom transfer along solvent wires: Water molecules stop the transfer. *J. Phys. Chem. A*, 110(1758), 2006.
- [121] R. L. Thom. *Spectroscopic Investigations of Intersystem Crossing and Triplet State Structure in Acetylene*. PhD thesis, Massachusetts Institute of Technology, 2006.
- [122] R. L. Thom, B. M. Wong, R. W. Field, and J. F. Stanton. Studies of intersystem crossing in acetylene. *J. Chem. Phys.*, 126:184307, 2007.
- [123] J. H. Timmermans, K. K. Lehmann, and G. Scoles. The intramolecular dynamics of allene in the region around 6000 cm^{-1} via eigenstate resolved IR spectroscopy. *Chem. Phys.*, 190:393, 1995.
- [124] A. Tramer, Ch. Jungen, and Lahmani F. *Energy Dissipation in Molecular Systems*. Springer, New York, 2005.
- [125] H. Umemoto, M. Oku, and T. Iwai. Collisional intersystem crossing of $\text{N}_2(a' \ ^1\Sigma_u^-)$ to produce triplet-state molecular nitrogen. *J. Chem. Phys.*, 118(22):10006, 2003.
- [126] G. Vacek, C. D. Sherrill, Y. Yamaguchi, and H. F. Schaefer III. The anomalous behavior of the Zeeman anticrossing spectra of $\tilde{A} \ ^1A_u$ acetylene: Theoretical considerations. *J. Chem. Phys.*, 104(5):1774, 1996.
- [127] N. van Veen, P. Brewer, and R. Behrson. Detection of the $a \ ^1\Pi_g (v'=0, 1) \leftarrow X \ ^1\Sigma_g^+ (v''=0)$ transition in N_2 by laser-induced fluorescence. *J. Chem. Phys.*, 77(9):4326, 1982.
- [128] E. Ventura, M. Dallos, and H. Lischka. The valence-excited states $T_1 - T_4$ and $S_1 - S_2$ of acetylene: A high-level MR-CISD and MR-AQCC investigation of stationary points, potential energy surfaces, and surface crossings. *J. Chem. Phys.*, 118:1702, 2003.
- [129] W. L. Virgo, K. L. Bittinger, A. H. Steeves, and R. W. Field. Contrasting singlet-triplet dynamical behavior of two vibrational levels of the acetylene $S_1 \ 2^13^1B^2$ polyad. *J. Phys. Chem. A*, 111(49):12534, 2007.
- [130] A. D. Walsh. The electronic orbitals, shapes, and spectra of polyatomic molecules. Part I. AH_2 molecules. *J. Chem. Soc.*, page 2260, 1953.
- [131] J. K. G. Watson, M. Herman, J. C. Van Craen, and R. Colin. The $\tilde{A} - \tilde{X}$ band system of acetylene. *J. Mol. Spec.*, 95:101, 1982.
- [132] H. R. Wendt, H. Hippler, and H. E. Hunziker. Triplet acetylene: Near infrared electronic absorption spectrum of the *cis* isomer, and formation from methylene. *J. Chem. Phys.*, 70(9):4044, 1979.

- [133] R. Wetmore and H. F. Schafer. Triplet electronic states of acetylene: cis and trans structures and energies. *J. Chem. Phys.*, 69:1648, 1978.
- [134] B. L. Wexler, B. E. Wilcomb, and N. Djeu. $6\ ^1S_0 - 6\ ^3P_0$ transition in ^{199}Hg : Determination of the A coefficient and self-pressure broadening. *J. Opt. Soc. Am.*, 70(7):863, 1980.
- [135] J. D. White, J. Chen, D. Matsiev, D. J. Auerbach, and A. M. Wodtke. Conversion of large-amplitude vibration to electron excitation at a metal surface. *Nature*, 433:503, 2005.
- [136] B. M. Wong. *Quantum Chemistry for Spectroscopy – A Tale of Three Spins* ($S = 0, \frac{1}{2}, \text{ and } 1$). PhD thesis, Massachusetts Institute of Technology, 2007.
- [137] Y. Yamaguchi, G. Vacek, and H. F. Schafer. Low-lying triplet electronic states of acetylene: cis 3B_2 and 3A_2 , trans 3B_u and 3A_u . *Theor. Chem. Acta.*, 86:97, 1993.
- [138] N. Yamakita, S. Iwamoto, and S. Tsuchiya. Predissociation of excited acetylene in the \tilde{A}^1A_u state around the adiabatic dissociation threshold as studied by LIF and H-atom action spectroscopy. *J. Phys. Chem. A*, 107(15):2597, 2003.
- [139] N. Yamakita and S. Tsuchiya. Zeeman quantum beat observed by ir-uv double resonance lif spectroscopy of acetylene in the $\tilde{a}^1a_u\ 3\nu'_3 + \nu'_6$ and $3\nu'_3 + \nu'_4$ ungerade vibrational states. *Chem. Phys. Lett.*, 348:53, 2001.
- [140] A. R. Ziv and W. Rhodes. The spectroscopic channel basis for radiative and radiationless processes: The effective system excited states and interference effects in absorption spectra. *J. Chem. Phys.*, 65:4895, 1976.

Kyle L. Bittinger *Curriculum Vitae*

EDUCATION **Massachusetts Institute of Technology**, Cambridge, MA

PhD, 2009

Department of Chemistry / George Harrison Spectroscopy Laboratory

Thesis: Spectroscopic Signatures of Doorway-Mediated Intersystem Crossing

University of Pittsburgh, Pittsburgh, PA

B.S., *Magna Cum Laude*, 2001

Major: Chemistry (Bioscience option)

Thesis: Angle-Energy Resolved Scattering in the Penning Ionization of H_2 by He^*

HONORS & AWARDS

DuPont Graduate Fellow, Department of Chemistry, M.I.T. (2001-2002), Mary Louise Theodore Award and Carrie T. Holland Scholarship, Department of Chemistry, University of Pittsburgh (2000-2001)

PUBLICATIONS & PRESENTATIONS

Virgo WL, **Bittinger KL**, Steeves AH, Field RW. Contrasting dynamical behavior of two vibrational levels of the S_1 $2^13^1B^2$ polyad of acetylene. *Journal of Physical Chemistry A* **111**, 12534 (2007).

Bittinger KL, Virgo WL, Field RW. Singlet-triplet coupling and the non-symmetric bending modes of acetylene $^1\tilde{A}_u$. *68th International Symposium on Molecular Spectroscopy* in Columbus, OH, June 18-23, 2007.

Bittinger KL. Perl in the Lab. *Atomistic Modeling And Simulation Seminar: Show and Tell Session*, M.I.T., November 8, 2006.

Gulati K, Longley EG, Dorko MJ, **Bittinger KL**, Siska PE. Angle-energy distributions of Penning ions in crossed molecular beams IV. $He^*(2^1S, 2^3S) + H_2 \rightarrow He + H_2^+ + e^-$. *Journal of Chemical Physics* **120**, 8485 (2004).